Consortium for Small-Scale Modelling

Newsletter

February 2011 *No. 11*

Deutscher Wetterdienst

MeteoSwiss

Ufficio Generale Spacio Aero e Meteorologia

ΕΘΝΙΚΗ ΜΕΤΕΩΡΟΛΟΓΙΚΗ ΥΠΗΡΕΣΙΑ

Instytucie Meteorogii i Gospodarki Wodnej

Administratia Nationala de Meteorologie

Agenzia Regionale per la Protezione Ambientale dell Emilia Romagna Servizio Idro Meteo Clima

Federal Service for Hydrometeorology and Environmental Monitoring

Amt für GeoInformationswesen der Bundeswehr

Centro Italiano Ricerche Aerospaziali

Agenzia Regionale per la Protezione Ambientale dell Piemonte

www.cosmo-model.org

Editors: Ulrich Schättler (DWD); Cosmin Barbu (NMA)

Table of Contents

This COSMO Newsletter contains the proceedings of a few of the many presentations given at the last COSMO General Meeting which took place from 6 to 10 September 2010 in Moscow, Russia. - For the presentations themselves, please refer to the COSMO web-site at http://www.cosmo-model.org/content/consortium/generalMeetings.priv/default.htm.

One important achievement of the General Meeting in Moscow has been the approval of the COSMO Science Plan 2010-2014. This important document for the future development of the COSMO model can be downloaded from the COSMO web-site at http://www.cosmo-model.org/content/consortium/reports/default.htm.

Last but not least, the last General Meeting has also seen the creation of a new Working Group Predictability and Ensemble Methods (WG 7), which is chaired by Chiara Marsigli from ARPA-SIMC.

For the next General Meeting, COSMO will gather in beautiful Rome from 5 to 9 September 2011.

Marco Arpagaus
COSMO Scientific Project Manager

Figure 1: Participants of the 12th COSMO General Meeting in Moscow

The effects of T2m assimilation on surface fluxes in COSMO-I2

Marco Galli[1], Massimo Milelli[2], Claudio Cassardo[1], Matteo Giorcelli[2,3]

1: University of Torino, Torino, Italy
2: ARPA Piemonte, Torino, Italy
3: ARIANET S.r.l, Milano, Italy

1. Introduction

Recent developments of the numerical weather prediction models make it possible to use very high resolution models in the daily operational routine. The COSMO-I2 operational configuration reflects this trend. The model setup makes it possible to produce operational weather forecasts all the Italian country at a resolution of 2.8 km.

Such a high resolution grid requires an adequate analysis procedure, so that the initial model fields can represent properly the characteristics of the atmospheric state typical of those scales. In particular, in this paper the attention is focused on the use of a high density weather stations network and on the assimilation of surface data, in particular the T2m (2 metres air temperature). ARPA Piemonte owns such a network, with a much higher number of stations in Piemonte region rather than the only 8 SYNOPs in the same area (see figure 1 for their geographical location).

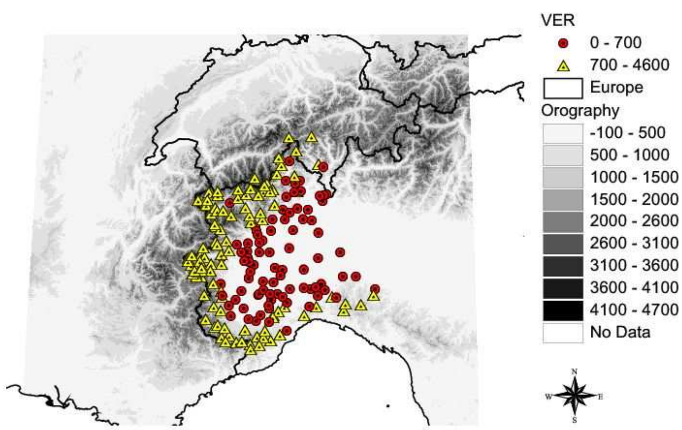

Figure 1: the ARPA Piemonte network of weather stations. The yellow triangles are the mountain stations (over 700 metres ASL), the red circles are the plain stations.

The goal of the work presented in this paper is to take advantage of such a network for enhancing the quality of the COSMO-I2 analysis production. In previous studies (Milelli et al., 2008; 2010), it has been shown how the assimilation of T2m has a major importance in making the forecast simulation differ significantly if it is included in the surface data assimilation or not. The step to this main goal presented in this paper deals with the study of the effect of the assimilation of the T2m on the surface fluxes, hence on how it influences the coupling between the soil state and the atmospheric state. It has been studied how the temperature data assimilation introduces perturbations in the model simulations.

2. Organization of the study

In order to get to this goal, it has been decided to carry out an experiment aimed at comparing the performance of COSMO-I2 with and without the T2m assimilation (from now on, these different model setups will be identified as TEMP - with T2m assimilation - and CTRL - without T2m assimilation). The experiment has been carried out in an operational-like framework.

This means that forecast simulations were performed initialising the model at 00 UTC and at 12 UTC, and carrying on, for each initialisation, a 24 hours simulation, with the first 12 hours of T2m assimilation and then 12 hours of free forecast for the TEMP, to be compared with the correspondent CTRL simulation. To have a better statistics for the results of the experiments, the simulations have been carried out not just for one day, but for a period of consecutive days. The first period goes from the 19th to the 25th of May 2009, and the second period from the 3rd to the 17th of January 2009. These periods have been chosen because the first one represents typical anticyclonic and sunny stable weather conditions in Piemonte (see figure 2), and the last one was characterised by a snow covered land and a strong surface temperature inversion (see figures 3 and 4).

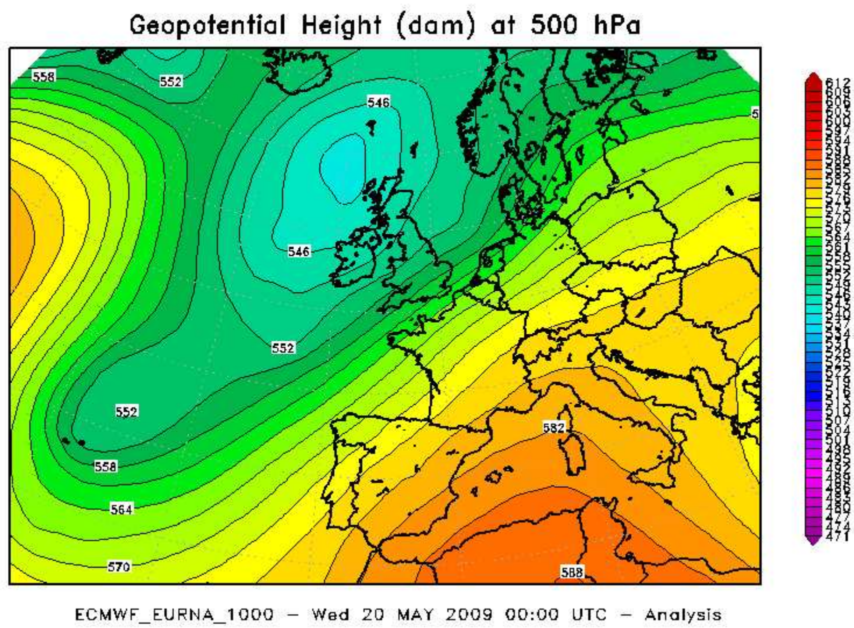

Figure 2: the anticyclonic conditions of the May period shown by the 500 hPa geopotential height by the ECMWF analysis.

It has to be mentioned that the operational setup of COSMO-I2 gets the boundary conditions from the COSMO-I7, which gets its own from the ECMWF IFS.

The area considered for this study is reported in figure 5.

The goodness of the TEMP with respect to the CTRL runs has been evaluated by comparing the mean error (ME) and the root mean square error (RMSE) of such simulations. These statistical indices have been calculated with respect to the ARPA ground stations network observations for the standard variables (T2m, RH2m, W10m[1]); for the land surface energy

[1]From here on, RH2m will stand for 2 metres relative humidity and W10m will stand for 10 metres wind

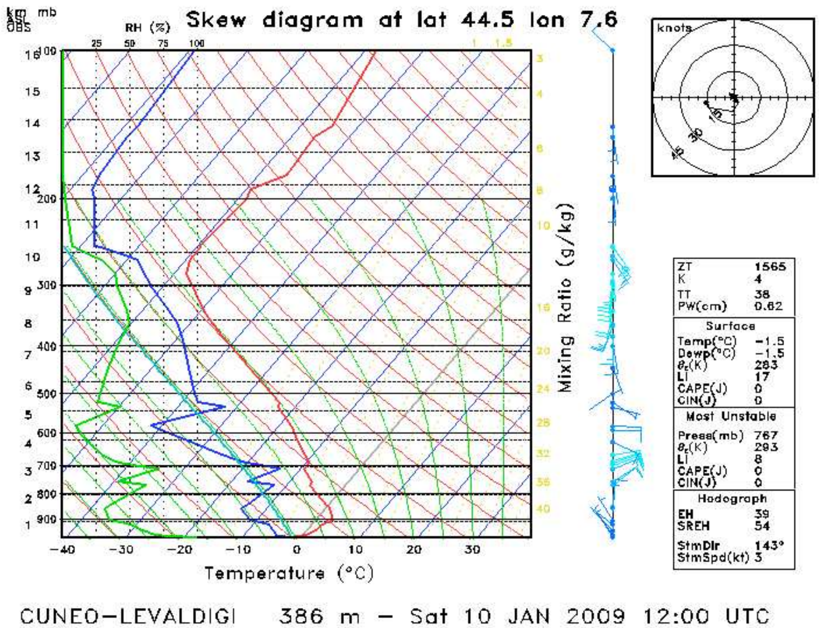

Figure 3: a radiosounding diagram from Cuneo Levaldigi to show the strong surface temperature inversion conditions characterising the January period.

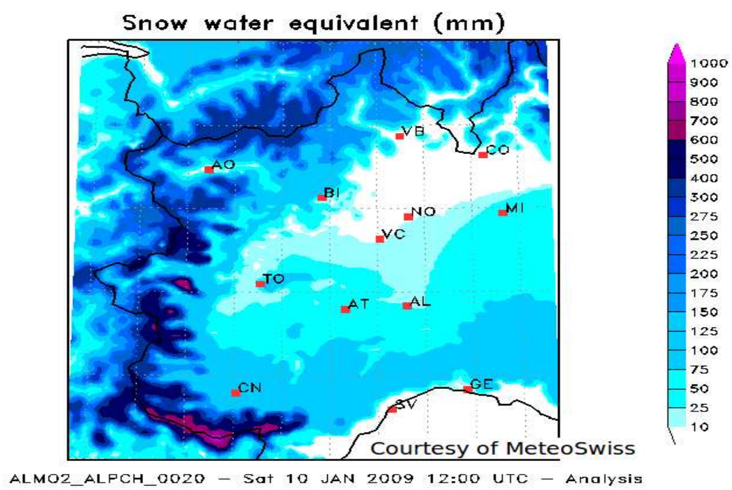

Figure 4: the snow coverage as represented by the snow cover analysis in the January period. Courtesy of MeteoSwiss.

fluxes, the COSMO ones have been compared with the output of a land surface dedicated model, UTOPIA (University of TOrino land Process Interaction with Atmosphere), considered as proxy data of reality. UTOPIA model is already operational in ARPA Piemonte for hydrological and agrometeorological monitoring purposes.

speed.

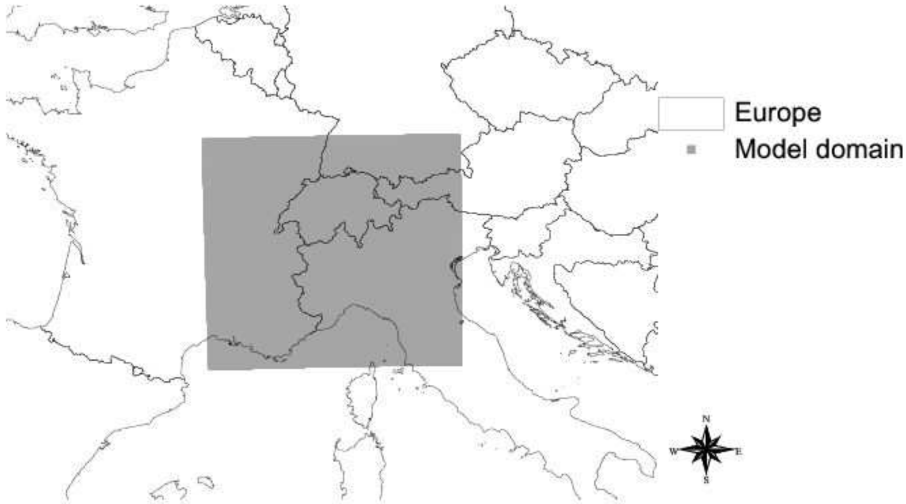

Figure 5: simulations domain. In grey the area integrated with the COSMO-I2 setup, in white the area involved in the COSMO-I7 runs.

3. The current COSMO performance

Effects on standard variables As a first step, the difference of the RMSE scores between the TEMP and the CTRL runs has been calculated, and its statistical significance has been assessed using the bootstrap technique. All the graphics in this section represent the differences of the RMSE calculated for the TEMP and the CTRL runs, for each forecast time (reported along the x-axis) and for each day of the test case (reported along the y-axis). White areas in the graphics represent a non significant difference in the statistical scores, green areas mean that the TEMP simulation shows a better RMSE than the CTRL and red areas mean that the TEMP simulation behaves worse than the CTRL.

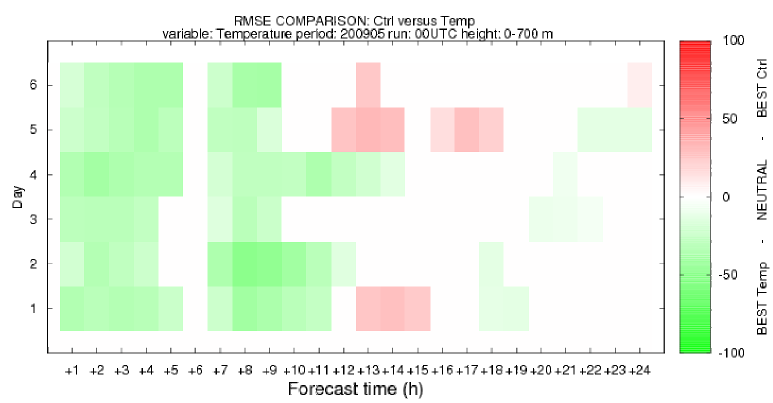

Figure 6: summary of the significance of the difference of the RMSE scores for T2m between the TEMP and the CTRL runs, May period, 00 UTC initialised runs.

Figures 6 and 7 are about the scores calculated for the temperature for the May case. For the 00 UTC initialised runs, the effect of the T2m assimilation on the COSMO description is positive just during the data assimilation process, then, at the start of the free forecast, the effects become negligible or slightly negative. By the end of the forecast runs, the effects

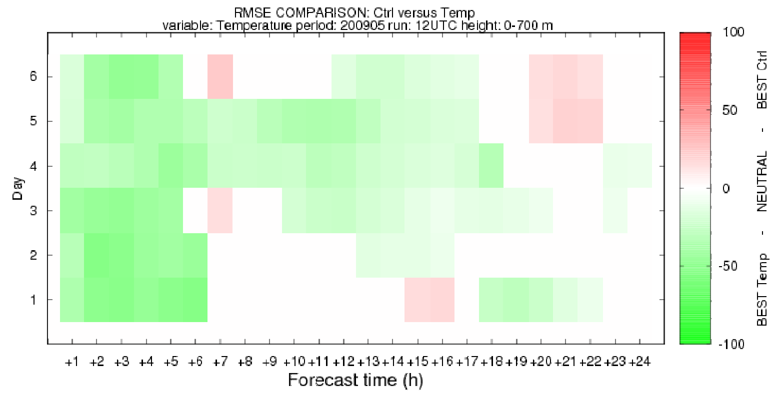

Figure 7: summary of the significance of the difference of the RMSE scores for T2m between the TEMP and the CTRL runs, May period, 12 UTC initialised runs.

turn out to be negligible or slightly good. For the 12 UTC runs the positive effects of the T2m assimilation last for some hours after the end of the nudging, and in only very few cases the result of the experiment is bad.

Temperature is the physical variable which is best affected by the assimilation of T2m. The variable with a worse response to the T2m assimilation is the RH2m. Figures 8 and 9 summarise the RMSE comparison between TEMP and CTRL.

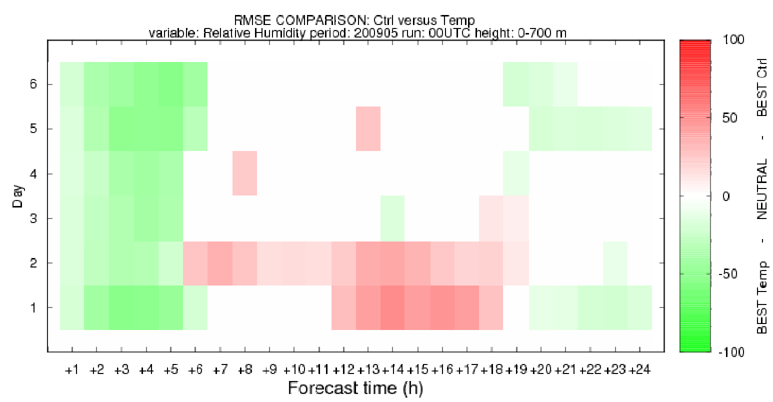

Figure 8: summary of the significance of the difference of the RMSE scores for RH2m between the TEMP and the CTRL runs, May period, 00 UTC initialised runs.

The effects on the RH2m description vary according to the day-night cycle rather than according to the time distance to the end of the data assimilation. In fact, from both figures it is possible to notice that the TEMP description is generally improved at night time, and worsens or shows no significant difference during day time.

For the January case, the scores of T2m and W10m are reported, because in these conditions it's wind speed more negatively affected by the T2m assimilation.

The effects on T2m are good for a longer time compared to the May case. The 00 UTC runs (figure 10) are positively affected by the T2m assimilation. In some days, the positive effect lasts for all the 24 simulated hours, for other it ceases during the data assimilation time,

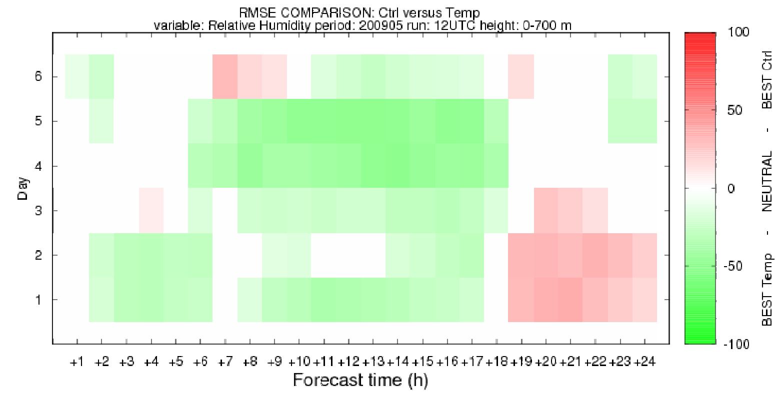

Figure 9: summary of the significance of the difference of the RMSE scores for RH2m between the TEMP and the CTRL runs, May period, 12 UTC initialised runs.

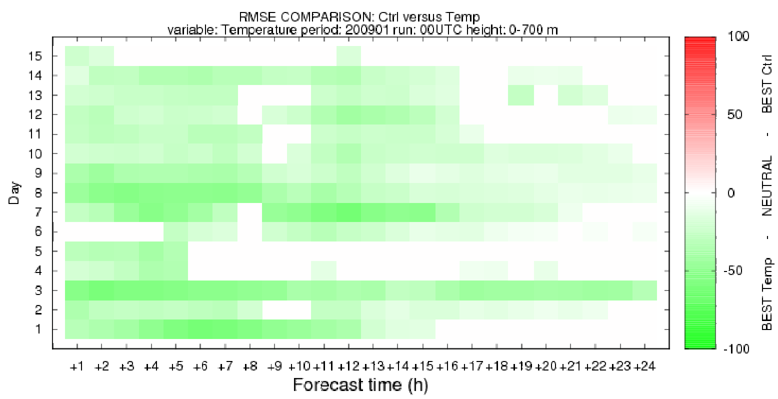

Figure 10: summary of the significance of the difference of the RMSE scores for T2m between the TEMP and the CTRL runs, January period, 00 UTC initialised runs.

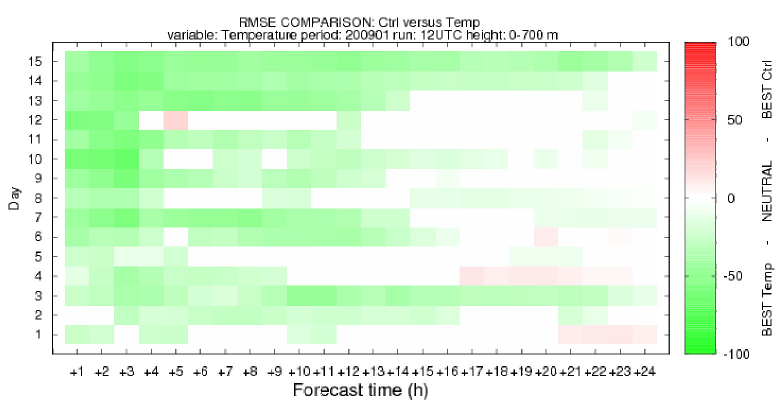

Figure 11: summary of the significance of the difference of the RMSE scores for T2m between the TEMP and the CTRL runs, January period, 12 UTC initialised runs.

and there are no worsening in the TEMP runs compared to CTRL ones. The 12 UTC runs (figure 11) show good results as well, even if there are some isolated forecast times and days in which the T2m description worsens.

The reason of this general great improvement has to be found in the presence of the strong temperature inversion: an improvement in the analysis “is trapped” in the lower atmospheric layers, and is not influenced by the development of convection.

On the other hand, if for T2m the results are very good, for W10m are not. Figures 12 and

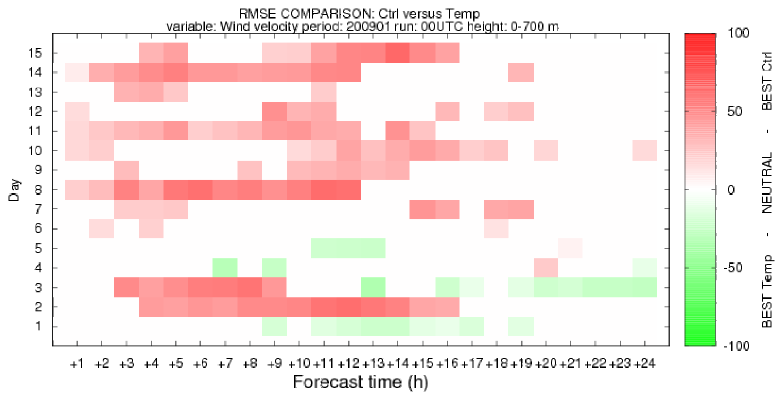

Figure 12: summary of the significance of the difference of the RMSE scores for W10m between the TEMP and the CTRL runs, January period, 00 UTC initialised runs.

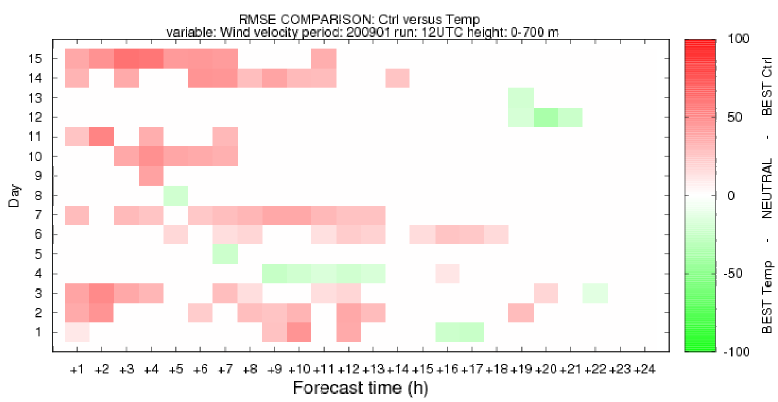

Figure 13: summary of the significance of the difference of the RMSE scores for W10m between the TEMP and the CTRL runs, January period, 12 UTC initialised runs.

13 show, in fact, how the RMSE generally worsens or, at least, is not significantly changed in the TEMP runs. In general, worsening is heavier for 00 UTC runs rather than 12 UTC ones, and during the data assimilation time window rather than in the free forecast time.

Effects on soil-atmosphere fluxes As previously mentioned in section 2, the comparisons of the statistical scores of TEMP and CTRL simulations has been carried out also for the soil-atmosphere fluxes, i.e. sensible heat flux and latent heat flux. The graphics in this section represent a comparison of the RMSE (top) and the ME (bottom) of the TEMP simulations (dotted line) and the CTRL simulations (marker with the confidence bar), at the different forecast times. The markers show a 90% confidence bar, obtained by using the bootstrap technique. The statistical scores have been calculated globally over all the experiment days, for each experiment (the May and the January one).

The data presented in this section are averaged along the different days for both experiments.

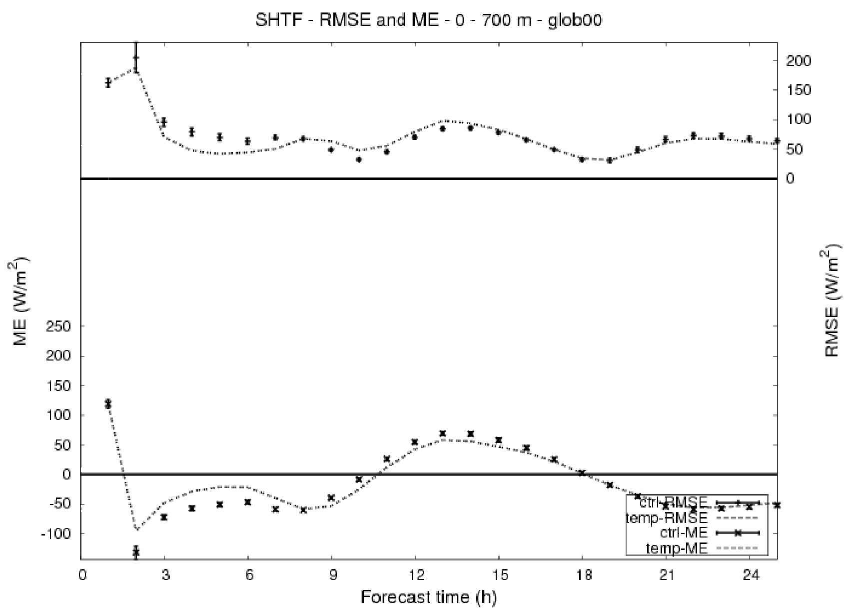

Figure 14: RMSE and ME for the sensible heat flux, May experiment, 00 UTC runs.

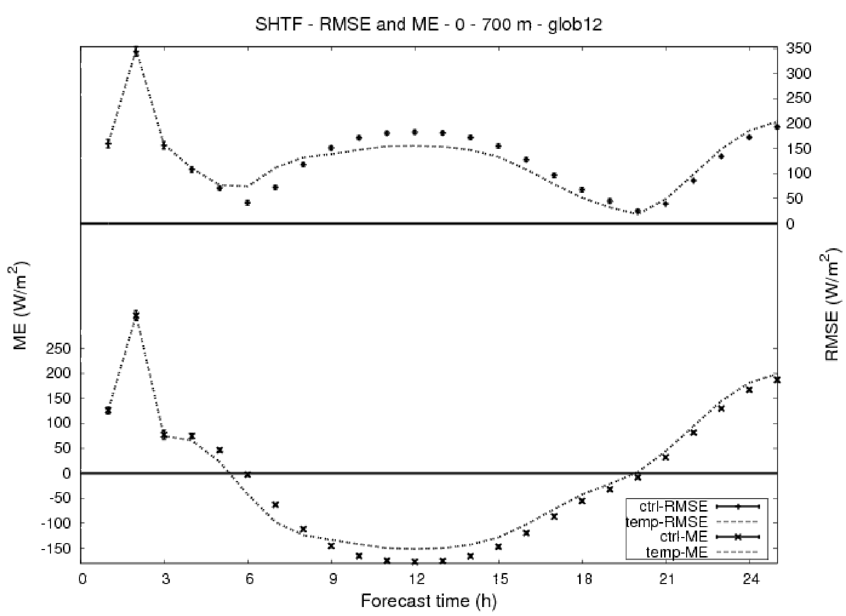

Figure 15: RMSE and ME for the sensible heat flux, May experiment, 12 UTC runs.

Figures 14 and 15 show a comparison of ME and RMSE of sensible heat flux for the May case, in particular for the runs initialised at 00 UTC. In the 00 UTC runs, TEMP simulations show better values of both indexes during the first hours of T2m assimilation; after dawn, but still within the assimilation window, TEMP values worsen.

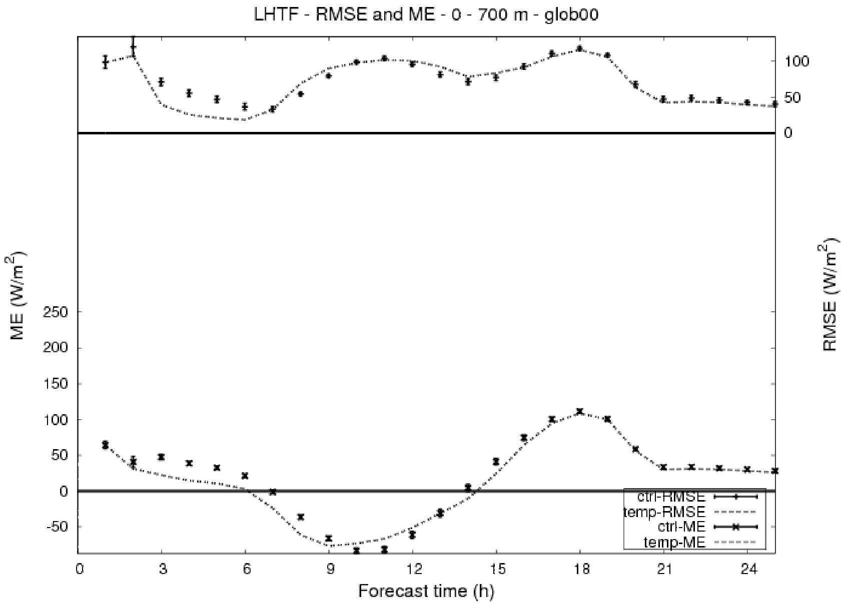

Figure 16: RMSE and ME for the latent heat flux, May experiment, 00 UTC runs.

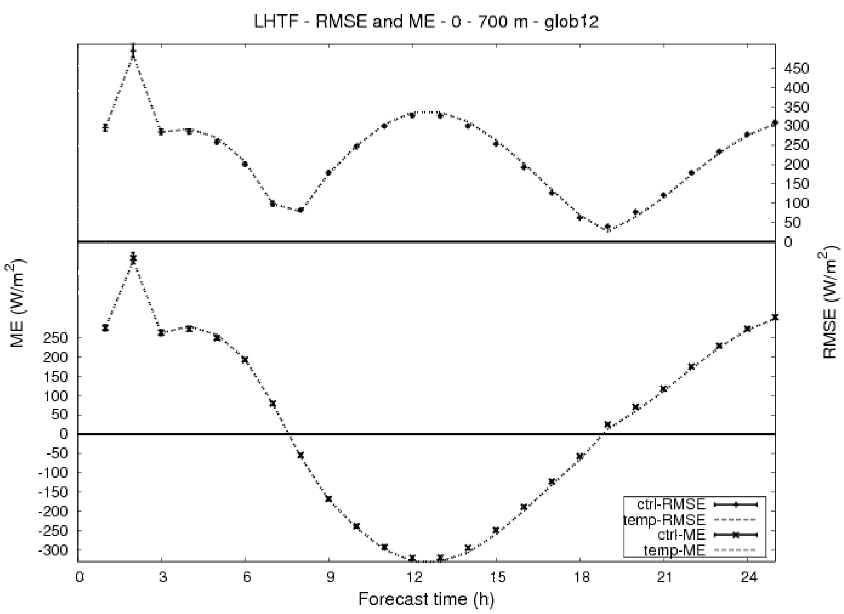

Figure 17: RMSE and ME for the latent heat flux, May experiment, 12 UTC runs.

Figures 16 and 17 show the corresponding values for the latent heat flux. The only important differences can be found in the 00 UTC runs. The TEMP simulations tend to have better values for the latent heat flux in the first hours of T2m assimilation, while they show worse values by the end of the nudging window.

Passing to considering now the January test case, it is possible to notice, from figures 18 and 19, that the sensible heat flux is generally described more poorly by the TEMP simulations than the CTRL ones. This phenomenon is longer in the 00 UTC runs than in the 12 UTC ones.

Figures 20 and 21 show, instead, the behaviour of the statistical indexes for the latent heat

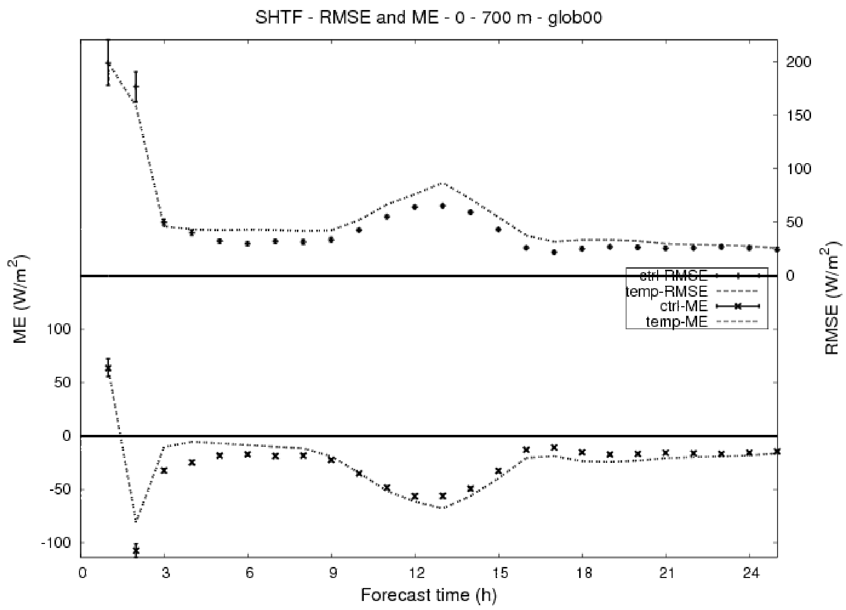

Figure 18: RMSE and ME for the sensible heat flux, January experiment, 00 UTC runs.

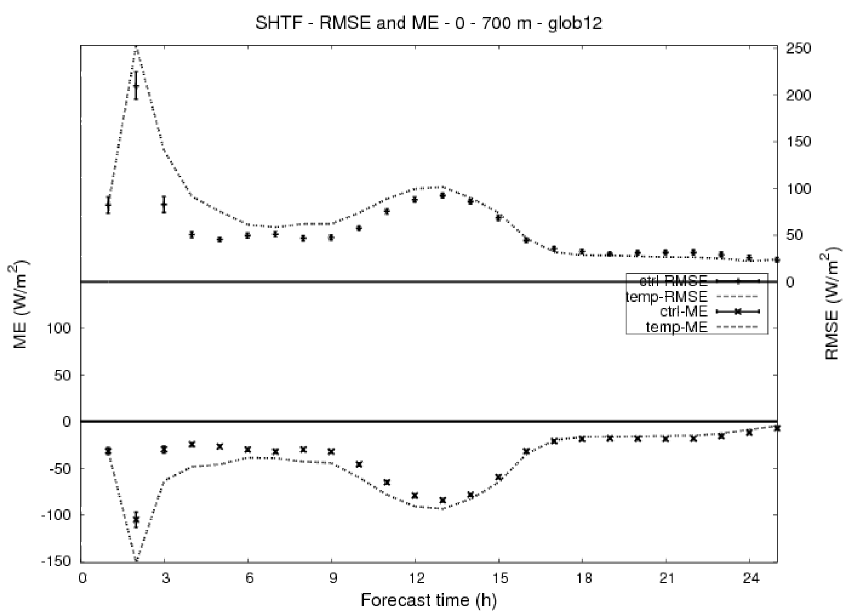

Figure 19: RMSE and ME for the sensible heat flux, January experiment, 12 UTC runs.

flux. Also in this case, the time interested by the T2m assimilation is characterised by worse scores in the TEMP rather than in the CTRL simulations.

In the January case, in general, the description of the soil-atmosphere energy transfer worsens, for both fluxes.

A common feature of all the graphics presented in this section is the initial high value of RMSE and ME. Further investigations are still needed to understand the reason of these spikes, but a first hypothesis to work on are initialisation problems of the first atmospheric layer compared to the soil thermal and hydrological state.

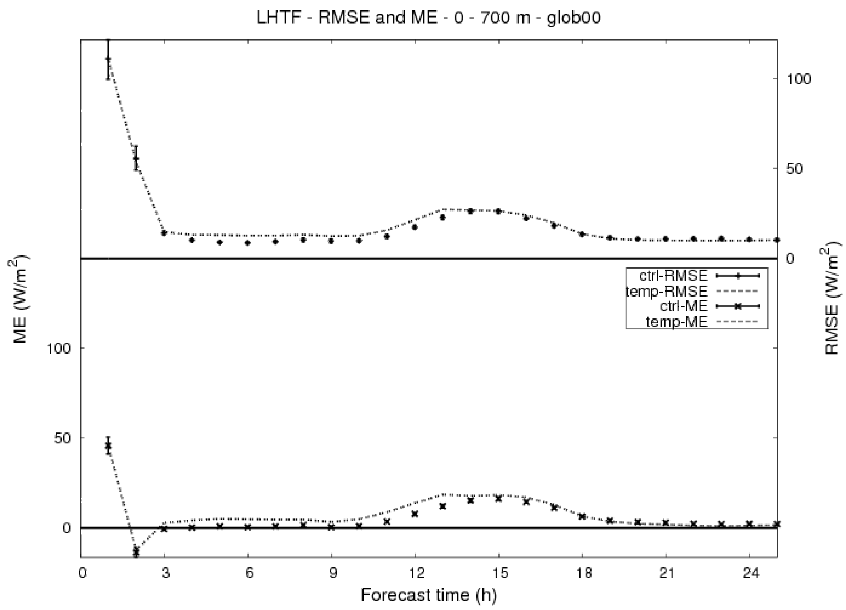

Figure 20: RMSE and ME for the latent heat flux, January experiment, 00 UTC runs.

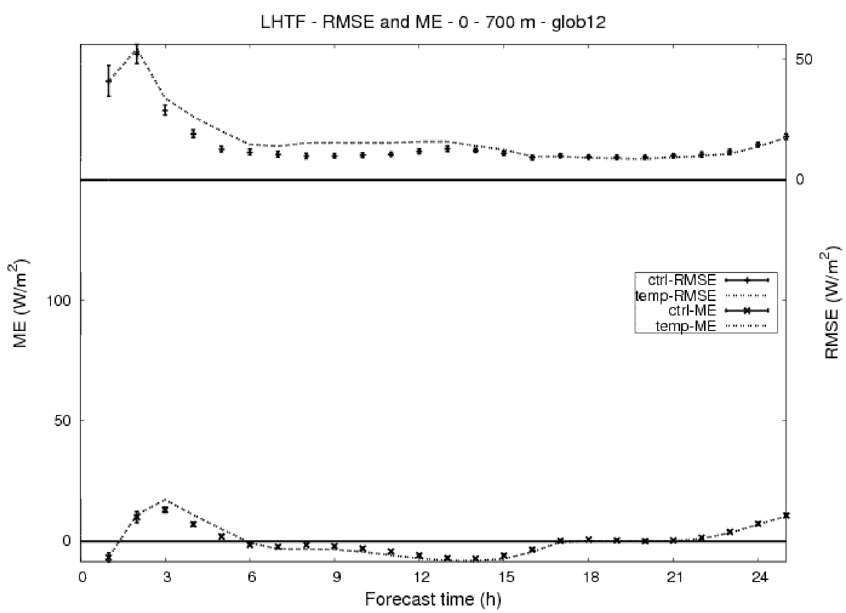

Figure 21: RMSE and ME for the latent heat flux, January experiment, 12 UTC runs.

Effects on the PBL height as an indicator of the stability profile An additional check has been performed on the PBL height, considering it as a way to investigate the atmospheric stability near the land surface. This aims to investigate the effects that the T2m assimilation introduces in the first vertical layers of the model above the surface.

In this part of the study, no comparison against real data has been performed because no enough real or proxy data were available. The only purpose of this part is to assess the statistical difference in the PBL height described by the TEMP and the CTRL simulations.

In the framework of this study, the PBL height has been defined as the point where holds

$$\theta(z = \text{surface}) = \theta_e(z = H_{PBL}),$$

where $\theta(z)$ is the potential temperature profile and $\theta_e(z)$ the potential temperature profile. The data presented in this section refer to a sample day of the May experiment.

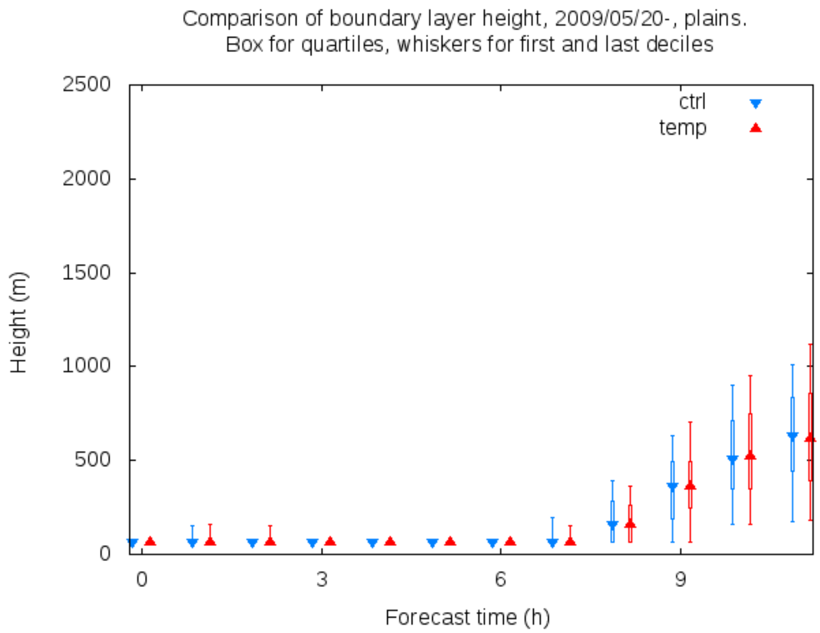

Figure 22: PBL height distributions at different forecast times, during the T2m assimilation time window, 00 UTC initialised run.

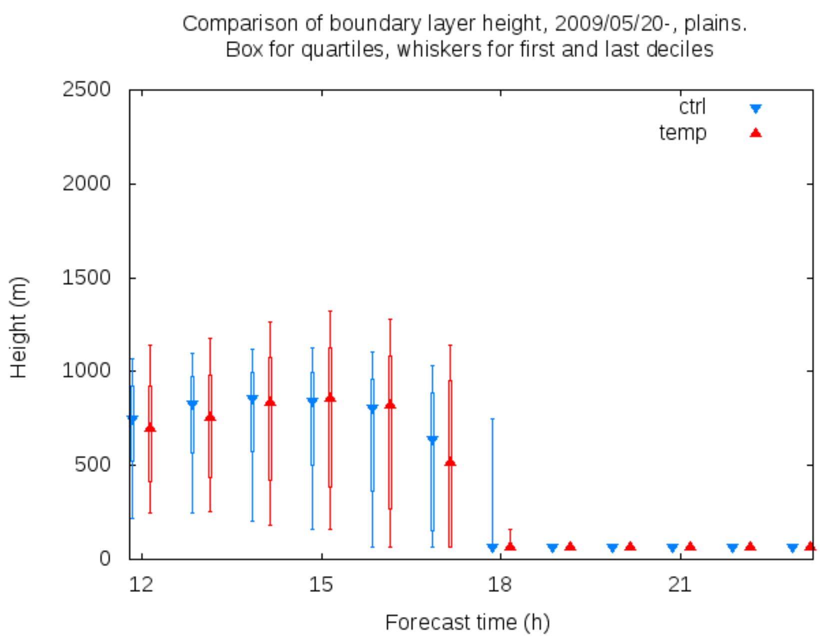

Figure 23: PBL height distributions at different forecast times, after the T2m assimilation time window, 00 UTC initialised run.

Figures 22 and 23 show the time series of the distributions of the PBL heights over the Piemonte domain (14641 points) for a sample day in the May period. The distributions are represented by their mean values (the triangular marker), the quartiles (the boxes) and the first and last deciles (the whiskers). The initialisation of this particular run is 00 UTC.

Due to the high number of data, the runs tests determine with a 99% confidence level that each corresponding distribution of the TEMP and of the CTRL simulations are statistically different, for each forecast time. This is true both for the distributions which refer to forecast times within the T2m assimilation window, and for the ones in the free forecast.

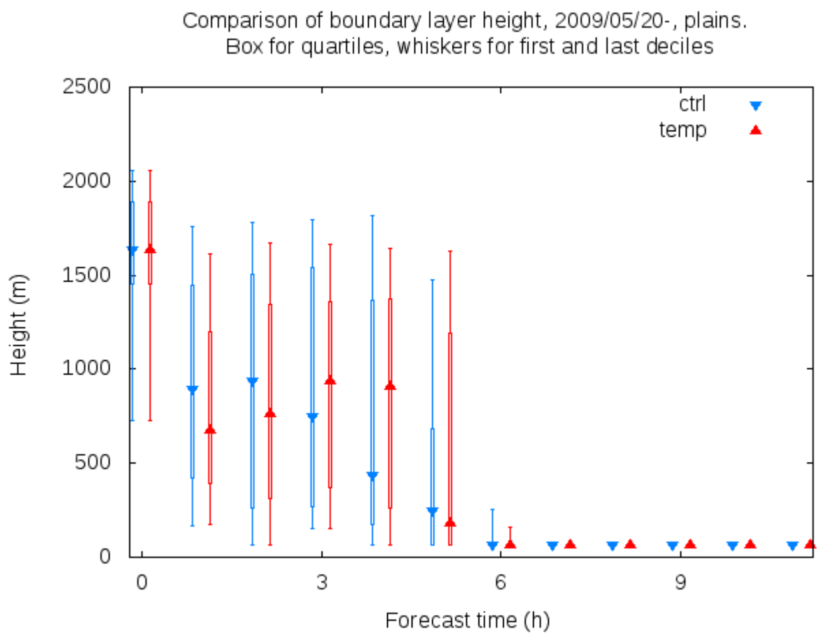

Figure 24: PBL height distributions at different forecast times, during the T2m assimilation time window, 12 UTC initialised run.

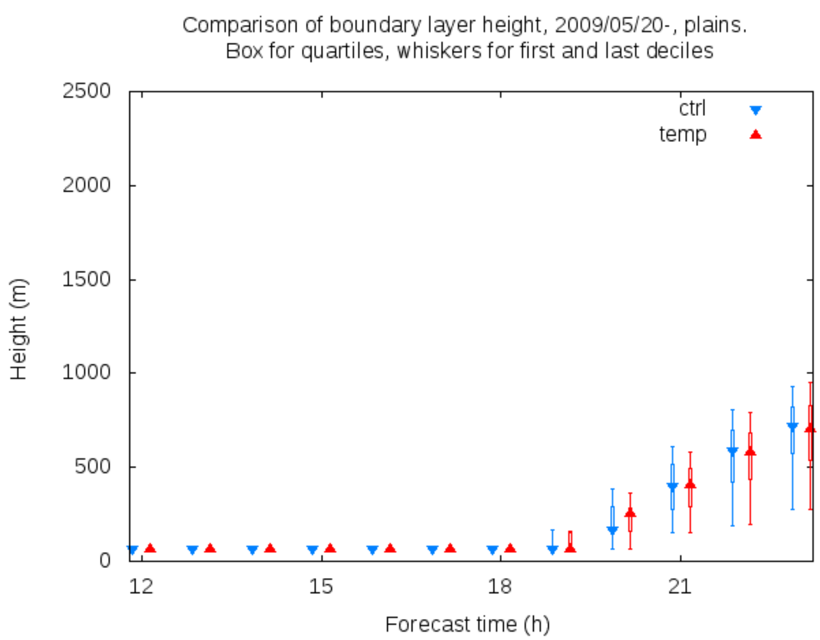

Figure 25: PBL height distributions at different forecast times, after the T2m assimilation time window, 12 UTC initialised run.

Figures 24 and 25 are conceptually similar to figures 22 and 23. They represent the simulation following by 12 hours the previous one. Also in this case the runs test makes it possible to state that, with a 99% confidence level, each TEMP distribution differs from the corresponding one of CTRL. This is true in general, for every day both of May and January periods (not shown for brevity), and for every initialisation time. Indeed, it is important to see that the PBL heights calculated by the 00 UTC COSMO simulations, for its last 12 hours, which should describe the same physical situation as the first 12 hours of the 12 UTC runs, in practice show very different PBL heights distributions, both in mean values and in spread. Also the model initialisation plays a central role, and not just the COSMO data assimilation.

Effects on the whole temperature profile To conclude the test performed by activating the T2m assimilation in COSMO, also the complete vertical temperature profile have been studied. The description of the temperature profile given by COSMO has been compared to the only radiosounding available on the considered domain, Cuneo Levaldigi. Unfortunately, due to problems in the operational measurements during May, only the January data can be used for this comparison. The statistical scores reported in this paper are, for brevity, only the ones about the ME, because this permits to distinguish between the model overestimations and its underestimations. The graphics presented are averaged over all the days of the January experiment.

It is possible to see in figure 26 that the T2m assimilation introduces a big deviation in the ME profiles. Not only, in the model layers closer to land surface, the magnitude of the errors is rather different, but also the sign in the ME changes. This means that the behaviour of the model changes not just quantitatively, but also qualitatively (the TEMP run underestimates rather than overestimating, at least in this case). Anyway, by the end of the simulation (figure 26) the errors committed by the different simulations become similar.

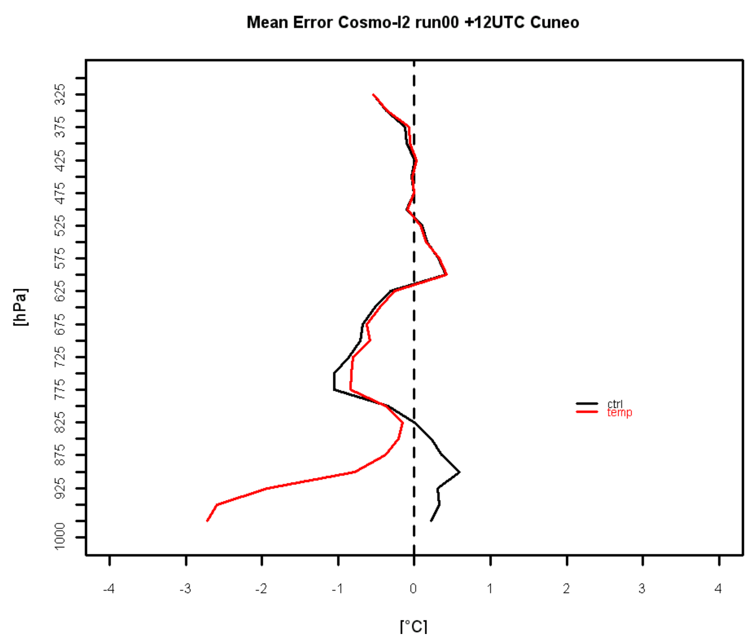

Figure 26: mean error vertical profile for temperature, 12 hours forecast time, 00 UTC initialisation.

Figures 28 and 29 refer to the 12 UTC initialised runs. It is possible to see from these figures how the error, at the end of the T2m assimilation, becomes different in the lower atmosphere, but not at the surface. In this case too, by the end of the simulations the errors of TEMP and CTRL experiments become more similar.

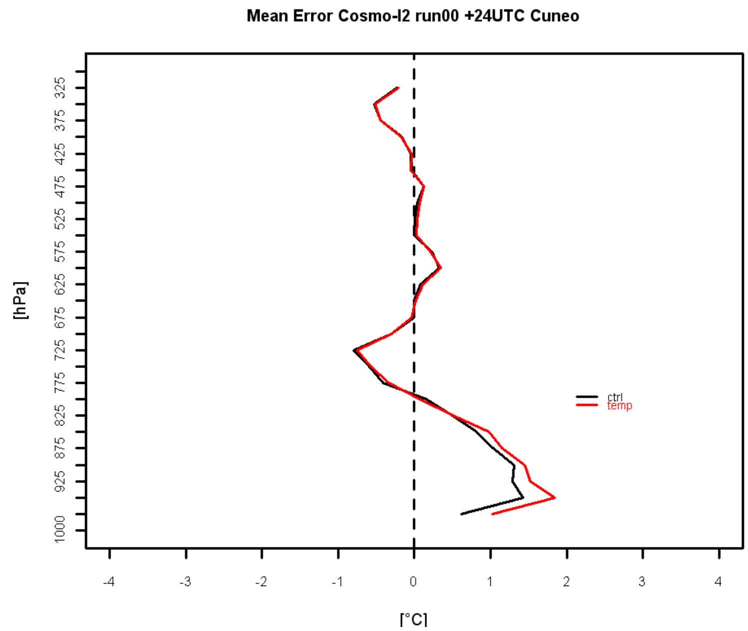

Figure 27: mean error vertical profile for temperature, 24 hours forecast time, 00 UTC initialisation.

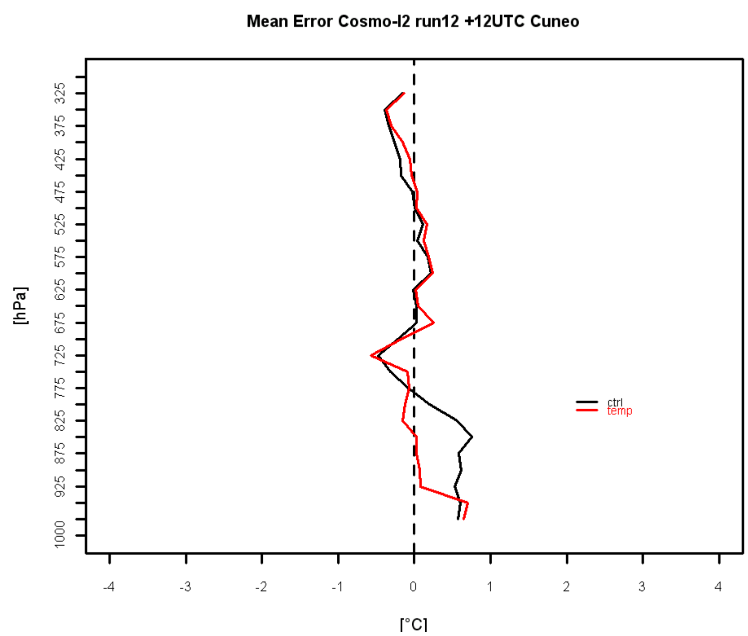

Figure 28: mean error vertical profile for temperature, 12 hours forecast time, 12 UTC initialisation.

All the figures relative to this section suggest, in any case, a revision of the parameters used for the vertical spread of the nudging increments.

Concluding remarks on the current COSMO performance Just to summarise all the different checks results, it is important to state that

T2m description is positively affected by its assimilation;

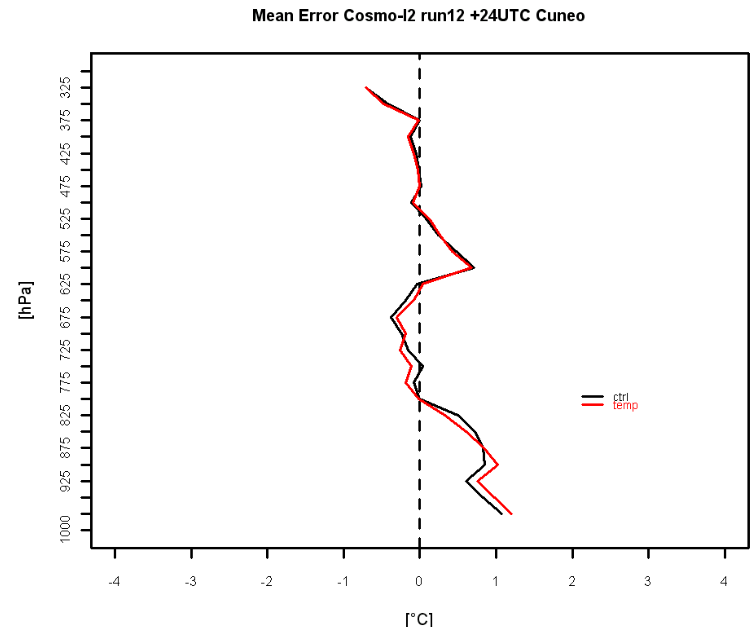

Figure 29: mean error vertical profile for temperature, 24 hours forecast time, 12 UTC initialisation.

RH2m and W10m description is neutrally or negatively affected, depending on the present atmospheric conditions;

surface fluxes description is neutrally affected in the May case, slightly negatively in the January case;

PBL height , hence lower atmospheric stability, differs significantly with or without the T2m assimilation;

temperature profiles are negatively affected by the T2m assimilation for the 00 UTC initialised runs, while positively affected for the 12 UTC runs.

4. The proposed developments: the FASDAS technique

The results of the checks shown in the previous sections suggest to improve the scheme involved in the T2m assimilation, in order to use and take advantage of the great availability of the T2m data in the analysis production. The approach chosen for enhancing the quality of the COSMO analysis production relies on the papers written by Alapaty et al. (2008; 2001), updating, in the surface level data assimilation phase, not just the atmospheric fields, but also the soil state related variables and the soil to atmosphere energy and moisture fluxes. This approach, of course, requires to investigate also the horizontal spreading of the nudging increments.

FASDAS technique (Flux Adjusting Surface Data Assimilation System) is based on the assumption that the T2m and RH2m assimilation should not have heavy consequences on the equilibrium of an atmospheric model.

Recalling the COSMO documentation of the nudging based data assimilation scheme, it is possible to write the time variation of a surface level variable α (let α stand for T2m or

Q2m[2]):

$$\frac{\partial \alpha}{\partial t} = P(\alpha, z, t) + G_\alpha(\hat{\alpha} - \alpha), \tag{1}$$

where P stands for describing all the model dynamics and its physical parametrizations, G_α is the nudging weighting factor, and $\hat{\alpha}$ is an observational value of α.

It is possible to write the two terms of the right hand side of (1) as

$$\begin{aligned} P(\alpha, z, t) &= \frac{\partial \alpha^P}{\partial t} \\ G_\alpha(\hat{\alpha} - \alpha) &= \frac{\partial \alpha^F}{\partial t}. \end{aligned}$$

Recalling that the time variation of a surface variable is proportional to the divergence of the corresponding flux, it is possible to write

$$\frac{\partial \alpha}{\partial t} = -\frac{H_1^\alpha - H_S^\alpha}{\rho C \Delta z}, \tag{2}$$

where H_1^α is the value of the particular flux at the first atmospheric level, H_S^α refers to the surface value, Δz is the thickness of the surface-first atmospheric level layer, and ρC is the product between air density and heat capacity.

Using equation (2), it is possible to calculate the flux associated to the assimilation of α:

$$H^{\alpha,F} = \rho C \left(\frac{\partial \alpha^F}{\partial t}\right) \Delta z. \tag{3}$$

This flux can be considered as the correction to be summed to the values of the fluxes given by the model physics to balance the α assimilation.

It is possible to use the result in equation (3), considering α standing both for T2m and for Q2m, so calculating the sensible heat flux (the energy flux related to T2m) and the latent heat flux (related to Q2m) corrections, and use the results to calculate how much the first soil layer temperature should be varied in order to maintain the equilibrium between all the components of the land-surface system:

$$\Delta T_g^F = \left(\frac{\partial T_g^F}{\partial t}\right) = (H_{\theta,S}^F - H_{q,S}^F)\frac{\Delta t}{C_g}, \tag{4}$$

where $H_{\theta,S}^F$ and $H_{q,S}^F$ are respectively the surface level sensible heat flux and the latent heat flux, Δt is the model time step, and C_g is the soil heat capacity. It must be noted that the minus sign for the latent heat flux is justified because a positive (negative) adjustment of T_g can cause a growth (decrease) of the latent heat flux, because it is a function of the saturation vapour pressure calculated at the temperature T_g.

It is important to observe, however, that the fluxes are adjusted so that T2m and Q2m are shifted towards the observed values. The fluxes are altered to allow the atmospheric structure in a realistic way, regardless of the reason of the errors of the simulated T2m and Q2m.

Before continuing, one must recall the state of art of the 2 metres values analysis. It is common practice (also for the COSMO soil moisture analysis) to attribute the main source of the T2m errors in wrong estimations of just one aspect of the soil state, usually its

[2]Q2m will denote, from this point on, the 2 metres mixing ratio. It will be used to describe atmospheric humidity content in place of RH2m.

```
PROGRAM lmorg
  [...]
timeloop: DO ntstep = nstart , nstop
    [...]
    IF (luseobs) CALL organize_assimilation ('surface',&
                                       izerror, yzerrmsg)
    [...]
    IF(luseobs) CALL organize_assimilation ('FASDAS',&
                                     izerror, yzerrmsg)
    [...]}
    CALL organize_data ('result', ntstep, lartif_data,&
                         1, 1, zgrids_dt,izerror, yzerrmsg)
    [...]
  END DO timeloop
  [...]
END PROGRAM lmorg
```

Figure 30: a schematic overview on how to plug the FASDAS scheme in COSMO.

hydrological state. Sometimes, however, the errors in the T2m values are due to other model errors rather than to be imputed to the data assimilation scheme; in this case, the correction of the soil state (in the COSMO case, the soil moisture) would be the introduction of an additional source of problems.

This kind of problems might be overcome using the FASDAS technique. Before continuing, some definitions are needed:

- q_a: mixing ratio of the surface layer
- Δq: time variation of the surface layer mixing ratio due to mixing
- $\psi_a \equiv q_a/\Delta q_a$: normalization
- $E = E_{\mathrm{dir}} + E_{\mathrm{can}} + \sum_{\mathrm{layers}} E_{\mathrm{trasp}}$: evapotranspiration considered as the sum of the direct evaporation, evaporation from the canopy and transpiration by the canopy from the different soil layers.

These can be used to write the correction to give to the soil water budget components in a balanced way:

$$E_\xi^F = \left(\frac{E_\xi}{E}\right)\psi_a\left(\frac{H_q^F}{\rho_w L}\right), \tag{5}$$

where ξ is a place holder for the components of the land surface system itemised above, ρ_w is the water density and L the evaporation latent heat. Each of these terms calculated in equation (5) should be used to correct the associated water balance equation.

The implementation of FASDAS should not be too invasive on the COSMO code: apart of minor interventions in some of the data assimilation routines, the main interventions should be limited to one routine, in the way shown in figure 30:

5. Conclusions

In the present report it has been analysed the possibility and the issues related to the use of T2m to improve the COSMO analysis production. This is a very important topic due to the great availability of T2m data. Before proposing an integration to the current data assimilation system, the current COSMO performances have been studied.

At the current stage, using T2m data in the assimilation has pros and cons: on the one hand the description of T2m itself is improved, but the other screen level variables might be negatively affected by the perturbations introduced by the T2m assimilation. In particular, the description of the land-surface energy balance is worsened.

The problem might be overcome by integrating the current data assimilation scheme with the FASDAS technique. This technique makes it possible for the observation nudging scheme to update not only the atmospheric fields of the assimilated variables, but also the related ones, such as the land-surface energy balance terms and the soil state.

As shown, the interventions to be performed on the COSMO code are projected to be rather isolated.

This work has been formalised as a WG1 activity, in agreement with USAM, ARPA-SIMC and Cristoph Schraff.

References

[1] Alapaty, K., D. Niyogi, F. Chen, P. Pyle, A. Chandrasekar, and N. Seaman, 2008: Development of the Flux Adjusting Surface Data Assimilation System for Mesoscale Models. *Journal of Applied Meteorology and Climatology*, 7, **2331-2350**

[2] Alapaty, K., N. Seaman, D. Niyogi, and A. Hanna, 2001: Assimilating Surface Data to Improve teh Accuracy of Atmospheric Boundary Layer Simulations. *Journal of Applied Meteorology and Climatology*, 7, **2331-2350**

[3] Milelli, M., E. Oberto and M. Turco, 2008: Screen-level data assimilation in COSMO-I2. *Cosmo News Letter*, 9, **12-18**

[4] Milelli, M., M. Turco and E. Oberto, 2010: Screen-level non-GTS data assimilation in a limited-area mesoscale model. *Natural Hazards and Earth System Sciences*, 10, **1129-1149**

Bias Correction of Humidty Measurements by Radio Sondes of Vaisala RS 92

Klaus Stephan and Christoph Schraff

Deutscher Wetterdienst, Frankfurter Strasse 135, 63067 Offenbach, Germany

1 Introduction

Moisture is very important for many atmospheric processes. A correct description of the moisture of NWP models is essential to simulate the hydrological cycle precisely. An appropriate way to get the model a realistic moisture field is to assimilate moisture observations. In all operational configurations of the COSMO model, radio sondes are the only source of observational information on humidity, except for sceen-level data, which are given very limited weight however. Therefore any systematic error in the radio sondes humidity data will likely be detrimental. Recently many investigations revealed that the humidity measurements of radio sondes seems to be biased compared to other humidity observations. In the two operational configurations of Deutscher Wetterdienst (DWD), COSMO-EU, which has a mesh width of 7 km and covers Europe, and COSMO-DE (2.8 km, Germany and environs) 56% resp. 81% of all radio sondes used are of type Vaisala RS 92. Miloshevich et al. (2009) investigated the accuracy of this type of radio sondes as a function of height, solar elevation angle and relative humidity. They mention two different reasons for the bias. First, there is a calibration error which leads to a small time-independent moist bias below 500 hPa and dry bias further above. The second error is caused by a solar radiation error and will lead to a significant dry bias during daytime. Keeping in mind that the radio sondes are mainly launched at about 00 and 12 UTC the dry bias will affect the COSMO models at daytime between 9 and 12 UTC. To reveal the influence on the COSMO models integrated water vapour (IWV) of the model analyses is compared to the independent IWV retrievals of GNSS zenith total delay measurements (Gendt et al., 2004). As shown in fig. , the model tends to be moister at night but is much drier about noon. A correction algorithm after Milosevisch et al. is now implemented within the COSMO code and briefly described in the following section. Section 3 presents the investigations of the application of the bias correction. A conclusion is drawn in section 4.

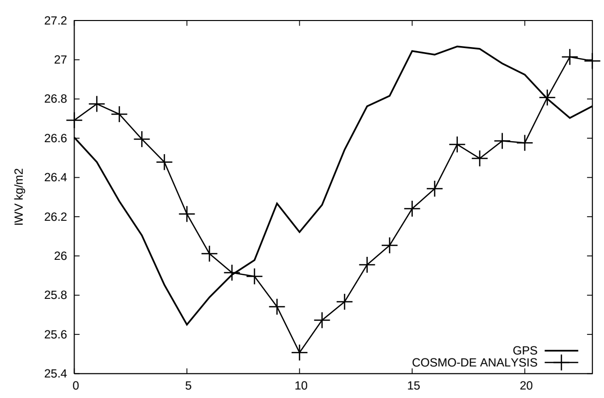

Figure 1: Comparison of integrated water vapour (IWV) retrieved by GNSS observations and analysed by the operational COSMO-DE for July 2010.

2 Bias correction algorithm

In Miloshevich et al. (2009) three inter-comparisons on the accuracy of Vaisala RS 92 in the mid-latitudes are combined and an empirical correction algorithm was designed. The algorithm takes into account that the accuracy is found to be dependent on pressure, relative humidity and the solar elevation angle. Two main sources of error are detected, a calibration error and a solar radiation error. As a matter of fact the latter depends on solar elevation angle and is affected by clouds, where the calibration error is time-independent and not affected by clouds. It has been found that the calibration error leads to a moist bias in the lower troposphere and to a dry bias in upper the troposphere. The solar radiation error leads to a dry bias. Both biases tend to be larger in higher altitudes and for dry conditions. The empirical correction algorithm is given in Eq. 1, with F(p,RH,time) as a polynomial function of pressure, relative humidity and solar elevation angle.

$$RH_{corr} = \frac{100 \cdot RH_{meas}}{100 + F(p, RH, time)} \tag{1}$$

$$\text{with} \quad F(p, RH, time) = \sum_{i=0}^{N} a_i(RH) \cdot p^i$$

The polynomial fit F(p,RH,time) is time-dependent, i.e. the order of the fit and the coefficients are different between night and day. Even more the daytime fit is only valid for a solar elevation angle $\alpha = 66°$. Therefore for daytime measurements another correction step is required to account for α. The component of solar radiation error (SRE) at $\alpha = 66°$ is given as the difference between the function F(p,RH,time) at day and at night. Any other angle is given by Eq. 2, where G is another polynomial function of α. All coefficients and more details can be found in Milosevisch et al. (2009).

$$SRE(\alpha) = (F(p, RH, 66°) - F(p, RH, night)) \cdot G(\alpha) \tag{2}$$

The correction algorithm described above is valid for clear sky conditions. This would restrict the operational usage in many cases. Therefore in addition to the algorithm of Milosevisch et al. (2009), in new bias correction in COSMO, cloudy conditions are accounted for. The bias caused by solar radiation error is reduced in dependence of the liquid water path above the measurement.
To apply the bias correction a new namelist switch *mqcorr*92 is defined, which can be set to

0 no bias correction

1 correction of solar radiation error

2 correction of total error (ie. the sum of calibration and solar radiation error

3 Experimental investigations

The bias correction has been tested experimentally for both COSMO configurations running operationally at DWD. The tests were performed over one month each in winter (March 2010) and summer (July 2010), applying the corrections of the total bias (see above). In the following the results will be described starting with the winter case. The attention is drawn to COSMO-DE.
The first half of March 2010 was dominated by cold winter weather with northerly wind. In the second half a south western flow established and the temperature increased. The IWV was low in the beginning and also arised towards the end of the month. In winter the bias in

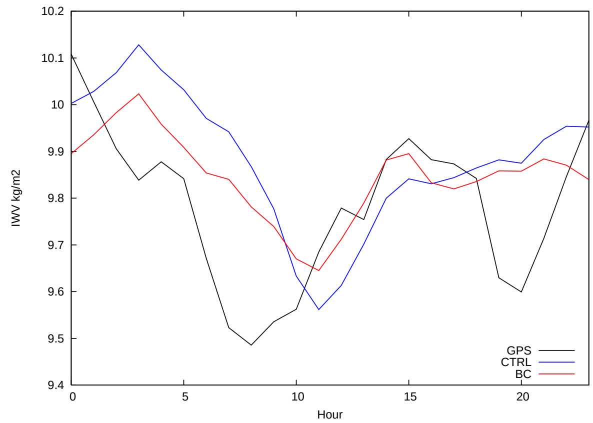

Figure 2: Comparison of IWV for March 2010 retrieved by GNSS observations (black line) and analysed by different COSMO-DE setups for March 2010: control run (blue), experimental run with bias correction of total bias (red).

terms of IWV is not as pronounced as in summer. Therefore the effect of the bias correction can not be expected to be very large. However, the bias could be reduced, as can be seen in Fig. . Besides the correction seen by the comparison of IWV only small effects of the bias correction on other parameters can be found. The impact on the humidity is visible in a verification against radio sondes (not shown). In the comparison between the operational run and the experimental run with bias correction the impact can be found at higher levels. Above 500 hPa the bias between model and observations as used in the respective assimilation set-up tends to be smaller in the experiment, which is mainly caused by the correction of the observation. As the observations in both runs are not equal, a comparison of the state of the model is difficult. Most of the other scores show an almost neutral impact.
This is different in summer. The test period was dominated by very hot conditions associated with several events of heavy rain fall and thunderstorms. The IWV reaches high values. In such conditions, which are organized more locally, moisture will have a greater influence as in winter, where the weather is more dominated by large scale advection. In summer the forecasts of both COSMO configurations are improved, when applying the bias correction. The positive impact is not restricted on moisture related variables (see fig.) but can be found for other variables, too. Fig. shows the verification against synoptical observations for temperature and dew-point depression. For both elements a small improvement is achieved

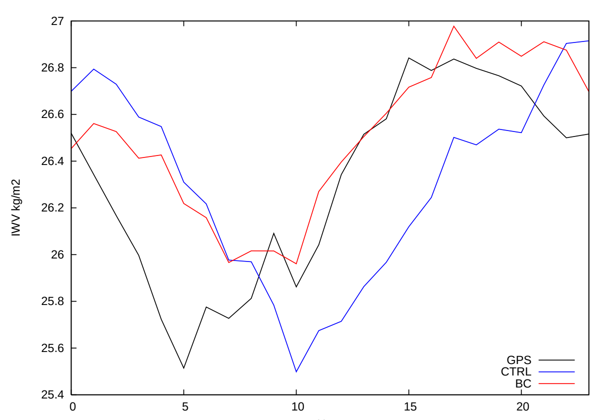

Figure 3: Comparison of IWV for July 2010 retrieved by GNSS observations (black line) and analysed by different COSMO-DE setups for March 2010: control run (blue), experimental run with bias correction of total bias (red).

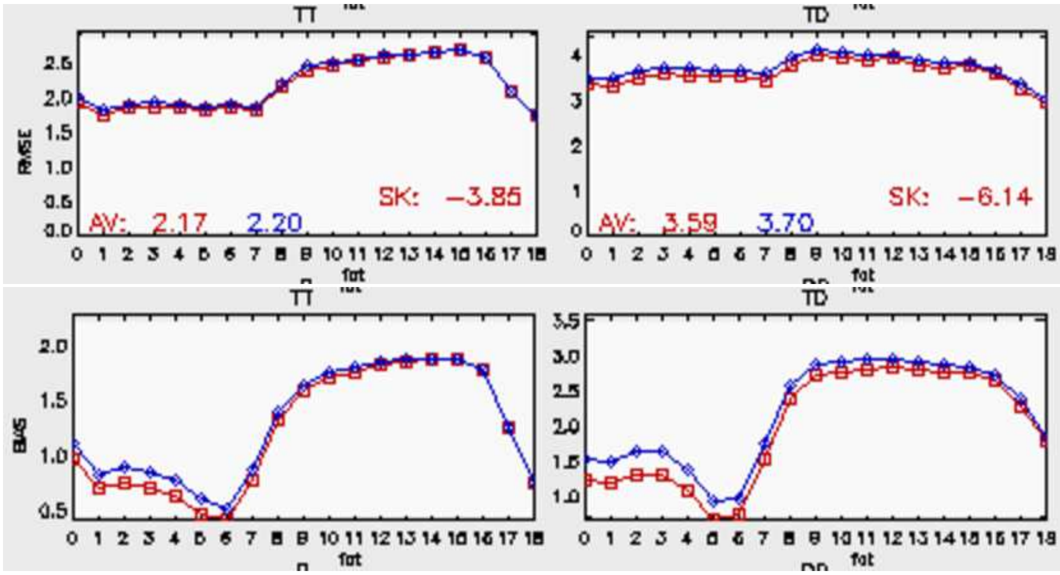

Figure 4: Verification of 2m temperature and 2m dew-point depression against synoptical observations for 12 UTC forecast runs in July 2010: control run (blue), experimental run with bias correction of total bias (red); top row: RMSE and bottom row: BIAS.

when applying the bias correction. The improvement is achieved mainly by decreasing the model bias of both elements. Of special interest is the improvement of precipitation forecast. Esp. 12 UTC forecast runs of COSMO-DE do not predict convective precipitation well in summer. Also in this regard an improvement due to the bias correction is visible, although the impact is not very large. In fig. ETS and FBI for a precipitation rate greater than 0.1 mm/h (calculated against radar observations) are shown for the 12 UTC forecast of control run and run with bias correction. A small improvement can be found within the first hours of the forecast when applying the bias correction.

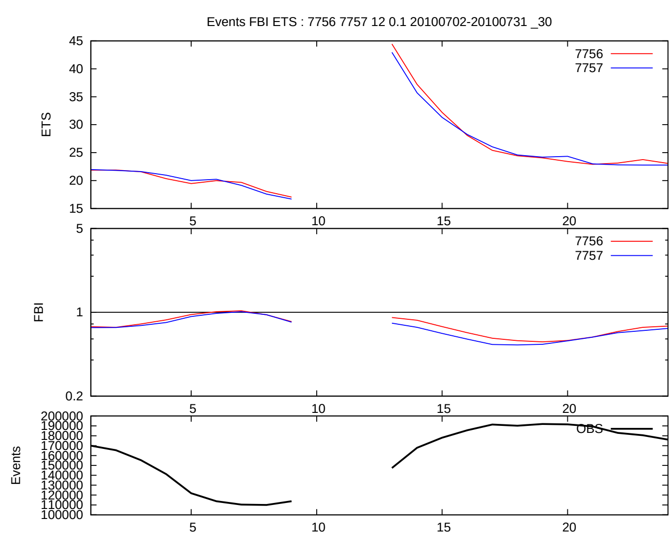

Figure 5: Verification of mean precipitation greater than 0.1 mm/h against Radar observations for 12 UTC forecast runs in July 2010: control run (blue), experimental run with bias correction of total bias (red).

4 Conclusions

A bias correction of relative humidity measured by Vaisala RS92 radio sondes is applied for COSMO configurations at DWD. The correction of the bias is found to be beneficial for the forecast. Especially in summer the improvement is visible in the verification, when correcting for the total bias of those humidity data. The correction of the total bias leads to a drier model state at nighttime and a moister state at daytime. An even more positive impact can be achieved if only the solar radiation error is corrected. Then the models become even more moist all over the forecast time. In winter both bias corrections are almost neutral compared to the control run.

In order to achieve a model state closer to reality, the decision was made to apply the correction of the total bias operationally. This will give the model developers the opportunity to tune the parametrization on the basis of a more realistic initial model state. However, the fact that the model performs better if its state is more moist might give evidence that there is a need to tune the parametrizations.

References

[1] Gendt, G., Dick, G., Reigber, C., Tomassini, M., Liu, Y. and Ramatschi, M., 2004: Near Real Time GPS Water Vapor Monitoring for Numerical Weather Prediction in Germany, *J. Meteo. Soc. Japan,* **82**, No. 1B, pp. 361–370

[2] Miloshevich, L. M., H. Vomel, D. N. Whiteman, and T. Leblanc, 2009: Accuracy assessment and correction of Vaisala RS92 radiosonde water vapor measurements, *J. Geophys. Res.,* **114**, D11305, doi:10.1029/2008JD011565.

LETKF for the nonhydrostatic regional model COSMO-DE

Hendrik Reich, Andreas Rhodin, Christoph Schraff

Deutscher Wetterdienst, Frankfurter Strasse 135, 63067 Offenbach, Germany

1. Introduction

Data assimilation for numerical weather prediction (NWP) at the convective scale meets with a number of challenges. They include: strongly flow dependent and unknown spatial balances between the different model variables, importance of nonlinear processes, non-Gaussian error statistics and large forecast errors in 'weather'-parameters due to imperfections in the physics, in particular in the cloud and boundary layer formulations.

The Local Ensemble Transform Kalman Filter (LETKF) (Hunt et al., 2007) offers some very attractive features: it is a simple algorithm, no tangent linear and adjoint versions of the prognostic model are required, and the forecast error covariance matrix is cycled and thus flow-dependent.

At Deutscher Wetterdienst (DWD) it is planned to use the LETKF on the global scale (GME/ICON, in a hybrid approach together with 3dVar) as well as on the local scale (COSMO-DE). COSMO-DE is a nonhydrostatic COSMO-version with a horizontal resolution of 2.8 km, covering Germany and parts of its neighbouring countries (Baldauf et al., 2010). The LETKF analysis ensemble will also serve as initial conditions for COSMO-DE EPS, a convection permitting EPS system under development at DWD.

The outline is as follows: we will give a short overview on the LETKF in section 2. In section 3 we present the results of our LETKF experiments and we conclude in section 4.

2. LETKF theory

Our Implementation follows (Hunt et al., 2007). The basic idea of the LETKF is to do the analysis in the space of the *ensemble perturbations*. This is computationally efficient, but also restricts corrections to the subspace spanned by the ensemble. An explicit localization is necessary to confine the ensemble size; this means to compute a separate analysis at every grid point, where only certain observations are selected. Thus, the analysis ensemble members are a locally linear combination of first guess ensemble members.

The analysis mean $\bar{\mathbf{x}}^a$ is given by

$$\bar{\mathbf{x}}^a = \bar{\mathbf{x}}^b + \mathbf{X}^b \tilde{\mathbf{P}}^a (\mathbf{H}\mathbf{X}^b)^T \mathbf{R}^{-1} (\mathbf{y} - \bar{\mathbf{y}}^b) \tag{1}$$

where $\bar{\mathbf{x}}^b$ is the first guess mean; $\mathbf{H}$ is the (linearized) observation operator and $\mathbf{X}^b$ are the first guess ensemble perturbations. The analysis ensemble is obtained via

$$\mathbf{X}^a = \mathbf{X}^b [(k-1)\tilde{\mathbf{P}}^a]^{1/2} = \mathbf{X}^b \mathbf{W}^a. \tag{2}$$

Here, k is the number of ensemble members and $\tilde{\mathbf{P}}^a$ is the analysis error covariance matrix which is (in the ensemble space) given by

$$\tilde{\mathbf{P}}^a = [(k-1)\mathbf{I} + (\mathbf{H}\mathbf{X}^b)^T \mathbf{R}^{-1} \mathbf{H}\mathbf{X}^b]^{-1}. \tag{3}$$

3. Experiments and results

We performed several preliminary experiments with successive LETKF assimilation cycles. In all experiments, 32 ensemble members were used. The initial ensemble members where drawn from the 3dVar B-Matrix of the global model GME. Conventional observations from the global network were assimilated. We have run a 3-hourly cycle up to 2 days (7-8 Aug. 2009: 1 quiet + 1 convective day) and used lateral boundary conditions (BC) from COSMO-SREPS (3 * 4 members) or deterministic BC.

In our first experiments we concentrate on general topics, such as the rms/spread ratio of the ensemble, the noise (as measured by dps/dt) and the general behaviour of LETKF (analysis increments, spread structures). The effect of parameter variation (e.g. localization length scales) was tested, but fine tuning is left to be done with longer running experiments.

The set of analysed variables is given by $u, v, w, T, pp, qv, qcl, qci$ (wind components including vertical velocity w, temperature, pressure pertubation, humidity, cloud water and cloud ice content). Here, 'analysed' means that linear combination is applied to these variables; other variables are taken from first guess ensemble members or ensemble mean.

We verify the LETKF results (i.e. the analysis *mean*) against the nudging analysis and observations. When comparing with the nudging analysis one has to take into account that the nudging scheme uses a larger set of observations. A verification tool (deterministic/ensemble scores) is currently under development within the COSMO consortium.

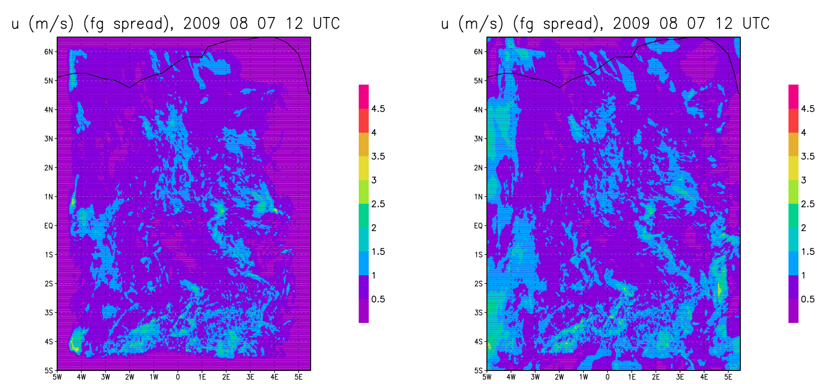

Figure 1: spread (wind component u in m/s) of first guess on 7 Aug. 2009 at 12 UTC (after 4 analysis cycles) for deterministic BC (left) and ensemble BC (right)

Fig.1 shows the spread of the u-wind component of the first guess ensemble, obtained with deterministic and ensemble BC, respectively. In the case of deterministic BC we observe a lack of spread at the lateral boundaries, whereas "new" spread is coming in from the west with ensemble BC. This demonstrates the need to use ensemble BC's, and it can be seen that a large amount of the whole domain is influenced by the spread stemming from the BC. As we will see later, the use of ensemble BC leads to some difficulties.

In order to test the implementation of the LETKF and it's capability of making use of observations we compare the analysis produced by the LETKF with a free forecast which uses the same BC but no observations. Fig.2 shows the temporal development of the first guess and free forecast rmse of the u-component of wind velocity (as measured with respect to the nudging analysis) on the 500 hPa level. One can see that the LETKF performs better than the free forecast on all levels.

Next we verify the LETKF analysis against observations; the results are shown in Fig. **??**.

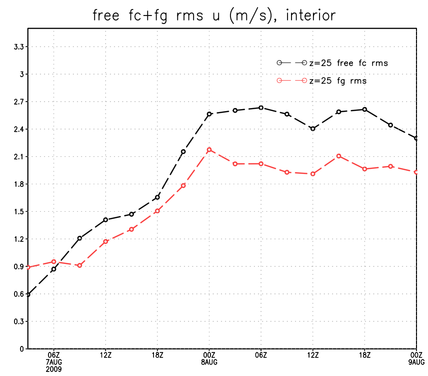

Figure 2: rms of u,(m/s) (interior) of first guess and free forecast; results for det BC.

The reduction of spread between first guess and analysis indicates that the LETKF makes use of the observations. As also the rmse of the analysis is smaller than that of the first guess we conclude that the LETKF is able to use the information contained in the observations. The spread of first guess and analysis is much smaller than the corresponding rmse; this means that the ensemble is underdispersive.

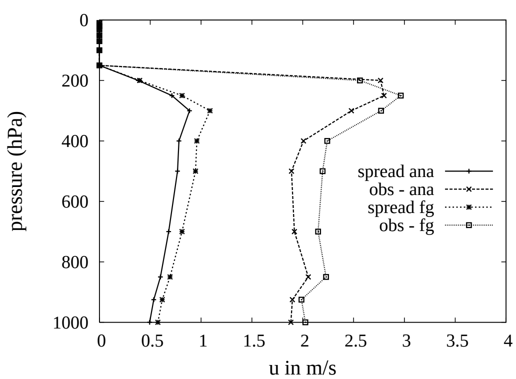

Figure 3: time average (20090807 15 UTC - 20090809 00 UTC)of obs-fg and spread of u,(m/s) (whole area), AIREP

The lack of spread is (partly) due to model error which is not accounted for so far. One (simple) method to increase spread is multiplicative covariance inflation:

$$\mathbf{X}_b \rightarrow \rho \mathbf{X}_b \tag{4}$$

with $\mathbf{X}_b$ being the ensemble perturbations and $\rho > 1$. The tuning of the inflation factor ρ takes much time, and it is expected that the optimal value will change in time, depending e.g. on observation density. For this reason, an adaptive procedure is preferable. (Li et al., 2009) propose an online estimation of the inflation factor. The idea is to compare the "observed" obs minus first guess, given by $(\mathbf{y} - H(\mathbf{x}_b))$ with the "predicted" one, given by $(\mathbf{R} + \mathbf{H}\mathbf{P}_b\mathbf{H}^t)$. This method was applied in a LETKF environment by Bonavita et al. (2010), where ρ was time and space dependent. Here, in a first step, we tested a version with a space independent ρ.

It is also assumed that the observation errors and thus the $\mathbf{R}$-matrix are specified incorrectly, and a correction is desirable. This can be achieved by comparing the observed observation covariance with the assumed one (in ensemble space) and correcting $\mathbf{R}$ automatically if necessary. Both methods (est. of inflation factor / $\mathbf{R}$ matrix) have been tested with reasonable numerical cost and success with a toy model, and have been implemented in the COSMO LETKF. For deterministic BC, a positive effect of the adaptive ρ inflation is visible, which is shown in Fig.4. In the case with ensemble BC the method was not succesful. Currently, an improved version with a space dependent ρ and doing the computation in ensemble space is tested.

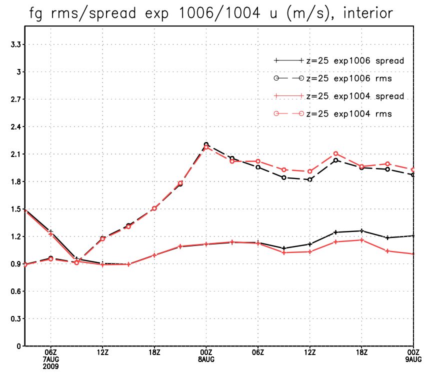

Figure 4: intercomparison of first guess rms and spread of u,(m/s) (interior); results for det BC and constant inflation factor ρ (exp1004) and adaptive covariance inflation (exp1006)

The LETKF produces an analysis ensemble as a (local) linear combination of the first guess ensemble. The analysis fields obtained are not necessarily balanced, and noise (e.g. external gravity waves, measured by dps/dt) might be present when starting the integration. Indeed we find an increased level of noise (as compared with the nudging scheme). Fig.5 (left plot) shows that noise is present in the whole domain.

We observed that the diagonal elements of weight matrices W are larger than the off diagonal elements; this means that the analysis ensemble member k gets the largest contribution from first guess ensemble member k plus (smaller) corrections from members $i \neq k$. Thus, the difference between analysis and first guess ensemble member k (the analysis increment) is small compared to the full fields, and hydrostatic balancing can be applied to this increment: this leaves the full fields nonhydrostatic as it should be in a nonhydrostatic model.

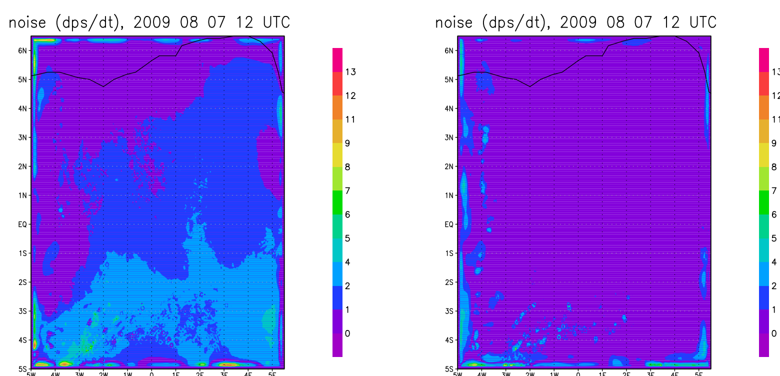

Figure 5: area plots of noise (dPs/dt) at the first time step; ens BC without hydrostatic balancing (left) and with hydrostatic balancing applied (right).

Applying this method reduces the noise in the interior of the domain (Fig.5, right plot); at the boundaries, there is still noise present.

4. Conclusions

We have tested the LETKF in preliminary, short assimilation cycles. The LETKF demonstrated its capability of assimilating conventional observations correctly. Problems such as a lack of spread and noise introduced by the ensemble BC were identified. The latter could be alleviated by applying hydrostatic balancing to the analysis increments. The effect of this balancing on the rms/spread ratio will have to be investigated. Furthermore, we will study the effect of the remaining noise on e.g. precipitation at the beginning of the integration.

The adaptive covariance inflation, which was tested in a simple version, was successfully applied in the case of deterministic BC. For ensemble BC a more sophisticated version is currently tested. Within the COSMO consortium, alternative methods to account for model errors are developed and will also be implemented in the LETKF.

In the future we will run experiments over a period of weeks or months. In this experiments, we will use more observations (radar data in particular) and do the analysis more frequently ($\approx$ all 15 min). With this more realistic setup, parameters as the localization length scales will have to be tuned.

References

[1] Baldauf M., Seifert A., Förstner J., Majewski D., Raschendorfer M., Reinhardt T., 2010: Operational convective-scale numerical weather prediction with the COSMO model. *submitted to MWR*

[2] Bonavita M., Torrisi L., Marcucci F., 2010: Ensemble data assimilation with the CNMCA regional forecasting system. *Q.J.R.Meteorol.Soc.* **136**: 132-145

[3] Hunt B.R., Kalnay E., Kostelich E.J., Szunyogh I., 2007: Efficient data assimilation for spatiotemporal chaos: A local ensemble transform Kalman filter. *Physica D* **230**: 112-126

[4] Li H., Kalnay E., Miyoshi T., 2009: Simultaneous estimation of covariance inflation and observation errors within an ensemble Kalman filter. *Q.J.R.Meteorol.Soc.* **135**: 523-533

[5] Stephan K., S. Klink, C. Schraff, 2008: Assimilation of radar derived rain rates into the convective scale model COSMO-DE at DWD. *Q.J.R.Meteorol.Soc.* **134**: 1315-1326

Introducing a sea ice scheme in the COSMO model

Jan-Peter Schulz

Deutscher Wetterdienst, Offenbach a. M., Germany

1 Introduction

The presence of sea ice on the ocean's surface has a significant impact on the air-sea interactions. Compared to an open water surface the sea ice completely changes the surface characteristics in terms of albedo and roughness, and therefore substantially changes the surface radiative balance and the turbulent exchange of momentum, heat and moisture between air and sea.

In order to deal with these processes the operational global model GME at the German Weather Service (DWD) includes a sea ice scheme (Mironov and Ritter 2004). In contrast, there was no such scheme in DWD's limited area model COSMO-EU (Doms and Schättler 2002, Schulz 2006) up to now. This model covers almost all Europe using a mesh size of 7 km, its lateral boundary conditions are provided by GME. Instead, the GME sea ice surface temperature is used to "emulate" the existence of sea ice in COSMO-EU by providing a realistic temperature at water points which are regarded as being ice covered. Using the threshold temperature value $T_{\mathrm{melt}} = -1.7°\mathrm{C}$ the COSMO-EU water points are distinguished between open water or ice covered. The albedo and the roughness length are set accordingly.

This procedure has the disadvantage that the GME sea ice surface temperature is transferred to COSMO-EU only once per day at 00 UTC, as part of the sea surface temperature (SST) analysis, and is then kept constant at this night time value during the data assimilation cycle and also during the forecasts. This means that there is no diurnal cycle of sea ice surface temperature possible in COSMO-EU. Furthermore, the ice temperature of GME may not fit well to the COSMO-EU surface conditions, depending on the weather situation, and may therefore introduce imbalances and noise.

For these reasons it was decided to implement a sea ice scheme in the COSMO model, the GME scheme has been selected for this. In the following sections a short description of the scheme is given and results of numerical experiments comparing COSMO-EU with and without the sea ice scheme are presented.

2 The sea ice scheme

The sea ice scheme by Mironov and Ritter (2004) accounts for thermodynamic processes, while no rheology is considered. It basically computes the energy balance at the ice's surface, using one layer of sea ice. From this the evolution of the ice surface temperature T_{ice} and the ice thickness H_{ice} are deduced. These two new prognostic variables allow for a better thermodynamically coupled treatment of sea ice in the COSMO model as lower boundary condition for the atmosphere. In particular, the scheme allows for very low surface temperatures which can be significantly lower than the water temperature below the ice.

The sea ice surface temperature T_{ice} is computed by the surface energy balance equation:

$$\frac{\Delta T_{\mathrm{ice}}}{\Delta t} = \frac{1}{c\,H_{\mathrm{ice}}}\left[\frac{Q_{\mathrm{A}} + Q_{\mathrm{I}}}{\rho_{\mathrm{ice}}\,C_{\mathrm{ice}}}\right] \tag{1}$$

where Q_{A} is the sum of all atmospheric energy fluxes at the ice's surface (solar and thermal radiation plus sensible and latent heat flux), Q_{I} is the vertical conductive heat flux through the ice layer of thickness H_{ice}, $\rho_{\mathrm{ice}} = 910$ kg m^{-3} is the ice density, $C_{\mathrm{ice}} = 2100$ J kg^{-1} K^{-1} the ice heat capacity, $c = 0.5$ a shape factor and t the time.

The internal heat flux Q_{I} through the ice layer is computed by

$$Q_{\mathrm{I}} = -\lambda_{\mathrm{ice}} \frac{T_{\mathrm{ice}} - T_{\mathrm{bot}}}{H_{\mathrm{ice}}} \tag{2}$$

where $\lambda_{\mathrm{ice}} = 2.3$ W m^{-1} K^{-1} is the ice heat conductivity and T_{bot} the temperature at the bottom of the ice layer. It is set constant to $T_{\mathrm{bot}} = -1.7°$C which is assumed to be the freezing temperature of salty sea water.

In the case of $T_{\mathrm{ice}} = 0°$C and $Q_{\mathrm{A}} \geq 0$ W m^{-2} all available energy at the ice's surface is used for melting, leading to a reduction of the sea ice thickness H_{ice} according to

$$\frac{\Delta H_{\mathrm{ice}}}{\Delta t} = -\frac{Q_{\mathrm{A}}}{\rho_{\mathrm{ice}}\, L_{\mathrm{f}}} \tag{3}$$

where $L_{\mathrm{f}} = 0.334 \cdot 10^6$ J kg^{-1} is the latent heat of freezing. In this case the heat flux Q_{I} is neglected.

In all other cases the evolution of H_{ice} is governed by the following equation:

$$\frac{\Delta H_{\mathrm{ice}}}{\Delta t} = \frac{Q_{\mathrm{I}}}{\rho_{\mathrm{ice}}\, L_{\mathrm{f}}} \tag{4}$$

This means that the internal ice heat flux Q_{I} is balanced by the amount of energy involved in the phase transitions between liquid and frozen water at the bottom of the sea ice layer, i. e. the interface between ice and water. If for instance $T_{\mathrm{ice}} < -1.7°$C, this will lead to an ice heat flux Q_{I} which is directed upward from the water into the ice layer. The source of this heat flux is assumed to be the latent heat of freezing of an equivalent amount of water, which while freezing will lead to a growing sea ice thickness H_{ice}.

3 The sea ice distribution

The horizontal distribution of the sea ice cover in the model domain is governed by the data assimilation scheme. This is the same with or without the sea ice scheme. It means that the sea ice scheme in COSMO-EU changes the way the sea ice is represented, but it can not create new sea ice points, it can not start freezing the water by itself.

In the model chain at DWD first the remote sensing based sea ice mask from NCEP (National Centers for Environmental Prediction, USA) is provided by the SST analysis to the global model GME. This GME sea ice mask is then again interpolated by the SST analysis to the COSMO-EU grid. During this last interpolation an additional high-resolution sea ice mask is used to improve the ice distribution on the COSMO grid in particular in the Baltic Sea. This high-resolution sea ice mask is issued by BSH (Bundesamt für Seeschifffahrt und Hydrographie, Germany) and is updated every few days.

4 Cold start from GME using the SST analysis

In order to test the sea ice scheme in COSMO-EU two continuous numerical parallel experiments, running in the same way as the operational analyses and forecasts, were carried out:

A reference experiment of COSMO-EU without sea ice scheme (called REF), and an experiment of COSMO-EU with sea ice scheme (called ICE). The period was 03 Feb. – 31 May 2010. This period was selected because most of the sea ice season in the model domain in early 2010 was covered. Only the first few weeks of freezing were skipped, this allowed to test a cold start of the sea ice scheme from the fields of the driving model, i. e. here the GME.

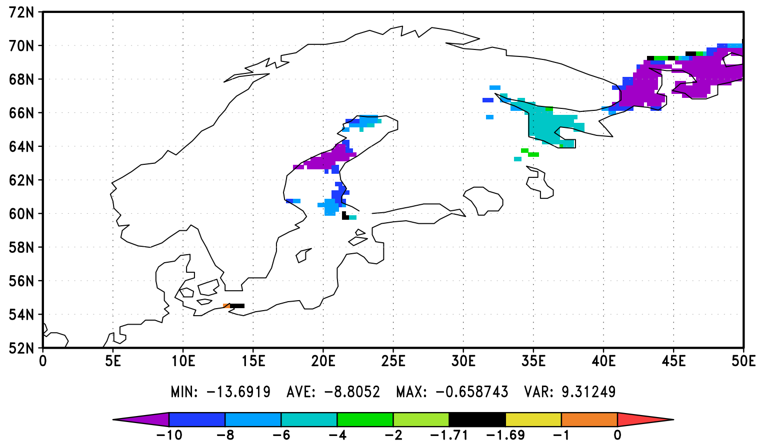

Figure 1: GME analysis of sea ice temperature (°C), 03 Feb. 2010, 00 UTC. Some parts of mainly the Gulf of Bothnia, the White Sea and the Barents Sea are already ice covered.

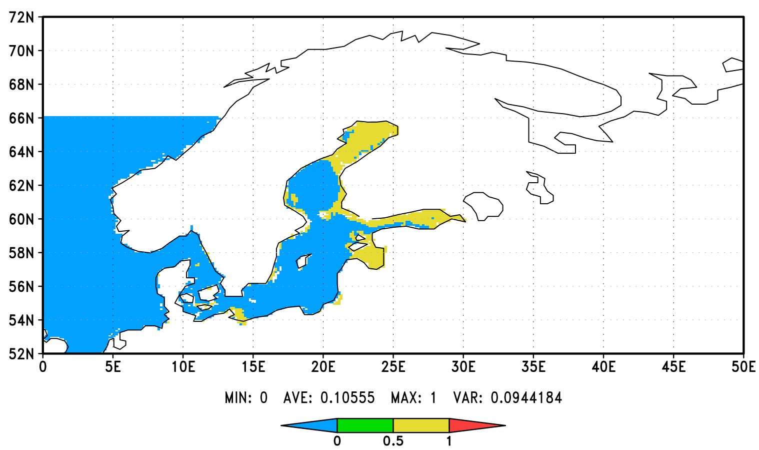

Figure 2: BSH observational sea ice mask used in the SST analysis for COSMO-EU, 03 Feb. 2010, 00 UTC. The mask covers the entire Baltic Sea and parts of the North Sea. A comparison with the GME sea ice distribution (Fig. 1) shows that BSH has more sea ice in the Gulf of Finland and the Gulf of Riga but less in parts of the Bothnian Sea.

Figure 1 shows the sea ice temperature as provided by the SST analysis to the global model GME on 03 Feb. 2010, 00 UTC. Some parts of mainly the Gulf of Bothnia, the White Sea and the Barents Sea are already ice covered. The temperatures in the Bothnian Sea and the Barents Sea have reached values below −10°C, temperatures in the White Sea range around −5°C. Figure 2 depicts the BSH observational sea ice mask on 03 Feb. 2010, 00 UTC. It is used in the SST analysis for COSMO-EU as a refinement for the NCEP ice mask. A comparison of the two sea ice distributions (Figs. 1 and 2) shows that BSH has more ice in the Gulf of Finland and the Gulf of Riga but less in parts of the Bothnian Sea.

Figure 3 shows the analysis of the surface temperature of water points which are regarded as being ice covered by the SST analysis for COSMO-EU running without sea ice scheme (REF), again on 03 Feb. 2010, 00 UTC. In the domain of the BSH mask (basically in the

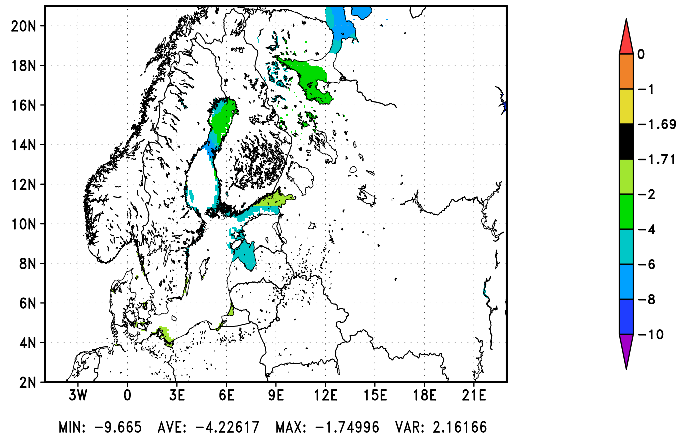

Figure 3: Analysis of surface temperature (°C) of water points which are regarded as being ice covered by the SST analysis for COSMO-EU without sea ice scheme (REF), 03 Feb. 2010, 00 UTC.

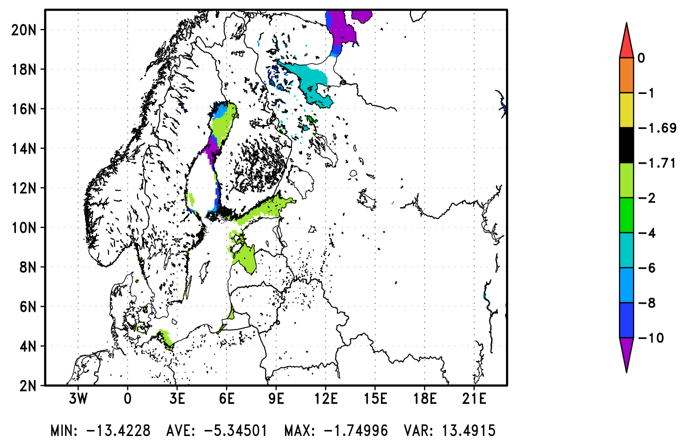

Figure 4: Analysis of sea ice temperature (°C) provided by the SST analysis for COSMO-EU with sea ice scheme (ICE), 03 Feb. 2010, 00 UTC.

Baltic Sea) the BSH ice distribution is used, outside of it (White Sea, Barents Sea) it is determined by GME, and therefore NCEP. Comparing the ice temperatures of GME and REF in the White Sea and Barents Sea it is noticed that REF is less cold than GME. The reason is that the SST analysis computes the sea ice temperature for REF in the following

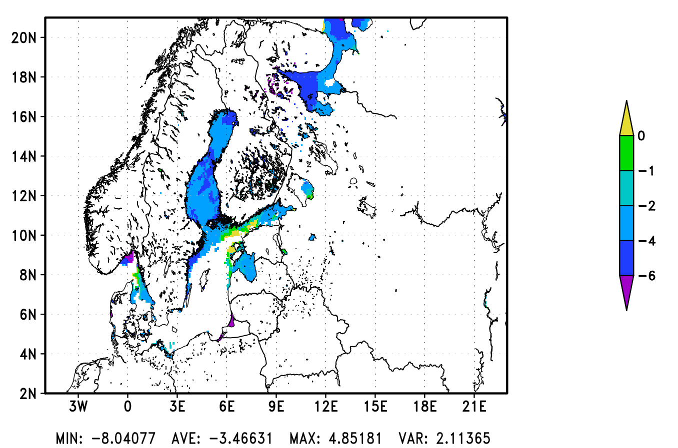

Figure 5: Difference of analysed surface temperature (°C) at sea ice points between COSMO-EU with and without sea ice scheme (ICE - REF), 07 Mar. 2010, 00 UTC.

way:

$$T_{\text{ice}}^{\text{REF}} = 0.5(T_{\text{ice}}^{\text{GME}} + T_{\text{melt}}) \tag{5}$$

with $T_{\text{melt}} = -1.7°\text{C}$. The idea behind this is that the atmospheric conditions may be very different between GME and COSMO-EU at certain regions, one may have clear sky and the other one cloudy conditions. Introducing the very cold GME temperatures in this example directly into COSMO-EU may have more negative than positive effects (M. Buchhold, pers. comm., 2009).

Within the domain of the BSH ice mask three cases need to be distinguished:

- GME = ice and BSH = ice, e. g. northern Bothnian Sea: Use same formula as outside BSH mask.
- GME = no ice and BSH = ice, e. g. Bothnian Bay: Create new ice point.
  Initialise: $T_{\text{ice}}^{\text{REF}} = T_{\text{melt}} - \epsilon, \epsilon = 0.05°\text{C}$.
  Then: Search in the neighbourhood for the warmest ice point which originates from GME. Use this temperature for $T_{\text{ice}}^{\text{REF}}$.
- GME = ice and BSH = no ice, e. g. central Bothnian Sea: Remove ice point, create water.
  Initialise: $T_{\text{ice}}^{\text{REF}} = T_{\text{melt}} + \epsilon$

Figure 4 shows the analysis of sea ice temperature provided by the SST analysis for COSMO-EU running with sea ice scheme (ICE), again for 03 Feb. 2010, 00 UTC. This is used as the actual cold start for ICE. Now, in the areas outside of the BSH ice mask and in the first case from before the GME sea ice temperatures are directly interpolated to the COSMO-EU grid:

$$T_{\text{ice}}^{\text{ICE}} = T_{\text{ice}}^{\text{GME}} \tag{6}$$

Consequently, here the cold start values in ICE are lower than the ones in REF (compare Figs. 3 and 4).

And in the second case from before, GME = no ice and BSH = ice, the newly created ice points are initialised as before, but the search in the neighbourhood for the warmest ice point which originates from GME is skipped. Therefore, several regions in the Bothnian Bay and the Gulf of Riga are warmer now (again compare Figs. 3 and 4).

In the third case from before there is no change.

The initialisation of the sea ice thickness works in a similar way. It is either directly interpolated from GME, or in case new ice points need to be created they are initialised with a thickness of 0.2 m.

A main difference between REF and ICE is actually the initialisation of $T_{\text{ice}}^{\text{REF}}$ according to (5). It leads to systematically higher ice temperatures in REF which is e. g. shown in Fig. 5 and which turns out to cause a warm bias of the surface temperature even on surrounding land areas (see Fig. 7).

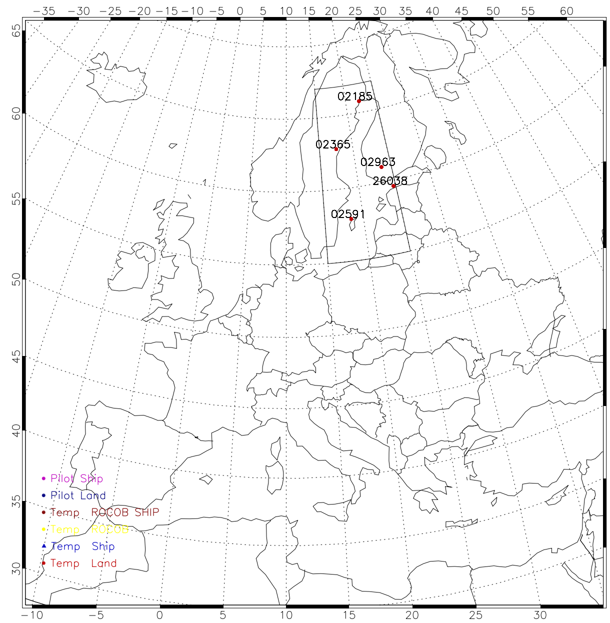

Figure 6: Verification domain for the 2-m temperature verifications shown in Figs. 7, 8 and 11. Additionally the locations of some radio sondes are indicated, two of them are used in Figs. 9 and 10.

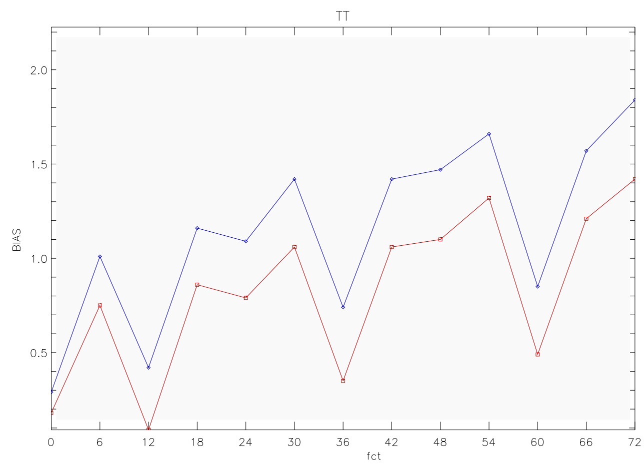

Figure 7: Bias of 2-m temperature (°C) versus forecast time (h) for the period 03 – 28 Feb. 2010, 00 UTC runs. Blue: Reference COSMO-EU without sea ice scheme (REF), red: COSMO-EU with sea ice scheme (ICE). All stations in the verification domain were used (see Fig. 6).

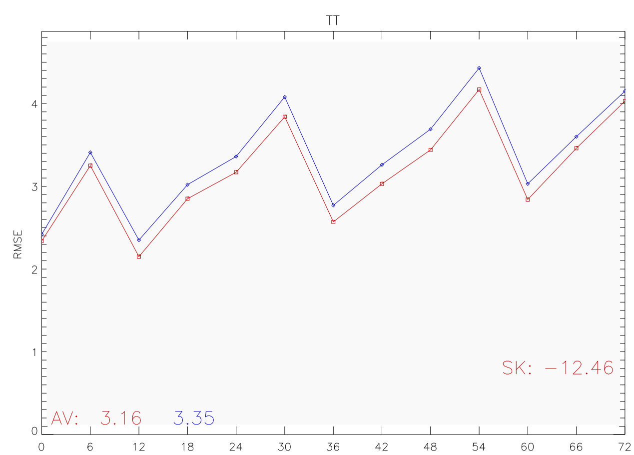

Figure 8: Same as Fig. 7, but for root mean square error of 2-m temperature (°C). Blue: REF, red: ICE. The reduction of its error variance in ICE amounts to about 12%.

5 Numerical parallel experiments

In this section an objective verification of the REF and ICE experiment is presented. The verification domain is shown in Fig. 6. Figure 7 compares the biases of the 2-m temperature versus the forecast time during the freezing period in February 2010. The REF experiment

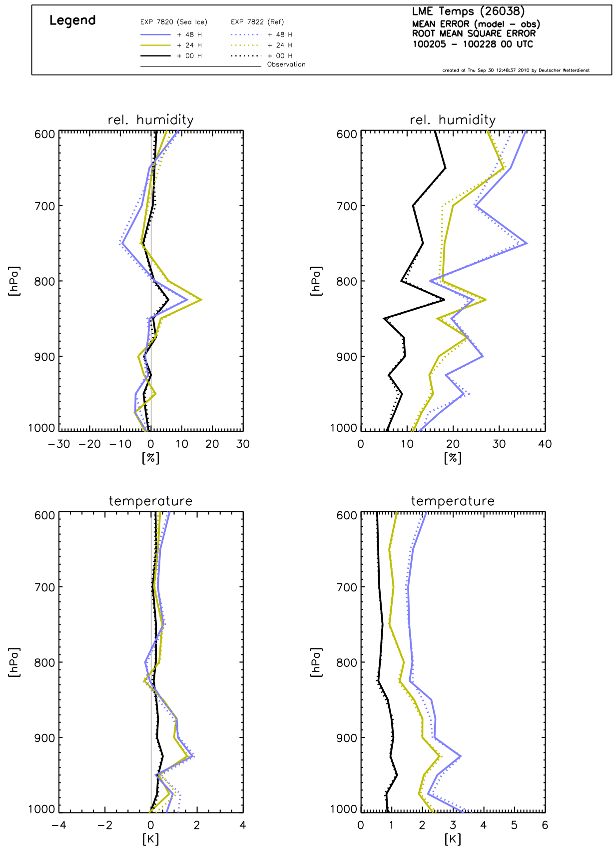

Figure 9: Upper air verification for Tallin, Estonia (Temp 26038) for relative humidity (top) and temperature (bottom) for the period 05 – 28 Feb. 2010, 00 UTC runs. Dotted lines: Reference COSMO-EU without sea ice scheme (REF), solid lines: COSMO-EU with sea ice scheme (ICE). Left column: Bias, right column: Root mean square error. Black lines: + 00h, yellow lines: + 24h, blue lines: + 48h.

shows a positive bias of up to 1.8°C, while in the ICE experiment the bias is reduced by up to 0.5°C. The root mean square error of the 2-m temperature is significantly reduced, namely, the reduction of its error variance amounts to 12% (see Fig. 8). This means that the surface temperature distribution even on surrounding land areas is much better captured by COSMO-EU with the sea ice scheme.

Figures 9 and 10 present upper air verifications of the two experiments with respect to relative humidity and temperature. They show a similar and consistent improvement of the model performance by the sea ice scheme as well. COSMO-EU without the sea ice scheme tends to develop a positive bias in the near-surface temperature. This is reduced by the sea ice scheme. The root mean square error of the near-surface temperature is slightly reduced as well. Figure 10 shows that bias and root mean square error of the relative humidity may benefit as well.

Figure 11 shows that during the melting period in April 2010 the REF experiment develops a negative bias of the 2-m temperature during day time. This is explained by the fact that the sea ice temperature is initialised by the SST analysis with night time values at 00 UTC which are kept constant during the entire forecast. A warming of the sea ice surface is not

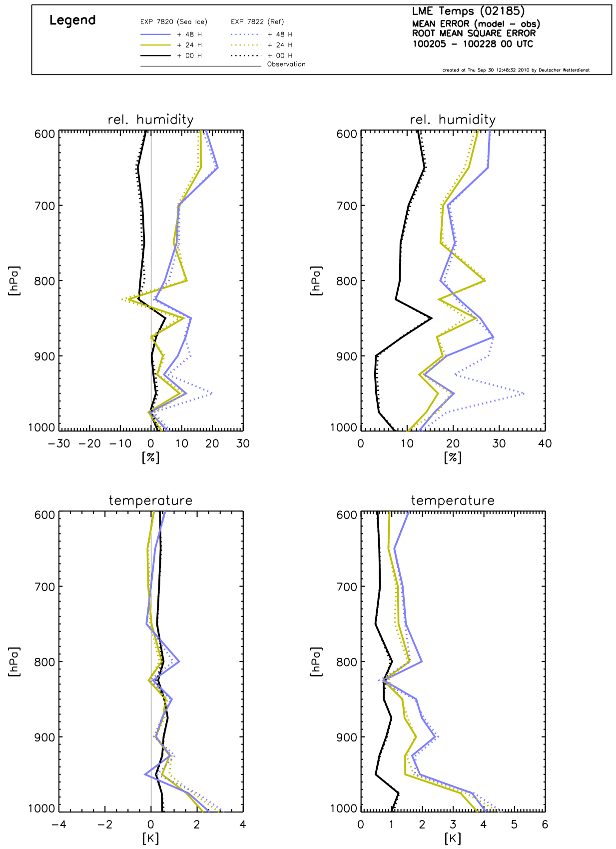

Figure 10: Same as Fig. 9, but for Lulea, Sweden (Temp 02185).

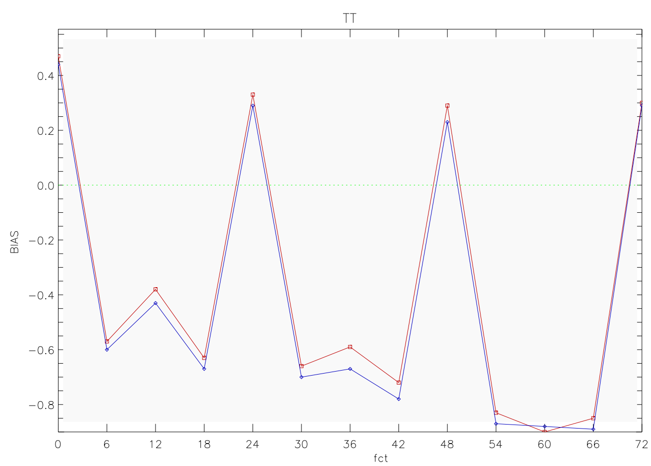

Figure 11: Bias of 2-m temperature (°C) versus forecast time (h) for the period 01 – 30 Apr. 2010, 00 UTC runs. Blue: Reference COSMO-EU without sea ice scheme (REF), red: COSMO-EU with sea ice scheme (ICE). All stations in the verification domain were used (see Fig. 6).

possible. On the other hand the ICE experiment allows for a diurnal cycle of the sea ice surface temperature, this slightly reduces the negative bias.

6 Conclusions

The sea ice scheme by Mironov and Ritter (2004) was implemented in the COSMO model. The scheme accounts for thermodynamic processes, it basically computes the energy balance at the ice's surface, using one layer of sea ice. From this the evolution of the ice surface temperature and the ice thickness are deduced. This allows for a better thermodynamically coupled treatment of sea ice in the COSMO model as lower boundary condition for the atmosphere. This means, the scheme allows for a diurnal cycle of sea ice surface temperature which was not present in the COSMO model before. Instead, the sea ice temperature was initialised by the SST analysis at 00 UTC and then kept constant at this night time value during the data assimilation cycle and also during the forecasts.

This behaviour of the sea ice scheme was successfully tested in COSMO-EU. The objective verification of a continuous numerical experiment for the period 03 Feb. – 31 May 2010 shows good improvements. In particular, the positive bias of the 2-m temperature during the freezing period in February is considerably reduced. Its root mean square error is even significantly reduced, namely, the reduction of its error variance amounts to 12%. This means that the surface temperature distribution even on surrounding land areas is much better captured by the model. In addition to the surface weather elements the upper air verification shows a similar and consistent improvement as well. In addition to this, here also the bias and the root mean square error of the relative humidity benefit. Furthermore, a negative bias of the 2-m temperature during day time, developed during the melting period in April, is reduced as well.

Acknowledgement

Thanks to the following colleagues at DWD: Martin Lange for adapting the code of the external sea surface temperature analysis to the sea ice scheme, Thomas Hanisch for including the sea ice scheme in the operational shell scripts for running the COSMO model at DWD, and Ulrich Damrath and Ulrich Pflüger for their verifications.

References

[1] Doms, G. and U. Schättler, 2002: A description of the nonhydrostatic regional model LM. Part I: Dynamics and Numerics, *Deutscher Wetterdienst*, Offenbach, **134** pp. (Available at: http://www.cosmo-model.org).

[2] Mironov, D. and B. Ritter, 2004: Testing the new ice model for the global NWP system GME of the German Weather Service; In: J. Cote (Ed.), *Research Activities in Atmospheric and Oceanic Modelling*, Rep. 34, WMO/TD 1220, WMO, Geneve, 4.21–4.22.

[3] Schulz, J.-P., 2006: The new Lokal-Modell LME of the German Weather Service, *COSMO Newsletter*, **6**, 210–212. (Available at: http://www.cosmo-model.org).

Testing of Snow Parameterization Schemes in COSMO-Ru: Analysis and Results

E.Kazakova[1,2], I.Rozinkina[1]

1: Russian Hydrometeocenter, Russia
2: Moscow State University, Russia

1. Introduction

Interaction between atmospheric and underlying surface blocks in the mesoscale model COSMO very significantly impacts the success of the 2m air temperature prediction. Snow cover presence is quite common in mid latitudes in winter. The snow parameterization TERRA_ML (called "EH" [1]) is utilized in the model COSMO. A new snow parameterization scheme is developed for potential use in the COSMO model (called "EM" or just "new" [4], [5]).

In this paper we analyze the results of two snow parameterization schemes comparison during the snow accumulation period with special focus at the snow melting processes at the end of the cold period. The issues related to the 2 m air temperature (T2m) forecasting depending on snow cover characteristics simulation are discussed. Experiments were conducted for the European Part of Russia for the periods of March 2009, December 2009 - February 2010, March 25-31 2010, April 1-10 2010.

2. Tools, data and area of study

The snow parameterization scheme "EM" was developed by E.Machulskaya and V.Lykosov [4], [5]. The heat and moisture transfer processes within the snow cover and snow - atmosphere heat and moisture fluxes are considered in this scheme.

The main differences between the "EM" scheme in relation to "EH"scheme in TERRA_ML model are:

1. multi-layer approach;
2. radiation is calculated explicitly (following exponential extinction law). Direct solar radiation penetrates into the snow cover heating not only the snow surface, but also the underlying layers. In case of low albedo (melting snow) this effect may be significant.
3. water phase conversion accounting the melted water's percolation with the following freezing and consequent heat release;
4. gravitational compaction is considered as well as metamorphic compaction.

Both schemes can operate within the multi-layer soil and vegetation model TERRA_ML, which generates turbulent fluxes and includes parametrization of snow and water fractions within the cell.

The schemes were numerically tested in the COSMO-Ru14 model with horizontal resolution 14 km. The objective verification of the scheme "EM" versus the traditional version of snow scheme "EH" with TERRA_ML within the model Cosmo-Ru in different weather conditions was executed for the periods mentioned above.

The results of consecutive 3-days forecasts were examined using the initial and boundary conditions from DWD which were applied as an initial data for COSMO-Ru model experiments during the studied periods. Short periods of integration (78 hours) was not sufficient to identify and prove any considerable differences between two schemes, therefore the predicted fields of surface pressure, precipitation, cloudiness, wind and geopotential were practically identical for both schemes.

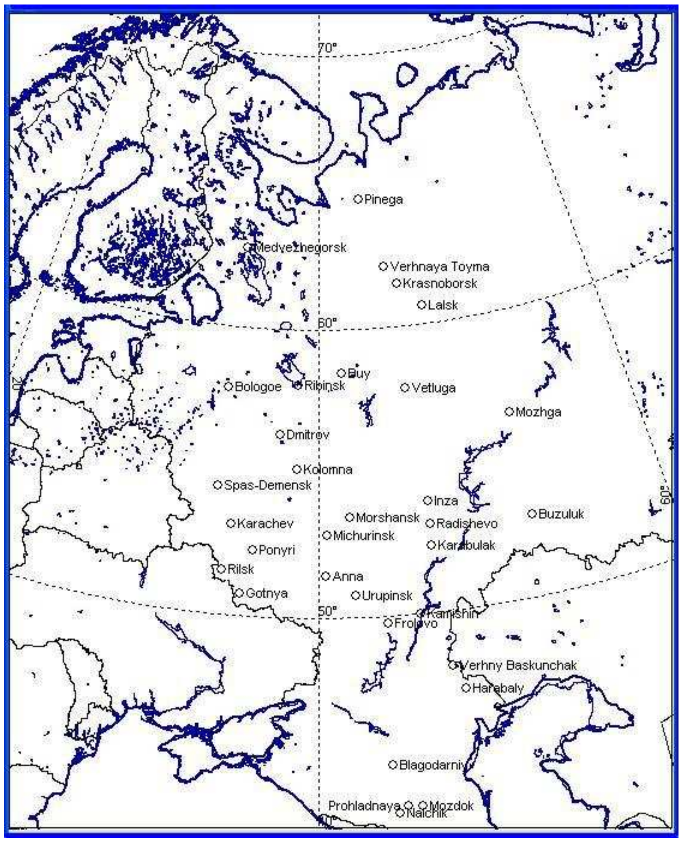

Figure 1: Stations selected for analysis

The forecasts were analyzed for day and night separately for the following elements:

- snow water equivalent (SWE),
- snow depth,
- air temperatures at 2 m (from atmospheric model).

Observation data from 33 specialized meteorological stations (Fig.1) for snow depth, water equivalent, 2m air temperature and precipitation were used for verification. In meridian direction the area exceeded 2000 km. Stations were segregated in three groups: "north", "centre", and "south". For northern stations no snow melting was observed for the entire period of February-March, for central stations the partial melting was registered, however, not resulting in complete disappearance of snow cover, for southern stations snow cover was unstable during the entire period.

3. Results of two snow parameterization schemes testing

3.1. Simulations of snow water equivalent

It was found that for almost all stations snow was observed practically during the entire winter cold period ($T \leq 0^oC$). The values of snow water equivalent (SWE) simulated by both schemes were very close, except for the period of snow cover melting during last several days of a cold season (Figs. 2, 3, 4). During this period the differences were significant. In southern area, when the amount of snow was small, with often alternate periods of melting-freezing, water equivalent differed insignificantly for both schemes. In the scheme "EM" snow melting occurs more slowly (Fig. 2).

The biggest errors for water equivalent calculated by both snow schemes (Fig.3) were most likely connected with essentially overestimated initial values of snow density obtained from DWD model. At the same time, the initial data of snow depth had a good correspondence to the data of direct measurements. In the system of initial fields calculation in DWD model water equivalent is calculated using the snow depth measurements data (snow depth is daily measured at all standard meteorological stations, though water equivalent is calculated only at few stations). The algorithm of these calculations may use the wrong values of snow density, which results in the errors of water equivalent in the model initial fields gives the overestimation of snow weight are 2-3 times in comparison with the reality at the end of winter and in single forecasts.

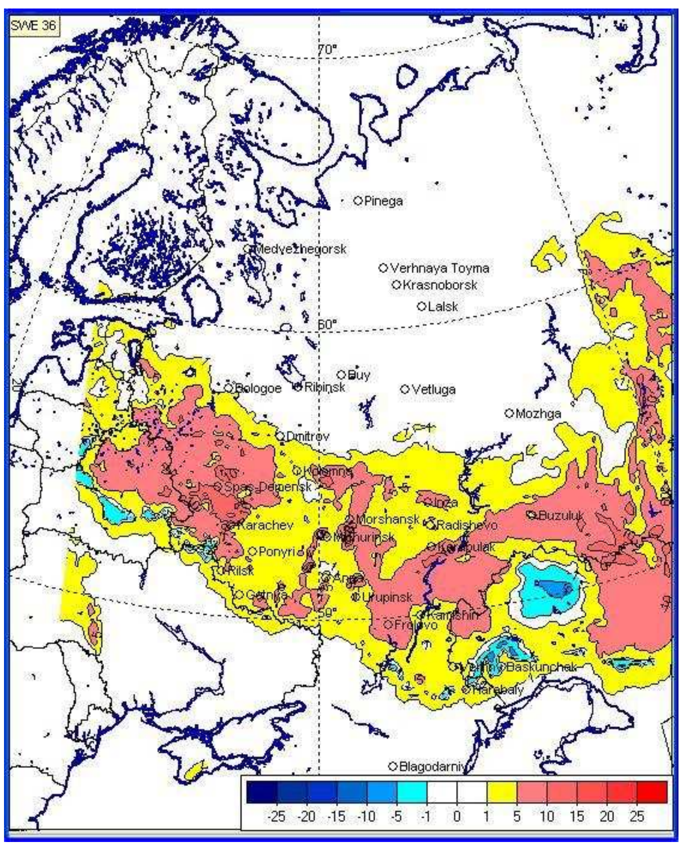

Figure 2: Difference of water equivalent forecasts (mm) on 36 h between different snow schemes (EM-EH) during the snow melting period. March 12, 2009.

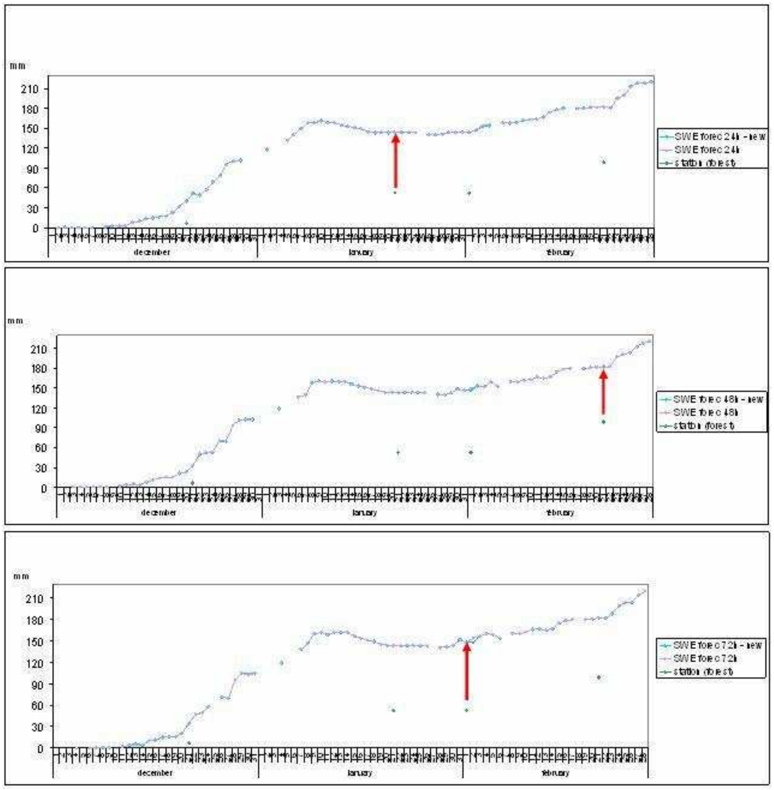

Figure 3: Difference of water equivalent forecasts (mm) on 36 h between different snow schemes (EM-EH) during the snow melting period. March 12, 2009.

Values of water equivalent forecasts are decreasing when the snow cover is melting, so that differences between forecast and measurements are decreasing as well (Fig.4). However, relative differences between two schemes become bigger in comparison with the winter period.

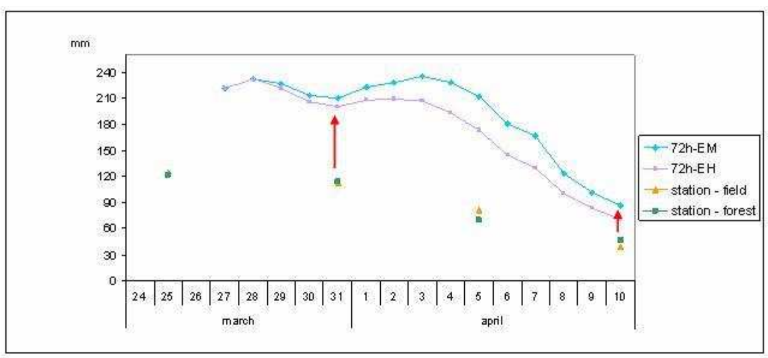

Figure 4: The example of snow water equivalent forecasts for one of the stations in the centre region for "EH" and "EM" schemes.

3.2. Snow depth simulation

On the basis of analyzed sets of forecasts it was determined that snow depth was stably well simulated by both schemes (Fig.5). Meanwhile, the "EM" scheme regularly overestimated the snow depth related to snowfalls, therefore the "EM" scheme had differences in the modeled snow depth essentially bigger in relation to direct measurements than scheme "EH" (Fig.5). Cases of snowfalls were studied in details. In absence of snowfalls, snow becomes more dense in the "EM" scheme, and the errors of snow depth values decrease. In southern regions when snow precipitation occurred at temperatures of 1-3 degrees below zero, both schemes calculated snow depth in a similar way and essential distinctions between them were not identified. In the experiments with the "EM" scheme snow completely descended more slowly than in the control "EH" run. Such conclusion confirms the previous received results on the detailed verification based on the observations at two observatories [3].

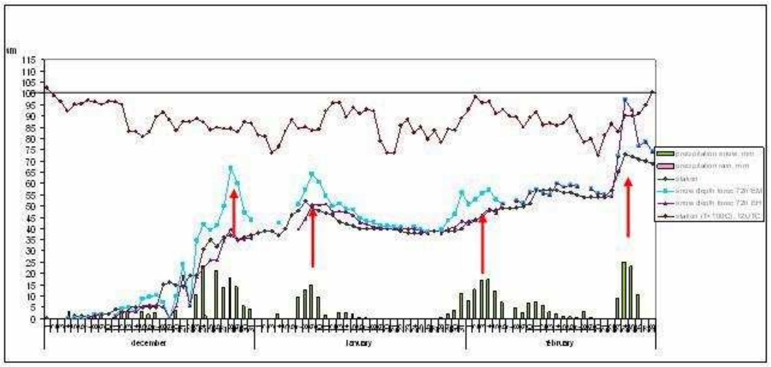

Figure 5: Example of snow depth forecasts (72 hours) for one of the stations in the northern region.

3.3. Snow density

The realistic simulation of snow depth, as well as big distortions in SWE simulations, significantly depends on the quality of the initial data used for integration. Snow depth is regularly measured at the majority of the WMO meteorological stations while SWE measurements are rare. Snow depth observations are transferred via communication channels in SYNOP-code and can be assimilated without distortion for model initial data generation. In order to have SWE initial data it is necessary to convert the snow depth (direct measurements) considering the snow density (estimated) into SWE. Therefore in order to understand the reason for big errors in SWE initial data assimilation we analyzed available measurements of snow density at the stations.

According to the measurements conducted with 5-10 days intervals, snow density changed during the 2009-2010 winter period: there were no very significant differences between the snow density in the forest and at the opened surface. Generally, the snow was most dense at the central region while at the south the highest snow compaction was registered at the end of snow period. The variability of snow density in the northern region was insignificant (tables 1 and 2).

The snow density was also calculated using 72h forecasts of snow depth and SWE for "EH" and "EM" schemes (tables 3, 4).

Version "EM" gives more friable snow during winter period then version "EH" and its values are close to measurements at the stations. However, both schemes are overestimating the snow density versus the measurements (Figs. 6, 7). During the snow melting period, "EM" scheme produces more significant snow density versus EH, which causes slower melting in the "EM" scheme.

The tables below show that there is a big dispersion in snow density data and using it directly as a constant during the whole season and for the entire region is not relevant.

region	Date														
	December			January						February					
	10	20	31	5	10	15	20	25	31	5	10	15	20	25	28
north		193					178		193		197		203		195
center		85					158		195	251	188	214	216	249	248

Table 1: Average snow density for the forest areas, kg/m^3

region	Date														
	December			January						February					
	10	20	31	5	10	15	20	25	31	5	10	15	20	25	28
north		170					197		199		201		196		196
center		137	198		197		209		210		217	230	240	244	255
south				105			136		184		195	229	308		

Table 2: Average snow density for the opened surface, kg/m^3

region	Date														
	December			January						February					
	10	20	31	5	10	15	20	25	31	5	10	15	20	25	28
north		217	241		273	358	380	377	368	383	376	351	373	292	373
center		177	251		263	347	376	359	301	351	345	344	363	347	385
south								123	299	292	349	391	413		

Table 3: Average snow density from EM: 72h forecast, kg/m^3

region	Date														
	December			January						February					
	10	20	31	5	10	15	20	25	31	5	10	15	20	25	28
north		356	351		375	389	396	396	395	396	376	351	373	292	373
center		294	339		350	389	394	388	380	387	345	344	363	347	385
south								208	347	331	341	372	410		

Table 4: Average snow density from EH: 72h forecast, kg/m^3

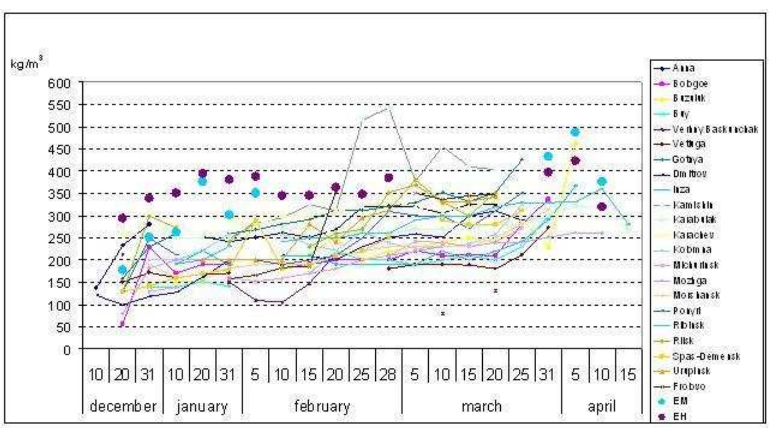

Figure 6: "Center" region's snow density according to field station measurements and 72h forecasts of EM and EH versions for the winter 2009-2010 period and March 25-April 10 2010.

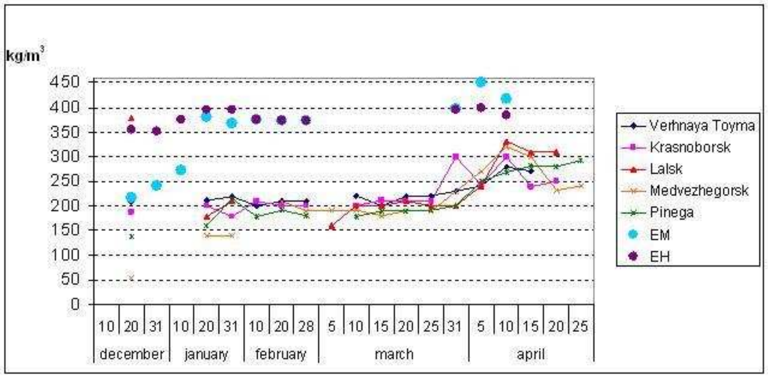

Figure 7: "North" region's snow density measured at the forest stations 72h forecasts by EM and EH for the winter 2009-2010 period and March 25-April 10 2010.

3.4. 2m air temperature simulation

One of the most important criteria of the correct work of Land-Surface Schemes (LSS) is the successful forecast of the temperature at 2 meters above the surface (T2m). The skill of this parameter forecast reflects the quality of the reproduction of all components of the land surface heat balance and the integral heat exchange between land surface and air in a model.

The "EM" scheme effects the simulated 2m temperature only in the regions of snow melting [2]. The northern and northeastern regions where no snow melting was observed or simulated both schemes gave similar results for T2m.

In the areas of snow melting the greatest positive effect in the simulation of T2m occurred at night during freezing of snow water melted in daytime. In these cases the nocturnal cooling of snow surface (and air temperature at 2 meters) occurred considerably less frequently, and the errors of T2m simulation were at 1.5 - 2^oC lesser in the "EM" scheme. This was typical for anticyclone cloudless conditions with the high daytime insulation when temperature during the day was higher than 0^oC (Fig.8). At the same time the direct sun radiation partly penetrates into snow layer and can slightly warm it in scheme "EM", as well as at night hours.

In the cases of cold weather without day snow melting and night water freezing the T2m in the experiments was practically identical for both schemes. At night hours with the clear sky conditions both schemes simulated the significantly greater cooling (up to 5-7^oC) than observed (Fig.8).

Most significant errors in T2m simulation in both schemes (new and control) occurred in the presence of snow in the cell, which didn't allow the temperature simulated by the model to fall below 0^oC (Figs.9, 10) while the real near-surface air was significantly warmer (up to 10-15 degrees). This happens in the cases when the direct solar radiation heated (at the time of light cloudy weather) the snow-free cells (roads, houses, branches of trees, etc.). This effect was especially perceived for the urbanized territories.

The updating of parameters determining the fraction of a cell covered with snow did not give the noticeable result for T2m improvement. (These numerical experiments were aimed to reproduce an effect of air heating in the snow-free parts of cells). Some effect was visible in a very narrow zone near the boundary of a snowcovered and snow-free areas. However, the effect in this zone was significant - the temperature increased 5-7 degrees, and for the stations within this area the temperature forecasts were considerably improved (Fig.11). The

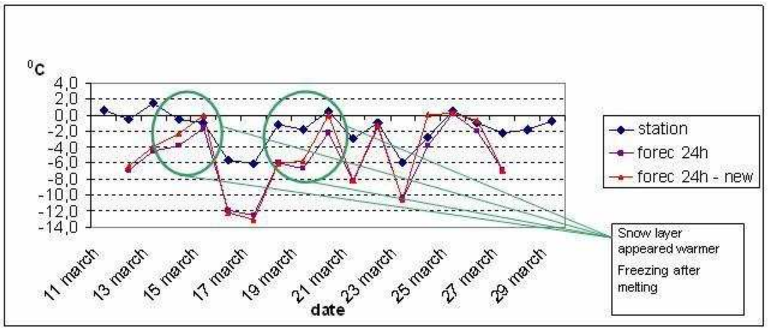

Figure 8: Typical sets of night T2m forecasts (24 hours) using the 'EM' (red line) and 'EH' (violet) schemes in comparison with observations (dark blue line).

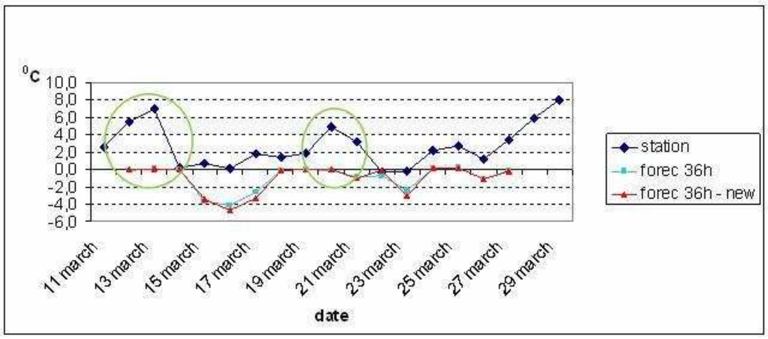

Figure 9: Typical rows of daily T2m forecasts (for 36 hours) with the use of "EM" (red) and "EH"

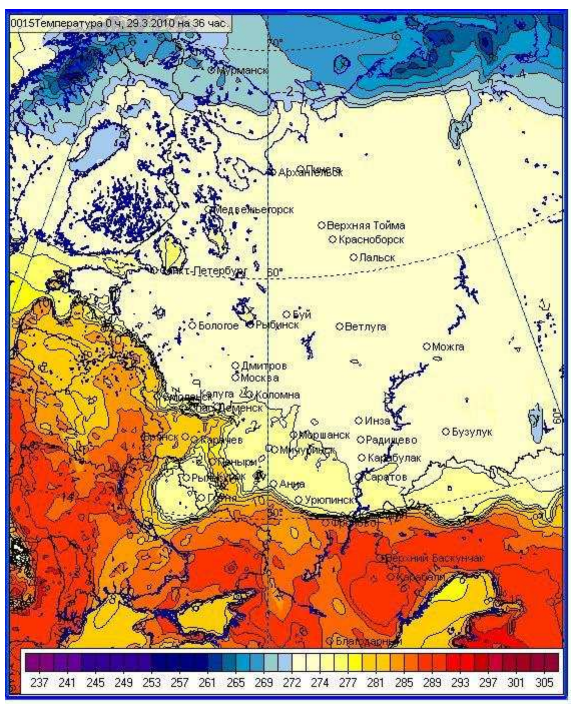

Figure 10: COSMO-Ru 2m 36 hours forecast: (color scale in K, isolines in ^oC), start: March 29, 2010. Practically at all the European part of Russia snow melted, while the forecasted T2m for huge area were "pasted" to zero value.

part of grid covered element was calculated as a function of water equivalent and parameter $cf_{snow}(zrss) = \max(0.01, \min(1.0, \frac{zwsnow}{cf_{snow}}))$, see COSMO code src_soil_multlay.f90 and [2]), SWE used in the model as initial data significantly differed from observations. Therefore updating the algorithm of parameterization of fractional covering without the functional dependence on a water equivalent (for example, with the replacement it with the functional dependence of snow depth or of air temperature) seems to be reasonable. Using snow depth initial data for fractional parameter will be more reliable since the snow depth is measured at meteorological stations and contain less mistakes then calculated SWE.

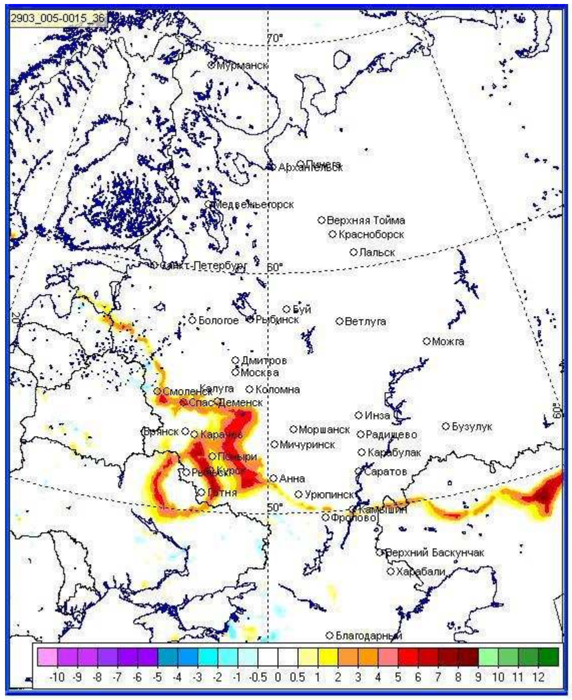

Figure 11: Difference in forecasts 2m (^oC) at maximal change of parameter of a fractional covering. In a narrow zone the temperature essentially increased.

5. Summary

The main results of the study are:

- SWE forecasts are considerably overestimated by both versions of model COSMO-Ru. It was caused by inaccuracy of SWE, and therefore the snow density initial data assimilated by the model, while the snow depth initial data was quite close to reality.
- During snow accumulation period the scheme tends to overestimate snow depth after snowfalls.
- During snow melting period snow scheme reproduce more realistically the following parameters:
  - time dependence of SWE;
  - T2m at night (due to using snow scheme "EM" there is the improvement of T2m forecast by 1.5-2^oC).

  It is related to the fact that snow scheme "EM" considered the freezing of daily melted water and following release of heat as well as heating of deeper snow layers during day-time resulted from penetration of solar radiation into snow.

- During snow melting period the biggest differences of T2m forecasts occured in vast regions for both versions (up to 10^oC). It happened since the surface temperature in the cells with the presence of snow could not be higher than 0^oC.
- Modifications of the snow fractional cover algorithm allowed to reduce the area with significant mistakes in air temperature.

6. Outlook

The 5 months statistics of the model skill T2m forecasts versus observations at different points at the European part of Russia demonstrated that the cumulative effect from transition the new snow scheme in TERRA_ML is especially positive for the areas where snow melts. This is mostly noticeable at night.

In order to improve the work of the scheme the following actions are suggested:

- The correction of algorithms of newly fallen snow density calculations in scheme "EM" (in "EM" scheme newly fallen snow is much more "friable" in comparison with "EH" scheme and the reality).
- The correction of algorithm of SWE initial data calculation using improved values of snow density.
- It seems reasonable to incorporate the scheme into the TERRA_ML model. The advantages of this scheme give positive effect which is most significant during snow melting periods even at short integration intervals, however, it is necessary to modify the algorithm of calculation of newly fallen snow density after snowfalls.

- It is necessary to optimize the snow density data considering the geographical differences calculating it as a function of temperature. It is important for receiving the initial information of snow.
- A problem the TERRA_ML model itself has - parameterization of fractional cell coverage depending on water equivalent. It seems reasonable to improve the algorithm taking into account snow-free surfaces during snow melting periods.

References

[1] Doms G., Heise E. et al., 2007: A Description of the Nonhydrostatic Regional Model LM, part 2: Physical Parameterization, *www.cosmo-model.org*.

[2] Kazakova E., Machulskaya E., Rozinkina I., 2010: Results of testing of the new snow parameterization scheme in spring snow melting conditions. Proceeding of State Institution Hydrometeorological Research and Development Center of Russian Federation . Issue 344. *Atmospheric physics and weather forecast*, pp.**147-164**.

[3] Machulskaya E., 2009: An examination of the quality of a new snow parameterization scheme combined with the COSMOs land surface scheme TERRA. *Research activities in atmospheric and oceanic modelling, CAS/JSC WGNE, WMO*, No. 39, p. **5.13-5.14**.

[4] Machulskaya E.E., Lykosov V.N., 2008: An advanced snow parameterization for models of atmospheric calculation, *COSMO Newsletter*, No.8, pp.**10-16**.

[5] Volodina E. E., L. Bengtsson, Lykosov V. N., 2000: Parameterization of heat and moisture transfer through snow pack for simulation of seasonal variations of land-surface hydrologic cycle, *Russian Journal of Meteorology and Hydrology*, No. 5, pp. **5-14**.

Preliminary results with very high resolution COSMO model for the forecast of convective events.

Antonella Morgillo

Arpa-Simc

amorgillo@arpa.emr.it

1 Introduction

Many operational weather centres tend to move towards an improvement of the spatial resolution of their numerical weather prediction models (NWP). The actual resolution of the highest resolution Limitated Area Model (LAM) is about 2-3 km, and it is well known that at this spatial resolution the convection is partly parametrized and partly not (i.e. it needs some kind of parametrization). The very high resolution models (at 1km scale) are called *storm permitting model*; the model should be able to create the convective clouds by its own and it should permits to the convection to grow up without any kind of parametrization. It's a common sense that an improvement of the spatial resolution will improve the prediction of local weather in particular with regard to the precipitation field in convective events. Several studies show that improving the resolution lead to a more realistic precipitation forecast in particular for some convective events like severe thumderstorm and so on (Weismann et al. 1997; Romero et al. 2001; Speer and Leslie 2002; Done et al. 2004, Lean et al. 2008; Roberts 2003). This should lead to a more *realism* in the forecast, even if much realism does not necessarily mean a better forecast (Roberts and Lean, 2008). But there are several reasons why an improved spatial resolution should lead to a better forecast. For example a better representation of the orography (more similar to the real one). But the main reason is that the increased resolution enables the model to represent the convection explicitly rather than by means of parametrization. Actually the COSMO model is running at ARPA-SIMC in two configurations: COSMOI7 and COSMOI2. The first runs with a spatial resolution of about 7 km and the last runs with a spatial resolution of about 2.8 km. In this work a first attempt to run COSMO model in an experimental configuration with a spatial resolution of $1km$ is made (hereafter COSMOI1). In this brief report the author wants to show some case studies run with COSMO model at 1km of spatial resolution. Sec. 2 describes the model configuration and the dataset used for the verification. In Sec. 3 few case studies are described in details, and in the last Section (Sec.4) some preliminary conclusions are presented.

2 Model configuration and verification dataset

Model configurations and domains

All the experiments were run with COSMO model version 4.9, and INT2LM version 1.10

- COSMOI7 - run with an horizontal spatial resolution of about 0.625 (about 7 km) and 297 X 313 grid points and 40 vertical levels. The boundary conditions (BC) are provided by IFS (ECMWF Integrate Forecast System) forecast, and the initial conditions (IC) from 12 hours previous COSMO assimilation cycle;

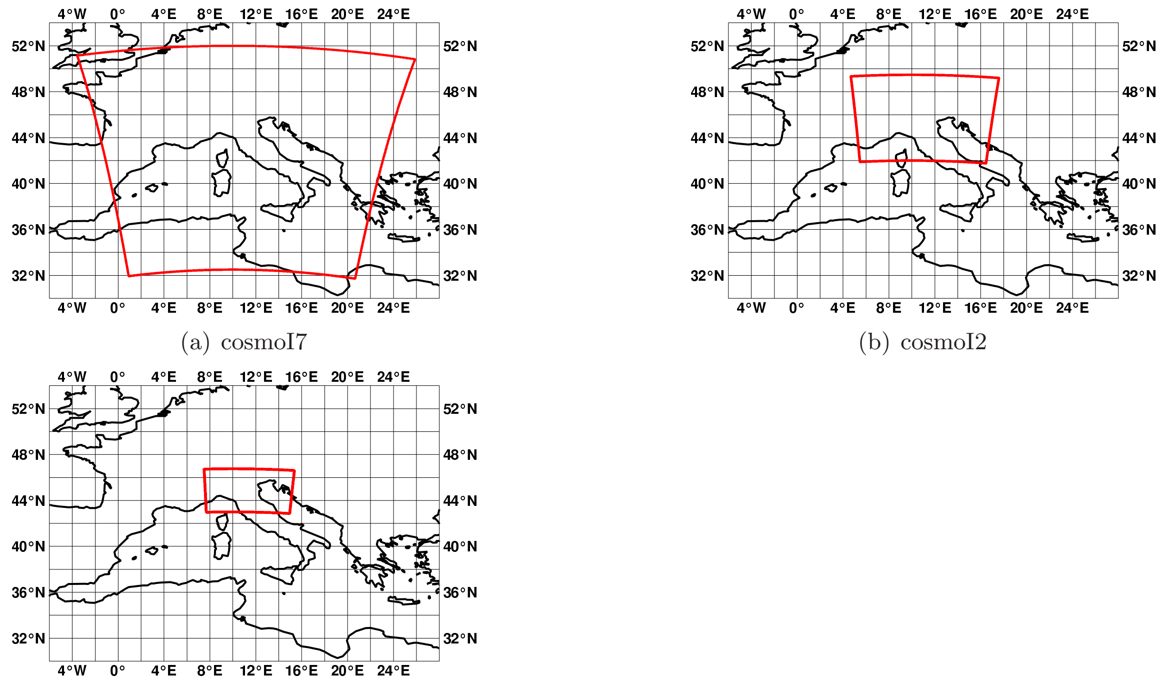

(a) cosmoI7

(b) cosmoI2

(c) cosmoI1

Figure 1: Integration domains for the three configurations

- COSMOI2 - run with horizontal grid lenght of about 0.025 (about 2.8 km), 341 X 300 grid points and 45 vertical levels. The IC and BC are provided by COSMOI7 forecast;
- COSMOI1 with grid lenght of about 0.01 (about 1 km), 551 X 400 grid points and with 45 vertical levels (like COSMO I2). The IC and BC are provided by COSMOI7 forecast;

The last two COSMO models are both nested into COSMOI7 without any previous assimilation cycle. The domains of both high resolution models are smaller than COSMOI7 domain. In particular, because of large amount of computer resource, the COSMOI1 domain is much smaller than the others. The domains of the three models are shown in Fig. 1.

Model physics

- Convection: In the COSMOI7 run the mass flux Tiedke scheme is used as convective parametrization. In the COSMOI2 and COSMOI1 configuration the grid scale are convection permitting and the parametrizzation of convection is turned off. Only the shallow convection is allowed
- Microphisics: For both very high resolution models the basic parametrization scheme for the formation of the grid scale clouds and precipitation is the DM-scheme with 4 prognostic variable (water vapour q_v, cloud water q_c, cloud ice q_i and graupel q_g).
- Assimilation: Only the 7km model was run with 12 hours previous assimilation cycle (nudging scheme) and this provides the initial and boundary conditions for the two nested models that run without any assimilation scheme.
- Numerics: Regarding the numerical integration in the COSMO I7 the Leapfrog scheme is used, while in both very high resolution models we use the Runge-Kutta scheme.

- Diffusion: The COSMOI7 runs without horizontal diffusion, while the high resolution models run with horizontal diffusion only on the boundary, i.e. we use a trhee dimensional domain mask that permits the horizontal diffusion only on the boundary, not inside the domain. While in the 7km the horizontal diffusion is not required, for the high resolution models, it becomes more important.

Dataset for the verification

The data used for the comparison are provided by the local radar network of Emilia Romagna and by the National radar network of the Italian National Civil Protection. The Emilia Romagna radar network is composed of two radar. One, San Pietro Capofiume, is located near Bologna, and the other, Gattatico, is located near Reggio Emilia.

3 Case Study

Key aspect of model forecast

One of the key aspects that caracterized the very high resolution forecast, is the representation of convection. We are interested in the model capability to reproduce the initiation of convection, defined as the moment in which the first precipitation (0.5 mm/h) begins to appear in the radar data (and in the model). The choice of focusing on the surface rainfall is due to the fact that it's easy to compare the model maps with the radar maps (they are more or less at the same resolution). All the models were run with 1-h output forecast. The COSMOI7 model was run for 36 hours, and COSMOI2 and COSMOI1 were run for 24 hours.

Three case studies have been run:

- 27 May 2009;
- 07 July 2009;
- 29 May 2010.

This case studies are all summers and convective event and all of them are very strong and intense.

Case study: 27 May 2009

Brief descripiton of event.

During the morning of May 27 a deep trough coming from North Europe brings a very cold air mass over a previous warm air mass located over North Italy. This unstable situation permits the growth of a lot of convective cells over North Italy in the first hours of day. In the middle of morning a large convective cell grows up in the Garda Lake area and moves toward south. More or less in the same hours a lot of convective systems begins to grow up in the Tosco-Emiliano Appennine and moves toward the Adriatic sea. In the early afternoon the convective cells from the Garda Lake hit Parma and Reggio Emilia cities with 55 mm/1h recorded at Parma rain gauge causing damages and floods in the city.

Comparison between different horizontal resolution.

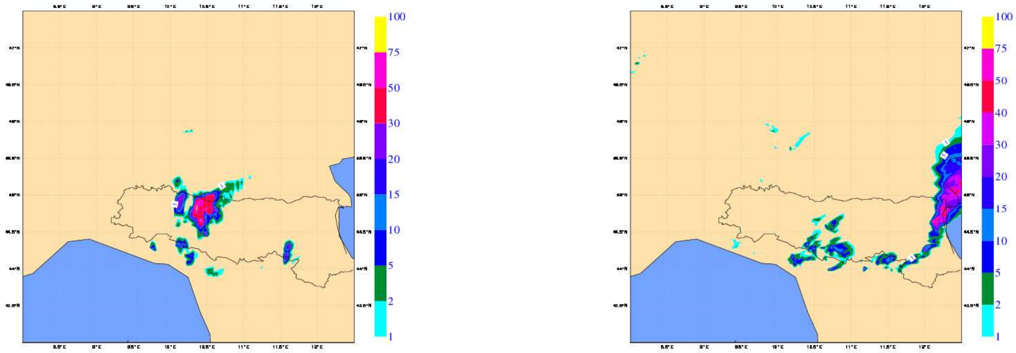

(a) Radar (b) COSMOI1

Figure 2: map of 1h cumulated precipitation at 3 p.m. from radar (on the right) and COSMOI1 model (on the left)

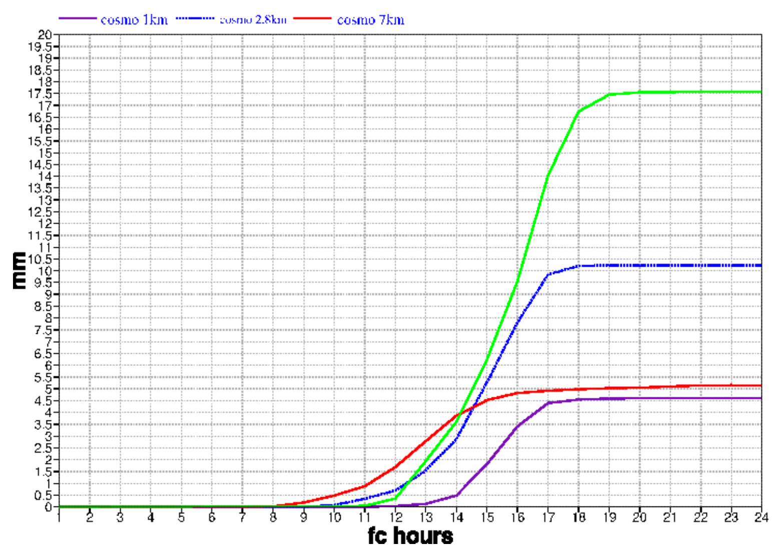

Figure 3: 24 hours cumulated hourly precipitation averaged over the Emilia Romagna region area. Red=COSMOI7, blue=COSMOI2, violet=COSMOI1, green = RADAR

All the model simulations started at 00 UTC. COSMOI2 and COSMOI1 both started with boundary and initial conditions provided by the COSMOI7 forecast. We decide to ignore the first hours of integration because the convection allowing model needed some hours to create their convective clouds. Fig.2 shows the 1-h cumulated precipitation map at 3 p.m. when the thunderstorm hits the Parma city, while Fig. shows the 24 hours cumulated precipitation averaged over the Emilia Romagna region. Some conclusion can be done:

- At 9 a.m. the model represents quite well the convective cell over the North-East of Italy, more or less near the Garda's Lake. This cell moves towards South-East in the following hours (not showed);
- at 2 p.m. the model has the convective cells over the northern boundary of the Emilia Romagna region, and also the orographic precipitation over the Tosco-Emiliano's Appennine (not showed);
- at 3 p.m. the strong convective cell that hits the city of Parma was captured by COSMOI1, but shifted towards the Eastern part of the region and underestimated (see

Fig.2).

- Fig. shows that COSMOI1 underestimates the 24 hours cumulated precipitation, and the convection begin 2 hours later with respect to the radar precipitation (radar begin to rain at 11 a.m., COSMOI1 at 1 p.m.).

Regarding the other two models we observe that:

- COSMOI2 begins its convection 1 hour earlier than radar, and underestimates the total precipitation;
- COSMOI7 underestimates the 24 total averaged precipitation and the initiation ofconvection begin 2 hours before the radar'one.

Case study: 07 July 2009

Brief descripiton of event.

In the night between 6 and 7 a strong South-West flux at the surface and the presence of humidity on the low layers permits the rising up of intense thunderstorms that develop in Northern Italy during the following day. The first precipitations occour in the first hours of the morning of 7, with a series of intense thunderstorms in the Appennine, and some intense and very localized thunderstorm in the north-east part of the cities of Modena and Bologna. In the following hours lots of severe convective cells move from west to east and hit all the region. The phenomena run out in the middle afternoon.

Comparison between different horizontal resolution.

All the three models captured the large convective system over the North Italy in the first hours of the 7th even if the two nested models overestimate the intensity of the rainfall in the cell (not showed). None of them have the little convective cells in the Emilia Romagna. Some considerations can be done from figure 4.

All the model simulations started at 12 UTC. The first 8 hours are negletted.

- COSMOI1 (and COSMOI2 too) totally underestimates the 24 hours total precipitation. Both of them miss the event in Emilia Romagna.
- COSMOI7 underestimates the 24 hours total average precipitation. It begins its convection too much early with respect the radar's one.

The events was totally missed by the three models. The most probably reason for this bad result is that all the nested models have enough CAPE and too much CIN that inhibited the triggering (not showed).

Case study: 29 May 2010

Brief descripiton of event.

In the early morning of May 29 an intense flux of cold air in the upper part of atmosphere joins with a north north-east flux in the middle atmosphere causing the growing up of some convective cells in Northern Italy. The first thumderstorms begin to appear for orographic uplift and then they organize themselves to form a large convective systems over Northern

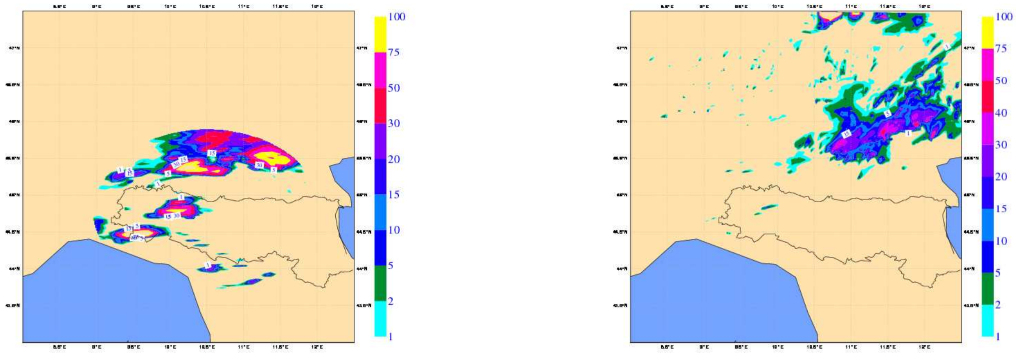

(a) Radar (b) COSMOI1

Figure 4: map of 1h cumulated precipitation at 10 a.m. from radar (on the right) and COSMOI1 model (on the left)

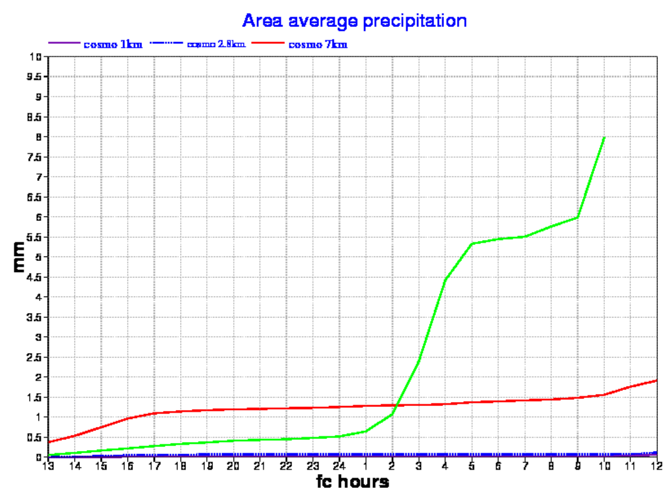

Figure 5: map of 24 hours cumulated precipitation averaged over the Emilia Romagna region. Red=COSMOI7, blue=COSMOI2, violet=COSMOI1, green = RADAR

Italy, over the Appennine and finally over the Emilia-Romagna region. Some convective thumderstorms begin to appear in the Tosco-Emiliano Appennine, in the north-east part and in the north-west part of the region. At 4 p.m. a strong thunderstorm hits the Copparo city (a very small town near Ferrara along the Po river). Copparo rain gauge records about 70mm/2hours.

Comparison between different resolutions.

- COSMOI1 shows the orographic precipitation over the Appennine, and some of the small convective cells over the north-east part of Italy between the 11 a.m. and 2 p.m.. It totally misses the precipitation in the east part of the Emilia-Romagna region, i.e. the precipitation along the Po river. It shows too many convective cells in the central part of the region (fig.6) but it misses totally the precipitation along the Po river;

- COSMOI1 has too much convective cells over the region (and over all the North Italy see Fig. 6)

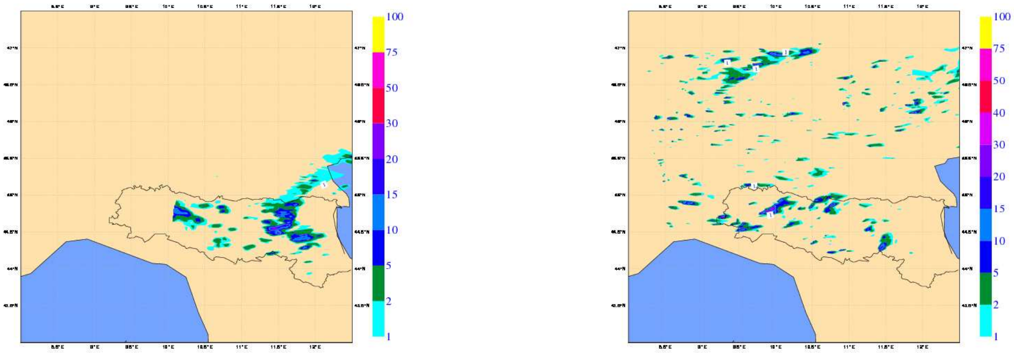

(a) Radar (b) COSMOI1

Figure 6: 1h cumulated precipitation map at 4 p.m. from radar (on the right) and COSMOI1 model (on the left)

- From figure 7 we see that COSMOI1 has the right initiation of convection and the same rising of the curve, but, unfortunately, it underestimates the 24h total precipitation averaged over the area;
- COSMOI2 (not showed) entirely misses the event. It shows a lot of little convective cells over North Italy, but none of them grow up to form the organized thunderstorm observed by the radar network; It anticipates of about 2 hours the initiation of convection;
- COSMOI7 shows all the convective activity between 9 a.m and 3 p.m. It simulates quite well the convective activity in the whole region, even if it anticipates the events of about 5 hours. The behaviour, the rising of the curve (as we can see from Fig. 7) and the total precipitation are very similiar to the radar's one. The curve seems to be simply shifted of about 5 hours. In that case the parametrized convection plays an important role for the beginning of the events. Unfortunately it does not reproduce the organized event over Copparo and along the Po river (not showed).

4 Summary and Outlook

In this work an experimental configuration of COSMO models run at different spatial resolution, spanning from 7km, to 2.8km and to 1km is described. These models have been run for few convective case studies from summer 2009 and 2010. The two high resolution models (COSMOI2 and COSMOI1) are both nested into COSMOI7 and have a very similar configuration. Both of them was run without a parametrized convection scheme. It is noticeable that COSMOI1 with explicit convection tends to initiate the convection later than the 7km (as you see from Table 1) but also with respect to the COSMOI2. In one case (07 july 2009) COSMOI1 (but COSMOI2 too) totally misses the event over the Emilia-Romagna.

A first result is that the very high resolution models without a parametrized convection have a delay in the initiaton of convection, compared with COSMOI7 (that has the convection parametrized). The second result is that the COSMOI1 model create too many small convective cells and (maybe for this reason) it usually underestimates the total averaged precipitation.

The reason for this work was to determine if running a very high resolution model (at 1km)

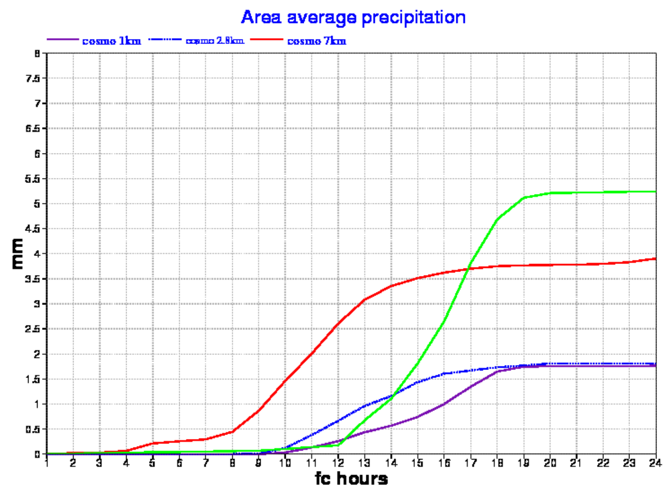

Figure 7: 24 hours cumualted hourly precipitation averaged over the E-R area. Red=COSMOI7, blue=COSMOI2, violet=COSMOI1, green = RADAR

would provide an improvement to the precipitation forecast with respect to COSMOI7 and especially respect the COSMOI2 forecast. From thiese few case it is difficoult to draw a general and robust conclusion, however the results presented here show a benefits in terms of initiation of convection and in terms of representation of convective cells. There are potential benefits for going on this way.

case studies		radar	COSMOI1	COSMOI2	COSMOI7
20090527 00	time	12 UTC	+2	-1	-2
20090527 00	tot prec	17.5 mm	4 mm	10 mm	4.5 mm
20090706 12	time	01 UTC	-	-	+9
20090706 12	tot prec	7.5 mm	0 mm	0 mm	1.5 mm
20100529 00	time	13 UTC	0	-2	-5
20100529 00	tot prec	5.0 mm	1.5 mm	1.5 mm	4.0 mm

Table 1: Table of amount of precipitaton over the 24 hours and the delay of initiation of convection with respect of radar's one

Acknowledgements

I would like to thank my collegues from my organization (ARPA-SIMC) Davide Cesari and Federico Grazzini, and from COSMO Consortium, Oliver Fuhrer (from Meteo Swiss) for useful discussion and input.

References

[1] Lean H.W.,e al., 2008; Characteristis of High-Resolution Versions of the Met Office Unified Model for forecasting convection over the United Kingdom. *Mon. Wea. Rev.*,**136**, 3408-3424.

[2] Roberts, N.M. 2003: Results from high resolution modelling of convective events (stage 1 report from Storm-Scale numerical modelling project *Met. Office Tech. Rep.*, **402** 47 pp.

[3] Romero R., C.A. Doswell, and R. Riosalido, 2001: Observations and fine-grid simulations of a convective outbreadk in north-eastern Spain: Importance of diurnal forcing and convective cold pools. *Mon. Wea. Rev.*, **129**, 2157-2182.

[4] Speer,M.S., and L.M. Leslie, 2002: The prediction of two cases of severe convection: implications for forecast guidance. *Meteor. Atmos.Phys.*, **80**, 1-4.

[5] Weisman M.L., W.C. Skamarock, and J.B. Klemp, 1997: The resolution dependence of exoplicitily modeled convective systems, *Mon. Wea. Rev.*, **125**, 527-548.

Various Implementations of a Statistical Cloud Scheme in COSMO model

Euripides Avgoustoglou

Hellenic National Meteorological Service, El. Venizelou 14, Hellinikon, Athens 16777, Greece

1 Introduction

The starting assumption towards the implementation of cloud cover in numerical weather prediction is that air inside all grid box volume is considered either saturated or unsaturated (Refs. [1], [2],[3]). From the physics standpoint however, this is an approximation to a very complex proccess (Refs. [4]). An obvious shortcoming of this hypothesis is that latent heat is released when condensation process occurs inside the grid box only after all its volume, is at least, saturated which might lead to an incorrect treatment to the initial cloud growth. Also, cloud cover might be affected by entrainmnet through grid box boundaries.

In order to partially account for these processes, in the radiation scheme of COSMO model, an alternative to default sub-grid scheme, based on relative humidity (denoted as SGRH), is proposed to account for the stratiform cloud-cover. In the emerging sub-grid *statistical* scheme (denoted as SGSL), a bivariate Gaussian distribution is invoked for the quasi-conservative properties of *saturation deficit* and *liquid water potential temperature* (Refs. [5], [6]). Within the context SGSL however, the cloud cover due to cloud ice content is treated in a rather naive fashion by simply stating cloud cover equal to 100% if *any* cloud ice is forecasted by the model. The resulting stratiform cloud cover from the implementation of SGSL in COSMO model is given by a two-parameter relation with respect to *cloud cover at saturation* and the *critical value at saturation deficit* (Refs. [7], [8]). The SGSL scheme is currently used in the moist turbulence scheme and the goal is to justify its use also in the radiation scheme within the scope of UTCS (Unified Turbulence Closure Scheme) priority project.

Additionally, the necessity for the effect of cloud-ice into the cloud cover (Refs. [9], [10]) led to a modification of SGSL to a sub-grid statistical liquid-ice scheme (denoted as SGSLI) (Ref. [11]) through the introduction of a mixed phase condensation heat via an *icing factor* defined as the ratio of cloud ice over total cloud water content.

As a part of a systematic investigation under the UTCS project, a comparison of the implementation of SGSL and SGSLI versus SGRH in the radiation scheme of COSMO model is presented over the wider geographical domain of the Balkans for a representative winter case with extended areas of stratiform clouds developed over a relatively weak wind field.

2 Analysis

For the implementation of the statistical cloud scheme the works of Sommeria and Deardorff (Ref. [5]) as well as Mellor (Ref. [6]) were followed. The subgrid low cloud fraction R and mean liquid water content $\overline{q}_l$ are estimated as

$$R = \int_{-\infty}^{\infty}\int_{-\infty}^{\infty} H(q_w - q_s) G dq_w d\theta_l \tag{1}$$

and

$$\overline{q}_l = \int_{-\infty}^{\infty}\int_{-\infty}^{\infty} (q_w - q_s) H(q_w - q_s) G dq_w d\theta_l \tag{2}$$

where q_w and q_s correspond to the total-water and saturation specific humidities respectively, θ_l is the liquid water potential temperature, H stands for the Heaviside function

$$H = \begin{cases} 0, & x < 0 \\ 1, & x > 0 \end{cases} \tag{3}$$

and G is a bivariate normal function

$$G = \frac{1}{2\pi\sigma_{\theta_l}\sigma_{q_w}(1-r^2)^{\frac{1}{2}}} exp\left[\frac{-1}{1-r^2}\left(\frac{\theta_l'^2}{2\sigma_{\theta_l}^2} - r\frac{\theta_l' q_w'}{\sigma_{\theta_l}\sigma_{q_w}} + \frac{q_w'^2}{2\sigma_{q_w}^2}\right)\right] \tag{4}$$

with primed quantities defined as $x' \equiv x - \overline{x}$ and the correlation factor $r = \overline{\theta_l' q_w'}/(\sigma_{\theta_l}\sigma_{q_w})$.

By assuming a linear approximation for q_s around the value $\overline{q}_{sl} = q_s(\overline{\theta}_l, \overline{p})$ and with the help of Clausius-Clapeyron equation the expressions for R and $\overline{q}_l$ become

$$R \approx \frac{1}{2}\left[1 + erf\left(\frac{Q}{\sqrt{2}}\right)\right] \tag{5}$$

$$\overline{q}_l \approx \frac{\sigma}{1+\beta\overline{q}_{sl}}\left[RQ + \frac{exp\left(\frac{-Q^2}{2}\right)}{\sqrt{2\pi}}\right] \tag{6}$$

where

$$Q = \frac{\overline{q}_w - \overline{q}_{sl}}{\sigma}, \qquad \sigma = (\overline{q_w'^2} + \overline{q_{sl}'^2} - 2\overline{q_w' q_{sl}'})^{\frac{1}{2}}, \qquad \beta = 0.622\frac{L^2}{R_d c_p T_l^2} \tag{7}$$

with T_l standing for the liquid water temperature, L is the latent heat for vaporization, R_d is the gas constant for dry air and c_p is the specific heat at constant pressure.

Sommeria and Deardorff (Ref. [5]), further approximated R through the linear part of an empirical curve that they drew for R by using an ensemble of 400 bivariate normal distributions

$$R \approx 0.5(1 + \frac{Q}{1.6}), \qquad 0 \leq R \leq 1 \tag{8}$$

In the statistical cloud scheme implemented in COSMO model, the low cloud cover is parameterized through a similar relation

$$R \approx A(1 + \frac{Q}{B}), \qquad 0 \leq R \leq 1 \tag{9}$$

The parameters A (cloud cover at saturation) and B (critical value of the saturation deficit) are denoted as *clc_diag* and *q_crit* and are tunable in the physical parameterization of COSMO model code. The default values of these parameters used in the present work were chosen to be 0.5 and 4.0 respectively.

Towards the evaluation of the validity of the cloud cover schemes, SGSL and SGSLI were tested in reference to the default SGRH scheme. But in order to further gauge how SGRH is perturbed by the statistical schemes mainly due to cloud-ice, three additional implementations were added and are inscribed as follows,

SGSL_I7 : SGSL is activated in COSMO_V4.11 and cloud cover is set 100% if cloud-ice is more than 10^{-7} Kg/Kg.

SGSL_low : SGSL is activated in the lower troposphere while the default SGRH scheme remains in the upper troposphere.

SGS_L_RH : SGSL is activated for grid points with *no* cloud-ice and SGRH scheme is used for the rest of the grid points.

Although these implementations are rather artificial, they contribute towards a better understanding of the *relative* value of SGSL/SGSLI versus SGRH schemes

3 Case Study

A 48-hour period was considered, starting from 12 UTC of December 24 2007. The boundary conditions came from a three-hour interval GME analysis on forty vertical levels and with horizontal grid of 0.05^0 ($\sim$ 50 Km). The domain under consideration (Fig. 1) covers the wider Balkan having domain of Greece in the center. In all implementations COSMO_V4.11 was utilized except for the test version SGSLI which is based on COSMO_V4.6. On the synoptics standpoint (Fig. 2), from the mean sea level pressure and 500 Hpa geopotential analysis charts, we may see that there was a relatively weak south-western wind field over the region. This feature, combined with the relatively cold air in the lower (850 Hpa) and middle troposphere (500 Hpa), led to extensive cloud cover rich in cloud-ice content as can can be inferred from the relative humidity analysis at 700 HPa.

Regarding radiation budgets (Fig. 3), it was found that there are relative differences especially for the thermal radiation budgets. The thermal radiation budgets at the top of the atmosphere showed that there was more outgoing thermal radiation from the implementation where the relative umidity scheme was invoked (i.e SGRH, SGSL_low, SGS_L_RH implementations). Correspondingly, the thermal radiation budgets at the surface showed that there was less outgoing thermal radiation from the default implementation of the relative humidity SGRH scheme.

Looking at the average cloud cover (Fig. 4), less high clouds were produced when the relative humidity scheme was invoked (i.e SGRH, SGSL_low, SGS_L_RH implementations). More medium and low clouds are produced from the default SGRH scheme while the SGSLI produced the least medium and low clouds

In the upper six-figure panel of Figs. 5 and 6 the total cloud cover of SGRH (upper left), SGSL (upper middle), SGSLI (lower left), SGSL_low (lower middle) and SGS_L_RH (lower right) were presented in reference to an infrared satellite picture. The encircled areas show that the relative differences favored slightly the statistical scheme in any of its implementations against the default SGRH. The other three panels show the cloud cover components for all implementations. In the first panel, the SGSL_I7 scheme was missed but it generally gave the same cloud cover as SGSL scheme.

An impact of cloud cover on 2m temperature is presented for Aghialos meteorological station which is positioned at the Central-East coast of mainland Greece (Fig. 8) against observations and in reference to its cloud cover (Fig. 7) Again the temperature profile is improved when the statistical scheme is used.

4 Summary and Outlook

The cloud cover was found sensitive to the statistical cloud scheme and looks consistent with the default SGRH scheme to the extent of a perturbation. Cloud cover patterns were similar for all implementations but less high clouds were produced when SGRH scheme was invoked. Also,more medium and low clouds were produced by the SGRH default scheme. However the statistical scheme is tunable and this can be modified (current research). Significant differences were found over thermal radiation budgets. Especially those at the top of the atmosphere can be further compared with satellite data. Within the framework provided by this test case as well as several others (Ref. [12]), the subgrid cloud cover scheme looks like a flexible alternative to the default scheme of COSMO model.

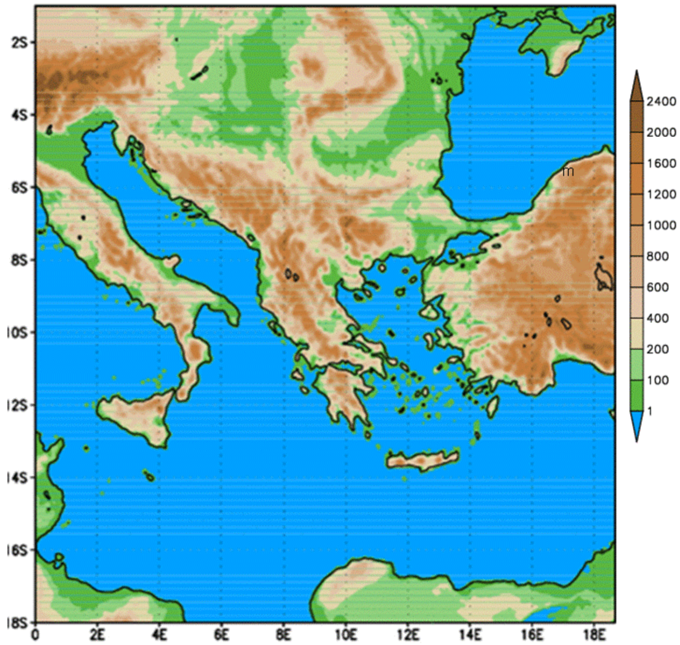

Figure 1: Domain of COSMO runs.

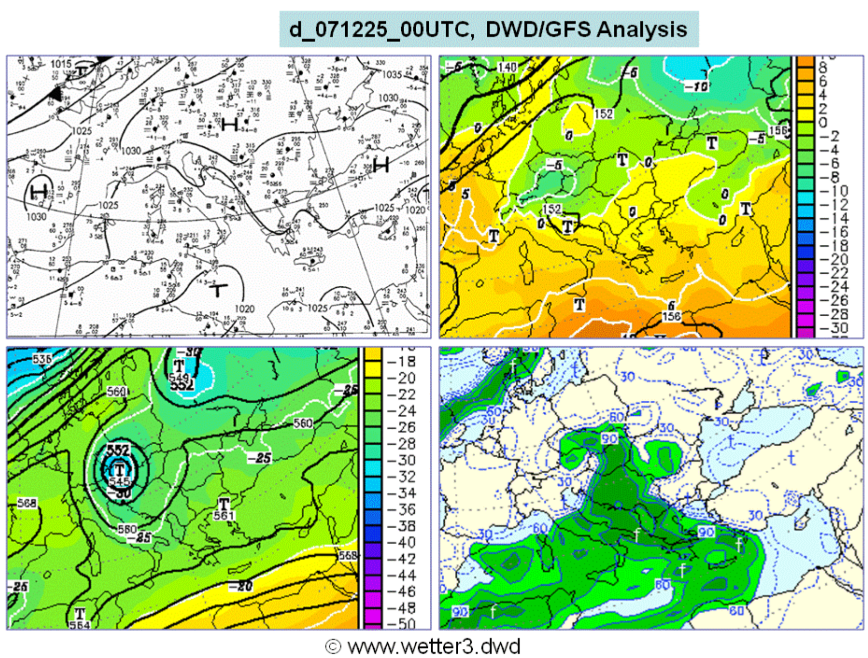

Figure 2: Surface (upper left) 850 Hpa (upper right), 500 Hpa (lower left) and 700 Hpa relative humidity (lower right) analysis at 00 UTC on the 25^{th} of December 2007.

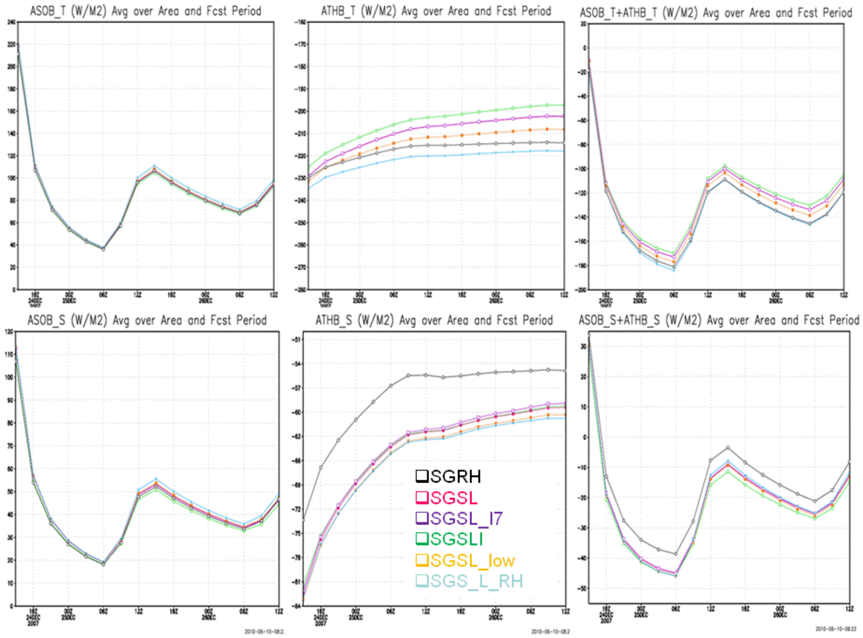

Figure 3: Average radiation balance for a 48-hour period starting from 12 UTC 24-12-2007. The upper left, middle and right figures show the solar, thermal and total radiation budgets at the top of the atmosphere. The lower left, middle and right figures show the solar, thermal and total radiation budgets at the surface.

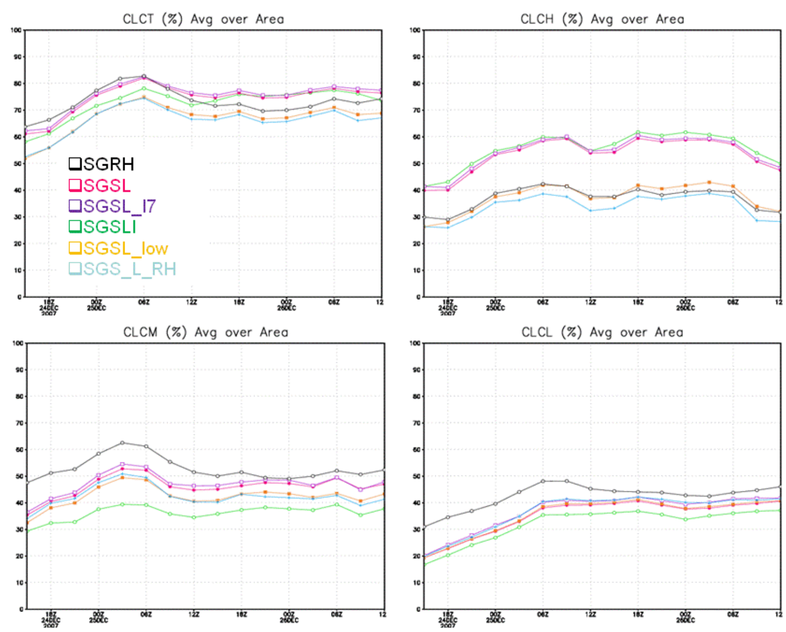

Figure 4: Average cloud cover for the different schemes over the domain and for a 48-hour period starting from 12 UTC 24-12-2007. Total, high, medium and low cloud cover is shown in upper left, right; lower left and right figures respectively

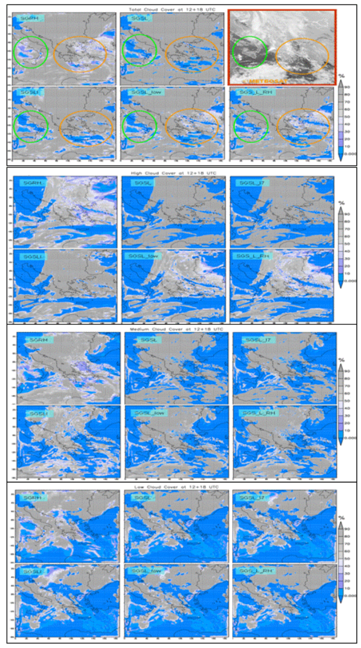

Figure 5: Cloud cover at $12 + 18$UTC (i.e. 25-12-2007 ar 06 UTC) for the different cloud schemes. From the top: The first six-figure panel from the top depicts the total, the second the high, the third the medium and the forth the low cloud cover. In every panel the figures are arranged as follows: upper left SGRH, middle SGSL, right SGSL_I7 (replaced by the infrared satelite picture in the total cloud cover panel); lower left SGSLI, middle SGSL_low, right SGS_L_RH.

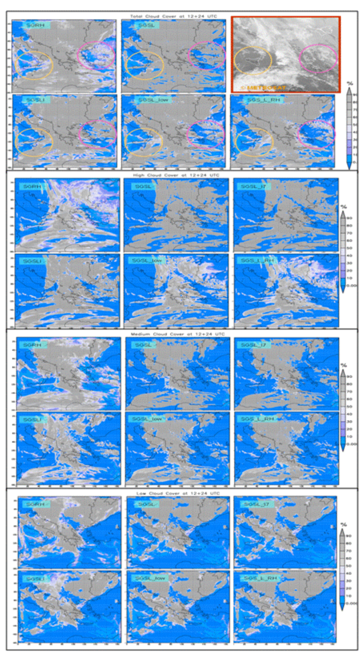

Figure 6: Cloud cover at $12 + 24$UTC (i.e. 25-12-2007 ar 12 UTC)for the different cloud schemes. From the top: The first six-figure panel from the top depicts the total, the second the high, the third the medium and the forth the low cloud cover. In every panel the figures are arranged as follows: upper left SGRH, middle SGSL, right SGSL_I7 (replaced by the infrared satelite picture in the total cloud cover panel); lower left SGSLI, middle SGSL_low, right SGS_L_RH.

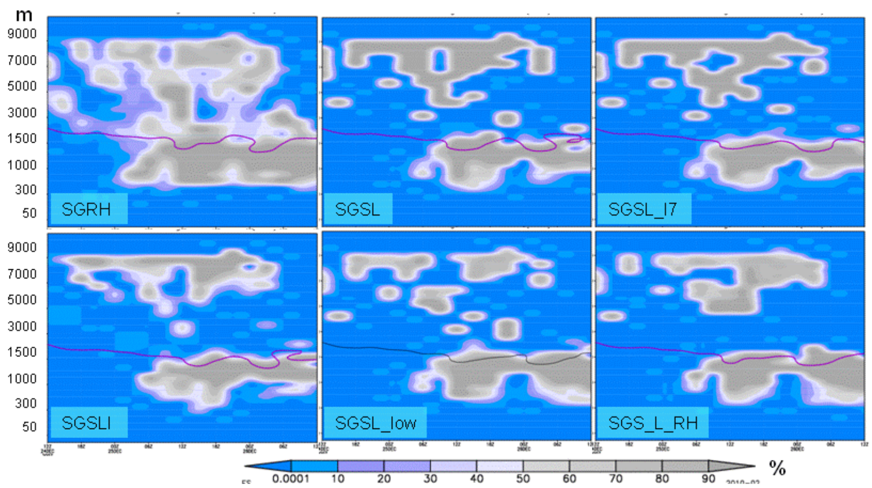

Figure 7: Profiles of cloud cover over Aghialos (Station #16665) for the different Cloud Cover Schemes in 3-hour intervals. The 48-hour Period starts from 12 UTC 24-12-2007. The vertical axis corresponds to model levels and is not linear with height. The purple curve depicts the 0^o C isotherm

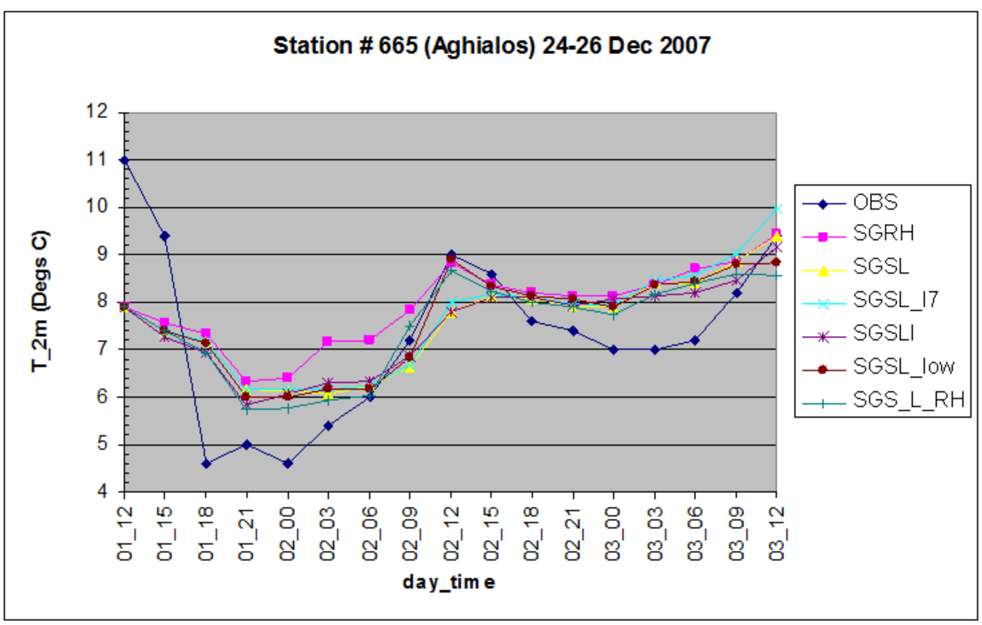

Figure 8: Profiles of 2m Temperatures over Aghialos (Station #16665) for the different Cloud cover Schemes in 3-hour intervals. The 48-hour Period starts from 12 UTC 24-12-2007.

References

[1] R. D. Schlesinger, 1973: A numerical model of deep moist convection: PartI. Comparative experiments for variable ambient moisture and wind shear. *Journal of the Atmospheric Sciences*, **30**, 835-856.

[2] J. T. Steiner, 1973: A three-dimensional model of cumulus cloud development. *Journal of the Atmospheric Sciences*, **30**, 414-435.

[3] G Sommeria, 1976: Three-dimensional simulation of turbulent process in an undisturbed trade wind boundary layer. *Journal of the Atmospheric Sciences*, **33**, 216-241.

[4] D.V. Mironov, 2009: Turbulence in the Lower troposphere: Second-order Closure and Mass-Flux Modeling Frameworks. *Lecture Notes in Physics*, **756**, 161-221.

[5] G. Sommeria and J. W. Deardorff, 1977: Subgrid-Scale Condensation in Models of Non-precipitating Clouds. *Journal of the Atmospheric Sciences*, **34**, 344-355.

[6] G. L. Mellor, 1977: The Gaussian Cloud Model Relations. *Journal of the Atmospheric Sciences*, **34**, 356-358.

[7] M. Raschendorfer, 2005: A new TKE-based Scheme for Vertical Diffusion and Surface-layer Transfer. *DWD Internal Report*.

[8] E. Avgoustoglou, T. Tzeferi, and I. Papageorgiou, 2006: Implementation of the Statistical Cloud Scheme Option; Preliminary Tests. *COSMO Newsletter* **6**, 88-93.

[9] J. W. Deardorff, 1976: Usefulness of Liquid-Water Potential Temperature in a Shallow-Cloud Model. *Journal of Applied Meteorology*, **15**, 98-102.

[10] S. A. Smith and Del A. D. Del Genio, 2002: A simple conceptual conceptual model of cirrus horizontal inhomogeneity and cloud fraction. *Quarterly Journal of the Royal Meteorological Society*, **128**, 149-171.

[11] M. Raschendorfer, 2008: Mixed water/ice phase in the SGS condensation scheme and the moist turbulence scheme. *Presentation*, 10^{th} COSMO General Meeting, Cracow, Poland.

[12] E. Avgoustoglou, 2010: Sensitivity Evaluation of Various Implementations of the SGS Cloud Scheme over Greece. *Presentation*, 12^{th} COSMO General Meeting, Moscow, Russia.

COLOBOC - MOSAIC parameterization in COSMO model v. 4.8

Grzegorz Duniec, Andrzej Mazur

Department of Numerical Weather Forecasts Institute of Meteorology and Water Management
61 Podleśna str. PL-01-673 Warszawa, Poland

Summary

Processes occurring on borderline between ground and bottom layer of the atmosphere in COSMO model vs. 4.8 might be parameterized in two different ways using MOSAIC and TILE parameterizations. Multiple test should be performed to allow operational use of one of these parameterizations. Authors implemented the MOSAIC approach. The tests were carried out on specially selected data. Terms were selected to cover the various physical conditions prevailing in the atmosphere and in soil. In the course of the tests different numerical and convection schemes were applied.

1. Introduction

The interaction between the Earth surface and the atmosphere is a very important source of water vapor and energy in atmosphere. Therefore it is very important to correctly parameterize physical processes that occur between the ground surface and the bottom layer of the atmosphere. The Earth surface is not homogeneous but covered with various types of vegetation and other elements of ground coverage. Ground can consist of various types of soil (clay, silt, mud, sands, sludge, etc.) characterized by differing physical properties such as thermal conductivity, porosity etc. To concern a non-homogenous ground surface a numerical model can include two parameterizations - MOSAIC and TILE approach.

2. MOSAIC approach

In MOSAIC approach (Ament 2006, 2008; Ament, Simmer 2008) every single grid of computing domain consists of n equal sizes located geographically. For every grid an average value of streams of latent heat, sensible heat, speed and humidity is calculated. For example, the flow of latent heat is computed using the following formula:

$$E_0 = -\frac{1}{N}\sum_{i=1}^{N} \rho_i \, K_{h,i}|v_h| \, (q_{atm} - q_{s,i}) \tag{1}$$

where: v - wind speed, ρ - total air density, q_{atm} humidity in the air, qs - humidity at the surface of the Earth, K_h - turbulent transfer coefficient, and the flow of sensible heat is

$$H = -\frac{1}{N}\sum_{i=1}^{N} c_p\rho_i \, K_{h,i}|v_h| \, (\theta_{atm} - \theta_{s,i}) \tag{2}$$

where: v - wind speed, ρ - total air density, K_h - turbulent transfer coefficient, c_p - specific heat at constant pressure, θ_{atm} - air temperature, θ_s - the temperature of the Earth's surface.

Other streams are calculated in a similar way. Exchange rates are determined using the local parameters, roughness and the Earth surface temperature, taking into account air temperature and wind speed. Radiation processes are calculated in two steps. In the first step it is calculated for each column using the average coefficient of albedo and emission of infrared (long-wave) radiation.
In the second step of the designated average net radiation processes for every grid are spread over the components using the local albedo and temperature coefficient for all sub-grids.

3. TILE approach

In a TILE approach we are dividing a surface inside the mesh grid computing on n classes. Contrary to MOSAIC, where a grid has been split into n identical items, in TILE approach each item has (or may have) different size. For each class of the surface the physical processes are calculated separately.
Latent heat flux is calculated from the formula:

$$E_0 = -\sum_{i=1}^{N} f_i\,\rho_i\,K_{h,i}|\vec{v_h}|\,(q_{atm} - q_{s,i}) \tag{3}$$

and sensible heat flux:

$$H = -\sum_{i=1}^{N} f_i\,c_p\rho_i\,K_{h,i}|\vec{v_h}|\,(\theta_{atm} - \theta_{s,i}) \tag{4}$$

where: f_i - coefficient of surface coverage of the class. Other streams are calculated in a similar way.

In both methods there is a simplifying assumption of homogeneous soil conditions inside every grid. Consequently, same values of temperature and humidity of soil are used in sub-grids in MOSAIC approach or for all classes of soil used in the TILE approach. Only parameters of surface roughness or surface resistance used to calculate the individual streams are equal.

4. Numerical Tests

In Institute of Meteorology and Water Management a MOSAIC approach has been implemented.
Meteorological fields selected from results of COSMO model to comparisons were as follows:

- T2M - air temperature, 2 m a.g.l and TD - dew point temperature, 2 m a.g.l,
- TSO - soil surface temperature, and WSO - soil water content,
- U10 - zonal wind component and V10 - meridional wind component, 10 m a.g.l.

Dates of experiments - selected data from six terms: 1.II.2009 - 00:00 UTC, 22.IV.2009 - 12:00 UTC, 16.X.2009 - 00:00 UTC and 06:00 UTC, 04.XI.2009 - 12:00 UTC, 21.XI.2009 - 06:00 UTC.

The above covered prevailed yet different weather conditions. Below one can find a brief description of these weather conditions together with synoptic situations.

The domain of experiments is shown in Figure 1. It covers Poland and its vicinity, with the basic grid size of 7 km.

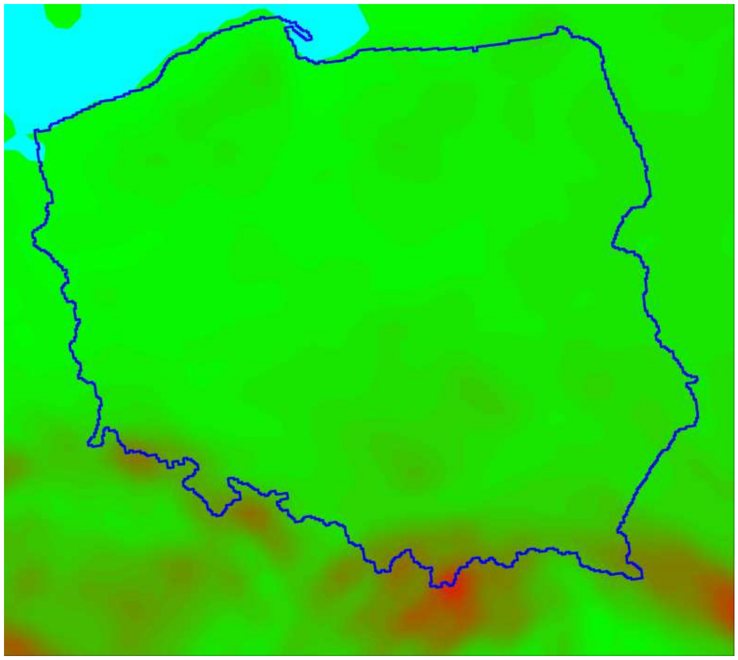

Figure 1: Domain for experiments

Meteorological conditions on 1 February 2009 at 00:00 UTC

Synoptic situation: Western Europe was in a range of low pressure zone with fronts. The eastern part of the continent was under the influence of widespread high pressure center. Over Poland, the weather was due to high pressure centre of 1035 hPa above the Gulf of Finland.

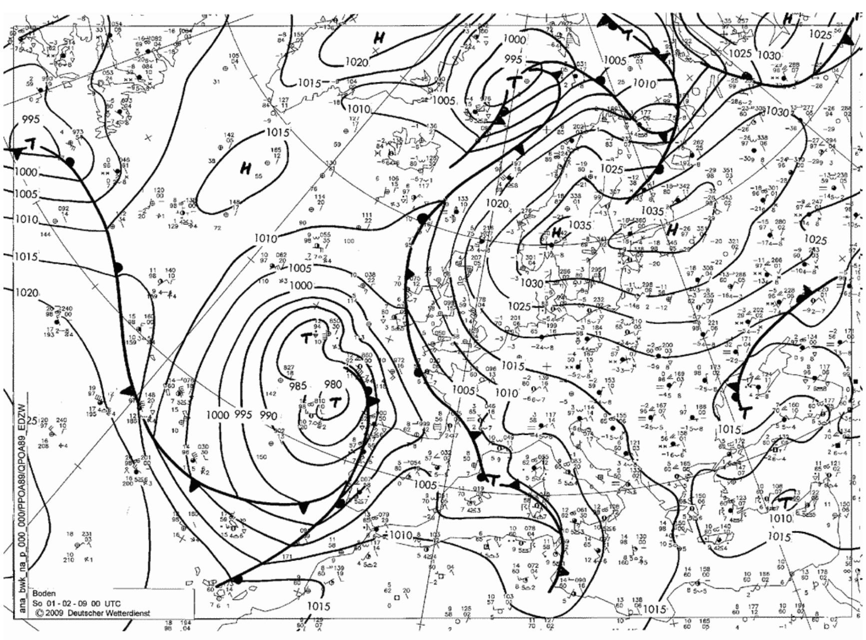

Figure 2: Synoptic situation, 1 February 2009, 00:00 UTC

Clouds: Stratocumulus, Stratus, scattered Cumulonimbus, Altocumulus and Altostratus.
Cloud cover: 100%.
Phenomena: snow, fog, fog freezing into rime.
Pressure reduced to sea level: from 1016.2 hPa to 1027.7 hPa.
Wind: weak and moderate, strong in mountains, mostly from east.
Air temperature: from -14.1°C to -1.5°C (mountains).

Meteorological conditions on 22 April 2009 at 12:00 UTC

Synoptic situation: Poland was under the influence of high pressure zone with center of 1025 hPa over Latvia and Belarus. In the western part of Europe - high pressure zone with center over southern Wales. Between these two zones - an occurrence of front passing over Poland during the next 24 hours and giving precipitation.

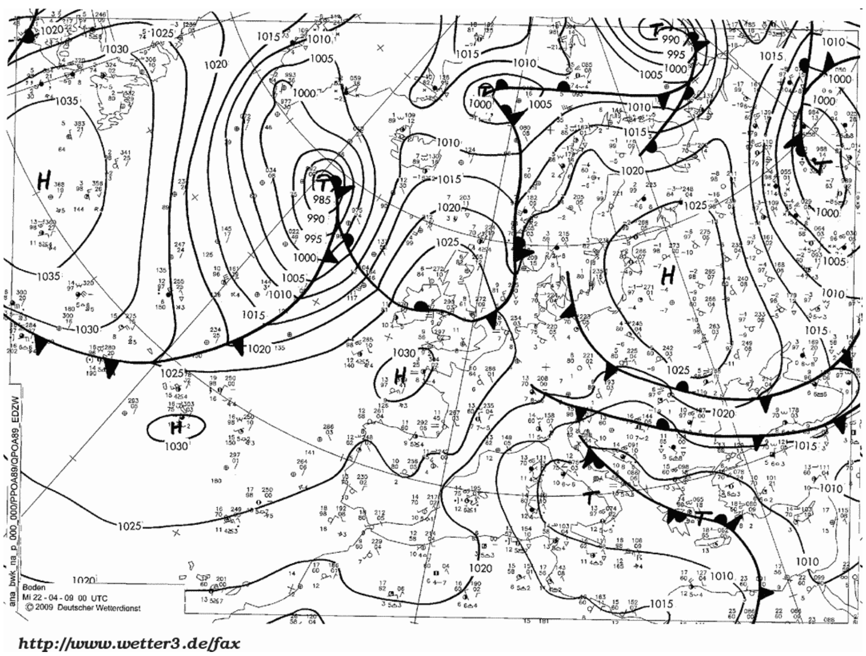

Figure 3: Synoptic situation, 22 April 2009, 00:00 UTC.

Clouds: Cumulus humilis and mediocris (locally Cumulonimbus), Altocumulus perlucidus, Cirrus fibratus and spissatus, Cirrostratus.
Cloud cover from 0 to 75%.
Phenomena: locally rainfall showers and storms (Świnoujście, Szczecin, Slubice)
Pressure reduced to sea level: 1015 hPa 1020 hPa.
Wind: weak and moderate (1-8 m/s), variable direction.
Air temperature: from 3.9°C to 18°C.

Meteorological conditions on 16 October 2009 at 00:00 and 06:00 UTC

Synoptic situation at 00:00 UTC: Central Europe, the Balkans as well as part of the Ukraine and Belarus were in a mass of cold air. Poland was in the range of low pressure zone with center of 1015 hPa over eastern Poland.

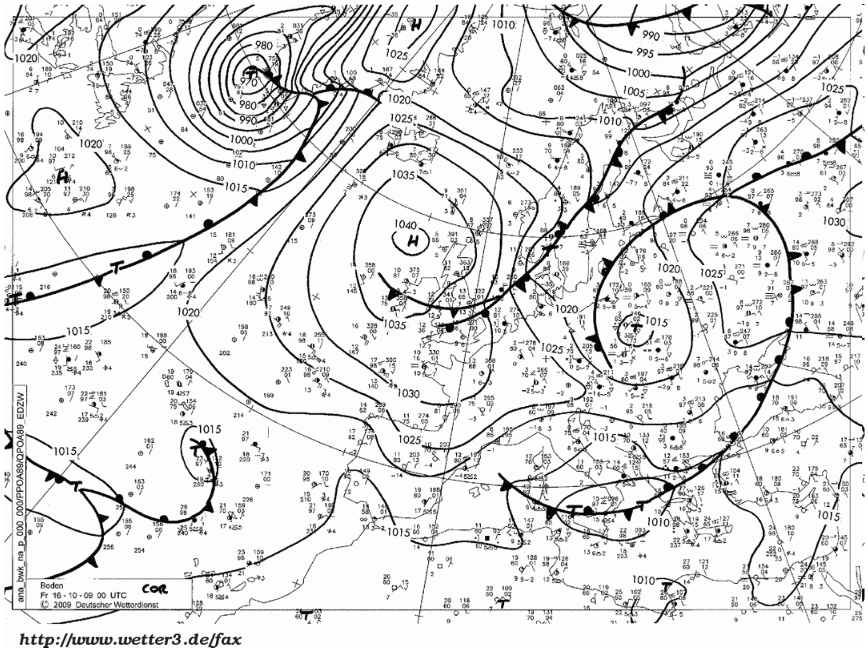

Figure 4: Synoptic situation, 16 October 2010, 00:00 UTC

Clouds: Stratus fractus and nebulosus, Stratocumulus, scattered Cumulonimbus, Altocumulus, Cirrus, Altostratus.
Cloud cover mostly 100%.
Phenomena: rain showers, locally heavy rain with snow, snow, fog and mist.
Pressure reduced to sea level: from 1013 hPa to 1019 hPa.
Wind: weak and moderate, variable directions, mostly from west.
Air temperature: from -2.7°C to 5.9°C

Synoptic situation at 06:00 UTC: as above
Cloud: Stratus fractus and nebulosus, Stratocumulus, Cumulus, Altocumulus, Altostratus, scattered Cumulonimbus.
Cloud cover 100%.
Phenomena: rain showers, locally heavy rain with snow, snow, fog and mist.
Pressure reduced to sea level: from 1010 hPa to 1019 hPa.
Wind: weak and moderate, variable.
Air temperature: from -11.2°C to 4.2°C.

Meteorological conditions on November 4, 2009 at 12:00 UTC

Synoptic situation: Poland was under the influence of high pressure zone with center over Russia, occlusion front passing from west to east.

Clouds: Stratocumulus, Stratus, Altocumulus, Altostratus, scattered Cumulonimbus and Cumulus.
Cloud cover mostly over 75%.
Phenomena: rain showers, rain with snow, snow, locally heavy rain with snow and freezing rain.
Pressure reduced to sea level: from 987.5 hPa to 1007.6 hPa.
Wind: weak in lowlands, strong in mountains to the strong lowland, variable direction, mostly from south.
Air temperature: from -7.3°C to 6.7°C.

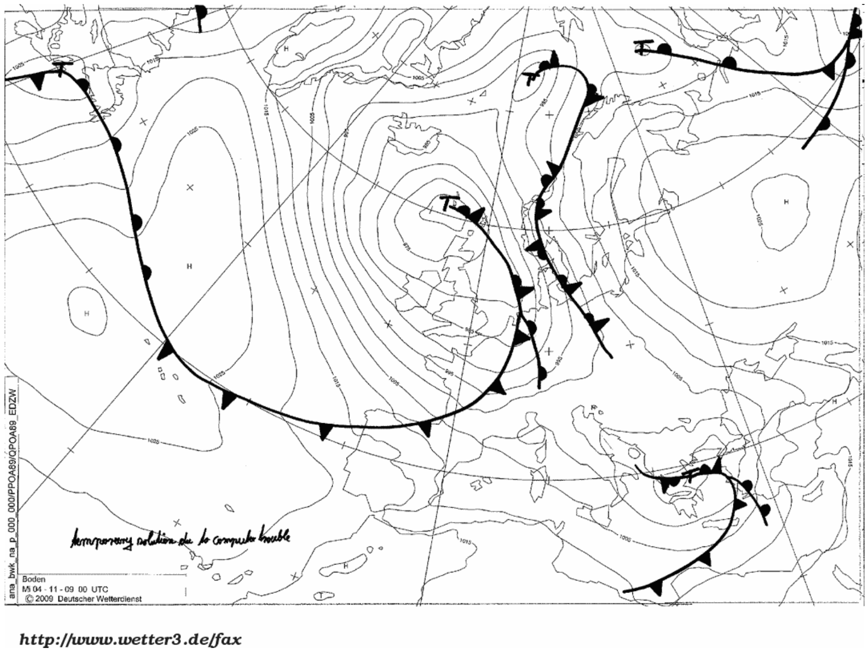

Figure 5: Synoptic situation, 4 November 2009, 00:00 UTC.

Meteorological conditions on 21 November 2009 at 06:00 UTC

Synoptic situation: Southern Europe was in under the influence of high pressure zone with the center over Switzerland. Poland in warm low pressure zone with the center of 980 hPa over Iceland.

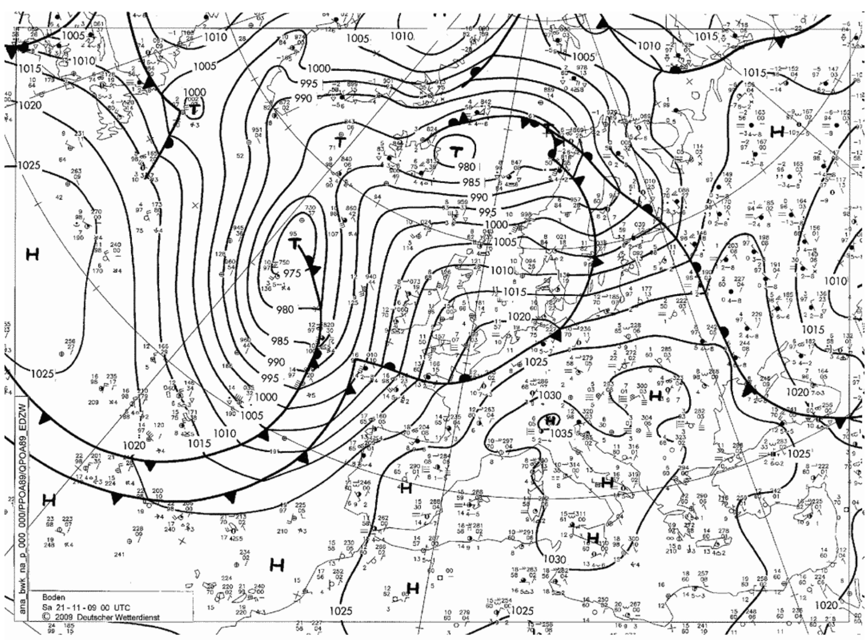

Figure 6: Synoptic situation, 21 November 2009, 00:00 UTC

Clouds: locally Stratocumulus, Altocumulus, Cirrostratus, Cirrus.
Cloud cover: mostly sunny.
Phenomena: mist.
Pressure reduced to sea level: from 1014.9 hPa to 1029.2 hPa.

Wind: weak and moderate, from western and south-western direction
Air temperature: from 1.8°C to 12.2°C.

5. Methodology and results

Following numerical schemes are implemented in COSMO model (Doms 2002, Schattler 2009, Jacobson 2000):

- three-point integration: explicit in horizontal plane, implicit in vertical (hereinafter referred to as leapdef with Tiedtkes convection scheme or as leapdef1 with Kein-Fritschs convection scheme)
- three-point, "leapfrog"-type semi-implicit integration (referred to as leapsemi with Tiedtkes convection scheme or as leapsemi1 with Kein-Fritschs convection scheme)
- two-point, third order Runge-Kutta scheme: explicit integration in the horizontal plane, implicit integration in vertical (default and standard, irungekutta=1, referred to as RungeKutta1)
- two-point, third order Runge-Kutta scheme: explicit integration in the horizontal plane, implicit integration in vertical (variant of the method with reduction of the total variation TVD, Total Variation Diminishing, irungekutta=2, referred to as RungeKutta2)

The following tests were carried out using:

- original version of COSMO v. 4.8 code referred to as orig
- modified version of code with of subs procedure fully disabled referred to as ctrl
- modified version of code with of subs procedure enabled, nsubs = 4, low-resolution input data only, identical sub-pixels - referred to as twins
- modified version of code with of subs procedure fully enabled, nsubs = 4, high resolution referred to as subs

The results were afterwards statistically analyzed. In the first step a comparison (for all possible combinations of numerical schemes and convection) between orig and ctrl, orig and subs, orig and twins, twins and ctrl, subs and ctrl, twins and subs, was carried out. In the second step a statistical parameters like correlation coefficient, deviation, covariance, variances etc. were calculated for all possible combinations of numerical schemes and convection. Finally, any possible difference occurred was analyzed comparing pairs of results as above.

Results were divided into two categories of "best configuration" and "the worst possible configuration". The first category contains results for which the highest value of correlation coefficient was obtained, and the second the lowest ones.

The best configuration
The best results have been obtained for the field of water content in the soil (Table 1) for the data from 1 February 2009, 22 April 2009, 21 November 2009, with shallow convection switched on and off correlation coefficient was equal to 1.

The best results for meridional wind component were obtained for 22 April 2009 (Table 2). The lowest value of the correlation coefficient equal to 0.991 was obtained for leapsemi1

Correlation coefficient WSO						
	leapdef	leapdef1	leapsemi	leapsemi1	RungeKutta1	RungeKutta2
orig-twins	1	1	1	1	1	1
orig-subs	1	1	1	1	1	1
orig-ctrl	1	1	1	1	1	1
ctrl-twins	1	1	1	1	1	1
ctrl-subs	1	1	1	1	1	1
subs-twins	1	1	1	1	1	1

Table 1: Correlation coefficient - water in soil (01.02, 22.04, 21.11.2009)

scheme and combination orig-subs, ctrl-subs and for subs-twins. For leapsemi and the same combinations result was slightly better and equal 0.992. For remaining combinations orig-twins, orig-ctrl, ctrl-twins and for all numerical schemes, correlation coefficient was equal to 1.

Correlation coefficient WSO						
	leapdef	leapdef1	leapsemi	leapsemi1	RungeKutta1	RungeKutta2
orig-twins	1	1	1	1	1	1
orig-subs	0.999	0.998	0.992	0.991	0.999	0.999
orig-ctrl	1	1	1	1	1	1
ctrl-twins	1	1	1	1	1	1
ctrl-subs	0.999	0.999	0.992	0.991	0.999	0.999
subs-twins	0.999	0.999	0.992	0.991	0.999	0.999

Table 2: Correlation coefficient, zonal wind component (22.04.2009)

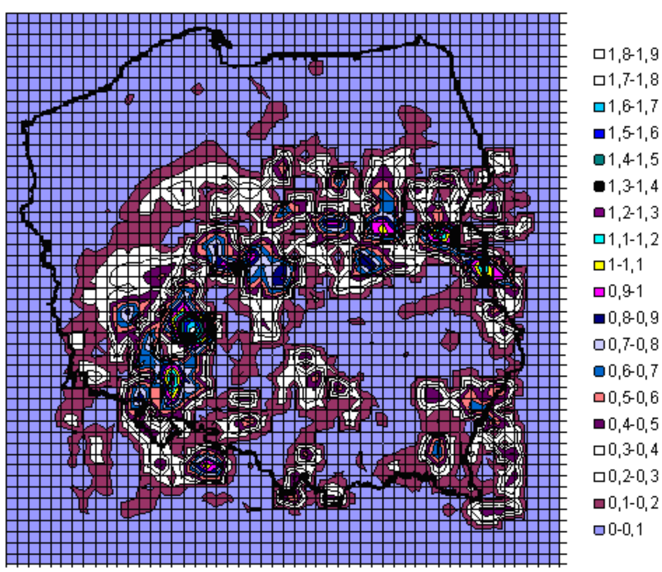

Figure 7: Differences between subs and twins, leapsemi1, zonal wind component (22.04.2009). Correlation coefficient 0.991

High value of the correlation coefficient for the dew point temperature (Table 3) was obtained for 1 February 2009. These results were obtained with shallow convection switch on. Values of a correlation coefficient were equal to 0.998 for leapsemi scheme with combination of orig-subs, ctrl-subs and subs-twins and for RungeKutta1 scheme with combination ctrl-subs. For combinations orig-twins, orig-ctrl, ctrl-twins for all schemes correlation coefficient was equal to 1.

Correlation coefficient - TD with shallow convection				
	leapdef	leapsemi	RungeKutta1	RungeKutta2
orig-twins	1	1	1	1
orig-subs	0.999	0.998	0.999	0.999
orig-ctrl	1	1	1	1
ctrl-twins	1	1	1	1
ctrl-subs	0.999	0.998	0.998	0.999
subs-twins	0.999	0.998	0.999	0.999

Table 3: Correlation coefficient, dew point temperature (01. 02.2009)

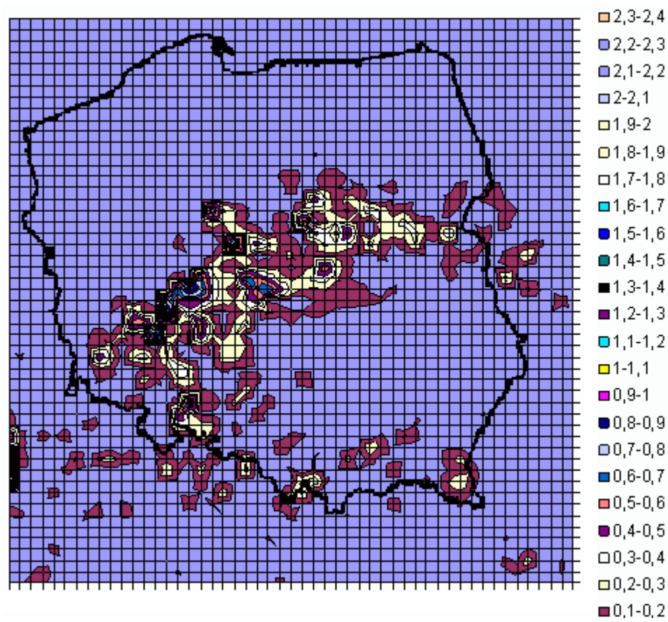

Figure 8: Differences between subs and twins, leapsemi, dew point temperature (22.04.2009). Correlation coefficient 0.998

The best results for air temperature were obtained for 16 October 2009 with shallow convection switched on (Table 4). For a combinations orig-twins, orig-ctrl, ctrl-twins and numerical schemes leapdef, leapsemi, RundeKutta1 and RundeKutta2 correlation coefficient was equal to 1. For combinations orig-subs, ctrl-subs and subs-twins and same numeric schemes a value of the correlation coefficient was in a range from 0.996 to 0.998.

Correlation coefficient - T2M with shallow convection				
	leapdef	leapsemi	RungeKutta1	RungeKutta2
orig-twins	1	1	1	1
orig-subs	0.998	0.998	0.998	0.998
orig-ctrl	1	1	1	1
ctrl-twins	1	1	1	1
ctrl-subs	0.998	0.998	0.998	0.998
subs-twins	0.998	0.998	0.998	0.998

Table 4: Correlation coefficient for air temperature (16.10.2009)

The best results for a surface temperature of the soil was obtained for the data of 1 February, 2009 with shallow convection switched on (Table 5). The correlation coefficient values vary in similar range as of air temperature. For a combination of the orig-twins, orig-ctrl, ctrl-twins and numerical schemes leapdef, leapsemi, RundeKutta1 and RundeKutta2 correlation coefficient was equal to 1. For other combinations of the orig-subs, ctrl-subs and subs-twins and same numeric schemes a value of the correlation coefficient was in a range from 0.997 to 0.998.

Correlation coefficient - TSO with shallow convection				
	leapdef	leapsemi	RungeKutta1	RungeKutta2
orig-twins	1	1	1	1
orig-subs	0.998	0.997	0.997	0.998
orig-ctrl	1	1	1	1
ctrl-twins	1	1	1	1
ctrl-subs	0.998	0.997	0.997	0.998
subs-twins	0.998	0.997	0.997	0.998

Table 5: Correlation coefficient for surface temperature (01.02.2009)

Correlation coefficient - V10 with shallow convection				
	leapdef	leapsemi	RungeKutta1	RungeKutta2
orig-twins	1	1	1	1
orig-subs	0.999	0.999	0.999	0.999
orig-ctrl	1	1	1	1
ctrl-twins	1	1	1	1
ctrl-subs	0.999	0.999	0.999	0.999
subs-twins	0.999	0.999	0.999	0.999

Table 6: Correlation coefficient for meridional wind component (16.10.2009, 06:00 UTC)

Worst case

The worst results were obtained for all the fields of meteorology (T2M, TD, TS, U10, V10, WSO) for data from 4 November 2009, for all numerical schemes and with shallow convection both disabled and enabled, for combinations orig-twins, ctrl-twins, and subs-twins.

Tables 7 and 8 show the case for which the value of the correlation coefficient was the lowest. The worst results were obtained for the air temperature T2M. In the case of shallow convection switched off the correlation coefficient value varied from 0.026 for numerical scheme leapdef, RundeKutta1, RundeKutta2 with combinations orig-twins, ctrl-twins, subs-twins to 0.049 for combinations orig-twins, ctrl-twins and a combination of subs-twins and leapsemi scheme.

As far or the other meteorological fields are concerned, correlation coefficients were slightly bigger but do not differ significantly from the values presented in Table 7, while with shallow convection switched on they were lower. For leapdef, the combination of orig-twins, ctrl-twins, subs-twins correlation coefficient yielded a value 0.02. For the RundeKutta1 and RungeKutta2 schemes with same combinations the value of the correlation coefficient was about 0.024. For leapsemi and combination of orig-twins, ctrl-twins, correlation coefficient was equal to 0.037 and for a combination of subs-twins about 0.044. So low value of the correlation might be most likely caused by numeric errors.

Correlation coefficient - T2M without shallow convection				
	leapdef	leapsemi	RungeKutta1	RungeKutta2
orig-twins	0.026	0.049	0.026	0.026
orig-subs	0.999	0.992	0.999	1
orig-ctrl	1	1	1	1
ctrl-twins	0.026	0.049	0.026	0.026
ctrl-subs	0.999	0.993	1	1
subs-twins	0.026	0.057	0.027	0.028

Table 7: Correlation coefficient for air temperature (04.11.2009)

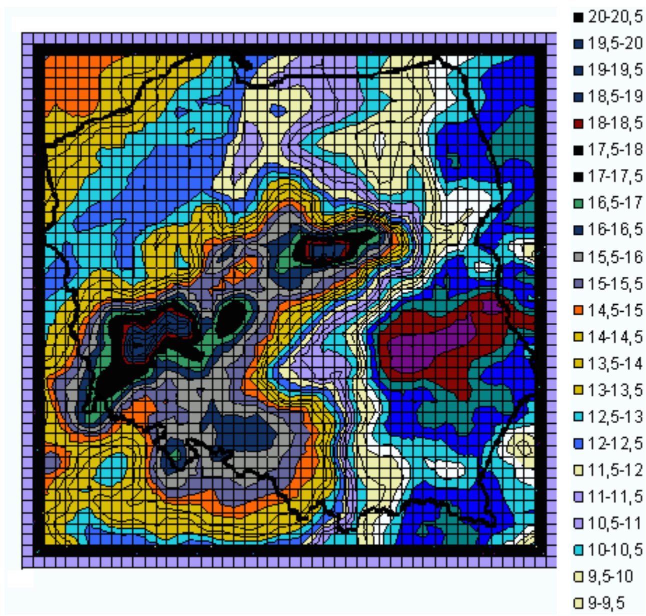

Figure 9: Differences between subs and twins, leapdef, air temperature T2M (04.11.2009). Correlation coefficient - 0.026

Correlation coefficient - T2M with shallow convection				
	leapdef	leapsemi	RungeKutta1	RungeKutta2
orig-twins	0.020	0.037	0.024	0.024
orig-subs	1	0.997	1	1
orig-ctrl	1	1	1	1
ctrl-twins	0.020	0.037	0.024	0.024
ctrl-subs	1	0.997	1	1
subs-twins	0.020	0.044	0.026	0.026

Table 8: Correlation coefficient for air temperature of the air, with shallow convection (04.11.2009)

As far or the other meteorological fields are concerned, correlation coefficients are of similar level. Only for 4 November 2009 there were extreme low value of the correlation coefficient.

There was also the initial comparison of the results obtained with the values of observation (measurements of meteorological stations) carried out. The following figure and Table 9 shows the results of the comparison for schemes leapdef and leapsemi for air temperature.

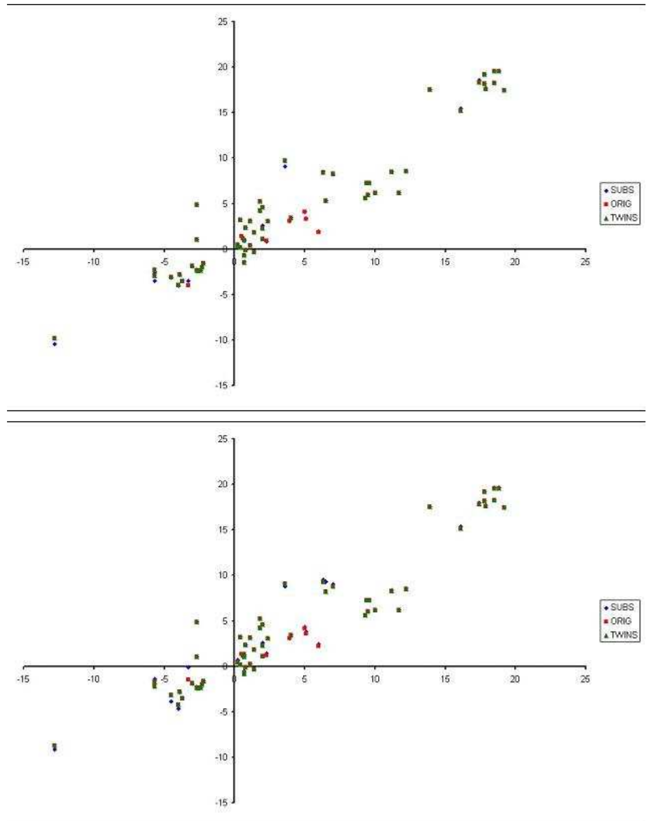

Figure 10: Results (T2M) vs. measurement values. Top: leapdef, bottom - leapsemi

Correlation coefficient (T2M)		
	leapdef	leapsemi
orig	0.9030	0.8990
twins	0.9085	0.9058
subs	0.9101	0.9097

Table 9: Comparison of observation results with COSMO/COLOBOC results obtained for air temperature with schemes leapdef and leapsemi the correlation coefficients

6. Conclusions

In this paper the results of tests carried out using the new MOSAIC parameterization in the meteorological numerical model COSMO, vs. 4.8, were presented. The tests were carried out using different convection parameterizations and numerical schemes. The correlation between the results obtained for specific fields of meteorology seems to be satisfactory. The value of the correlation coefficient varies in range of 0.85 to 1. Only for 4 November 2009 data there has been actually null correlation, caused most likely by numeric errors.

In the future it is planned to carry out tests using more different initial conditions to examine the impact of the parameterization on the structure of bottom layer of the atmosphere. The results will be compared with the values of actual measurements.

References

[1] F. Ament, 2006: Energy and moisture exchange processes over heterogeneous land surfaces in a weather prediction model, *Thesis for dissertation*

[2] G. Doms, U. Schattler, 2002: A Description of the Non-hydrostatic Regional Model LM, *Part I: Dynamics and Numerics,* DWD.

[3] G. Doms, J. Forstner, E. Heise, H.-J. Herzog, M. Raschendorfer, T. Reinhardt, B. Ritter, R. Schrodin, J.-P. Schulz, G. Vogel, 2007: A Description of the Non-hydrostatic Regional Model LM, *Part II: Physical Parameterization*, DWD.

[4] U. Schattler, G. Doms, C. Schraff, 2009: A Description of the Non-hydrostatic Regional Model LM, *Part VII: Users Guide*, DWD.

[5] F. Ament, C Simmer, *Improved Representation of Land - Surface Heterogeneity in a Non-Hydrostatic Numerical Weather Prediction Model*, Bonn University, Germany.

[6] F. Ament, 2008: COSMO_SUBS, MeteoSwiss.

[7] D. J. Stensrud, 2007: *Parameterization Schemes - Keys to Understanding Numerical Weather Prediction Models*, Cambridge University Press.

[8] W. R. Cotton, R. A. Anthes, 1989: *Storm and Cloud Dynamics*, Academic Press, INC.

[9] R. K. Smith, 1997: *The Physics and Parameterization of Moist Atmospheric Convection*, Kluwer Academic Publishers.

[3] J. F. Louis, 1997: *A parameterizartion model of vertical eddy fluxes in the atmosphere*, Boundary Layer Meteorol., **17**, 187 202.

[7] M. Tiedtke, 1989: *A comprehensive mass flux scheme for cumulus parameterization in large scale model*, Mon. Wea. Rev., 1779 1800.

[12] M. Z. Jacobson, 2000: *Fundamentals of Atmosferic Modeling*, Cambridge University Press.

[13] www.wetter3.de/fax - synoptic maps.

20th of July 2007 tornado - towards prediction

Jan Parfiniewicz

Institute of Meteorology and Water Management 61 Podlesna str., PL-01673 Warsaw, Poland

1. Introduction

A multi-scale synoptic analysis of the 8-minute tornado case in Poland has been performed based on 3D Virtual Synoptic Laboratory concept. The key issue of How to predict a similar tornado in the future? has been analyzed, taking into account the predictability potential of particular components of the system. This text, as additional to Newsletters No. 9 - 10 (Parfiniewicz, 2008,2010), will focus on predictability analysis heading for final conclusion (hoping for being useful when organizing operational short term warning system).
About the case. On July 20, 2007, about 16:05 UTC, the Czestochowa district was struck by tornado, which destroyed dwellings, farm buildings, transmission lines and poles, falling down tens of hectares of forest, and displacing automobiles. Strong hailstorms were observed an hour before, during, and after the tornado. According to the eyewitness reports, the hailstones were initially of pea size, then large and irregular ice pieces, some 5 cm or more in diameter. The ground was covered by a thick ice layer reaching to the knees. During the tornado and right afterwards, horizontally moving hailstones of a tennis-ball size were observed. The tornado trail was about 14 km long and the destruction track was up to 500 m wide. The mean speed of displacement was around 45 km/h. On the basis of the type of damage, the tornado was classified as between F1 and F2 in Fujita-Pearson scale or T4 in the 11-step TORRO scale. The wind speed in the vortex could reach 60 m/s (Bebot et al., 2007).

2. Synoptic background

To carry out analysis there was created something like Virtual Synoptic Laboratory (based on 3D visualization) using Vis5d and elaborating a number of tools like the one to produce reflectivity composites and Doppler retrievals. It was recognized that the dominant driving process for the abrupt convection over Europe was an inflow in the upper troposphere of a cold arctic air over a warm and humid tropical air. Deep massive drop of cold Arctic air started moving over the Atlantic from Greenland towards the British Isles, eventually modifying the formation of the Atlantic branch of the polar jet stream. After 8 days of the cold air movement over North Atlantic, the Atlantic branch of the jet stream extended north-easterly over Europe parallel to elongated tongue of hot and moist tropical air masses on its east side (Newsletter 9). The synoptic situation was difficult to analyze, as evidenced by differences in the MSL synoptic analysis made by English, German, Dutch, and Polish services and points to a difficulty in working out a concept of how to analyze the development of upper fronts. The NWP model outputs ran on 14 km grid size with 35 levels has been used to demonstrate the process. 3D inspection of the potential temperature topography shows quite significant slope of 315 K isentropic surface - the upper cold front. And this cross-isobaric sliding over hot subtropical air beneath must have been responsible for the abrupt convection. The W-E vertical cross-section of potential temperature, with overlapping radars reflectivity at 16

UTC (Fig. 1) demonstrates that a process of this type generates the so-called convective alias potential instability and releases a strong convection.

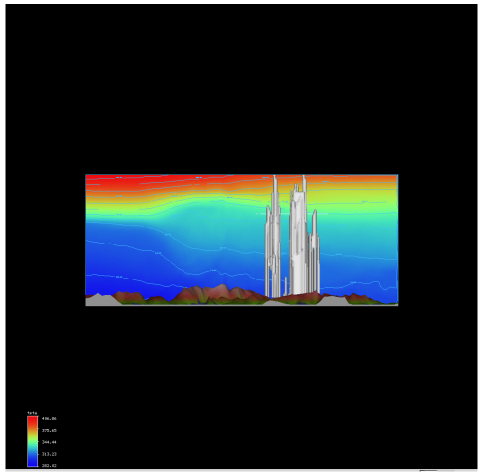

Figure 1: W-E cross section potential temperature + reflectivity at 16 UTC on 20 July 2007

The following steps in the development of the convective situation were distinguished:

[A] Nocturnal disintegration of the preceding convective complex; 00-04 UTC,

[B] Development and disintegration of individual convective cells; 04-10 UTC,

[C] Formation of a convective cluster, and an initiating cell for a further supercell formation, i.e., a very strongly moving and abruptly upwelling huge cumulonimbus cloud; 10-14 UTC,

[D] Formation of a supercell from the merging of slowly-moving clockwise convective complex with a huge cumulonimbus cloud abruptly upwelling, being embedded in the positive vorticity region; 14-16 UTC,

[E] Mature supercell stage, with a tornado in the Czestochowa region (16:05 16:15 UTC) and a convective complex originated over the Tatra mountains and Slovakia; 16-18 UTC.

We will now focus on the supercell transition from early to mature stage, step [D] to [E] (Fig. 2(a)-2(b)) (for more, see Newsletter 9, Fig.9 a - f).

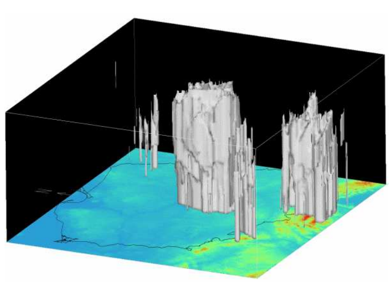

(a) 16 UTC

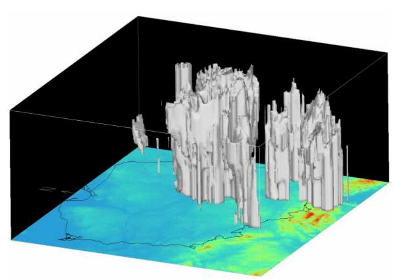

(b) 18 UTC

Figure 2: 3D composite model image of radar reflectivity- 20 July 2007

3. The detailed, sub-synoptic description of the convective process over southern Poland

To describe the process of convection evolution and to identify different cloudiness forms, characteristic acronyms have been introduced (e.g., HCP = Huge Convective Pattern), and successive numbers have been assigned to them as they appeared in time (see [6]). The abbreviation ⇒means conversion of one object into another. Each term responds its adequate 3D reflectivity composite, altogether illustrating 4D evolution of the process. Concerning stage [D] (14-16 UTC):

14:00 huge Cb - HCb0607 - consolidates and grows up, slowly propagating eastwards; the CuHCb09ensembleTatry creates a vast cloud complex with a built-in HCb; Cu10 elongates and collocates NE, according to the steering stream.

14:30 - vast HCb0607 is getting anticyclonal rotation (AC), very slowly propagates easterly, enforcing lightning activity trying to get in touch with Cb10; CuHCb09ensembleTatry still active; Cu10 consolidates and very fast (in less than half hour) transforms into huge Cb ⇒ HCb10 and propagates over about 100 km northeasterly. The Brzuchania radar echo top map taken at 14:20 UTC (Fig. 3(a)) is showing these two separated convective cells: HCb0607-A (bigger but lower) and HCb10-B (smaller but higher).

15:00 - HCb0607 transforms into singular huge convective cell HCPCb0607 with two rotating AC tops (cores) huge HCb, and very slowly propagates east, still waiting for huge Cb HCb10 with deduced cyclonic circulation (C); at 14:40Z lightning strokes of two cells merge overtaking their fusion; HCb10 spreads up and enlarges, transforms into huge convective pattern HCPCb10, slows down and catches up HCPCb0607; CuHCb09ensembleTatry creates convective doublet HCPCbdubletTatry on Polish and Slovakian sides. At 15:30 from these two giant convective patterns, with huge HCb: HCPCb0607 and HCPCb10, after their fusion, there appears the giant supercell Sc060710 (see Fig. 3(b)) with a double core system (one of them is getting transformed into tail; thus fulfilling the supercell definition: mesocyclon core, overshooting and tail); HCPCbdubletTatry is more vigorous behind the Tatras range on the Slovakian side and weakens on the Polish side ⇒ HCPCbSlovakia.

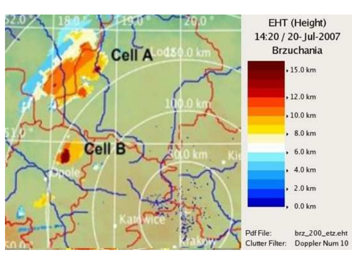

(a) 14:20 UTC - two separated convective cells: A (bigger but lower) and B (smaller but higher)

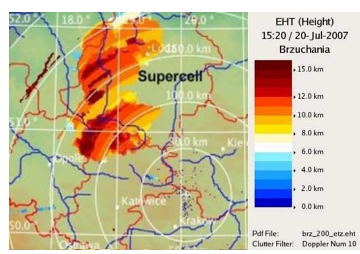

(b) 15:20 UTC - the supercell complex just after the cells A and B merged

Figure 3: The Brzuchania radar echo top map

16:00 the giant supercell Sc060710, with merged precipitation cores, forms a bow with initial tail stage, on the southern bow periphery, close to tail the tornado is forming at the moment; HCPCbSlovakia; in Jesioniki mountains and Pradziad hill new CPCb11 appear.

17:00 - the giant supercell Sc060710 slowly propagates east, the bow-like precipitation core is now reversed west, the large tail is built-up and directed southwesterly (comment: the west-ward reversing of the bow and the SW tail direction point to the anticyclonic macrorotation, while the tornados mesocyclon inside supercell should rotate cyclonally; according to the eye-witness, the tornado has extinguished at 16:15); CPCb11 is towering and elongate according to steering stream north-east heading to fuse with tail of Sc060710; HCPCbSlovakia reconsolidates and slightly propagates north.

17:30 - the giant supercell Sc060710 keeps slowly propagating east, the reversed bow like precipitatation core regenerates (pulsing); CPCb11 strengthens up north from Pradziad hill still heads towards tail of Sc060710; HCPCbSlovakia weakens.

18:00 - Sc060710 keeps holding slightly weakens; remains strong multi-nuclei precipitation core which transforms from bow into linear form, whereas the tail is keeping its holding. The neighboring systems CPCb11 and HCPCbSlovakia dissipate.

4. How to predict a similar tornado in the future?

Predictability. The synoptic analysis of the convective process that has led to a supercell and tornado incident was partially deterministic and partially stochastic. The first macro stage, comprising the 8-day pre-convective period and developing over North Atlantic as a large-scale process, was relatively easy to predict. The second stage, developed over Europe which was providing extraordinary growth of instability and might be limited to one-day forecast was also relatively well predicted by operational NWP model. So, the synoptic background on which the convective process has developed was recognized correctly, at least from synoptic point of view. However, the convective process by itself, which might be confined to convective cloudiness, as it appears and vanishes before aggregation into convective complex, was undoubtedly stochastic. It seems that the game the convective clouds played before 14:40 UTC must remain unpredictable. But since the moment the lightning strokes of huge but slowly convective complex and fast propagating Cb have merged, overtaking their fusion (compare Fig. 4(a)-4(b)), it was clear that we would have a supercell and possibly tornado. Since that moment, parallel processing of radar and lightning data should foresee further supercell development and propagation.

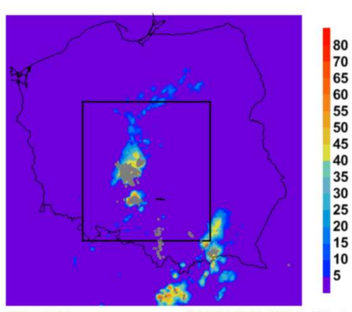

(a) 14:30 UTC, the time interval 14:30-40 UTC

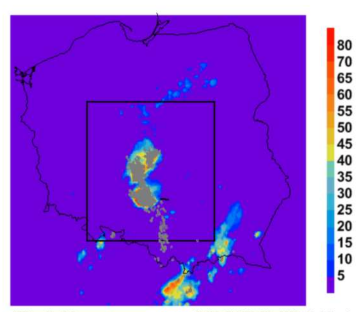

(b) 15:30 UTC, the time interval 15:30-40 UTC

Figure 4: Radar reflectivity map (in dBz) indicated by colored scale and lighting strokes locations denoted by small grey squares together with tornado location shown by black bar and selected space domain 340x340 km used in our considerations

The potential of NWP models. The applied COSMO model computer simulations with different grid resolutions have been used, with the grid step squeezed up to 2.8 km starting from 00 and 12 UTC (Newsletter 9, Fig.11). The typical wind jump and related vortex tube trace were simulated by the COSMO-Model 2.8 km/50 levels but the problem occurred with convective cloud water structures. The conclusion was that the object that was 30 km wide and 18 km high must not be treated stochastically, and should be reasonably restored by the model.

The potential of radar wind retrieval. The significance of the radar reflectivity assimilation in the process of successive absorbing new data and rerunning the dedicated tornado forecasting model is obvious and essential. Typically, the assimilation concept bases on the latent heat release. The assimilation of Doppler wind component is more complicated as the rational way to enhance the models vigor is to include into the data the rotational wind part. This needs application of retrieval technique. Here, a single Doppler retrieval technique has been used to obtain 3D distribution of the tornado-like wind structure showing descending spiral motion with the maximum downward velocity just above the tornado (Newsletter 10).

The potential of total (IC+CG) lightning rate data. (after [1], [6]). Many lightning characteristics gathered during supercell event observations, as reviewed and reported recently by Tessendorf, ([9]), have indicated that the IC/CG ratio tends to increase with increasing storm severity and its electrical activity. Thus, this ratio could also be used as an indicator of enhanced severe weather potential. Moreover, (see [3]), basing on his experience with severe and tornado storms in Central Florida (USA), have noticed that sudden increases in the lightning rate, referred to as lightning jumps, have preceded the occurrence of severe weather phenomena by 10 or more minutes. These jumps were typically 30-60 flashes/min2, and were easily identified as anomalously large time derivatives of the lightning flash rate. For our case of supercell event (see Fig. 5), one of the local maximum values of time derivative of total lightning rate was of the order 10 strokes/min2 and occurred about 5 minutes before the visible appearance of tornado.

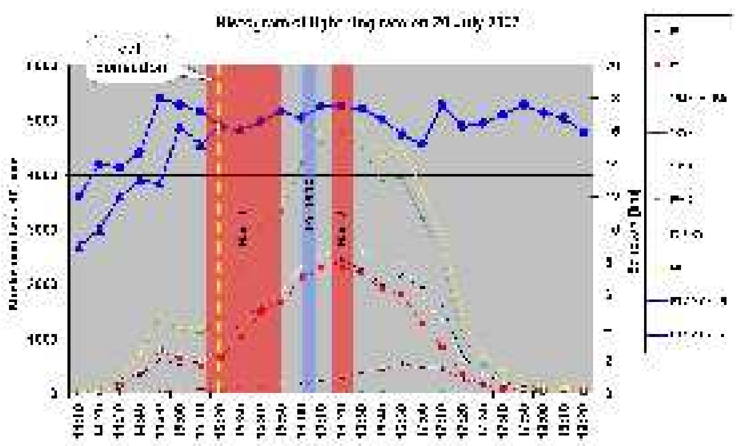

Figure 5: Histogram of lightning frequency for different types of discharges detected by the SAFIR/PERUN network system in the chosen area containing two separated convective cells (see Fig. 3(a)) and the considered supercell complex after cell aggregation (see Fig. 3(b)), i.e., positive and negative return strokes of cloud-to-ground flashes (RS+ and RS), intracloud discharges (IC), and not fully recognized discharges named isolated points (IP). Additionally, the time changes of radar echo top of those cells and supercell are overlapped with the same time interval.

Taking into account the particular stages of dynamic evolution of the considered supercell convective complex and using the space domain that was especially chosen for this purpose, the time variation of frequency of different types of lightning discharges detected by the SAFIR/PERUN network system (see [8], [10]) were examined, i.e., the positive and negative return strokes (RS+ and RS) of cloud-to-ground flashes (CG), intracloud discharges (IC), and other, not fully recognized discharges, isolated points (IP). It was found (see Fig.5) that the first peak of lightning frequency histogram, with a total of 1422 lightning strokes per 10 minute interval and for 4 stroke types detected by the SAFIR/PERUN system, preceded by 25 minutes the onset of first heavy hail gush, by 1 hour and 10 minutes the moment of visible tornado onset, and by 1 and half hour the second episode with heavy hail gush. The next, much more distinct peak of such lightning frequency, with a total of 5065 lightning strokes per 10 minute interval, followed by 65 minutes the onset of first heavy hail gush and by 20 minutes the moment of visible tornado and overlapped with the onset of the second episode with heavy hail gush. The tornado incident was preceded by a meaningful jump of IP and IC counts per 10 minute interval, whereas counts of RS were from 7 to 9 times lower, with nearly the same small number of RS+. As a result, a growing value of the ratio IC/RS+RS+ was obtained - about 6 times greater than that one observed during ordinary thunderstorms in Poland (see [1]).

5. Conclusions

Virtual Synoptic Laboratory concept has been adopted to understand the synoptic background on which the convective process has developed. The predictability analysis (phenomenological approach) concerned the potential of particular components of the system, i.e., NWP model output, radar and lightning data. The first macro stage, comprising several days of the pre-convective period and the second one-day forecast stage developing over Europe, which provide necessary growth of instability are hoped to be well predicted by our operational models. However the 3rd stage lasting for a few hours and precede supercell formation has been recognized as difficult to predict. The process of successive absorbing (assimilation) of new radar and lighting data during this period will be essential for tuning the model and extending the successful forecast range. Based on the optimistic facts that: 1) the non-hydrostatic and compressible COSMO model has shown inclination to restore the characteristic typical wind jump and related vortex tube, 2) the assimilation of Doppler rotational wind component provide a quite realistic approximation of the tornados like funnel oscillation, and, 3) that the lightning data occurred to be a good proxy of the visible tornado it seems rational to head for prediction. One of the solutions is a moving nested grid of about 100km wide and 20km high with resolution 0.5km/100m (or less) being accurately positioning every 10 minute accordingly to radar data inflow and stimulating by lighting data assimilation. The alternative would be overlapping, pre-configured nested grids system.

Acknowledgments: to Stanislaw Michnowski for inspiring lightning studies, to David Schultz for stimulating comments, to Piotr Baranski (the lighting expert) for close collaboration.

References

[1] Baranski, P., P. Bodzak, A. Maciazek, 2002: Some results of the SAFIR, radar and field mill observations for selected thunderstorms near Warsaw. *Abstracts of the 2002 SAFIR Workshop, Budapest.*

[2] Beblot, G., I. Holda, K. Rorbek, 2007: The tornado in the Czestochowa region on 20 July 2007, *IMGW, Oddzial Krakow, Gornoslaskie Centrum Hydro-Meteorologiczne w Katowicach*, p.**18** (in Polish).

[3] Goodman S.J., D. Buechler, S. Hodanish, D. Sharp, E.R. Williams, R.A. Boldi, A.M. Matlin, M.E. Weber,1999: Total lightning activity associated with tornadic storms. In: *Proceedings of the 11th Int. Conference on Atmospheric Electricity*, Gunthersville, Alabama, USA, June 7-11, 1999, pp. **515-518**.

[4] Parfiniewicz J., 2008: 20th of July 2007 Explosive Convection over Europe. The COSMO Perspective, 5 Working Group on Verification and Case Studies, *COSMO Newsletter 9* (available at http://www.cosmo-model.org/content/model/documentation/newsLetters/), **79 85**

[5] Parfiniewicz J., Baranski P., Gajda W., 2009: Preliminary Analysis of Dynamic Evolution and Lightning Activity Associated with Supercell Event: Case Story of the Severe Storm with Tornado and Two Heavy Hail Gushes in Poland on 20 July 2007, *PUBLS. INST. GEOPHYS. POL. ACAD. SC.*, D-73 (412), 2009, p.**65 - 88**

[6] Parfiniewicz J., 2009: Tornado w rejonie Czestochowy - 20 lipca 2007 *Czesc 1: Analiza synoptyczna. Czesc 2: symulacje komputerowe i analiza 3D.* Prz.Geof. LIV, 3-4 s.**147 181**. (in Polish).

[7] Parfiniewicz J., 2010: Retrieving tornados like wind structure (20.07.2007, Czestochowa, Poland case) using singular radar Doppler velocity , 5 Working Group on Verification and Case Studies, *COSMO Newsletter 10* , p. **70 71**

[8] SAFIR, 2003: 3000 Software User Manual (Data Analysis Module, DAMen-2.1), Vaisala SA, Europarc de la Sainte Victoire, 13590 Meyreuil, France, July 2003.

[9] Tessendorf, S.A. 2009: Characteristics of lightning in supercells, Chap. 4, pp. 83-114. In: H.D. Betz, U. Schumann, and P. Laroche (eds.), *Lightning: Principles, Instruments and Applications*, Springer Netherlands, DOI: **10.1007/978-1-4020-9079-0_4**.

[10] Vaisala, 2003: SAFIR 30003, User Manual, DS Settings and Control Manual, Release 2.3, Helsinki, Finland, July 2003.

Seasonal and monthly verification of COSMO_PL

Joanna Linkowska, Katarzyna Starosta

Institute of Meteorology and Water Management, Centre of Numerical Weather Prediction, Warsaw

1 Introduction

At the beginning of the paper the results of seasonal verification of COSMO_Pl model are presented. The period from September 2009 to August 2010 was taken into account. The second part of the article presents the results of monthly verification of the 24h accumulated precipitation in May 2010, distinguished by very high rainfall throughout the country. The model data were verified with SYNOP stations.

2 The verification method

For continuous parameters the mean error (ME) and the root mean square error (RMSE) were calculated. To verify the diurnal behavior of the model, the couples forecast-observation were stratified according to the hour of the day (frequency of 3 hours) and the season of the year. The model started at 00 UTC with the forecast range 72h. The verification was performed for the following parameters:

- Temperature at 2 m above ground level;
- Dew point temperature at 2m above ground level;
- Mean sea level pressure;
- Wind speed at 10m above ground level;
- Total cloud cover.

Calculations were performed for four seasons, SON 2009, DJF 2009/2010, MAM, 2010, JJA 2010.

For the 24 accumulated precipitation indices FBI, ETS from contingency table were calculated. The following precipitation thresholds were taken into account: 0.2, 2, 5, 10, 20, 25, 30, 35, 40, 45, 50 mm. The time series plots for total precipitation are also presented. The 24h accumulated precipitation in May 2010 was selected. As the month was extremely wet, the amount of long-term average precipitation throughout the country was exceeded. The results were calculated for all stations and separately for four different geographical terrains: coast, flat region, low mountains, and mountains.

3 Results of seasonal verification

3.1 The 2m temperature

Figure 1 presents the results of verification of the air temperature for all Polish stations for each season. Daily and seasonal cycles of ME and RMSE are observed. The largest diurnal amplitude of errors occurred in autumn (SON). The temperature at this season was underpredicted during daytime (09UTC-18 UTC) with minimum at 12UTC-15UTC and overpredicted at nighttime (21UTC-06UTC) with maximum at 00UTC-03UTC. Two maxima of RMSE (00UTC-03UTC and 12UTC-15UTC) and two minima (06UTC-09UTC and 18UTC-21UTC) were observed. The smallest errors were observed in spring (MAM). ME range from -0.8 to 0.6. Predicted values are lower than those observed in the morning (06UTC-09UTC). For the remaining hours of a day the model calculates the value only slightly higher than those observed. Error RMSE reaches a maximum at 12 UTC and minimum during the night (18UTC-06UTC). In winter the mean error was negative for the whole forecast range. The difference between maximum of RMSE at 12 UTC and minimum at night (21UTC-03UTC) was only about one degree .In summer (JJA), the predicted values are higher than those observed during the night (21UTC-03UTC), while during the day (apart from the first forecast day) are lower than those observed. RMSE reaches a maximum at 12 UTC and a minimum generally about 21 UTC.

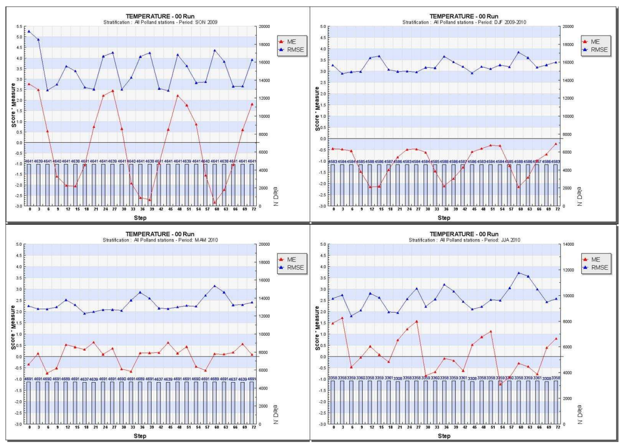

Figure 1: ME,RMSE, Temperature 2m, SON 2009-JJA 2010, Poland

3.2 Dew point temperature 2m

The large differences of diurnal cycle of errors for the seasons were observed. For all forecast range, model values of the dew point temperature were higher than observed during the spring and the summer, while in the winter the forecasted values were smaller than observed. However, in autumn ME was negative during the daytime (09UTC-18UTC) and positive during night-time (21UTC-06UTC) with a maximum at 03 UTC. For RMSE clear diurnal cycle occurs in the summer with a maximum at 15 UTC and a minimum at 06UTC. For the other seasons, the error performance is rather smooth.

3.3 Mean sea level pressure

MAE and RMSE of atmospheric pressure for all seasons (except the summer) clearly increase with forecast time. The values of RMSE during the summer are smaller for the first day (1) and bigger for the two others (1.5-1.8). ME is positive and increases with the forecast range for autumn (SON). For other seasons, in general ME is negative except the first 9 hours of the forecast (winter, spring) and the last few hours of the forecast range (summer).

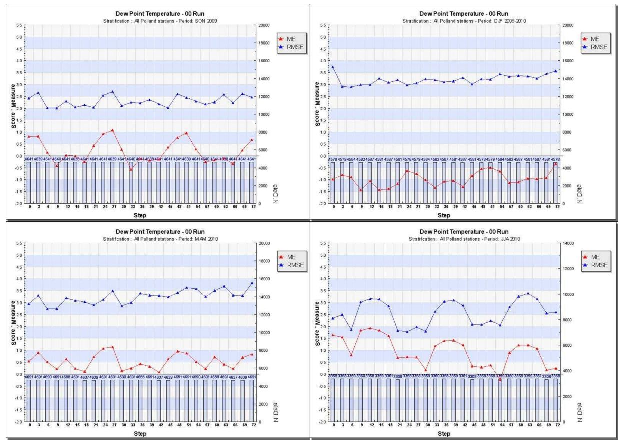

Figure 2: ME,RMSE , Dew point temperature 2m, SON 2009 JJA 2010, Poland

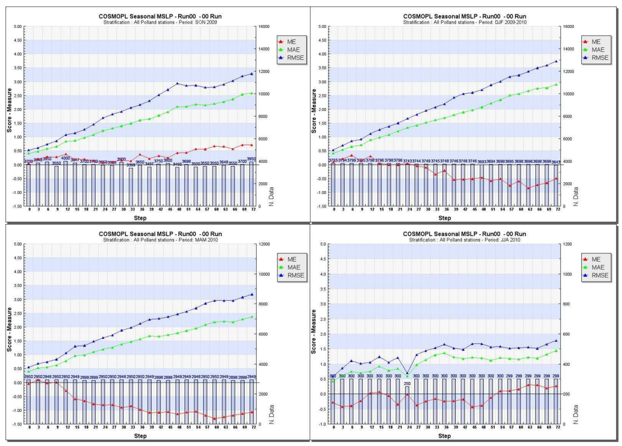

Figure 3: ME, MAE, RMSE, Mean sea level pressure, SON 2009 JJA 2010, Poland

3.4 The 10m wind speed

Seasonal RMSE of the wind speed increases with the forecast range for all seasons. The amplitude of RMSE is small (from 1.5 to 2). The ME performance is marked by diurnal distribution, larger errors occurring at night and the lowest in the morning (09UTC-12UTC).

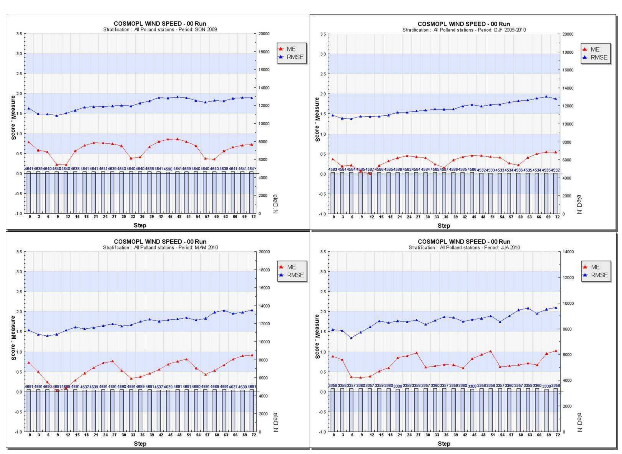

Figure 4: ME, RMSE, 10m wind speed, SON 2009 - JJA 2010, Poland

3.5 The total cloud cover

The smallest cloud cover forecast errors occur during winter (DJF).This season RMSE amplitude is small. In winter ME oscillates around zero. In autumn (SON) ME is positive for all forecast steps. In spring (MAM), ME is also positive for most steps in the forecast (except for the first day). In summer, ME is above zero during nighttime (21UTC-06UTC) and below zero during daytime (09UTC-18UTC). Clear diurnal cycle of error is observed in autumn (SON) and spring (MAM) with a minimum error around noon and a maximum around midnight.

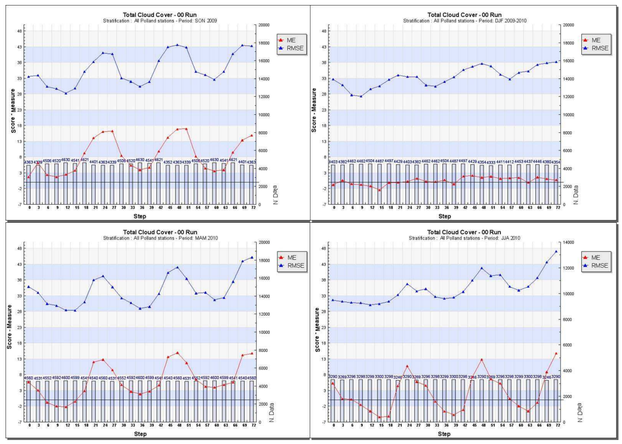

Figure 5: ME, RMSE, Total cloud cover, SON 2009 JJA 2010, Poland

4 Monthly precipitation May 2010

In May 2010, a very high rainfall throughout the country occurred. The highest rainfall was recorded between the 16th and the 18th. Comparing the time series plots for the whole country in the first and second day of heavy rainfall on the 16th and the 17th, the model predicts lower amount of accumulated precipitation than was observed. For the next two days of the 18th and the 19th the model provides more accumulated precipitation than actually occurred. On a mountain terrain the model predicts the highest rainfall a day later, i.e. on the 17th than actually occurred on the 16th. Also on a low-mountain and flat areas a one day delay of the highest rainfall occurred. Time displacement between the forecast and observation is also seen the other days of the month.

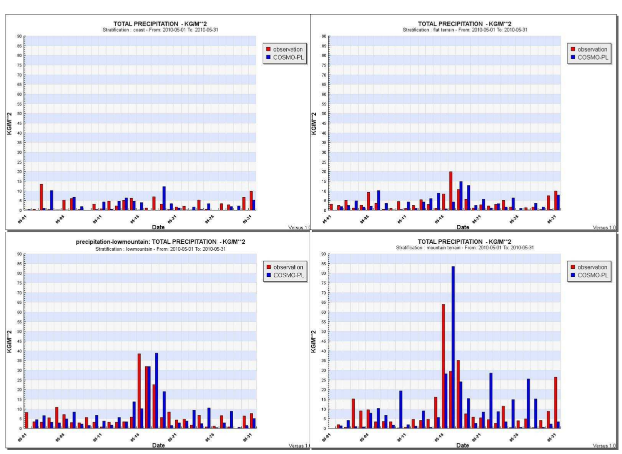

Figure 6: Time series plot, total 24h accumulated precipitation, May 2010, Poland, coast terrain, flat terrain, low mountain terrain, mountain terrain

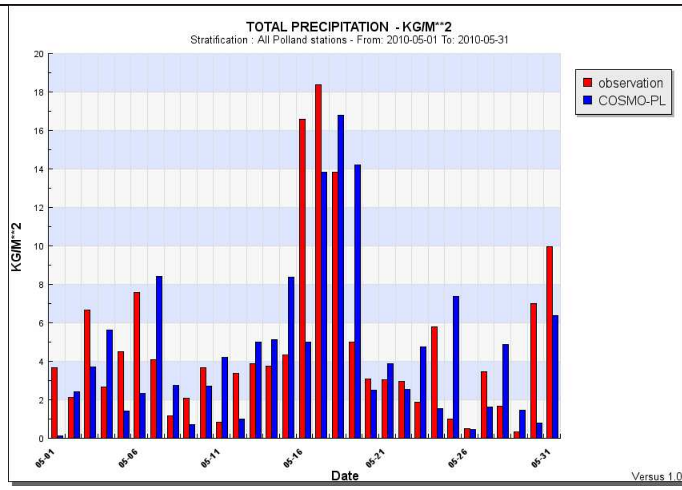

Figure 7: Time series plot, total 24h accumulated precipitation, May 2010, all Poland stations

On a mountain terrain, for small precipitation thresholds the first and second day of forecast, a bit more rainfall is predicted than observed ($FBI > 0$). For bigger thresholds the model underestimates the precipitation ($FBI < 0$). 72-hour forecast seems to be better than 48 hours one. For low- mountain areas FBI is above zero for lower thresholds on the second day of the forecast. FBI is positive for all thresholds on the third day of the forecast (72 hours). For the highest precipitation thresholds forecasts for 24 and 48h rainfall are underestimated. The value of FBI on the first forecast day oscillates around zero. For flat and coastal terrains on the first forecast day and the lowest thresholds the positive FBI was observed. The negative FBI rises with precipitation thresholds on the first 24 hours forecast. On the second and third day of the forecast FBI is positive for all precipitation thresholds.

When analyzing the performance of FBI for all stations, rainfall on the second and third forecast days are overestimated ($FBI > 0$). FBI fluctuates around zero on the first forecast day. May 2010 had a large number of days with heavy rain. FBI is reliable even on the threshold of 50 mm.

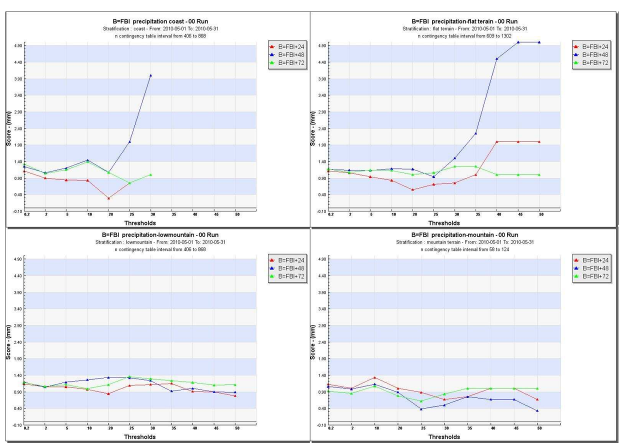

Figure 8: FBI, 24h accumulated precipitation, May 2010, Poland, coast terrain, flat terrain, low mountain terrain, mountain terrain

The accumulated precipitation in the mountains is well predicted for high thresholds, while rainfall forecast for flat and coastal terrains is better for small precipitation thresholds. On a flat terrain the number of cases with heavy rain is small. Analysing the value of ETS the best forecast is on the first forecast day and the worst for the second one. On the flat terrain and coastal areas for small precipitation thresholds the value of ETS decreases with forecast step. It means an increase of forecast errors.

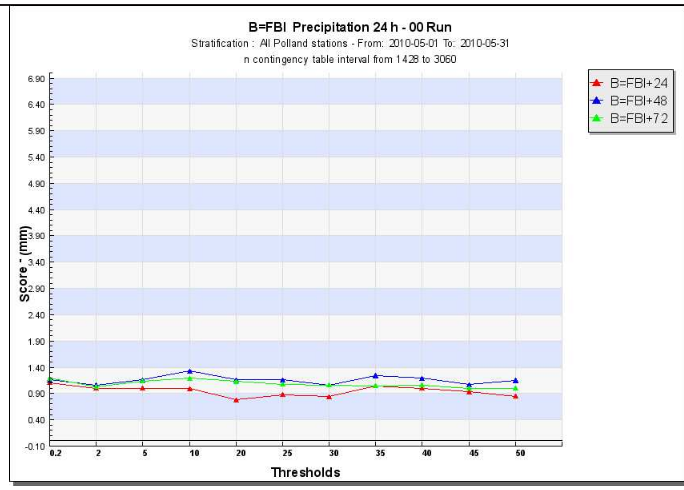

Figure 9: FBI, 24h accumulated precipitation, May 2010, all Poland stations

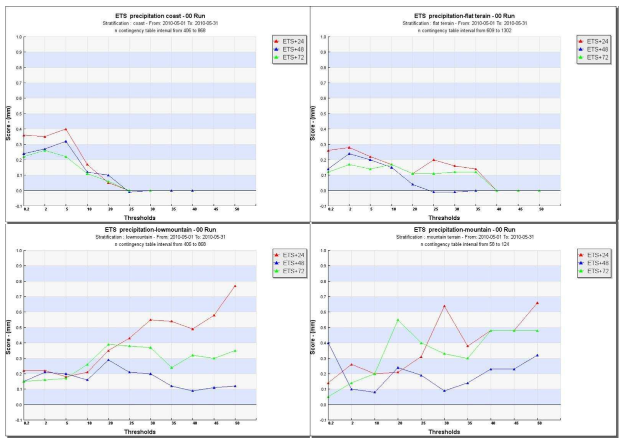

Figure 10: ETS, 24h accumulated precipitation, May 2010, Poland, coast terrain, flat terrain, low mountain terrain, mountain terrain

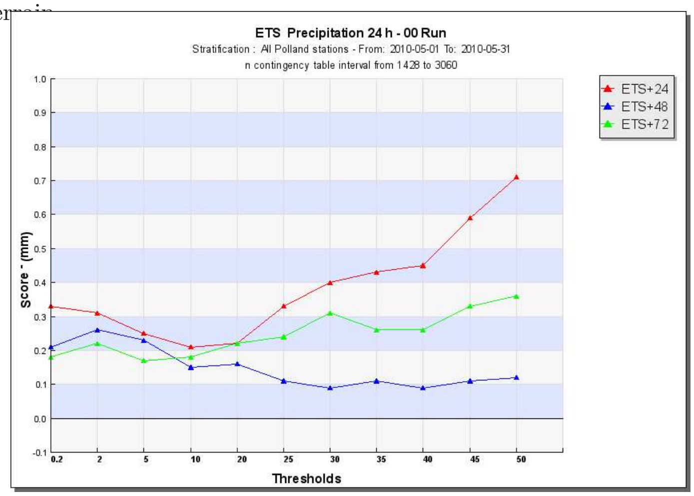

Figure 11: ETS, 24h accumulated precipitation, May 2010, all Poland stations

5 Conclusions

Seasonal (SON 2009, DJF 2009/2010, MAM 2010, JJA 2010) verification results of continuous parameters and monthly (May 2010) 24h accumulated precipitation were shown in this paper. Diurnal, seasonal cycles of ME for almost all considered continuous parameters (T2m, dew point, total cloud cover, wind speed) were observed for all seasons. RMSE and MAE of the mean sea level pressure increase with forecast range for all seasons. The best accumulated precipitation forecast was observed on low mountain area considering all precipitation thresholds as well as forecast range.

Analysing mesoscale structures using the COSMO numerical weather forecast, case study - 9 Oct. 2010

Amalia Iriza, Cosmin Barbu, Rodica Claudia Dumitrache, Bogdan Maco, Mihaela Bogdan

National Meteorological Administration,
Sos. Bucuresti- Ploiesti, nr.97, Bucharest, Romania

1. Introduction

Mesoscale convective systems are defined as an ensemble of convective clouds whose ascending currents are continuously fed due to mesoscale circulation, determining severe weather phenomena at ground level on an area of at least 100km. In the past years, in Romania as well as in other European countries a series of extreme weather phenomena have been observed: flash floods, intense wind and large hail. Such phenomena often produce material damage and loss of human lives. Given the context, weather forecasting and issuing warnings with a high degree of confidence is mandatory. Taking these facts into account, it follows that numerical weather forecasts at high resolution can be of real help in anticipating such phenomena.

The COSMO model was implemented and is running in the National Meteorological Administration twice a day for two spatial resolutions (7 km and 2.8 km). The numerical weather forecast from the model is processed and illustrated graphically and is used daily in elaborating the weather forecast.

On the 9th October 2010 Regional Meteorological Centre Constanţa issued three "Warnings for immediate meteorological phenomena" addressed to the Ministry of Environment, Emergency Situation Inspectorate (ISU) and harbour master offices for the following regions: Constanţa, Tulcea, Brăila, Galaţi, Ialomiţa and Călăraşi. The warned phenomena were: intense wind from North-West for the next 6 hours (medium speed 40 - 60 km/h, gust speed 75 - 85 km/h), especially in the west part of the Black Sea, at the seaside and in the Delta of the Danube. As an associated phenomenon: rain - in quantities of over 15-20 l/m^2 on local areas. The first warning was issued at 9.45 and was put up to date at 15.55 and 21.55.

The COSMO regional model anticipated the phenomenon since the 7th October 2010 (three days' anticipation), suggesting the formation of a mesovortex structure in the South-East of Romania and the Black sea seaside. The forecast for maximum wind speed from the COSMO model was approximately 70 - 80 km/h. Precipitation quantities estimated by the model also concur with the observed ones.

2. Data and methods

Starting with June 2009, the COSMO model is run twice a day for two spatial resolutions (7 km and 2.8 km), on two domains which cover the area of Romania.

Characteristics for COSMO-7 km:

- Domain dimension: 201x177 grid points, 40 vertical levels

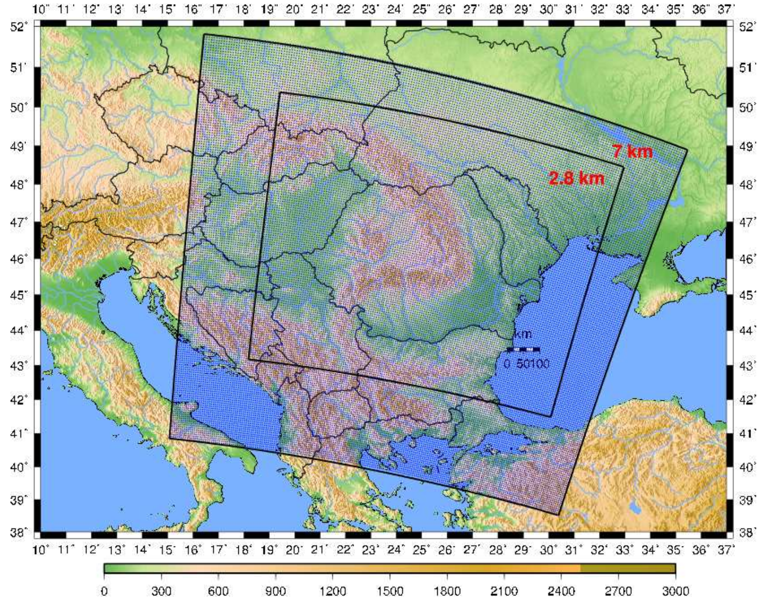

Figure 1: COSMO operational domains in Romania

- Model version: 4.6
- Coordinates system: rotated geographical coordinates (lat/lon), with an Arakawa-C type grid
- Boundary conditions: interpolated from the data coming from the GME global model (00, 12 UTC)
- Spatial discretisation: second order centred difference
- Time integration scheme: Runge-Kutta (irk_order = 3), time step dt = 72 sec
- 78 hours forecast period
- Data assimilation: surface observations

Characteristics for COSMO-2.8 km:

- Domain dimension: 361x291 grid points, 50 vertical levels
- Model version: 4.6
- Coordinates system: rotated geographical coordinates (lat/lon), with an Arakawa-C type grid
- Boundary conditions: interpolated from the data coming from the COSMO 7km run (00, 12 UTC)
- Spatial discretisation: second order centred difference
- Time integration scheme: Runge-Kutta (irk_order = 3), time step dt = 25 sec
- 30 hours forecast period
- No data assimilation

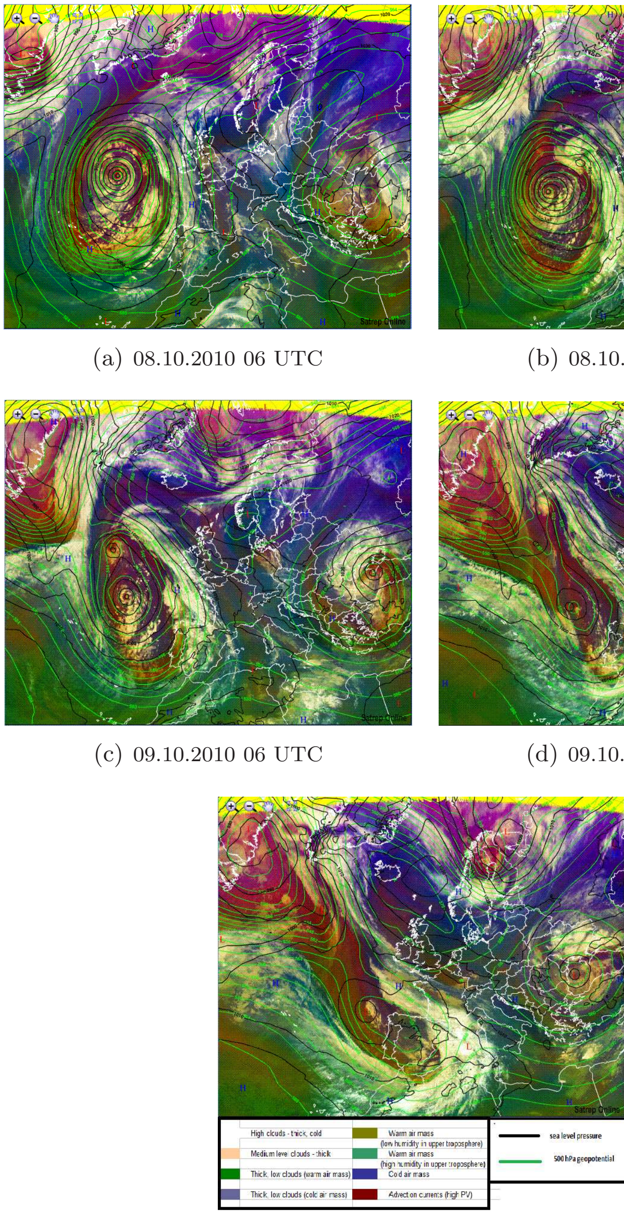

(a) 08.10.2010 06 UTC

(b) 08.10.2010 18 UTC

(c) 09.10.2010 06 UTC

(d) 09.10.2010 18 UTC

(e) 10.10.2010 06 UTC

Figure 2: Satellite images

At the beginning of the analysed period (8-10 October 2010), of interest for the geographical space of Romania is the East-European Anticyclone, which extended over the North, Centre, East and South-East of the continent, and the barometric depression formed over the Middle East. A cold air nucleus centred above the East of our country and the black Sea was also observed in the medium troposphere (500hPa) - (see Fig. 2(a),2(b)). This nucleus had been detached from the trough previously situated above Russia; it was amplified and travelled South-East on the anterior side of the ridge which extended beyond the Ural Mountains.

During the day of 8 October, the cold air nucleus from the superior strata of the atmosphere led to the amplification of the mesoscale structure on ground level which was blocked from travelling East by the ridge which had extended to the area of the Caspian Sea. This led to an inverse - western - trajectory of the cyclone. On the 9th of October, the cyclone activity grew very much and the retreat of the anticyclone towards East allowed the cyclone to reach the East of Romania and the west of the Black Sea in its mature phase (Fig. 2(c), 2(d)). Subsequent, on the 10th of October the cyclone came to occlude (the axis which connected the ground nucleus to the one in the middle troposphere is vertical), gradually lost its intensity and averted from the country (Fig. 2(e)) (http://www.satreponline.org).

This synoptic context favoured strong wind intensification in the eastern and south-eastern parts of Romania, especially during the 9th October, when the cyclone was situated over these regions in its maximum intensity phase. The wind manifested mostly in Dobrogea, at the seaside and in the Delta of the Danube, where wind gusts reached a speed of 13 m/s to 30 m/s. The registered wind speed was that of 30 m/s at Mahmudia, 20 m/s at Sulina, 17 m/s at Mangalia, 16 m/s at Constanţa. Higher quantities of precipitation were registered on the same day, over 15 mm locally and over 30 mm isolated (up to 52 mm at Adamclisi Constanţa County). These quantities were mostly due to the wet air mass (containing water vapours from the area of the Black Sea), which was brought by the cyclone to the East of Romania.

The evolution of a mesoscale cyclone structure formed in the north-west of the Black sea could be observed on radar and satellite images (Fig.3) starting with the afternoon of 9 October 2010 up until the morning of the following day.

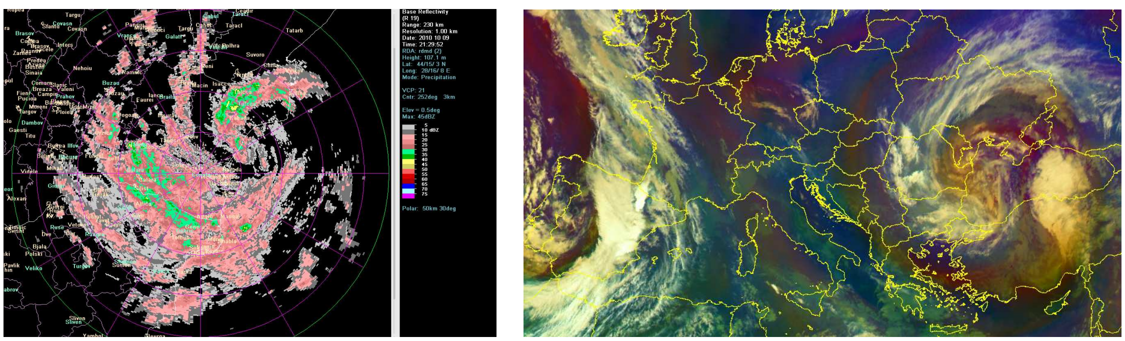

(a) Radar reflectivity (b) RGB satellite image

Figure 3: 09.10.2010 - 18 UTC

3. Results

The mesoscale cyclone structure of Mediterranean provenance formed over the area of the Black sea on the 9th October 2010 was simulated by the COSMO model starting with the 7th October (Fig. 4(a), 4(b)), on a three days' anticipation. The model caught the breakthrough of cold air of polar provenance behind the front, as well as the maintaining of the warm air on its anterior side. The contact between the masses of cold and hot air is emphasised in the forecast from the COSMO model through the convergence line which can be observed in the parameter for wind.

Forecasts from the model in the following days (Fig. 4(d)-4(l)) confirmed the initial one, seizing the evolution in time of the cyclone until 10 October 2010 (Fig. 5(b)), when it occluded. The real evolution of the structured could be followed both on radar reflectivity (Fig. 3(a)), as well as on satellite images (Fig. 3(b), Fig. 5(a)).

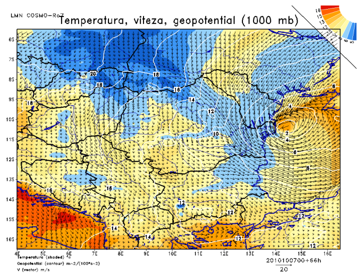

(a) Forecast from 07.10.2010 +66 hours, 1000 hPa

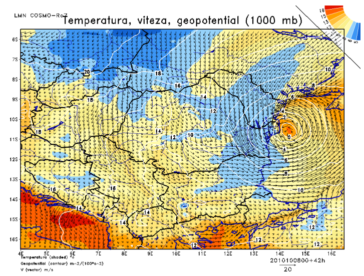

(b) Forecast from 08.10.2010 +42 hours, 1000 hPa

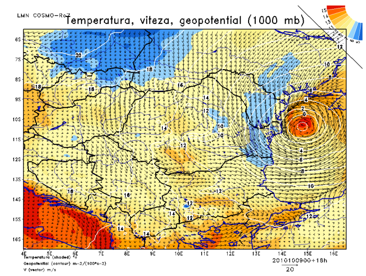

(c) Forecast from 09.10.2010 +18 hours, 1000 hPa

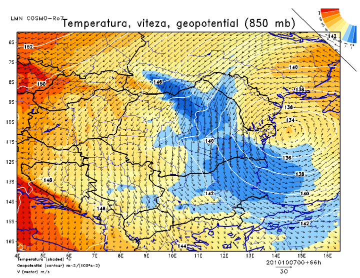

(d) Forecast from 07.10.2010 +66 hours, 850 hPa

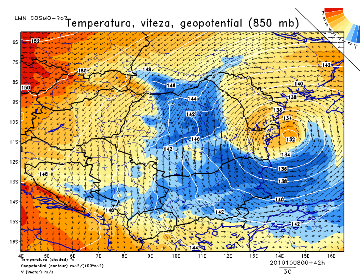

(e) Forecast from 08.10.2010 +42 hours, 850 hPa

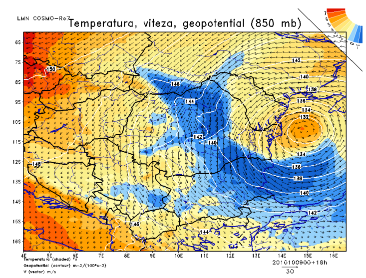

(f) Forecast from 09.10.2010 +18 hours, 850 hPa

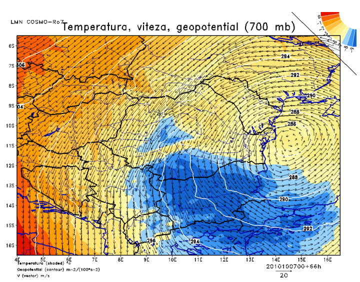

(g) Forecast from 07.10.2010 +66 hours, 700hPa

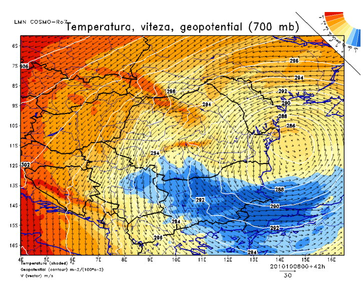

(h) Forecast from 08.10.2010 +42 hours, 700 hPa

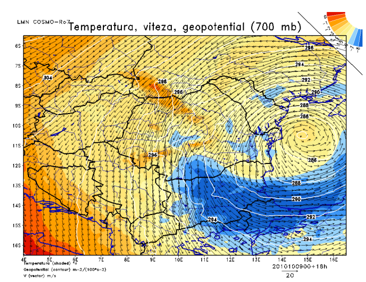

(i) Forecast from 09.10.2010 +18 hours, 700 hPa

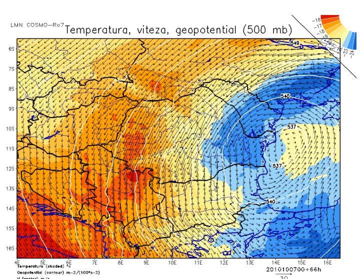

(j) Forecast from 07.10.2010 +66 hours, 500 hPa

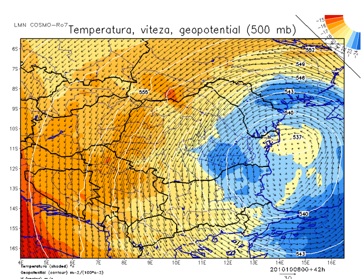

(k) Forecast from 08.10.2010 +42 hours, 500hPa

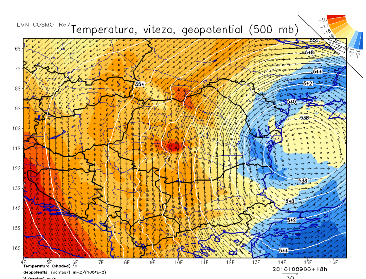

(l) Forecast from 09.10.2010 +18 hours, 500 hPa

Figure 4: COSMO 7km forecast: wind speed (vector), temperature (shaded), geopotential (contour) - 09.10.2010

According to the representation of the spatial distribution for the observed quantities of cumulated precipitation for 24 hours, in the area of Constanţa County were measured quantities of over 25 de l/m2 (Fig. 6(d)). The COSMO model estimated correctly the precipitation in both spatial distribution and quantities, starting with the integration from 7 October 2010 (Fig. 6(a)-6(c)). This can also be observed in the radar reflectivity parameter which was simulated by the model COSMO (Fig. 7(b)), which concurs with the satellite images for precipitation clouds (Fig. 7(a)).

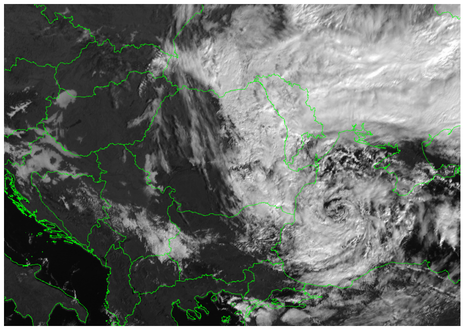

(a) RHV satellite image

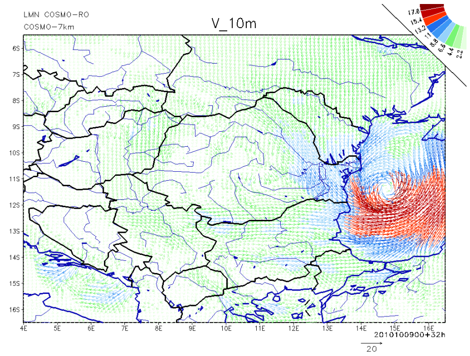

(b) COSMO 7km forecast on 09.10.2010 +32 hours, wind-10 m

Figure 5: 10.10.2010 - 08 UTC

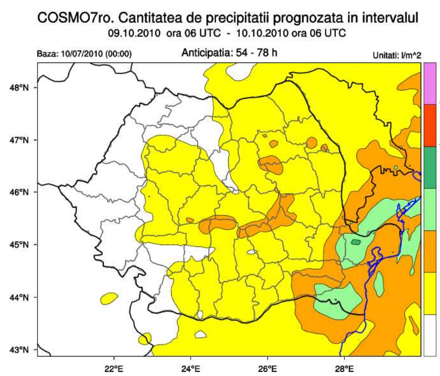

(a) Forecast from 07.10.2010 +78 hours

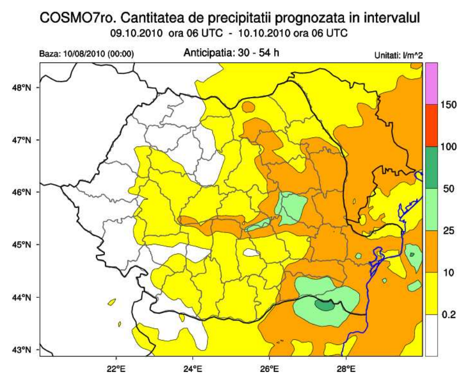

(b) Forecast from 08.10.2010 +54 hours

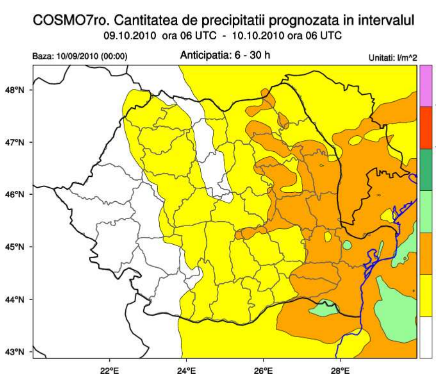

(c) Forecast from 09.10.2010 +30 hours

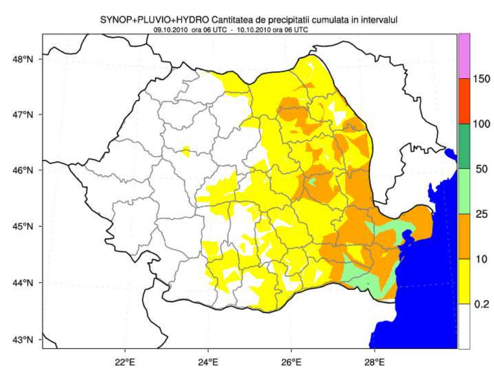

(d) Observations

Figure 6: 24 hours cumulated precipitation for 09.10.2010 (forecast from COSMO 7km and observations)

4. Conclusions

High resolution models on a limited area do not solve forecast problems entirely. Nevertheless, due to the higher spatial run-down in comparison to global models, they can prove to be of real support to the meteorologists in taking decisions regarding severe weather phenomena.

Numerical simulations made with the regional weather forecast model COSMO for the atmospheric instability situation on 9 October 2010 anticipated by the regional Meteorological Centre Constanţa by three "Warnings for immediate meteorological phenomena" show that

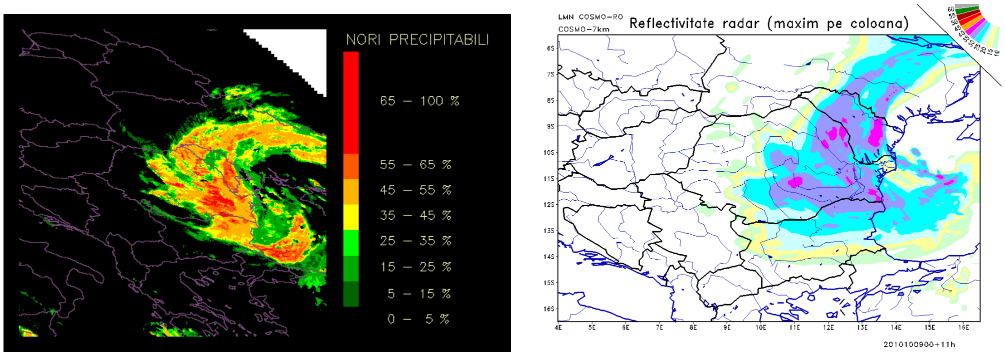

(a) Satellite image - precipitation clouds

(b) Radar reflectivity - column maximum COSMO 7km

Figure 7: 09.10.2010 - 11 UTC

the model has a high ability to forecast such phenomena.

After analysing different meteorological parameters from the COSMO numeric model (wind speed and direction for various atmospheric levels, air temperature, pressure and so on) the mesoscale cyclonic structure of Mediterranean provenance formed in the area of the Black Sea seaside on the 9th October 2010 could be identified. The phenomenon was correctly anticipated by the COSMO model starting with the day of 7 October 2010, three days previous to the occurrence of the phenomenon. The breakthrough of cold air of polar provenance behind the front, as well as the maintaining of the warm air on the anterior side of the cyclone which were visible on satellite images were also emphasised by the COSMO model. The contact between the two masses of cold and warm air is noticeable in the convergence line present in the parameter for wind.

The following runs of the COSMO model on the dates of 8 and 9 October 2010 confirmed the initial forecast and showed the evolution in time of the cyclone up to the date of 10 October 2010, when the structure occluded.

The parameter for cumulated precipitation in 24 hours was also correctly estimated by the COSMO model in both spatial distribution and quantities, starting with the run from 7 October 2010, as was the radar reflectivity parameter which concurs with satellite imaging of rain clouds.

References

[1] Domms G., Schattler U., 2001: The Multi-Layer Version of the DWD Soil Model TERRA_LM. *Technical Report No. 2*, Deutscher Wetterdienst, Offenbach, Germany

[2] Kain J.S., Fritsch J.M., 1993: Convective Parameterization for Mesoscale Models: The Kain-Fritsch Scheme. In: *The Representation of Cumulus Convection in Numerical Models. Meteorological Monograph No. 46*, American Meteorological Society: **165-170**.

[3] Louis J.F., 1979: A parametric model of vertical eddy fluxes in the atmosphere. *Bound. Layer Meteor., 17*: **187-202**

[4] Ritter B. , Geleyn J.F., 1992: A comprehensive radiation scheme for numerical weather prediction models with potential application in climate simulations. *Mon. Wea. Rev.*, 120: **303-325**

[5] Skamarock W. C., Klemp J. B., 1992: The stability of time-split numerical methods for the hydrostatic and nonhydrostatic elastic equations. *Mon. Wea. Rev.*, 120: **2109-2127**

[6] Thomas S., Girard C., Domms G., Schattler U., 2000: Semi-implicit scheme for the DWD Lokal-Modell. *Meteor. Atmos. Phys.*, 75: **105-125**

[7] Tiedtke M., 1989: A comprehensive mass flux scheme for cumulus parameterization in large scale models. *Mon. Wea Rev.*, 117: **1779-1799**

[8] Wicker L., Skamarock W., 1998: A time-splitting scheme for elastic eqations incorporating second-order Runge-Kutta time differencing. *Mon. Wea. Rev.*, 126: **1992-1999**

[9] http://www.satreponline.org

Increase of COSMO–LEPS horizontal resolution and its impact on the probabilistic prediction of precipitation events

Andrea Montani, C. Marsigli and T. Paccagnella

ARPA–SIMC, Bologna, Italy

1. Introduction

One of the main challenges for numerical weather prediction (NWP) is still recognised as quantitative precipitation forecasting. The use of the probabilistic approach via the ensemble forecasting has now become commonplace to tackle the chaotic behaviour of the atmosphere and to support forecasters in the management of alert procedures for events with little deterministic predictability. In the framework of limited–area ensemble forecasting, the COSMO–LEPS system (Montani et al., 2003) was the first mesoscale ensemble application running on a daily basis in Europe since November 2002. A number of system upgrades had a positive impact on COSMO–LEPS forecast skill of precipitation in the short and early medium–range, documented by Montani et al. (2010).

As computer power resources increase, it was investigated the extent to which an increase in horizontal resolution of COSMO–LEPS runs could have a benefit on the probabilistic prediction of those surface fields, like precipitation and 2–metre temperature, heavily affected by orography and mesoscale processes. For this reason, a number of system upgrades were tested and their impact was studied, focusing the attention to the performance of COSMO–LEPS for heavy precipitation events.

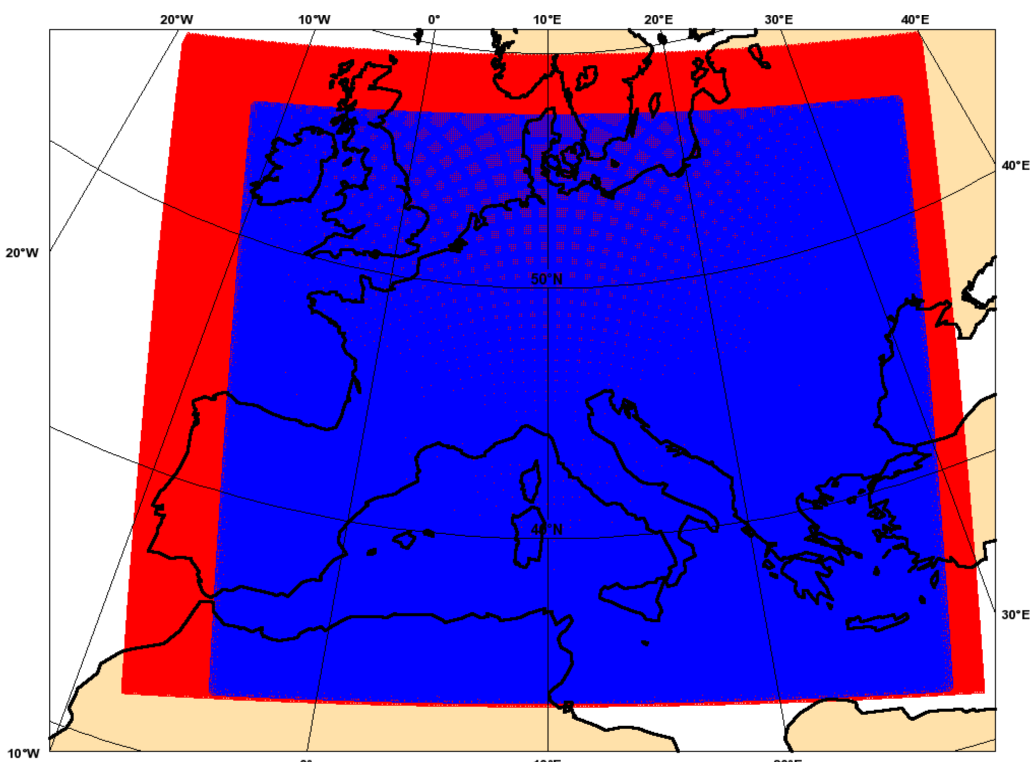

Figure 1: Integration domain for COSMO–LEPS "oper" (blue) and "test" (red).

Table 1: Main features of the "oper" and "test" COSMO–LEPS.

	"oper"	"test"
EnsembleSize	16 members	16 members
ForecastLength	132h	132h
InitialTime	12 UTC	12 UTC
HorizontalResolution	10 km	7 km
VerticalResolution	40 ML	40 ML
Time–step	90 s	60 s
NumberofGridPoints	306x258x40= 3.157.920	511x415x40= 8.482.600
Subgrib–scale Orography	FALSE	TRUE
Use of external database for vegetation cover	FALSE	TRUE
ModelVersion	4.7	4.8
Perturbations:	convect. scheme (TD or KF)	convect. scheme (TD or KF)
	tur_len (500 or 1000)	tur_len (150 or 500 or 1000)
	pat_len (500 or 10000)	pat_len (500 or 2000 or 10000)
		crsmin (50 or 150 or 200)
		rat_sea (1 or 20 or 40)
		rlam_heat (0.1 or 1 or 5)

More precisely, the following modifications were introduced:

- increase of the horizontal resolution from 10 to 7 km;
- enlargement of the integration domain so as cover completely Central and Southern Europe (see Fig. 1);
- introduction of new "stochastic" perturbations in COSMO–LEPS runs.

From June to November 2009, both the operational system (referred to as "oper") as well as the new one (referred to as "test") were run in parallel. Afterwards, the relative merits/shortcomings of the systems were assessed on the basis of a number of probabilistic indices (Marsigli et al., 2008). Table 1 summarises the main properties of "oper" and "test", indicating the common features as well as the innovations of the new system.

2. Methodology of verification

The performance of COSMO–LEPS (both "oper" and "test") is analysed considering the probabilistic prediction of 12–hour accumulated precipitation exceeding a number of thresholds for several forecast ranges. As for observations, it has been decided to use the data obtained from the SYNOP reports available on the Global Telecommunication System (GTS), since this is recognised to be a homogeneous and stable dataset throughout the verification period (June to November 2009).
In order to assess the skill of the system over complex topography, verification is first performed in the domain ranging from 43N to 50N and from 2E to 18E. This domain, sometimes referred to as MAP D-PHASE area (Mesoscale Alpine Programme, Demonstration of Probabilistic Hydrological and Atmospheric Simulation of flood Events in the alpine region), is the common terrain of investigation for the Forecast Demonstration Project which took place during the Operation Period of D-PHASE (Zappa et al., 2008; Rotach et al., 2009). Within

Table 2: Main features of the verification configuration.

variable:	12–hour accumulated precipitation (18–06, 06–18 UTC);
period:	from June to November 2009;
region 1:	43–50N, 2E–18E (mapdom);
region 2:	35–58N, 10W–30E (fulldom);
method:	nearest grid–point;
observations:	SYNOP reports;
fcst ranges (h):	6-18, 18-30, 30-42, 42-54, 54-66, 66-78, 78-90, 90-102, 102-114, 114-126;
thresholds:	1, 5, 10, 15, 25, 50 mm/12h;
scores:	ROC area, BSS, RPSS, OUTL;

this domain (referred to as "mapdom"), a fixed list of 412 SYNOP stations is considered and the relative reports in terms of total precipitation are used to evaluate the COSMO–LEPS skill. In addition to this, it has been also considered a second (larger) domain, which includes approximately the full COSMO–LEPS domain, ranging from 35N to 58N and from 10W to 30E. Within this further domain (referred to as "fulldom"), a list of 1542 stations is taken and the performance of "oper" and "test" is also assessed.
The SYNOP reports have undergone a simple quality control firstly based on the "surpassing" of a confidence level (provided in the data retrieved by ECMWF archive) for the full report. In addition to this, for cases of very high precipitation records, the values are compared, whenever possible, to those taken from nearby non–GTS stations. In case of discrepancy between non–GTS and SYNOP reports, the latter is discarded and the relative data not used in the computation of the scores.
As for the comparison of model forecasts against SYNOP reports, we select the grid point closest to the observation. Little sensitivity to the results is found when, instead of the nearest grid point, a bi-linear interpolation using the 4 nearest points to the station location, is used to generate the model forecasts. Therefore, the results shown hereafter will be relative only to the nearest grid-point method.
The performance of COSMO–LEPS is examined for 6 different thresholds: 1, 5, 10, 15, 25 and 50 mm/12h.
As already mentioned, verification was performed over a 6–month period, from June to November 2009. For the full period, the following probabilistic scores are computed: the Brier Skill Score (BSS), the Ranked Probability Skill Score (RPSS), the Relative Operating Characteristic Curve (ROC) area and the Percentage of Outliers (OUTL). For a description of these scores, the reader is referred to Wilks (1995) and to Marsigli et al. (2008). The main features of the verification exercise are summarised in Table 2.

3. Performance of the systems

As already mentioned, both "oper" and "test" COSMO-LEPS were run continuously once a day from June to November 2009. Afterwards, both systems were verified against the precipitation observed by a network of about 412 (1542) SYNOP stations covering the so–called "mapdom " ("fulldom"). The skill of the two systems in terms of prediction of 12–hour accumulated precipitation is summarised in Fig. 2, where the Ranked Probability Skill Score (RPSS) is plotted against the forecast range for both "oper" and "test" configurations.

It can be noticed that "test" COSMO-LEPS has higher RPSS for all forecast ranges. The difference between the two systems is consistent throughout the full forecast range, up to day 5, with a larger gap in favour of "test" COSMO-LEPS more evident for the first two days

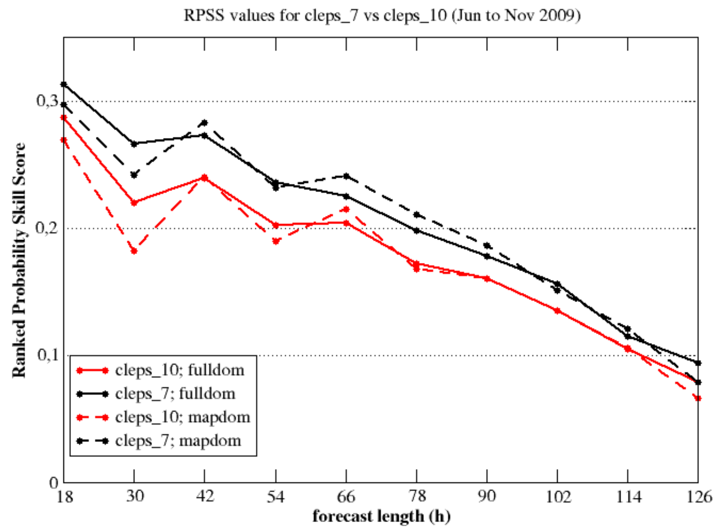

Figure 2: Ranked Probability Skill Score for "oper" (red) and "test" (black) COSMO–LEPS, calculated over the 6–month period from June to November 2009. Solid (dashed) lines refer to scores over the "fulldom" ("mapdom").

of integrations. This holds when verification is performed either in the Alpine area (dashed lines, relative to "mapdom") or over the entire integration domain (solid lines, relative to "fulldom").

If the attention is now focused on the performance of both systems for a specific event, many of the above comments still hold. Fig. 3 shows the scores of "oper" and "test" in terms of ROC area and BSS for the event "12–hour accumulated precipitation exceeding 10 mm".

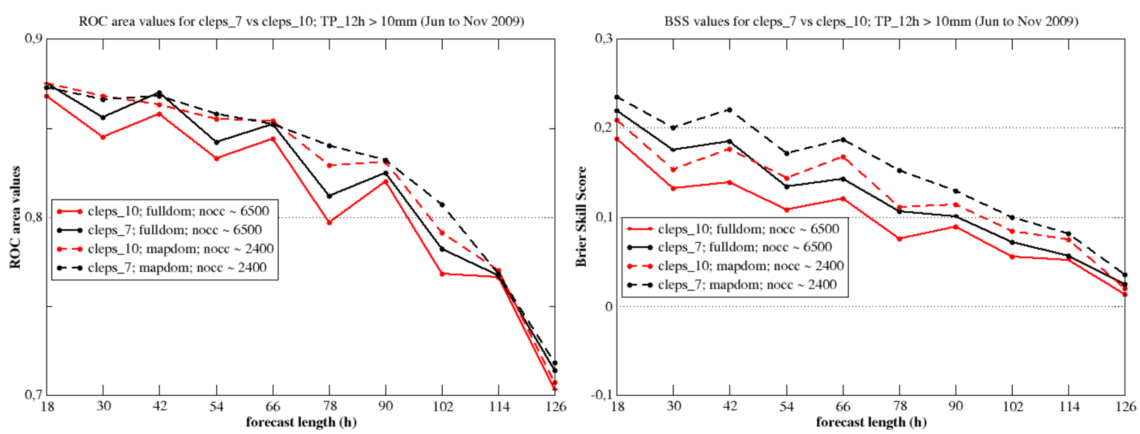

Figure 3: ROC area values (left panel) and BSS (right panel) for "oper" (red) and "test" (black) COSMO–LEPS relative to the event "precipitation exceeding 10mm in 12 hours" for the forecast ranges of Table 2. Both scores are calculated over the 6–month period from June to November 2009. Solid (dashed) lines refer to scores over the "fulldom" ("mapdom").

As for the ROC area (left panel), it can be noticed that the impact of enhanced resolution in "test" runs is almost negligible for short forecast ranges, if the verification is performed over the "mapdom". Instead, a larger and positive impact is noticeable for verification over the "fulldom", up to fc+102h. As for the BSS, the performances of "oper" and "test" COSMO–LEPS indicates a clear margin in favour of the higher–resolution system. This latter result holds for both verification domains.

Finally, the attention is focused on the ability of the "test" system to reduce the number of outliers with respect to "oper", thanks to the higher resolution as well as to the introduction

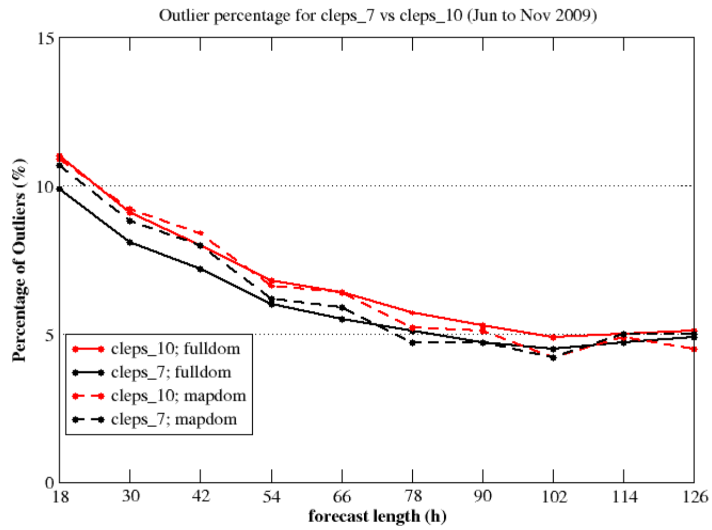

Figure 4: Percentage of Outliers for "oper" (red) and "test" (black) COSMO–LEPS, calculated over the 6–month period from June to November 2009. Solid (dashed) lines refer to scores over the "fulldom" ("mapdom").

of new perturbations which should ensure a larger spread among "test" forecasts. Fig. 4 shows that, in the 7–km system (black lines), the number of outliers is reduced for all forecast ranges, except the longest one, with respect to the operational system. The impact is more evident over the "fulldom", where the higher–resolution system outperforms "oper' with a 12–hour gain in predictability. It can also be noticed that, for all configuration and verification networks, there is a sort of "plateau" at about 5% of outliers, which seems, at the moment, a limit for the number of outliers in COSMO–LEPS systems.

4. Summary and Outlook

The results presented in the previous sections are based on a long and statistically significant sample (6–month period and several hundreds of SYNOP stations). They show the potential of the higher–resolution COSMO–LEPS, which can provide more accurate rainfall forecasts, thanks to a better description of orographic and mesoscale–related processes. In addition to this, the introduction of new model perturbations proved to have a positive effect on the forecast skill of the ensemble system.

Following the indications provided by different probabilistic scores, the 7–km COSMO–LEPS was implemented operationally in December 2009 and has been running on a daily basis since then. As for the future, it is envisaged to continue the systematic verification of the system, to monitor the added value of the higher resolution in the ensemble runs and to study new possible ameliorations.

References

[1] Marsigli C., Montani A., Paccagnella T., 2008.:A spatial verification method applied to the evaluation of high–resolution ensemble forecasts. *Met. Appl.*, **15**, 125–143.

[2] Montani A., Capaldo M., Cesari D., Marsigli C., Modigliani U., Nerozzi F., Paccagnella T., Tibaldi S., 2003. Operational limited–area ensemble forecasts based on the 'Lokal Modell'. *ECMWF Newsletter No. 98. Available from: European Centre for Medium–Range Weather Forecasts, Shinfield Park, Reading RG2 9AX, UK.*

[3] Montani A., Cesari D., Marsigli C., Paccagnella T., 2010.: Seven years of activity in the field of mesoscale ensemble forecasting by the COSMO-LEPS system: main achievements and open challenges. *COSMO Technical Report No. 19. Available from COSMO website: http://www.cosmo-model.org.*

[4] Rotach M.W., Ambrosetti P., Ament F., Appenzeller C., Arpagaus M., Bauer H.-S., Behrendt A., Bouttier F., Buzzi A., Corazza M., Davolio S., Denhard M., Dorninger M., Fontannaz L., Frick J., Fundel F., Germann U., Gorgas T., Hegg C., Hering A., Keil C., Liniger M.A., Marsigli C., McTaggart-Cowan R., Montani A., Mylne K., Ranzi R., Richard E., Rossa A., Santos-Muoz D., Schr C., Seity Y., Staudinger M., Stoll M., Volkert H., Walser A., Wang Y., Werhahn J., Wulfmeyer V., Zappa M., 2009.: MAP D-PHASE: Real-time Demonstration of Weather Forecast Quality in the Alpine Region. *Bull. Amer. Meteor. Soc* **90**,1321-1336, DOI: 10.1175/2009BAMS2776.1

[5] Wilks, D.S., 1995.: Statistical Methods in the Atmospheric Sciences. *Academic Press*, New York, **467**.

[6] Zappa M., Rotach M.W., Arpagaus M., Dorninger M., Hegg C., Montani A., Ranzi R., Ament F., Germann U., Grossi G., Jaun S., Rossa A., Vogt S., Walser A., Wehrhan, J., Wunram C., 2008.: MAP D-PHASE: real-time demonstration of hydrological ensemble prediction systems. *Atmos. Sci. Let.*, **9**, 80–87, DOI: 10.1002/asl.183.

A study on the spread/error relationship of the COSMO-LEPS ensemble

M. Salmi, C. Marsigli, A. Montani, T. Paccagnella

ARPA-SIMC, HydroMeteoClimate Service of Emilia-Romagna, Bologna (Italy)

1 Introduction

This work aims at providing an evaluation of some statistical properties of the COSMO-LEPS ensemble. In particular, the relationship between the spread and the forecast error of the COSMO-LEPS ensemble is here evaluated, with the purpose of quantifying the capability of the ensemble of representing the forecast error, in a statistical sense. The analysis is performed for two upper-air meteorological variables: geopotential height at 700 hPa and temperature at 850 hPa. The dependence of this relation from the forecast range, from the season, and from the spatial location is also assessed.

2 Assessing the spread/skill relationship

The operational mesoscale ensemble COSMO-LEPS (COSMO Limited-area Ensemble Prediction System) runs over large part of Central and Southern Europe, with a spatial resolution of 7 km (from Dec 2009). COSMO-LEPS has been designed to provide probabilistic predictions of surface parameters, especially for severe weather, in late-short to early-medium range (up to day 5.5). COSMO-LEPS is a downscaling of the ECMWF EPS, where 16 EPS members are selected and used to provide initial and boundary conditions to the COSMO runs. A set of COSMO model physics parameters are also perturbed, following the results of the SREPS and CONSENS Priority Projects.

In general, an ensemble should provide, among other kinds of information, an estimation of the reliability of the forecast: if the ensemble forecasts are quite different from each other, it is clear that at least some of them are wrong, whereas if there is good agreement among the forecasts, there is more reason to be confident about the forecast (Kalnay, 2002). That is, the spread (which is a measure of atmospheres predictability) can be used as a predictive variable to forecast the forecast error. In order to assess the COSMO-LEPS spread/skill relationship, here the COSMO-LEPS ensemble spread is computed and compared against the error of the ensemble mean (calculated with respect to a reference analysis).

The ensemble spread is defined as the ensemble standard deviation, the RMS distance of each member from the ensemble mean, while the forecast error is the RMS error of the ensemble mean with respect to the ECMWF analysis.

For this work, the COSMO-LEPS forecasts in terms of geopotential height at 700 hPa and temperature at 850 hPa have been considered, for two different seasons: summer (JJA) and autumn (SON) 2009. ECMWF operational analyses (horizontal resolution of approx. 25 km) are extracted over a regular lat-lon grid (0.25x0.25 deg) and used as the reference analyses. The 10-km COSMO-LEPS runs are interpolated on the same 0.25x0.25 deg regular lat-lon grid of the ECMWF data.

In order to express the spread/skill relationship, ensemble spread and error of the ensemble mean have been computed (separatley for each meteorological parameter, for each season and for each forecast range) for each point of the domain over the whole period. Hence, each grid point of the domain is characterized by a couple of numbers: a value of spread and a value of error. Following Wang and Bishop (2003), spread values are then split into 10 subgroups of equal population: each error value is therefore assigned to the group of its corresponding spread value. For each class, an average spread value is computed, together with the corresponding average error value. Finally, the average values are plotted in a graph. The slope of the resulting line expresses how the two quantities are correlated. If the line lies above the bisector, then the spread is underestimated and the system simulates too little uncertainty. On the contrary, if the line lies below the bisector, then the effective error committed by the ensemble mean is smaller than the one simulated by the spread.

3 Results

The results of the present work are presented in a comprehensive manner in Salmi (2010). Here, only the main outcomes are briefly described.

Dependence on season and forecast range.

The spread/error relationship is shown in Fig. 1 for the two meteorological parameters and for the two seasons. In the computation of the ensemble spread and error, an orography mask is applied, in order to reduce the spurious error due to mountains. The effect of the mask is to eliminate from the computations all the points of the forecast fields in which orography value is greater than 1000 m.

For what concerns the Z700 fields (top row), there is generally a good relationship between error and spread, especially in summer. In autumn a poor correlation is evident between the two quantities for the +24 h forecast range. Spread values are generally overestimated after day 2.

In terms of T850, spread and error are well correlated during summer, while they have an evident non-linear relation in autumn. During both seasons, values of spread are slightly underestimated. Short-term forecast ranges present worse slopes than those of the medium-range. In autumn the correlation is quite poor for the +24h forecast range and improves clearly only from day 4.

The curved form of the spread/skill lines for the T850 indicates that, in the central spread categories, the error and the spread are uncorrelated, since a wide range of error values correspond to specific spread values.

Geographical dependence.

In order to highlight possible dependencies of the spread-skill relationship upon the geographical position and also to help to comprehend the reason of the un-correlation seen in the previous section, the domain is divided into 4 sub-areas. Each area is identified with a specific colour, as shown in Fig. 2.

Then, all the 10965 grid points of the domain are drawn on scatter-plots, without grouping them. Each point is coloured according to its geographical position as described by Fig. 2.

Results for T850 for the last three forecast ranges (+72 h in the top row, +96 h in the middle row and + 120h in the bottom row) during summer (left column) and autumn (right column) are shown in Fig. 3.

In the summer season, the relation is reasonably good over the whole domain at the +96 h and +120 h forecast ranges, while at +72 h the points of the blue and black areas (respectively

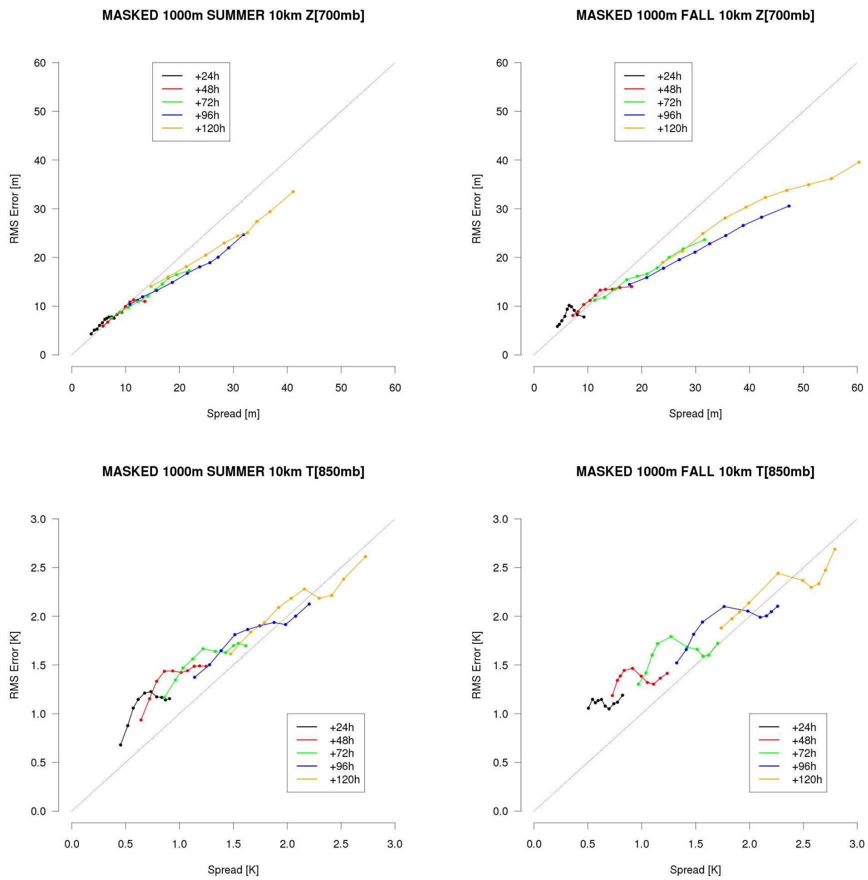

Figure 1: Spread/skill relationship of the COSMO-LEPS forecasts for Z700 (top row) and T850 (bottom row) and for 2 seasons (summer in the left column and autumn in the right column). The different colours are relative to the 5 considered forecast ranges.

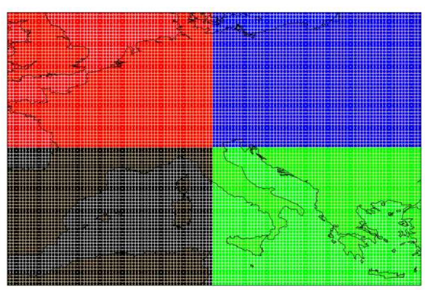

Figure 2: Subdivision of the domain in 4 areas.

north-east and southe-west areas) are markedly not distributed along the diagonal.

On the contrary, the scatter-plots for the autumn season show clouds of points not distributed along the diagonal, with the exception of the green dots (south-east area) for the longer forecast ranges. In each plot there are two very distinct groups of points with different trends, depending on the position: in the southern belt (green and black areas) or in the northern one (red and black areas). Spread and skill seem here to be uncorrelated, even though in the eastern Mediterranean Basin the relation is slightly better. In general, it can be underlined that both spread and error rise when rising the latitude and that the relationship appears to be slightly better over the eastern Mediterranean Basin.

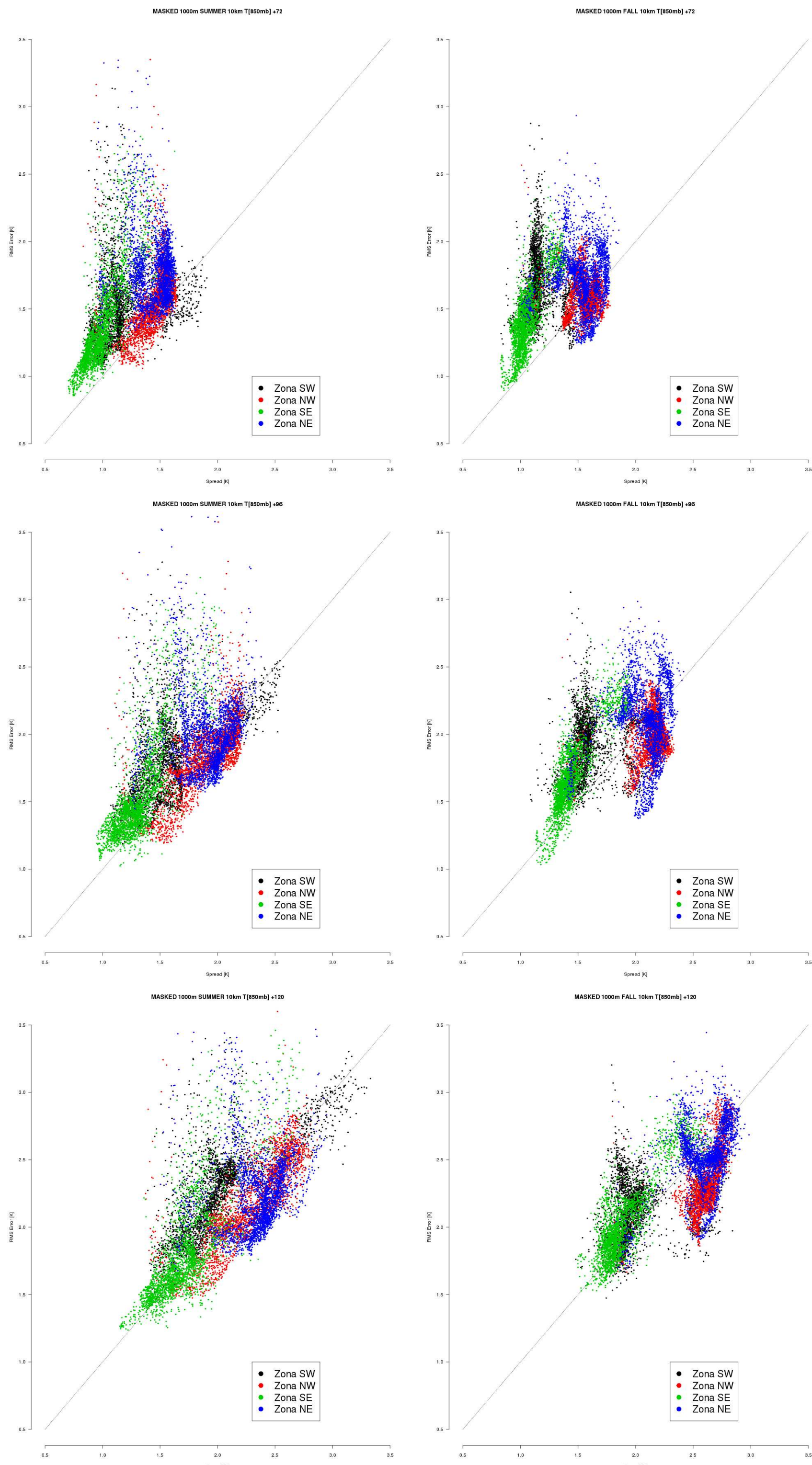

Figure 3: Scatter plots of the spread and skill values of the COSMO-LEPS forecasts of T850. The plots are relative to the 2 seasons (summer in the left column and autumn in the right column) and are for 3 different forecast ranges (+72 h in the top row, +96 h in the middle row and + 120h in the bottom row). The different colours are relative to the 4 areas in which the domain has been divided.

The scatter-plots regarding the 700hPa geopotential height (not shown) are far more regular, showing a good linear relationship between spread and error, for all areas.

4 Conclusions

In general, the spatial distribution of the ensemble spread and of the ensemble mean error for the considered variables are generally correlated, especially after the second forecast-day. This means that the spread plays a predictive role in the geographical distribution of the forecast skill.

The spread tends to underestimate the error in T850 field, particularly in the short-term forecasts. On the contrary, for what concerns the Z700, the spread tends to slightly overestimate the error, especially for medium-range forecasts. The spread-error spatial correlation is generally better for the Z700 than for the T850.

Furthermore, the COSMO-LEPS spread-error spatial relationship over Europe strongly depends on geographical position and season. The correlation is better during summer rather than in autumn, especially over Central Europe.

In general, the Mediterranean Basin (compared to Central Europe) presents a better correlation between spread and skill, along with lower values for both. This means that it is an area characterized by smaller uncertainty of the atmosphere and that perturbations applied to the system grow proportionally to this uncertainty.

This is a preliminary study, which needs to be extended to other variables, such as precipitation and 2-meters air temperature.

References

[1] Kalnay, E, 2002: Atmospheric Modeling, Data Assimilation and Predictability. *Cambridge University Press*, pp. **364**.

[2] Wang, X., C. H. Bishop, 2003: A comparison of Breeding and Ensemble Transform Kalman Filter Ensemble Forecast Schemes. *Journal of Atm. Sci.*, 60, p. **1140-1158**.

[3] Salmi, M., 2010: The spread/error relationship on the COSMO-LEPS limted-area ensemble predicition system. Graduation thesis, *University of Bologna*, pp. 41.

Initial condition perturbations for the COSMO-DE-EPS

Carlos Peralta and Michael Buchhold

Deutscher Wetterdienst (DWD), Frankfurter Str. 135, 63067 Offenbach, Germany

1. Introduction

The numerical weather prediction model COSMO-DE, which simulates deep convection explicitly, is a configuration of the COSMO model with a horizontal grid size of 2.8 km [1]. It runs operationally at DWD since 2007, covering the area of Germany and producing forecasts with a lead time of 0-21 hours. A 20-members ensemble prediction system (EPS) based on COSMO-DE runs pre-operationally at DWD since December 9 2010. Operational use is envisaged to start in 2012, after an upgrade to 40 members and inclusion of statistical postprocessing. COSMO-DE-EPS includes perturbations of initial and boundary conditions, and model physics. This contribution describes the current implementation of initial perturbations in COSMO-DE-EPS.

The current setup of the lateral boundary conditions uses forecasts of different global models, while different configurations of the COSMO-DE model are used for the variation of model physics [4]. The perturbations of the initial conditions of the ensemble use two simple approaches: varying parameters during the Nudgecast (assimilation) phase of COSMO-DE and taking differences with members of a BC-EPS (boundary conditions EPS). The BC-EPS consists of 4 COSMO simulations with a 7km grid, driven by 4 different global models (GFS, GME, IFS and GSM) and the aim is to take into account the uncertainty at coarser scales to define initial perturbations. The concept of BC-EPS is based on the COSMO Short Range EPS (SREPS) developed at ARPA-SIMC [4], which is driven by the global models IFS, GME, GFS and UM. During the development phase of the COSMO-DE-EPS we have used SREPS boundary data, and all results presented in this contribution make use of COSMO-SREPS. The BC-EPS is the provider of boundary data during the pre-operational phase of COSMO-DE-EPS.

This contribution is organized as follows. A brief discussion of varying Nudging parameters is presented in Section 2. The setup of initial perturbations based on the BC-EPS is discussed in Section 3. The perturbations are filtered out close to the surface, and this is discussed in Section 4. Some numerical checks conducted on the perturbations are discussed in Section 5, and a method to hydrostically balance the perturbations is discussed in Section 6. Some preliminary results are presented in Section 7. The ensemble lacks variability close to the surface, and a way to remedy this can be to disturb soil moisture fields. Some sensibility studies on this regard are presented in Section 8.

2. Nudging perturbations

The current method for data assimilation in COSMO-DE is based on the Nudging technique, which is a very pragmatic approach with many parameters that control how the model relaxes to the observation increments [8]. The optimal values are empirically determined. We tested modifications of these parameters during the Nudgecast period of the ensemble forecast (first 1-1.5 hours). The most important parameters are the correlation length scale for the mass, wind and humidity observations (`rhinfl, rhvfac`, and `rhiflsu`), the coefficient of latent heat nudging (LHN) increments derived from radar observations (`lhn_coef`), parameters controlling the amount of geostrophic wind corrections for balancing the mass field increments (`qgeo` and `qgeotop`), and parameters controlling the amount of divergent and non-divergent wind increments (`fnondiv` and `cnondiv`). The default values of these parameters can be found in Schaettler et al. [6].

We have conducted several simulations modifying these parameters and found that they introduce variability only on the very small scales.

3. Initial condition perturbations based on BC-EPS

In order to introduce variability on the large scales we follow a multi-boundary technique. We have written a parallel program which calculates differences between undisturbed BC-EPS and COSMO-EU fields at start time, and adds them to the COSMO-DE analysis fields, using the formula

$$f = f_0 + W(k)(f_{BC} - f_{EU}), \tag{1}$$

where $f = (U', V', T', QV')$ are the disturbed fields, and $f_0 = (U_0, V_0, T_0, QV_0)$ are the undisturbed fields, while f_{BC} and f_{EU} denote the corresponding BC-EPS and COSMO-EU reference field respectively. All the fields have to be interpolated to the COSMO-DE grid using the operational `int2lm` routine [5]. The pressure perturbation PP' is calculated using the same equation but only on the last model level (see Section 6). A low pass exponential filter $W(k)$ is applied on every model level k, to the fields (U', V', T', QV').

4. Vertical filter

Sudden changes in model levels for the perturbed variables can arise during the interpolation process from COSMO-EU and BC-EPS to COSMO-DE resolution, since these models use a coarser resolution. This is especially true closer to the surface, where model levels are adapted to the local orography. The surface temperature and surface humidity may not be consistent if all the fields are perturbed in the same way, especially close to the boundary layer. This can result in spurious surface fluxes and humidity adjustments, and sudden condensation or evaporation. Our aim is to introduce a large scale perturbation without disturbing the surface layer and without triggering internal boundary layer fluxes. One way to achieve this is by keeping the surface layer undisturbed, slowly increasing the perturbation with height, using a low-pass exponential filter

$$W(k) = \exp\left(-\left|\frac{k}{N_{ke}}\right|^{\gamma} \ln\epsilon\right), \quad 0 \le |k| \le N_{ke}, \tag{2}$$

where N_{ke} is the number of model levels (N_{ke}=50 for COSMO-DE), $\epsilon = 2.2 \times 10^{-16}$ is the machine zero, and γ is the (integer) order of the filter. A small value ($\gamma < 16$) indicates strong filtering of the perturbations on lower levels, while a high value ($\gamma > 16$) indicates soft filtering. Typically, 5-10 levels closest to the surface are undisturbed. Figure shows the behaviour of $W(k)$ as a function of model level k, for $8 \le \gamma \le 24$. The curves correspond, from right to left, to $\gamma = 24, 20, 16, 10$ and 8.

5. Numerical check on QV and QC

Occasionally, it may happen that taking simple differences between the BC-EPS and EU fields produces unphysical values of the specific humidity QV′ (i.e., QV′ < 0). In order to

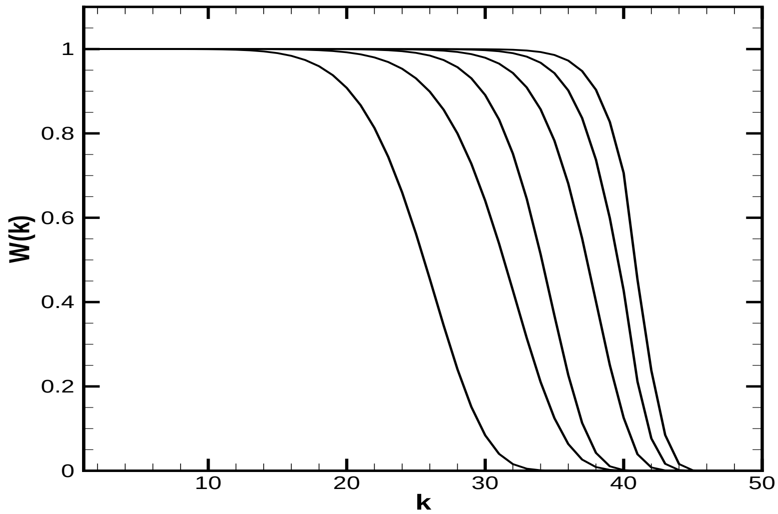

Figure 1: Vertical filter $W(k)$ as a function of model level k, for $\gamma = 24, 20, 16, 14, 10$ and 8 (from right to left).

avoid this situation a numerical check is performed on this variable, so that QV′ is in the range $R_{min}\, QV^* \leq QV' \leq R_{max}\, QV^*$, where R_{max} and R_{min} are adjustable parameters (currently set to 1.15, and 0.05 respectively) and QV^* is the specific humidity for saturated water vapour pressure, calculated analytically using the formula

$$QV^* = \left(\frac{R_d}{R_v}\right) \frac{P_v}{P_a - (1 - R_d/R_v)P_v} \tag{3}$$

where P_v is the saturation water vapour pressure (in Pa), P_a is the air pressure (in Pa) and R_v and R_d are the gas constants of water vapour and dry air (in J/(kg K)). The saturation water vapour pressure is given by the Magnus Formula:

$$P_v = b_1 \exp\left(\frac{b_{2w}(T - b_3)}{T - b_{4w}}\right) \tag{4}$$

where T is the temperature and b_1, b_{2w}, b_3 and b_{4w} are constant parameters. The Magnus Formula also requires the air pressure as input. The air pressure is calculated using the COSMO-DE routine `reference_atmosphere` [5]. In some upper levels the air pressure can be too small, and the Magnus Formula can lead to negative values for QV^*. To avoid this situation the calculation is limited to levels in which P > 100 hPa. For levels in which P < 100 hPa QV′ is also checked, and set to $QV' = 10^{-6}$ if $QV' < 0$.

Finally, the specific cloud water content QC is also checked and set to 0 if $QV' < 0.95\, QV^*$. The variable QC is only checked in this way to be consistent with QV, and it is not disturbed in any other way.

6. Calculation of the pressure perturbation PP'

In order to avoid direct sources of vertical wind, the total analysis perturbations should be balanced hydrostically. This is achieved by using the hydrostatic equation derived from the vertical momentum equation, neglecting subgrid scale processes and setting the total derivative of vertical wind to zero. Integrating this equation for the analysis increments $\Delta P'$ of pressure perturbation, a recursive equation is obtained, that gives the pressure increments as a function of reference pressure, T' and QV', calculated in the way described in the previous Section (see equation (3.87) in Schraff and Hess [7]). The pressure increments are calculated from the last to the first model level. Since the equation is recursive, $\Delta P'$ at the model level N_{ke} is needed. This is given as $(\Delta P')_{N_{ke}} = C(PP' - PP_0)$, where C is an empirically chosen factor (currently set to 0.7) and PP_0 the undisturbed analysis field.

During the interpolation from BC-EPS to the COSMO-DE grid some artificial artifacts can appear in the pressure fields close to the surface (this is particularly true when doing the interpolation from the GFS members of BC-EPS to COSMO-DE). Therefore $(\Delta P')_{N_{ke}}$ is additionally smoothed on each model level by replacing its value at a particular grid point by the mean of the values on a box with N×N grid points. Typically, N =20 is enough to ensure a smooth field. The pressure perturbation PP' is finally calculated as $PP' = PP_0 + \Delta P'$ from model $k = N_{ke} - 1$ to $k = 1$ (note that no vertical filter is applied on PP').

7. Effect of the perturbations on a forecast

Several example 24 hours forecasts were conducted, all starting at 00 UTC. These simulations make use of 4 members of the COSMO-SREPS, 1 for each global model, corresponding to COSMO-SREPS members 1 (IFS), 5 (GME), 9 (GFS) and 13 (UM).

Figure shows the effect of using different vertical filters on the spatial mean of the vertical velocity field at 850 hPa. Member 1 corresponds to a reference (undisturbed forecast), and members 2-5 correspond to an initial perturbation using equation (1) with SREPS member 1, 5, 9 and 13 respectively. Spurious gravity wave oscillations are triggered when the surface boundary layer is disturbed (Figure d, γ = 24), and greatly reduced for stronger filtering (Figure a-c, γ = 8-14).

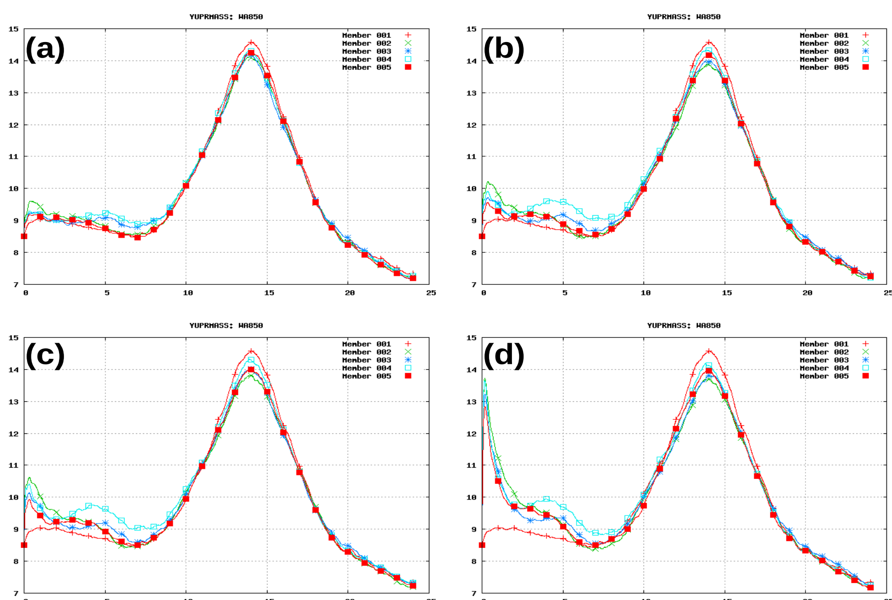

Figure 2: Spatial mean of the vertical velocity at 850 hPa (in m s^{-1}) as a function of forecast time for (a) $\gamma = 8$, (b) $\gamma = 12$, (c) $\gamma = 14$ and (d) $\gamma = 24$. Member 1 corresponds to a reference (undisturbed forecast), and members 2-5 correspond to an initial perturbation using equation (1) with SREPS members 1, 5, 9 and 13 respectively.

Figure shows an example of the effect on total precipitation after 3 hours of forecast, using different COSMO-SREPS members to disturb the initial conditions. The plots show differences in total precipitation between a reference (undisturbed) forecast and a forecast with initial condition perturbations using COSMO-SREPS member: (a) 1, (b) 5, (c) 9 and (d) 13, with the vertical filter set to $\gamma = 14$.

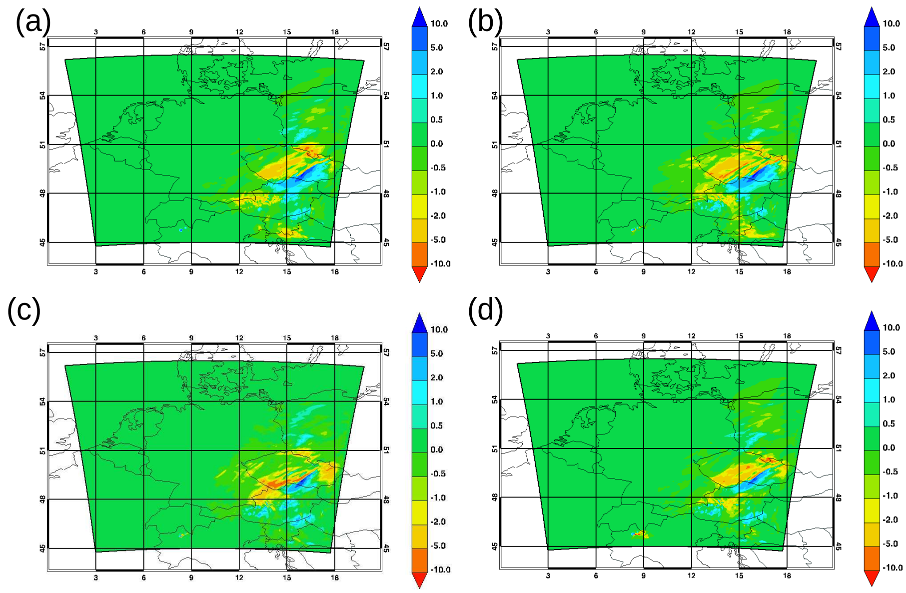

Figure 3: Difference in total precipitation (in mm) after 3 hours between a reference (undisturbed) forecast and a forecast with initial condition perturbations using COSMO-SREPS member: (a) 1, (b) 5, (c) 9 and (d) 13.

Figure shows the individual effect of using initial, boundary, and model physics variations. Each curve represents the spatiotemporal mean of the spread calculated for a period of 29 days (between May 20 and July 27 2009), as a function of forecast time. The solid curve shows the spread for a 10 members ensemble with initial condition perturbations based on equation (1), using COSMO-SREPS 1,5,9 and 13 (members 2-5), and disturbing the Nudging parameters indicated in Section 2. The dashed curve shows the spread of a 10 members ensemble with only model physics perturbations (parameters changed can be found in Gebhardt et al. [4]). The dotted curve with circles shows the spread of a 8 members ensemble with only boundary condition perturbations. The smaller number of members of this last ensemble comes from selecting pairs of COSMO-SREPS global models (1, 4, 5, 8, 9, 12, 13, 16, or two per global model). Most of the gain from disturbing the initial conditions occurs during the first 6 hours of the forecast. After that, the boundary condition perturbations dominate.

The effect of combining initial and boundary conditions, and model physics perturbations in one 15 members ensemble can be appreciated in Figure , which shows the spatiotemporal mean as a function of forecast time for a period of 15 days, between October 7 and November 24 2009 (solid curve). This ensemble uses COSMO-SREPS members 1,5, 9 for the initial and boundary condition perturbations and a selected number of COSMO-DE parameters disturbing the model physics [4]. As a comparison, the dashed curve in Figure shows the spread for a 15 member ensemble excluding initial condition perturbations (only boundary conditions and model physics). After $\sim$ 6 hours both curves are almost identical.

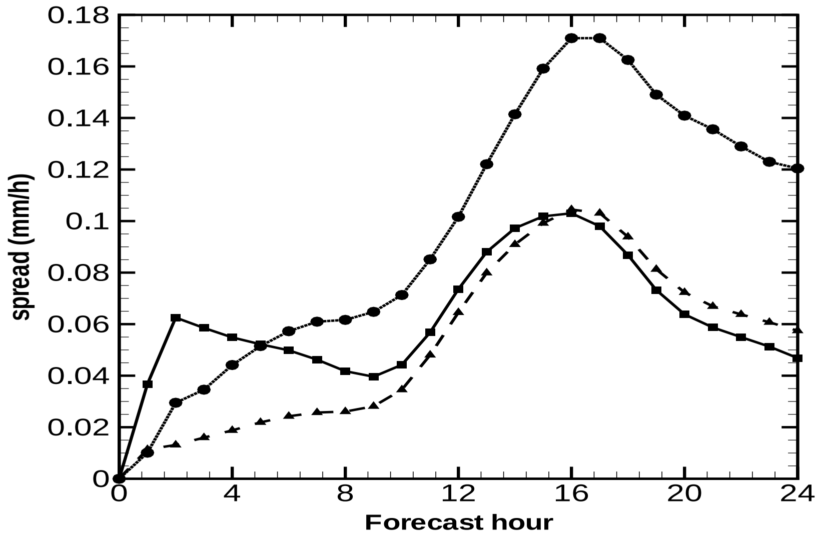

Figure 4: Spatiotemporal mean of the spread for a period of 29 days (between May 20 and July 27 2009) as a function of forecast time. The different curves correspond to a 10 members ensemble with only initial condition perturbations (solid, squares), a 10 members ensemble with only model physics perturbations (dashed, triangles) and an 8 members ensemble with only boundary condition perturbations (dotted, circles).

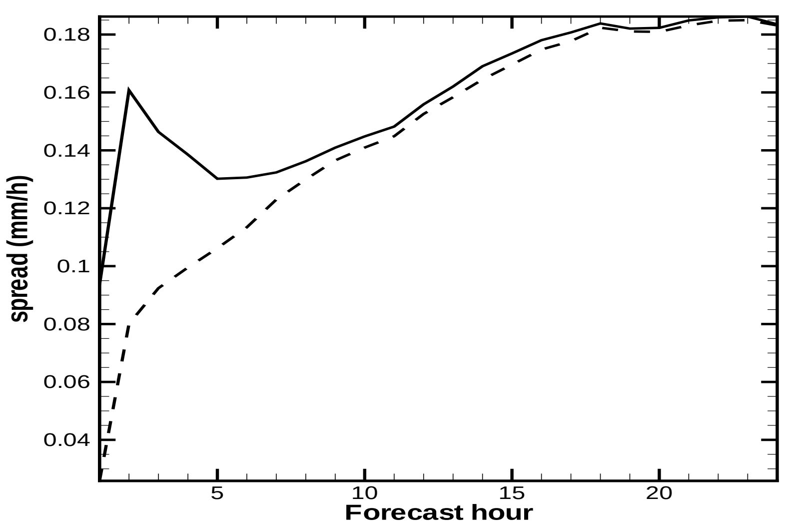

Figure 5: Spatiotemporal mean of the spread for a period of 15 days (between October 7 and November 24 2009) as a function of forecast time. The different curves correspond to a 15 members ensemble with combined model physics, initial and boundary condition perturbations (solid curve) and with only model physics and boundary condition perturbations (dashed curve).

8. Disturbing soil moisture fields

The current setup of the COSMO-DE-EPS suffers from a lack of perturbations of the soil and on levels closest to the surface. This lack of variability is also present in COSMO-SREPS. Recently, [3] have developed a technique to tackle this deficiency by disturbing soil moisture fields in COSMO-SREPS using an approach similar to Sutton and Hamill [9]. In the same spirit, we are currently conducting non-EPS simulations to test the effect of disturbing soil moisture fields in COSMO-DE.

We briefly report here some sensibility studies using a very simple method to disturb the soil water content W_SO. There are eight layers, with the lowermost layer containing the climatological water content (1, 2, 6, 18, 54, 162, 486 and 1458 cm). No soil analysis is performed in the COSMO-DE routine. Therefore, we retrieve the soil moisture field W_SO from the COSMO-EU analysis and interpolate it to the COSMO-DE grid. This field is then inserted into the COSMO-DE analysis and a forecast is run with this perturbed field, starting at 00 UTC. The original W_SO field can be totally replaced by the interpolated COSMO-EU-analysis W_SO field, or a fraction of W_SO can be added or subtracted.

Figure shows W_SO (at 1 and 6 cm depth), 1 h after the start of the forecast for the operational COSMO-DE and for a simulation in which the COSMO-DE field W_SO was completely replaced by the interpolated W_SO field from COSMO-EU. The forecast was started at 06 UTC, for July 2 2009. The humidity is slightly higher for the disturbed simulation. The relative difference is ~ 9.4 % at 1 cm and ~ 8.7 % at 6 cm. Interestingly, the differences are quite small considering that COSMO-EU uses a soil-moisture analysis, while W_SO quantity develops completely free in COSMO-DE. Figure shows the total precipitation after 6 hours of an undisturbed forecast using COSMO-DE (left) and introducing the W_SO fields from COSMO-EU (right). Differences are very localized and on small scales. Additional simulations were conducted, adding or subtracting a fraction of the W_SO field from COSMO-EU, giving similar results.

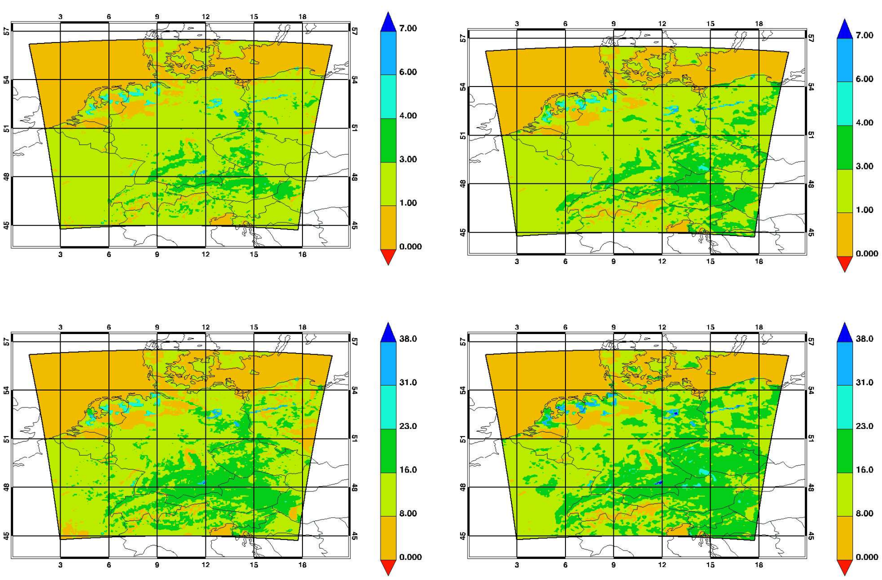

Figure 6: Soil moisture W_SO (in kg m^{-2}) for the operational COSMO-DE and a disturbed forecast using W_SO from COSMO-EU at 1 cm depth (upper row, left to right) and at 6 cm (lower row, left to right). The fields are shown 1hr after the start of the forecast.

9. Summary and Outlook

The inclusion of initial conditions in COSMO-DE-EPS has a positive effect, increasing the spread during the first 6 hours of the forecast. Later on, the spread is similar to the one introduced by boundary and model physics variations. However, note that this is true only

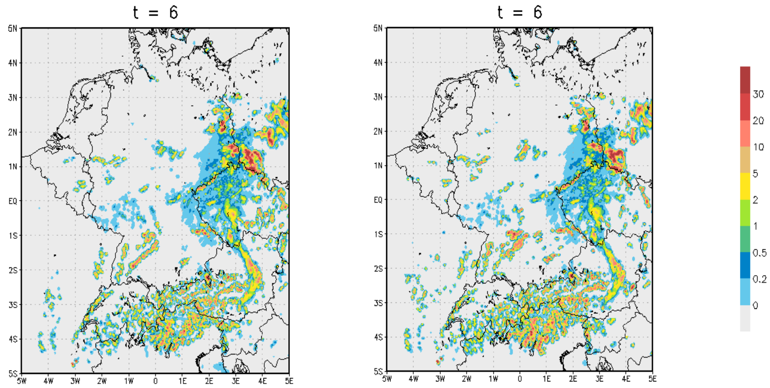

Figure 7: Total precipitation (in mm) after 6 hours for the operational COSMO-DE (left) and a disturbed forecast using W_SO from COSMO-EU (right).

on average, and not in general for each individual case.

One way to introduce spread at the surface boundary layer is to disturb soil moisture field. Disturbing soil moisture fields by interpolating the W_SO from COSMO-EU to the COSMO-DE grid and replacing this field (or a fraction of it) at the beginning of the forecast produces localized differences in total precipitation. No soil moisture perturbations have been included in COSMO-DE-EPS.

A more detailed study describing the combined effect of initial and boundary conditions perturbations and variations of model physics (including verification) will be reported elsewhere.

Acknowledgements

We thank S. Theis and Z. Ben-Bouallègue for very useful comments. We also thank B. Ritter, G. Zängl, U. Schättler and T. Hanisch for assistance during the development of the initial perturbations code.

References

[1] M. Baldauf, K. Stephan, S. Klink, C. Schraff, A. Seifert, J. Förstner, T. Reinhardt, and C.-J. Lenz. The new very short range forecast model LMK for the convection-resolving scale. In *Second THORPEX International Science Symposium, 2006. Volume of extended abstracts, Part B*, volume 10, 2006.

[4] C. Gebhardt, S. Theis, M. Paulat, and Z. Ben-Bouallegue. Experimental ensemble forecasts of precipitation based on a convection-resolving model. *Accepted for publication in Atmos. Res.*, 2010.

[3] F. Gofa and P. Louka. Soil moisture perturbations for COSMO-SREPS. In *12th COSMO General Meeting*, 2010.

[4] C. Marsigli, A. Montani, and T. Paccagnella. The COSMO-SREPS ensemble for short-range: system analysis and verification on the Map D-PHASE DOP. In *Proceedings of*

the Joint MAP D-PHASE Scientific Meeting-COST 731 mid-term seminar, pages 9–14, 2008.

[5] U. Schaettler. *A Description of the Nonhydrostatic COSMO-Model Part V: Preprocessing*. Consortium for Small-Scale Modelling, 2009.

[6] U. Schaettler, G. Doms, and C. Schraff. *A Description of the Nonhydrostatic COSMO-Model Part VII: User's Guide*. Consortium for Small-Scale Modelling, 2009.

[7] C. Schraff and R. Hess. *A Description of the Nonhydrostatic COSMO-Model Part III: Data Assimilation*. Consortium for Small-Scale Modelling, 2003.

[8] K. Stephan, S. Klink, and C. Schraff. Assimilation of radar-derived rain rates into the convective-scale model COSMO-DE at DWD. *Q. J. R. Meteorol. Soc.*, 134:1315–1326, July 2008. doi: 10.1002/qj.269.

[9] C. Sutton and T. M. Hamill. Impacts of perturbed soil moisture conditions on short range ensemble variability. In *20th Conference on Weather Analysis and Forecasting/16th Conference on Numerical Weather Prediction*, 2004.

Upscaled and fuzzy probabilistic forecasts: verification results

Zied Ben Bouallègue

Deutscher Wetterdienst (DWD), Frankfurter Str. 135, 63067 Offenbach, Germany

1 Introduction

The combined use of high resolution models and ensemble forecasting techniques is expected to be an optimal framework to provide probabilistic quantitative precipitation forecasts [3]. High resolution models simulate convective processes explicitly and ensemble forecasting techniques take into account the sources of uncertainty.

However, during a verification procedure, high resolution model forecasts suffer of the well known double penalty problem [5]. Small displacements in space or time between forecasted and observed precipitation events penalize twice the forecast in a point to point comparison. This limitation in terms of predictability should be reflected by an ensemble forecast which aims to provide information about the uncertainty of the prediction. Nevertheless, ensemble forecasts of surface variables present very often an important drawback: underdispersiveness.

The double penalty problem affects probabilistic forecasts as long as the uncertainty in position is not well represented. Then, it is still meaningful to use spatial verification techniques in order to better characterize the potential of a probabilistic forecast. Taking into account the spatial environment of each grid point forecast is a simple way to address this problem [2] and to perform scale analysis [7]. Neighborhood approaches can also be used to derive or improve existing forecasts [15, 13].

Two spatial techniques and their derived products are investigated here. First, the neighborhood method, which smoothes the probabilistic forecast, produces a fuzzy probabilistic forecast. This method is a cheap solution to enlarge the sample of an ensemble forecast. Secondly, the upscaling technique, which modifies the scale of the forecast, produces an upscaled probabilistic forecast. The upscaling procedure allows to provide information at different scales of interest.

The purpose of this report is double: firstly to evaluate the performance of an ensemble forecasting system, secondly to provide a guideline for the generation of new probabilistic products. We focus here on daily precipitation.

2 Dataset and Methodology

Dataset

The COSMO-DE-EPS is an ensemble prediction system using the convection-permitting model COSMO-DE, a 2.8 km grid-spacing configuration of the COSMO model covering the area of Germany. An experimental version of the system is used where boundary conditions and physics perturbations are applied without initial condition variation [4]. Note that the introduction of the initial condition perturbations in the new version of the system is described in [11].

The ensemble forecasts start at 00UTC and comprise 15 members. 55 days are available with this configuration during the summer of 2009 from 14 June 2009 to 30 September 2009. The precipitation observations are radar data. The observations possibly affected by bright band effects are rejected from the verification process.

The neighborhood method: fuzzy probabilistic forecasts

The first spatial technique applied here is the so-called neighborhood method, developed by [15]. Originally, this method was designed to derive probability forecasts from deterministic ones. [13] describe how to apply this method to ensemble forecasts. The processed probability at a given grid point corresponds to the mean probability within a given environment. This environment is a circular neighborhood defined by a radius of influence (called hereafter size parameter of the process).

The upscaling process: upscaled probabilistic forecasts

The second spatial procedure performed here consists of dividing the domain into squared windows. In this procedure, the length of the window is the size parameter. The maximum value of each member within each window represents the precipitation field on the new spatial scale. The upscaled probability fields are calculated from those values and refer then to an event that occurs anywhere within the defined window.

For verification purposes, other types of upscaling can be investigated. Rather than the maximum, the 90 percent quantiles within the windows (or the 95%, 99%) can be chosen to represent the realization of a member at the new spatial scale. The use of the quantiles instead of the maximum allows to alleviate the sensitivity to possible outliers in observation data and small scale variability [14].

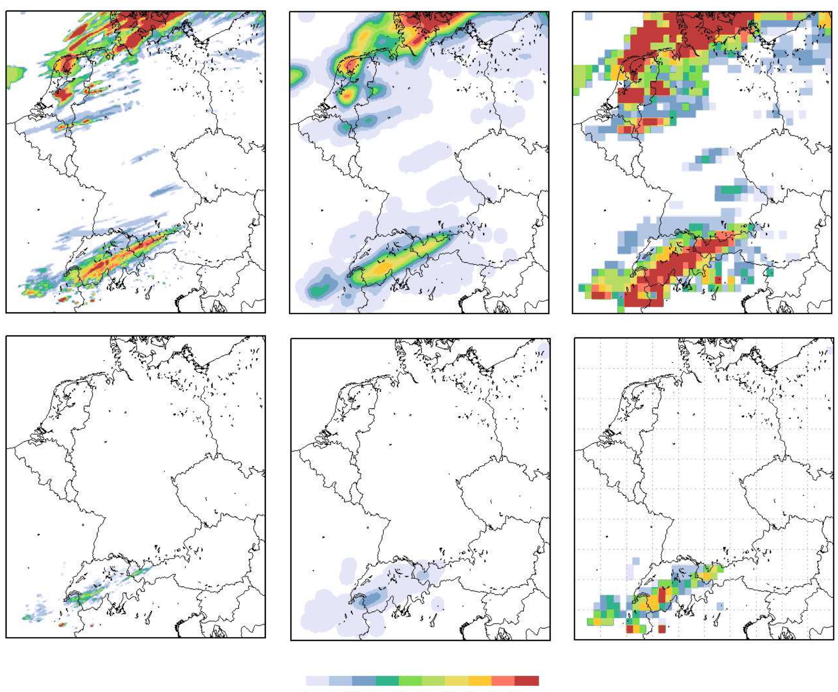

Figure 1: Example of 18 June 2009: Probability of precipitation exceeding 1mm/24h (top) and 10mm/24h (bottom). From left to right : original products, fuzzy products (the neighborhood method is applied with a size parameter of 10 grid points), upscaled products (within 10×10 grid points boxes).

Example of processed probability fields

An example of fuzzy and upscaled probabilistic forecasts is shown in Figure 1. The fuzzy probabilistic forecasts are a common application in image processing which is called low pass filtering or convolution kernel [12]. The smoothing of the original field can be done by 'eye' since all the information needed to construct the smoothed field is already contained in the original one. This is not true for the upscaled probability forecast where the spatial variability of each precipitation forecast (of each member) must be known beforehand.

3 Verification measures

Score measure

Among the numerous existing verification scores, the most common one for the evaluation of probabilistic forecasts is the Brier score (BS). It is defined as the average square difference between the forecast probability and the observation. The BS can be decomposed in three terms [10]: reliability (REL), resolution (RES) and uncertainty (UNC).

The reliability term measures the statistical consistency between the probabilistic forecast and the frequency of occurrence of the observed event given the forecast probability. The resolution term measures the capacity of the system to distinguish between event and non event. The uncertainty is a function of the observation only. Another attribute, the sharpness (SHP), which depends only on the forecast is also examined here. The sharpness is defined as the mean squared departure of the forecast probabilities from the climatological probability. It corresponds to the reliability term of a random forecast [16].

Skill score

We use Brier skill scores (BSS) for the evaluation of the impact of the processes described above. The BSS is defined as (Wilks 1995):

$$BSS = \frac{BS_{ref} - BS}{BS_{ref}}, \tag{1}$$

where BS_{ref} is the Brier score of a reference forecast, the object of the comparison. Similarly, reliability, resolution and sharpness gain are defined as:

$$G_{REL} = \frac{REL_{ref} - REL}{REL_{ref}}, \qquad G_{RES} = \frac{RES - RES_{ref}}{RES_{ref}}, \qquad G_{SH} = \frac{SH - SH_{ref}}{SH_{ref}},$$

since the reliability is counted negatively (the lower the better) and the resolution and sharpness positively (the higher the better).

The BS is not well adapted to compare forecast performance at different scales, as we do with upscaled probabilistic forecasts. In fact, its uncertainty component, which is a function of the observation only, differs from scale to scale. It is then worth to use a BSS as a measure of the performance at each scale. Mason [9] has shown that using a random forecast as reference for the calculation of the BSS leads to a measure of the 'usefulness of the information' adapted to forecasts with high sharpness. We define then the gain in skill score as:

$$G_{SS} = \frac{BSS^{ran} - BSS^{ran}_{ref}}{BSS^{ran}_{ref}},$$

where BSS^{ran} is the BSS of the upscaled forecast compared to a random forecast at the corresponding scale and BSS^{ran}_{ref} is the BSS of the original ensemble forecast compared to a random forecast at the original scale.

Amplitude distribution

We use in this study two more verification measures. The first one focuses on the amplitude distributions. The discrepancy from uniformity (D) measures the deviation from a uniform rank histogram. It is defined as [1]:

$$D = \sum_{i=1}^{K+1} \left| p_i - \frac{1}{K+1} \right| ,$$

where K is the number of members and p_i is the relative frequency of rank i. This measure summarizes the information contained in a rank histogram. In other words, it is an estimation of the fit between forecasted and observed amplitude distributions. A value of 0 indicates a flat histogram. This measure is applied hereafter to the probability integral transform (PIT) histogram, equivalent to the rank histogram in probability space [6].

Spatial distribution

The second tool allows spatial structure analysis: the empirical (semi-)variogram. It is complementary to the first one since an amplitude distribution conveys no information about the spatial structure of a field. The empirical variogram is a well known function of geostatistics which is also commonly used for meteorological applications (see Marzban and Sandgathe [8] and references therein). It can be seen as a tool to gauge the texture of a field. It is defined as:

$$\gamma(y) = E\left(|z(i) - z(j)|^2\right) ,$$

where $z(i)$ is the value of the field at a location i, y is the distance between the points i and j and E is the expected value operator. The variogram quantifies the spatial extent of correlation.

4 Results and Discussion

Fuzzy probabilistic forecasts

We investigate the impact of the neighborhood method in function of its size parameter. First, we compare the processed fields to the original probabilistic forecast in terms of accuracy, sharpness, reliability and resolution. The original probabilistic forecast is the reference for skill scores and gain calculation.

The general impact of the neighborhood method is shown in Figures 2(a) and 2(b). The method allows to improve the score and we note that an optimal size parameter exists in terms of BS. The optimum size parameter is similar for all the thresholds, around 40 grid points. On the other hand, the sharpness decreases linearly with the radius of influence. Figures 2(c) and 2(d) focus on the two main attributes of the forecast: reliability and resolution. Fuzziness slightly increases the resolution but has a large positive impact on the reliability. We can also note that the maximum gain in resolution is reached for smaller size parameters compared to the maximum gain in reliability.

To go further in the description of the neighborhood method impact, we compare the amplitude distribution of the processed fields and the observation distribution. The discrepancy from uniformity is shown in Figure 3(a). The fit between the amplitude distributions is improved and has an optimum for a size parameter around 40 grid points. The neighborhood method enlarges the spatial spread and has a positive impact on the pointwise amplitude distribution.

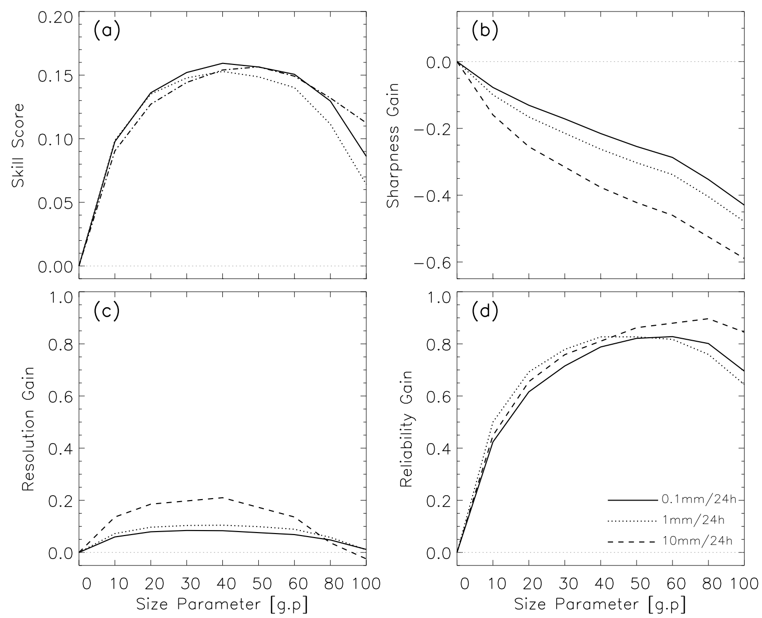

Figure 2: (a) Brier skill score, (b) sharpness gain, (c) resolution gain and (d) reliability gain in function of the neighborhood method size parameter (in grid points). The reference for the skill and gain calculation is the original probabilistic forecast.

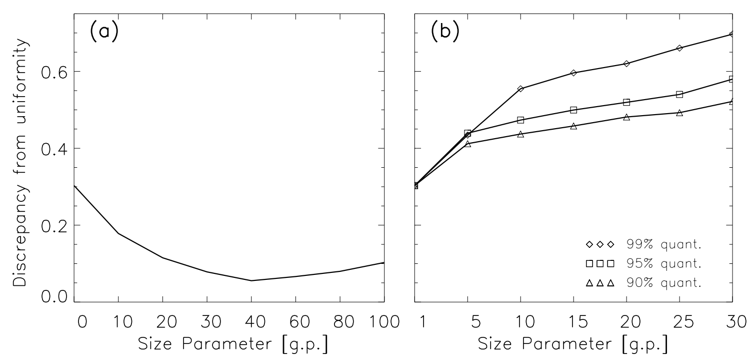

Figure 3: Discrepancy from uniformity (a) in function of the size parameter (in grid points) of the neighborhood method and (b) for the upscaling processes.

In order to highlight the reason of the improvement due to the application of the neighborhood method, we analyze the spatial distribution of the original error fields. The error is defined as the absolute difference between the observation and the original probabilistic forecast. The empirical variogram in Figure 4(a) represents the spatial correlation of this error. We note that above 40 grid points the spatial correlation of the error is no more significant. The neighborhood method introduces spatial correlation in the probability field (and then in the uncertainty representation) that corresponds to the spatial correlation of the original probabilistic forecast error.

Considered as products, we have finally to quantify the usefulness of the fuzzy probabilistic forecast compared to cheaper solutions. The reference for the computation of the BSS is no more the raw original probabilistic forecast but the deterministic forecast. To make a fair comparison, the smoothing is contemporarily applied to the reference and to the probabilistic forecast. Figure 5(a) shows that the BSS tends to zero in this case. The information within a

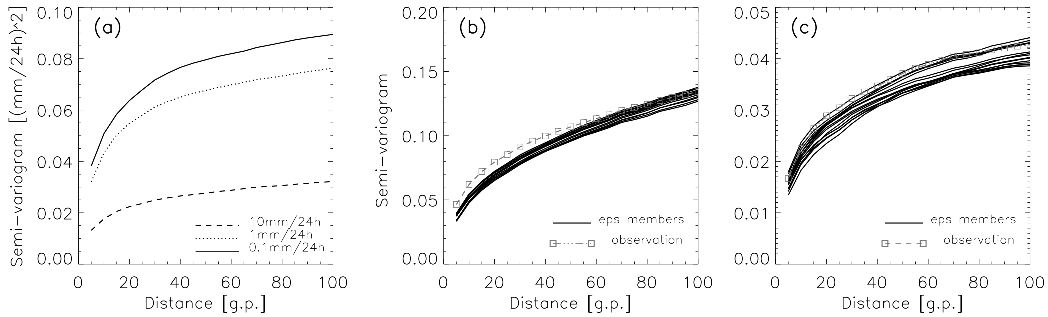

Figure 4: (a) Empirical semi variogram of the absolute difference between probabilistic forecast and binary observation in function of the distance (in grid points). Empirical semi variogram of binary precipitation fields defined with a threshold of (b) 0.1mm/24h and (c) 10mm/24h.

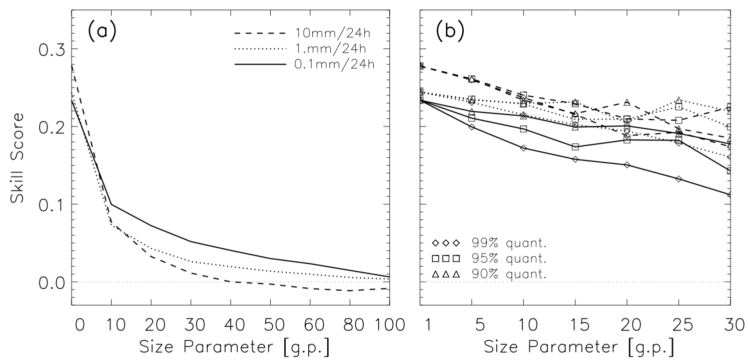

Figure 5: Brier skill scores in function of the size parameters (in grid points) of (a) the neighborhood method and (b) the upscaling process. The reference is the deterministic forecast. The neighborhood method or the upscaling process is applied contemporarily to the probabilistic forecast and to the reference.

fuzzy ensemble forecast is not useful if the filtering process is too strong: the same information can be provided by a cheaper fuzzy deterministic forecast.

Upscaled probabilistic forecasts

We analyze now the results of the probabilistic forecast at different scales. Three types of upscaling are compared using the 90%, 95% and 99% quantiles within a window as representative of the variable at the new scales. We first comment the results independently of the choice of quantile.

The impact of the upscaling processes is shown in Figure . The reference for the gain calculation is the probabilistic forecast at the model grid resolution. In Figure (a), we see an improvement of the forecast (excepted for the lowest threshold) and in Figure (b) an increase of the sharpness with the size parameter. The impact of the upscaling is especially remarkable for high thresholds. On Figure (c), the upscaling has a clear positive impact on the resolution term for medium and high thresholds. The benefit of the upscaling in terms of resolution increases with the threshold. In terms of reliability (Figure (d)), a loss of quality is registered for all the thresholds.

The spread reduction is intrinsic to the upscaling technique. The uncertainty concerning the exact location of an event is reduced as the size parameter increases. The width of the forecast amplitude distribution is then reduced. The discrepancy from uniformity measured in Figure 3(b) shows that the observations tend to fall more often outside of the forecasts distribution

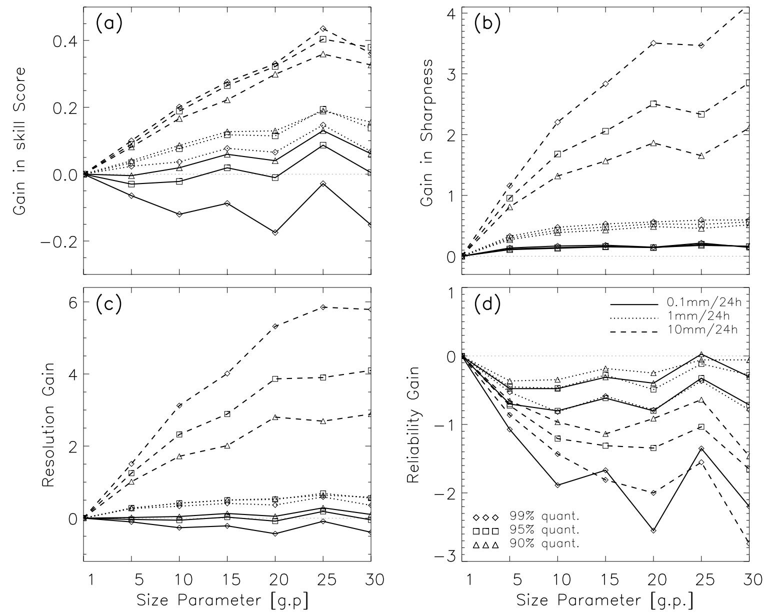

Figure 6: (a) Gain in BSS, (b) sharpness gain, (c) resolution gain and (d) reliability gain in function of the upscaling processes size parameter (in grid points). The gains compare the upscaled probabilities to the original forecast.

as the scale increases. The spread reduction is too severe compared with observation and induces then a more pronounced underdispersive situation.

The general usefulness of the upscaled forecast is investigated comparing the upscaled probabilistic forecasts to upscaled deterministic forecasts. We see in Figure 5 that the BSS is positive for all the upscaling size parameters and for all the thresholds. The upscaled probabilistic forecasts at larger scales can then be considered as better than the deterministic upscaled forecast.

Finally, we can make some remarks concerning the impact of the choice of quantile. The results for the 90%, 95% and 99% quantiles show more significant differences for low thresholds. The spatial variability of the individual members and the observation are then analyzed. Figures 4(b) and 4(c) show the empirical variograms of the ensemble members and observation binary fields defined by two thresholds (respectively 0.1 and 10 mm/24h). For the lowest threshold, we note important differences between the observation spatial variability and the spatial variability of the different members. Small structures of low intensity are described within the radar observation fields which are not represented in the forecasts. This situation can explain the sensitivity of the results to the choice of quantile.

6 Summary and Recommendation

We investigated two spatial methods applied to ensemble probabilistic forecasts. Verification results have been shown for daily precipitation during a summer period. A guideline for the use of those methods to generate new probabilistic products can be drawn.

Concerning the application of the neighborhood method, an optimal size parameter in terms of BS was found. However, we noted that this optimal solution (40 grid points) leads to an important loss of sharpness and the resulting forecast has a similar quality as a smoothed deterministic forecast. Since the maximum gain, specially in terms of resolution, is realized at the beginning of the environment extension, we advocate the use of a smaller radius of influence. For example, a size parameter of 10 grid points maximizes the gain in resolution and improves the reliability up to a factor of 2.

Concerning the upscaling procedure, the choice of the size parameter relies on the expectation of the user. For all investigated scales, the upscaled probabilistic forecast performs better than the upscaled deterministic forecast. Moreover, for high thresholds, the forecast resolution is improved after upscaling compared to the original fine scale probabilistic forecast. The better discrimination at large scales between event and non event is then of high relevance for decision making. The negative impact of the upscaling on the reliability can be solved later by the application of a calibration technique.

Acknowledgements

We thank S. Theis and C. Peralta for very useful comments and remarks.

References

[1] V. J. Berrocal, A. E. Raftery, and T. Gneiting. Combining Spatial Statistical and Ensemble Information in Probabilistic Weather Forecasts. *Monthly Weather Review*, 135:1386, 2007.

[2] E. E. Ebert. Fuzzy verification of high-resolution gridded forecasts: a review and proposed framework. *Meteorological Applications*, 15:51–64, March 2008.

[3] J. M. Fritsch and R. E. Carbone. Improving Quantitative Precipitation Forecasts in the Warm Season: A USWRP Research and Development Strategy. *Bull. Amer. Met. Soc.*, 85:955–965, July 2004.

[4] C. Gebhardt, S. E. Theis, M. Paulat, and Z. Ben Bouallègue. Experimental ensemble forecasts of precipitation based on a convection-resolving model. *Accepted for publication in Atmos. Res.*, 2010.

[5] E. Gilleland, D. Ahijevych, B. G. Brown, B. Casati, and E. E. Ebert. Intercomparison of spatial forecast verification methods. *Weather and Forecasting*, 24(5):1416–1430, 2009.

[6] T. Gneiting, A. E. Raftery, A. H. Westveld, and T. Goldman. Calibrated Probabilistic Forecasting Using Ensemble Model Output Statistics and Minimum CRPS Estimation. *Monthly Weather Review*, 133:1098, 2005.

[7] D. Harris, E. Foufoula-Georgiou, K. K Droegemeier, and J. J. Levit. Multiscale statistical properties of a high-resolution precipitation forecast. *Journal of Hydrometeorology*, 2(4):406–418, 2001.

[8] C. Marzban and S. Sandgathe. Verification with Variograms. *Weather and Forecasting*, 24:1102, 2009.

[9] S. J. Mason. On Using “Climatology” as a Reference Strategy in the Brier and Ranked Probability Skill Scores. *Monthly Weather Review*, 132:1891, 2004.

[10] A. H. Murphy. A New Vector Partition of the Probability Score. *Journal of Applied Meteorology*, 12:595–600, June 1973.

[11] C. Peralta and M. Buchhold. Initial condition perturbations for the COSMO-DE-EPS. *Submitted to COMSO newsletter*, 2011.

[12] N. M. Roberts and H. W. Lean. Scale-Selective Verification of Rainfall Accumulations from High-Resolution Forecasts of Convective Events. *Monthly Weather Review*, 136: 78, 2008.

[13] C. S. Schwartz, J. S. Kain, S. J. Weiss, M. Xue, D. R. Bright, F. Kong, K. W. Thomas, J. J. Levit, M. C. Coniglio, and M. S. Wandishin. Toward Improved Convection-Allowing Ensembles: Model Physics Sensitivities and Optimizing Probabilistic Guidance with Small Ensemble Membership. *Weather and Forecasting*, 25:263, 2010.

[14] M. S. Tesini, C. Cacciamani, and T. Paccagnella. Statistical properties and validation of Quantitative Precipitation Forecast. *COSMO newsletter*, 10:45–54, 2010.

[15] S. E. Theis, A. Hense, and U. Damrath. Probabilistic precipitation forecasts from a deterministic model: a pragmatic approach. *Meteorological Applications*, 12:257–268, September 2005.

[16] D. S. Wilks. *Statistical methods in the atmospheric sciences*. Academic Press, New York, 467pp., 1995.

Evaluation of Central European and Eastern Alpine seasonal climate simulated with CCLM: double nesting vs. direct forcing techniques

Goran Georgievski, Klaus Keuler, Andreas Will and Kai Radtke

BTU Cottbus
Lehrstuhl für Umweltmeteorologie

1. Introduction

Various types of Regional Climate Models (RCMs) have been applied for dynamical downscaling of low-resolution global climate (General Circulation Model - GCM) simulations or atmospheric reanalyses for different regions of the world (see for example Fu et al. 2005; Jacob et al. 2007; Rockel and Geyer, 2008). With increasing computational power the grid size of RCMs is decreasing, but new issues concerning the use of nested RCM as a climate downscaling technique arises. Many of them have received considerable attention in the scientific literature (Sun and Ward (2007) and references therein). For example, physical parameterization schemes were designed to mimic unresolved processes on the coarser GCM grid (50 - 200 km) and they are not adequate for convection permitting ($\sim 2km$) RCM simulations, but most of the RCMs apply the same parameterization schemes as the GCMs. Another example is the sensitivity to the spatial resolution and temporal update of lateral boundary conditions. Denis et al (2003) found that satisfactory results are achieved when spatial resolution is degraded by up to factor of 12, but their nested experiment was at 45 km resolution and today the RCM community is going towards approaching a convection resolving scale in regional climate simulations (see Hohenegger et al. 2009. for the Cosmo Climate Local Model (CCLM) example).

At the last CCLM Assembly (September 2009, Karlsruhe) a Convection Resolving Climate Simulations (CRCS) working group was established. One of the first issues that turns out at the working group session was, if there are some standard techniques, hints, and settings how to design an experiment in order to perform high resolution (grid scale 3 km or less) climate simulations? In the frame of the Local climate Model Intercomparison Project LocMIP (Gobiet et al 2009), we have performed several experiments at $0.09^\circ(\sim 10km)$ and $0.025^\circ(\sim 2.8km)$ grid resolution. Comparison of results for two various nesting techniques (direct and double) and evaluations against their forcing fields were performed. This newsletter, together with technical documentation (namelist, run scripts, and other input and output files) available on the CCLM community web site, might be considered as a first step towards setting standard rules for convection resolving climate simulations with the CCLM model.

The article is organized as follows. Three experiments, abbreviated as CEU (Central Europe), EA1 (Eastern Alps direct nesting) and EA2 (Eastern Alps double nesting), are presented and briefly described in the next section, followed by results in section 3. Summary and outlook are provided in the final section.

2. Experimental setup

Topography and evaluation domains are shown in figure 1. Relevant namelist parameter settings of int2lm and cclm are sumarized in the tables 1 and 2, respectively. The resolution of simulation CEU is 10 km and settings are similar to the COSMO-EU (Schulz and Schättler,

2009) standard configuration used at DWD for operational weather forecast at date, with different forcing and some modification specific for climate simulations[3].

Lateral boundary conditions (LBC) are interpolated from ECMWFs integrated forecast system (IFS) dataset (Untch et al. 2006) at 3h intervals. EA1 and EA2 are simulated at 2.8 km resolution and namelist settings are similar to COSMO-DE (Baldauf et al, 2009) setup with the same climate modifications as for the 10km simulation. Lateral boundary conditions for the EA2 are interpolated from the CEU simulation at 3h intervals, so this is an example of a double nested experiment, while the EA1 is directly driven by IFS lateral boundary conditions updated every 3h (figure 2). Some differences between CEU and COSMO-EU were necessary in the preprocessing step due to the fact that lateral boundary conditions are provided by different sources (IFS and GME). The same differences also apply for EA1, EA2 simulations in comparison to COSMO-DE. The main difference between 10 km (CEU) and the 2.8 km (EA1 and EA2) simulations is that former is performed with three time level (leap-frog) scheme, while the latter utilizes the two time level (Runge-Kutta) scheme (l2tls=.TRUE.). Convection parametrization in the former utilizes Tiedtke scheme and the latter shallow convection (itype_conv=3). The grid scale precipitation (itype_gscp) scheme used for both 2.8 km simulations includes all available components (rain, snow, ice and graupel), while CEU utilize only three of them (rain, snow and ice).

All simulations are performed for two seasons: summer 2007 (May, June, July, and August - MJJA) and winter 2007/2008 (November, December, January, and February - NDJF). Analysis is performed for three evaluation domains as defined in the framework of the LocMIP project (figure 1 adopted from Gobiet et al, 2009). Domains D10 and L10 (land only inside D10 domain) are chosen since they represent the entire Alpine region. Domains D3 and D1 represent regions of interest for which high-resolution observations should be available in the near future.

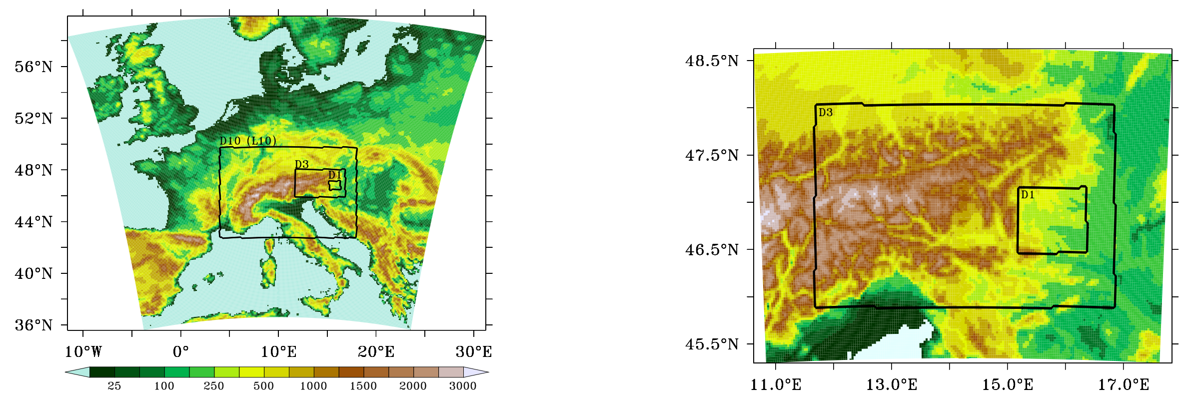

Figure 1: Model domains with topography and evaluation domains for experiment CEU (top) and experiments EA1 and EA2 (bottom). Results will be discussed for the 3 black rectangular evaluation domains: L10 (land only inside D10 domain), D3 and D1. The largest domain L10 only exist for the CEU experiment.

[3]There are two main differences between climate simulations and weather prediction: (*i*) the discretization of the soil layers and (*ii*) the CO_2 concentration. Usually 9 soil layers with grid stretching (ratio between two neighbouring layers) 2 are used in climate simulation instead of 7 layers in weather prediction mode with grid stretching 3 and CO_2 concentration is set to default 360 ppm constant value, while in climate mode equivalent CO_2 increasing in time is considered.

experiment	CEU	EA1	EA2
LBC and SST data	IFS 0.225°	IFS 0.225°	CEU 0.09°
lmgrid	$252 \times 260 \times 40$	$192 \times 132 \times 50$	$192 \times 132 \times 50$
hincbound	3h	3h	3h
irefatm	1	2	2
ivctype	1	2	2
dlon, dlat	0.09°	0.025°	0.025°
lvertwind_ini	T	T	T
lvertwind_bd	F	F	F
lprog_qi	T	T	T
lprog_qrqs	F	F	T
lprog_qg	F	F	F
lprog_rho_sno	F	F	F
lboundaries	F	F	F
itype_w_so_rel	1	1	1
itype_t_cl	1	1	0
itype_rootdp	3	3	3
lmulti_layer_lm	T	T	T
lmulti_layer_in	F	F	T
lbdclim	T	T	T
lforest	T	T	T
lsso	T	F	F
l_cressman	T	T	T

Table 1: Relevant int2lm namelist parameter settings. Preprocessing is performed with int2lm_1.9_clm3 version.

experiment	CEU	EA1	EA2
dt	60s	25s	25s
l2tls	F	T	T
lhdiff_mask	F	T	T
ldyn_bbc	F	T	T
rlwidth	Not used	30000 m	30000 m
irunge_kutta	Not used	1	1
lgsp	T	T	T
lprogprec	T	T	T
itype_conv	0	3	3
lconv_inst	F	T	T
ltype_gscp	3	4	4

Table 2: Relevant cclm namelist parameter settings. All simulations are performed with cclm_4.8_clm6 version.

3. Precipitation and temperature at 2m

We analysed and evaluated the monthly mean air temperature at 2m (T_2m) and the monthly sum of precipitation averaged over the evaluation domains described in the previous section. The results are compared with three reference data sets: (*i*) IFS, (*ii*) E-OBS (Haylock et al, 2008) and (*iii*) GPCC (precipitation only for summer season and November to December 2007) data (see Schneider et al 2008 for the description of the GPCC dataset).

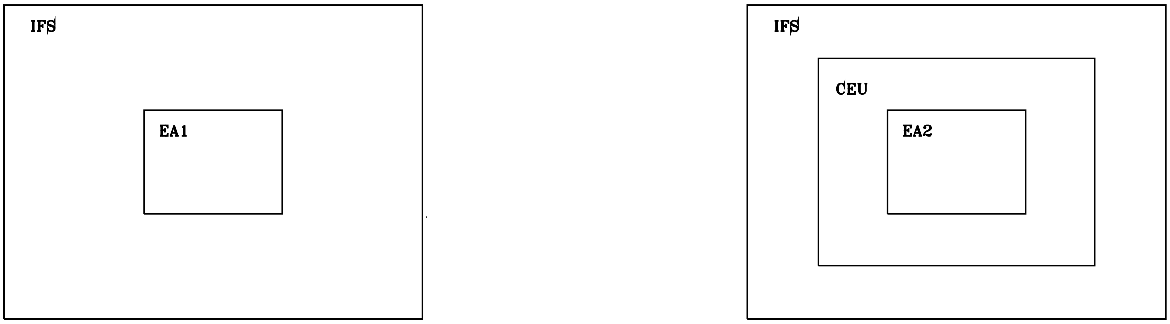

Figure 2: Nesting schemes: direct nesting scheme (on the left hand side) IFS data are used for forcing EA1 experiment; double nesting scheme (on the right hand side) IFS data are used for forcing CEU experiment, and then CEU simulation is used as the forcing for EA2 experiment.

Figure 3 shows monthly precipitation sums (left), and T_2m monthly means (right). Both averaged over L10 evaluation domain (figure 1, top). During the summer months (MJJA) CEU has less ($\sim 15mm/month$) precipitation than the IFS dataset, but it has the same amount as GPCC interpolated observed precipitation for May and August, slightly more ($\sim 20mm/month$) in June, and less ($\sim 10mm/month$) in July. In total (4 month sum) CEU generates only 13 mm less than GPCC and is closer to the climatological observation than IFS analysis which has 40 mm higher value than GPCC. The other observational dataset E-OBS is the driest one, up to 20 mm/month less precipitation then GPCC. During winter CEU is up to $20mm/month$ wetter than IFS dataset and even $25-30mm/month$ than the observed GPCC (November and December only) precipitation, and up to $40mm/month$ wetter than E-OBS. During February, the difference between CEU and IFS reduces to $5-10mm/month$, but this is still $\sim 20mm/month$ more than E-OBS, while the GPCC precipitation was not available for January and February. CEU obtained T_2m averaged over the L10 domain shows a small cold bias of up to $1K$ during the July and most of the winter months (November, January and February) in comparison to IFS driving data. In comparison with E-OBS observation, CEU has even more pronounced cold bias during winter since E-OBS is about $0.5K$ warmer than IFS dataset. During summer, there is no significant difference between IFS and E-OBS dataset.

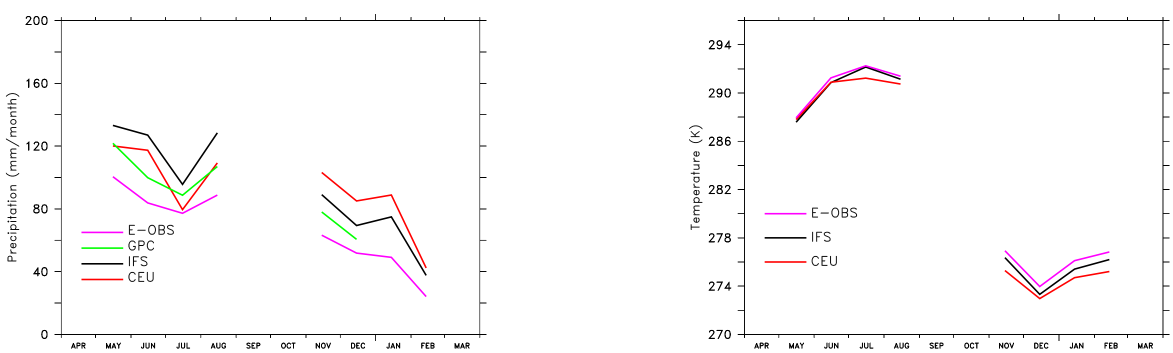

Figure 3: Precipitation in $mm/month$ (left) and T_2m in K (right) for the L10 domain (land points of D10, figure 1).

Figure 4 shows the same results for D3 domain. Both high-resolution simulations (EA1 and EA2) show a wet bias in summer compared to their forcing data (IFS and CEU, respectively) and both observational (GPCC and E-OBS) datasets. In extreme case the bias is up to $\sim 90mm/month$ (June compared to E-OBS). Such a huge discrepancy from reference data sets, especially compared to CEU simulation, indicates a considerable influence of the different settings (namelist parameters, table 2, domain and resolution) of the two high-resolution simulations compared with the CEU simulation. CEU fits nicely between the two (IFS and GPCC) reference datasets in May and June, but has a dry bias ($\sim 30mm/month$) in July and fits with E-OBS dataset. In August CEU precipitation is the same as GPCC reference data. Similar as for the L10 domain, E-OBS interpolated observation presents the driest climate for the D3 domain. During the winter months both high-resolution simulations precipitation are more or less the same as the precipitation of their corresponding forcing (EA1 driven directly by IFS and EA2 driven by CEU) indicating a substantial influence of convection on the wet summer bias. Since IFS precipitation fits better with both observational data sets (GPCC and E-OBS), EA1 (IFS driven simulation) shows better results than EA2 (double nested, CEU driven simulation). CEU performs similar as on L10 domain, it has a dry bias during summer and a wet bias during winter compared with IFS data. Similar as before T_2m (figure 4, right) of CEU has a weak cold bias of about $1K$ during July, November and February and agrees quite well with IFS data during the other months. EA2 shows warm bias compared to its forcing data (CEU), but fits better with IFS data. EA1 is slightly warmer than IFS forcing data. E-OBS is slightly warmer than IFS, therefore both high-resolution simulation during summer (especially EA1) are in good agreement with E-OBS.

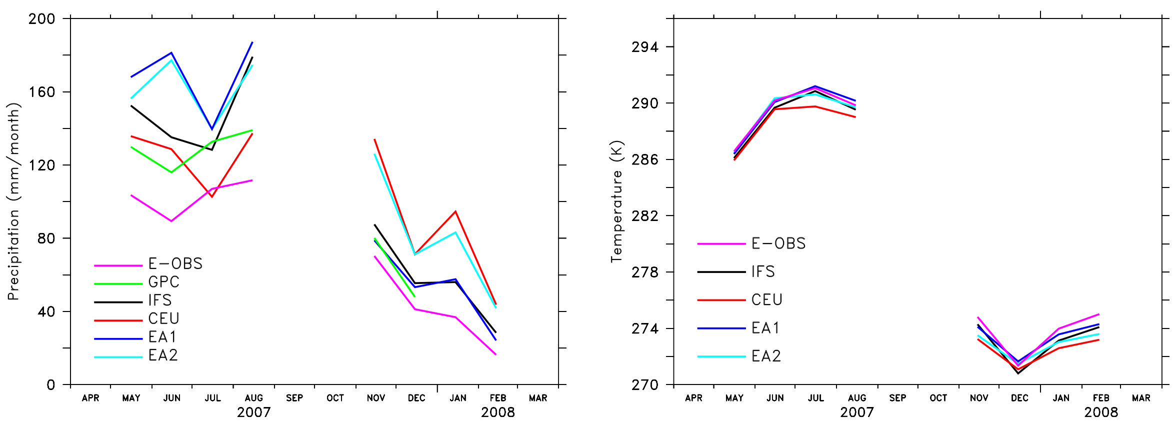

Figure 4: Precipitation in $mm/month$ (left) and T_2m in K (right) for the D3 domain.

Results for D1 domain (figure 1) are shown in figure 5. During summer both high-resolution simulations produce more precipitation than the simulations providing the lateral boundary conditions (forcings data), with exception of EA1 in May, which is a bit dryer than IFS. However, CEU has a strong dry bias compared to its IFS forcing, therefore EA2, although wetter than its forcing (CEU), is drier than IFS and it shows about $50mm/month$ less than GPCC in July but exactly the same amount of precipitation in August. In total, during summer only directly nested high-resolution run EA1 produces more precipitation than IFS. However, note the large deviation between IFS and GPCC. Except for July IFS has much more precipitation than GPCC. E-OBS is up to $30mm/month$ dryer than GPCC interpolated observation. During winter EA1 has a dry bias compared to its IFS forcing. EA2 has equally distributed their positive and negative discrepancies from its forcing CEU data, but it is in very good agreement with IFS data. EA1 is in good agreement with E-OBS in November, January and February. Temperature shows similar distributions as for the D3 domain, except that D1 is about 3K warmer in summer, and about 2K in winter. In general it can be seen that during summer EA1 and EA2 show similar climate to each other, while during the winter each highly resolved simulation is more similar to their corresponding forcing. This is probably due to the predominating influence of large scale dynamics on the climate during the winter months, while during the summer local convective processes predominate the climate in the region

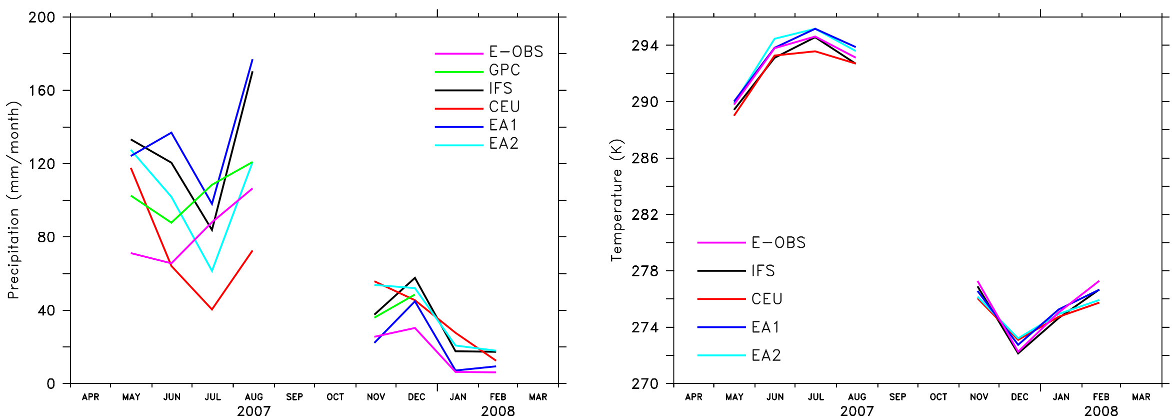

Figure 5: Precipitation (left) in $mm/month$ and T_2m in K (right) for the D1 domain.

The phenomenon can be even better seen on the spatial distribution of temperature and precipitation, therefore, in addition to the area-averaged values of the evaluation domains, the geographical distribution of model results compared to their forcing is presented. Our focus is on continental Central Europe, especially the Alpine region and the mid-range mountains. Figure 6 depicts the difference fields between CEU and IFS forcing for seasonal means of JJA 2007 and DJF 2007/2008. Summer is characterized with increased precipitation in CEU compared with IFS in the central region north of the Alps and along the eastern and above the ocean along the northern border of the domain. CEU produces a considerable decrease (more than $2mm/day$) in precipitation in flatland, especially in the Po valley and the Panonian basin. A decrease can also be seen along the north and north western coastlines of the Baltic Sea and the Atlantic ocean. During the winter CEU produces more precipitation in the northern and north-eastern region. Sea-land contrast can be seen especially along the southern Scandinavian coastline. Above the British island sea-land contrast and a better presentation of topographic features interferes and both effects contribute to the different precipitation pattern between the two models. Some features typical for better presentation of surface properties i.e. the downscaling effect could be also seen for some mid-range mountains and intermediate watersheds. See for example the region around Rhone valley, Vosges, and Jura mountain, or the region of the Pyrenees, together with the watershed of Ebro and Garone rivers. Furthermore, orographic precipitation (see Roe, 2005, for a comprehensive review) i.e. the shadowing effect behind Dinaric Alps and Apennine especially during winter seems to be by far better represented with CEU model due to a better horizontal resolution. Higher precipitation during winter on the south-eastern flank of the Alps is probably due to overemphasized mesoscale processes above the Adriatic Sea and corresponding cyclonic circulation in the CEU compared to IFS model. This is also in agreement with results from our work in progress, evaluation of CCLM simulations with IFS and Tiedke convection scheme. However, to make final conclusion, which model provide a better climate reproduction, a high-resolution observations are needed.

Although a height correction is applied to the temperature fields, topographic signatures could be still seen in the temperature difference distribution. Mountain ranges which are better resolved in CEU and therefore higher, are colder than their counterparts in the IFS forcing dataset. During the summer, the Po watershed and the Pannonian basin are warmer than the corresponding areas in the IFS dataset. All of the central, north, and north-eastern Europe is characterized by a cold bias of up to $1.5K$ in the CEU simulation. During winter the situation is quite similar. One exception is the Po watershed which is colder then the corresponding area in the IFS dataset, indicating different regional and seasonal dynamics. Again, high-resolution observations are needed in order to make final conclusion which of the models provided a better presentation of the real conditions during the specific season.

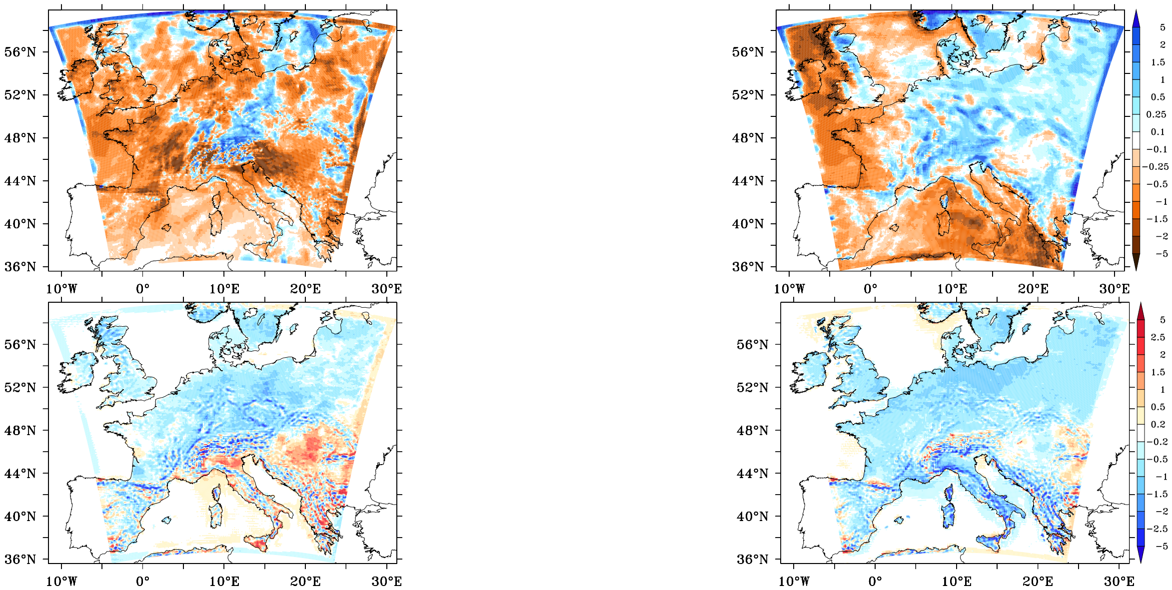

Figure 6: Precipitation (top) difference between CEU and IFS in mm/day and T_2m in K (bottom) for JJA 2007 (left) and DJF 2007/2008 (right).

The uncertainty caused by the nesting model technique (direct versus double nesting) is presented by the comparison of EA1 versus EA2 simulations (figure 7). The comparison of precipitation fields between both EA experiments indicates that a direct nested simulation overestimates precipitation at lateral boundaries, resulting especially during the winter in a dryer interior of the domain. During winter, both direct and the double nested simulations resemble features of their driving simulations. During summer overestimated precipitation in the direct simulation is limited only to the western and northern lateral boundary and it does not influence the results in the interior of the domain. This seasonaly different behavior is due to predominating influence of large scale dynamics on the climate during the winter months, while during the summer local convective processes predominate the climate in the region. A similar conclusion follows from the comparison of temperature field differences (figure 7, bottom) for summer and winter. It can be seen that the two simulations during the summer exhibit negligible difference in the interior of the domain, while during the winter differences are up to 1K. Problems for the EA1 experiment in the lateral boundary zone can be seen in the spatial distribution of total precipitation, especially during the winter (figure 8). For the EA1 experiment precipitation amount reaches extreme value of about 90 mm/day in the western lateral boundary zone (10.81E, 45.77N) and there are similar phenomana along the southern and northern domain border, while for the EA2 experiment precipitation values are not above 10 mm/day. This feature is probably due to the strong transition in topography fields from coarse ($\sim 25km$) to fine ($\sim 2.8km$) resolution resulting in a strong artificial vertical uplift and therefore an overestimated precipitation in that region. However, this still needs a further examination.

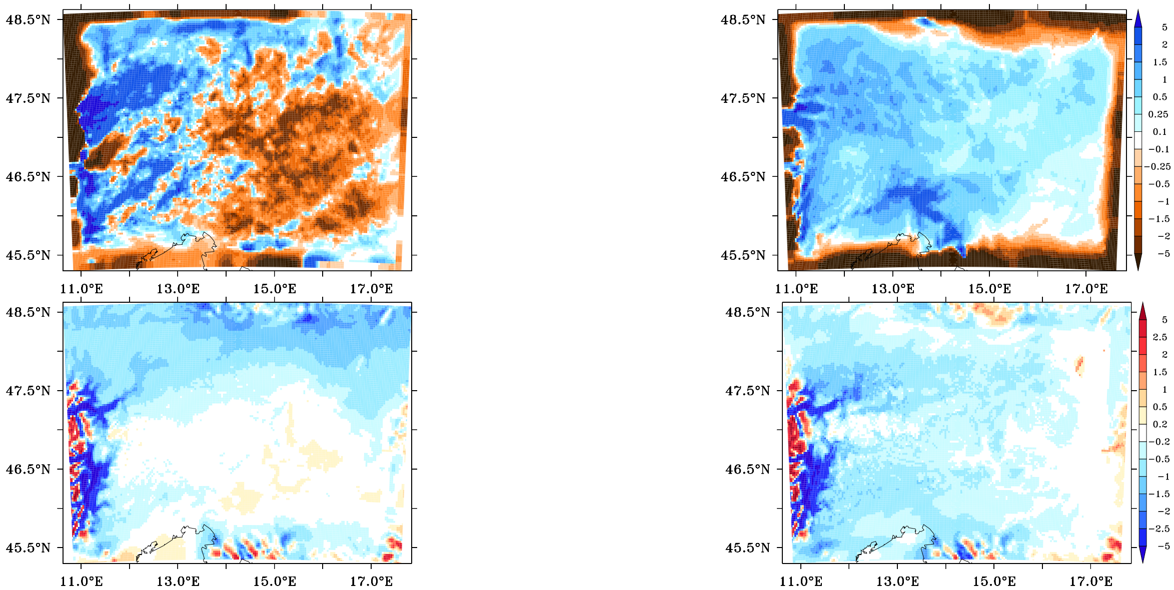

Figure 7: Precipitation (top) difference between EA2 and EA1 in mm/day and T_2m in K (bottom) for JJA 2007 (left) and DJF 2007/2008 (right).

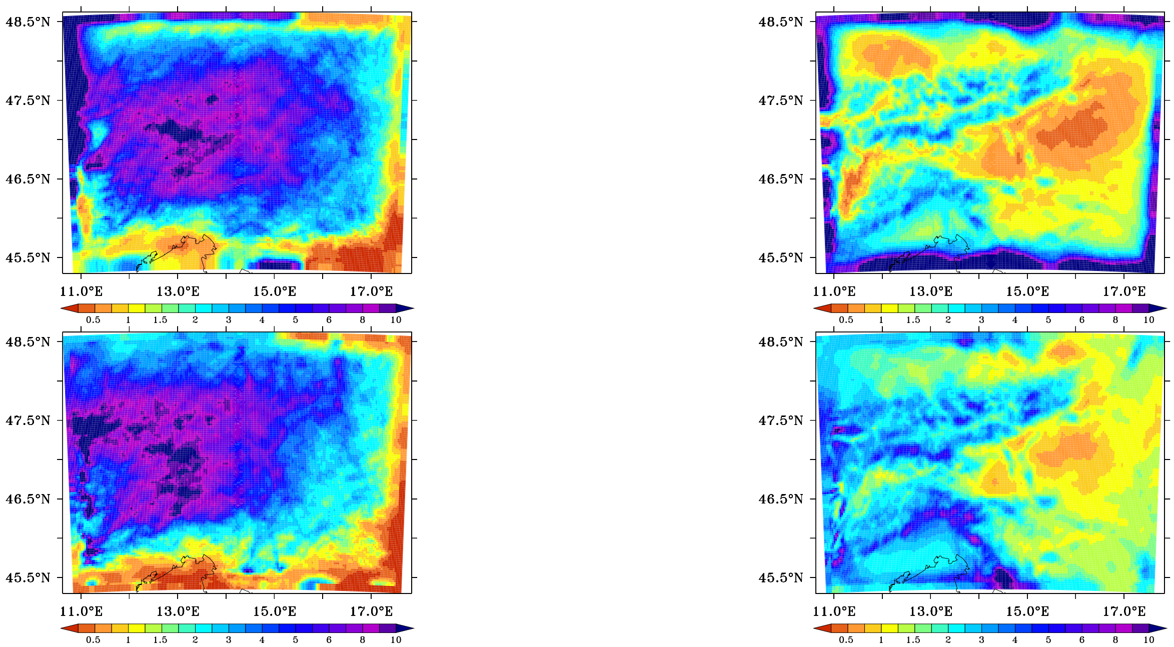

Figure 8: Total precipitation EA1 (top) and EA2 (bottom) in mm/day and for JJA 2007 (left) and DJF 2007/2008 (right).

4. Summary and Outlook

Results from three CCLM simulations have been presented and compared with available observational data sets. These results proved to be acceptable, since they are in the range of internal variability of the model. The simulation at 10 km for Central Europe (CEU) indicates that the model even in this version has some problems already known from previous versions, that is in particular a cold bias of about $1K$ compared with driving fields of IFS data. In the precipitation field, a dry bias of about $20mm/month$ is the predominate feature during summer and a wet bias in winter of similar amount if compared with the IFS data. However, perhaps the most striking feature of the total precipitation comparison are the discrepancies between all three reference data sets (the wettest IFS up to $40mm/month$ more than E-OBS, and GPCC up to $20mm/month$ more than E-OBS) and the fact that during summer CEU simulation fits in the middle of the range and agrees quite well with GPCC data set. However, during winter CEU is the wettest one. Two models (CEU and IFS) provide different seasonal means as a consequence of the dynamical downscaling (better surface features presentation within CEU simulation) and different physical parameterization (for example convection scheme).

The analysis of the two high-resolution simulations indicate that averaged temperatures do not deviate much from their forcing fields. However, total precipitation shows significant deviation from all the other datasets. In D3 domain during summer, both EA simulations have about the same amount of precipitation, up to $90mm/month$ more than E-OBS. During winter EA2 is wetter than EA1, and the former has about the same amount of precipitation as its driving CEU simulation, and the latter has about the same amount of precipitation as its driving IFS re-analysis. An explanation for that is probably the predominant role of local convective processes during summer, and therefore similar performance of the two high resolution simulations with the same physical parametrizations, while during winter large scale dynamics dominate the climate system and therefore driving fields play a predominat role for the nested model performance. However, both EA simulations are wetter than interpolated observations (E-OBS and GPCC). When interpreting results in D1 domain, it has to be taken into account that this domain contains less then 10 grid points of coarse resolution reference data sets. However, double nested (EA2) simulation is drier than EA1 in summer and wetter in winter. The comparison of the precipitation fields of the two EA simulations indicates that the transition between the double nested and its driving simulation is much smoother than the transition between the direct nested and its driving simulation.

Although, the benefit of the double nesting can be seen against the results with direct driving (smoother transition and dynamical adaptation of forcing fields in the lateral boundary zone), it remains an open issue which of the two EA simulations gives a better presentation of climate since appropriate high resolution observations are not yet available. According to Denis et al (2003), satisfactory results for direct nesting are achieved when spatial resolutions degraded by up to a factor of 12 are imposed between forcing data and the nested experiment. In our case, the factor between IFS and EA1 resolution is 9, below but very close to the suggested critical value. Further examinations and new experiments are needed in order to confirm the factor of 12 or to provide a new critical value of the resolution factor between driving and nested simulation's resolutions. Until then, we suggest to perform double nesting when the ratio between forcing data and simulation is bigger than 9.

References

[1] Baldauf, M., J. Förstner, S. Klink, T. Reinhardt, C. Schraff, A. Seifert, K. Stephan (2009): Kurze Beschreibung des Lokal-Modells Kürzestfrist COSMO-DE und seiner Datenbanken auf dem Datenserver des DWD, *Deutscher Wetterdienst* (http://www.dwd.de)

[2] Denis, B., R. Laprise, D. Caya (2003): Sensitivity of a regional climate model to the resolution of the lateral boundary conditions.*Clim Dyn*,**20:107-126**

[3] Frei, C., C. Schär, 1998: A precipitation climatology of the Alps from high-resolution rain-gauge observations.*Int. J. Climatol.* **18: 873-900**

[4] Fu, C., S. Wang, Z. Xiong, W.J. Gutowski, D.K. Lee, J.L. McGregor, Y. Sato, H. Kato, J.W. Kim, M.S. Suh, 2005: Regional Climate Model Intercomparison Project for Asia. *Bull. Amer. Meteor. Soc.*, **86**, 257266.

[5] Gobiet, A., H. Truhetz and LocMIP contributors, 2009: Local climate Model Intercomparison Project (LocMIP). Wegener Center for Climate and Global Change, *University of Graz* (http://www.uni-graz.at/en/igam7www.htm)

[6] Haylock, M.R., N. Hofstra, A.M.G. Klein Tank, E.J. Klok, P.D. Jones, M. New. 2008: A European daily high-resolution gridded dataset of surface temperature and precipitation. *J. Geophys. Res (Atmospheres)*, **113**, D20119, doi:10.1029/2008JD10201

[7] Hohenegger, C., P. Brockhaus, C.S. Bretherton, C. Schär, 2009: The Soil Moisture Precipitation Feedback in Simulations with Explicit and Parameterized Convection. *J. Climate*, **22**, 5003-5020.

[8] Jacob D, Bärring L, Christensen OB, Christensen JH, de Castro M, Déqué M, Giorgi F, Hagemann S, Hirschi M, Jones R, Kjellström E, Lenderink G, Rockel B, Sánchez E, Schär C, Seneviratne SI, Somot S, van Ulden A, van den Hurk B (2007): An inter-comparison of regional climate models for Europe: model performance in present-day climate. *Clim Change* **81:3152**

[9] Rockel, B., B. Geyer, 2008: The performance of the regional climate model CLM in different climate regions, based on the example of precipitation, *Meteorol. Z.*, Volume 12, Number 4, **487-498**

[10] Roe, G.H., 2005: Orographic precipitation. *Annual Review of Earth and Planetary Sciences* Vol. 33: **645-671**

[11] Schneider, U, T. Fuchs, A. Meyer-Christoffer, B. Rudolf (2008): Global Precipitation Analysis Products of the GPCC. Global Precipitation Climatology Centre (GPCC), DWD, Internet Publikation, 1-12. (pdf 1414 KB). Updated version of Rudolf, B. (2005): Global Precipitation Analysis Products of the GPCC. DWD, Klimastatusbericht 2004, 163-170. ISSN 1437-7691, ISSN 1616-5063 (Internet www.ksb.dwd.de), ISBN 3-88148-402-7

[12] Schulz, J-P. U. Schättler (2009): Kurze Beschreibung des Lokal-Modells Europa COSMO-EU (LME) und seiner Datenbanken auf dem Datenserver des DWD, *Deutscher Wetterdienst* (http://www.dwd.de)

[13] Sun, L., M. N. Ward, 2007: Climate Downscaling: Assessment of the Added Values Using Regional Climate Models. *In:* Climate Prediction and Agriculture - Advances and Challenges (editors: M. V. K. Sivakumar and J. Hansen), Chapter 2, **15-29**. Springer Berlin Heidelberg

[14] Untch, A, M. Miller, M. Hortal, R. Buizza, P. Janssen, 2006: Towards a global meso-scale model: The high-resolution system T799L91 and T399L62 EPS, *ECMWF Newsletter No. 108* Summer 2006.

List of COSMO Newsletters and Technical Reports

(available for download from the COSMO Website: `www.cosmo-model.org`)

COSMO Newsletters

No. 1: February 2001.

No. 2: February 2002.

No. 3: February 2003.

No. 4: February 2004.

No. 5: April 2005.

No. 6: July 2006; Proceedings from the COSMO General Meeting 2005.

No. 7: May 2008; Proceedings from the COSMO General Meeting 2006.

No. 8: August 2008; Proceedings from the COSMO General Meeting 2007.

No. 9: December 2008; Proceedings from the COSMO General Meeting 2008.

No.10: January 2010; Proceedings from the COSMO General Meeting 2009.

COSMO Technical Reports

No. 1: Dmitrii Mironov and Matthias Raschendorfer (2001):
Evaluation of Empirical Parameters of the New LM Surface-Layer Parameterization Scheme. Results from Numerical Experiments Including the Soil Moisture Analysis.

No. 2: Reinhold Schrodin and Erdmann Heise (2001):
The Multi-Layer Version of the DWD Soil Model TERRA_LM.

No. 3: Günther Doms (2001):
A Scheme for Monotonic Numerical Diffusion in the LM.

No. 4: Hans-Joachim Herzog, Ursula Schubert, Gerd Vogel, Adelheid Fiedler and Roswitha Kirchner (2002):
LLM ⁻ the High-Resolving Nonhydrostatic Simulation Model in the DWD-Project LITFASS.
Part I: Modelling Technique and Simulation Method.

No. 5: Jean-Marie Bettems (2002):
EUCOS Impact Study Using the Limited-Area Non-Hydrostatic NWP Model in Operational Use at MeteoSwiss.

No. 6: Heinz-Werner Bitzer and Jürgen Steppeler (2004):
Description of the Z-Coordinate Dynamical Core of LM.

No. 7: Hans-Joachim Herzog, Almut Gassmann (2005):
Lorenz- and Charney-Phillips vertical grid experimentation using a compressible non-hydrostatic toy-model relevant to the fast-mode part of the 'Lokal-Modell'

No. 8: Chiara Marsigli, Andrea Montani, Tiziana Paccagnella, Davide Sacchetti, André Walser, Marco Arpagaus, Thomas Schumann (2005):
Evaluation of the Performance of the COSMO-LEPS System

No. 9: Erdmann Heise, Bodo Ritter, Reinhold Schrodin (2006):
Operational Implementation of the Multilayer Soil Model

No. 10: M.D. Tsyrulnikov (2007):
Is the particle filtering approach appropriate for meso-scale data assimilation?

No. 11: Dmitrii V. Mironov (2008):
Parameterization of Lakes in Numerical Weather Prediction. Description of a Lake Model.

No. 12: Adriano Raspanti (2009):
Final report on priority project VERSUS (VERification System Unified Survey).

No. 13: Chiara Mirsigli (2009):
Final report on priority project SREPS (Short Range Ensemble Prediction System).

No. 14: Michael Baldauf (2009):
COSMO Priority Project "Further Developments of the Runge-Kutta Time Integration Scheme" (RK); Final Report.

No. 15: Silke Dierer (2009):
COSMO Priority Project "Further Developments of the Runge-Kutta Time Integration Scheme" (RK); Final Report.

No. 16: Pierre Eckert (2009):
COSMO Priority Project "INTERP"; Final Report.

No. 17: D. Leuenberger, M. Stoll, A. Roches (2010):
Description of some convective indices, implemented in the COSMO model.

No. 18: Daniel Leuenberger (2010):
Statistical Analysis of high-resolution COSMO Ensemble forecasts, in view of Data Assimilation.

No. 19: A. Montani, D. Cesari, C. Marsigli, T. Paccagnella (2010):
Seven years of activity in the field of mesoscale ensemble forecasting by the COSMO-LEPS system: main achievements and open challenges.